Impact of Alginate on the Physicochemical Properties and Reactivity of Iron Oxides

Tarek Najem

A thesis submitted to the University of Ottawa in partial fulfilment of the requirements for the Doctorate in Philosophy degree in Earth Sciences, Specialization in Chemical and Environmental Toxicology

Ottawa-Carleton Geoscience Centre
and the Department of Earth and Environmental Sciences,
University of Ottawa,
Ottawa, Canada

Abstract

Iron (Fe) minerals often associate with natural organic matter (OM), ranging from complex compounds like humic acids to simple ligands such as citrate and oxalate, in soils and aquatic systems. These Fe-OM interactions occur through microbial mediation, OM sorption to Fe minerals, or mineral formation in the presence of OM (coprecipitation). Such associations influence the sorption capacity of Fe minerals for foreign species (e.g., phosphate, arsenate, trace metals), their thermodynamic stability, and overall physicochemical and mineralogical characteristics. This study aimed to (1) examine how OM affects the properties and bioavailability of common Fe (oxyhydr)oxides—ferrihydrite (Fh), lepidocrocite (Lp), and goethite (Gt). These minerals were synthesized in the presence of Na-alginate (as a model OM) at C/Fe ratios of 0, 0.5, 1.0, and 1.5 mol:mol. OM notably altered mineral surface area, porosity, and crystallinity. Surprisingly, microbial Fe(III) reduction kinetics were comparable between coprecipitates and pure minerals. However, the extent of reduction varied by mineral: 2-line Fh coprecipitates showed ~15% lower reduction, whereas Lp and Gt coprecipitates exhibited only 5–7% higher reduction relative to pure minerals. These findings suggest that OM effects on Fe bioavailability are mineral-specific and more complex than previously thought, emphasizing the need to consider both mineral type and OM interactions in Fe cycling studies.

To further explore the impact of additional environmental variables, the study (2) investigated how phosphate (P) sorption mode, adsorption versus coprecipitation (P/Fe 0, 0.01, and 0.1 mol:mol), influences the properties and reactivity of alginate-Fh composites (C/Fe 0 and 1.0). P-OM-Fe coprecipitates showed the highest microbial and chemical reducibility. High P loading, irrespective of sorption mode, nearly completely stabilized Fh against transformation to more crystalline phases—more effectively than alginate alone. Notably, coprecipitated P and OM

together conferred added resistance to mineral transformation following biotic reduction. These findings underscore the importance of considering both OM and P, and how P is incorporated, when evaluating the environmental stability and reactivity of Fe minerals, with implications for soil fertility, contaminant mobility, and nutrient cycling.

Finally, the study (3) evaluated the effect of γ-irradiation (25 kGy) as a sterilization method on OM-Fe coprecipitates. Post-irradiation, Fe(III) dissolution and reduction increased with OM content, and particle size varied based on the mineral coprecipitate type, while specific surface area and porosity were altered. Mössbauer spectroscopy revealed increased Fh crystallinity after irradiation, although bulk mineralogy remained unchanged. Interestingly, microbial reduction rates post-irradiation remained similar to untreated samples, yet the extent of Fe(III) reduction, particularly for Fh coprecipitates, increased by up to 28%. Slight increases in bioreduction were also seen for select Lp and Gt coprecipitates. These results highlight that γ-irradiation can modify key physical and chemical characteristics of Fe-OM composites, potentially skewing measurements of bioavailability and contaminant binding in sterilized samples.

Taken together, these findings deepen our understanding of how OM, phosphate, and experimental treatments affect the environmental reactivity and transformation of Fe (oxyhydr)oxides. This knowledge is essential for improving models of carbon cycling under reducing conditions, and for developing strategies to manage nutrient and metal mobility in soils and sediments.

Résumé

Les minéraux de fer (Fe) s'associent souvent à la matière organique (MO) naturelle, allant de composés complexes comme les acides humiques à des ligands simples comme le citrate et l'oxalate, dans les sols et les systèmes aquatiques. Ces interactions Fe-MO se produisent par médiation microbienne, par sorption de la MO aux minéraux de fer ou par formation de minéraux en présence de MO (coprécipitation). De telles associations influencent la capacité de sorption des minéraux de fer pour d'autres espèces solubles (p. ex., phosphate, arséniate, métaux traces), leur stabilité thermodynamique et leurs caractéristiques physico-chimiques et minéralogiques. Cette étude visait à (1) examiner l'influence de la MO sur les propriétés et la biodisponibilité d'(oxyhydr)oxydes de fer communs: ferrihydrite (Fh), lépidocrocite (Lp) et goethite (Gt). Ces minéraux ont été synthétisés en présence d'alginate de sodium (comme MO modèle) à des rapports C/Fe de 0, 0,5, 1,0 et 1,5 mol:mol. La MO a considérablement modifié la surface minérale, la porosité et la cristallinité mais la cinétique de réduction microbienne du Fe(III) était comparable entre les divers coprécipités et les minéraux purs. Cependant, l'ampleur de la réduction variait selon le minéral : les coprécipités Fh à 2 lignes présentaient une réduction inférieure d'environ 15 %, tandis que les coprécipités Lp et Gt présentaient une réduction supérieure de seulement 5 à 7 % par rapport aux minéraux purs. Ces résultats suggèrent que les effets de la MO sur la biodisponibilité du Fe sont spécifiques à chaque minéral et plus complexes qu'on ne le pensait auparavant, soulignant la nécessité de prendre en compte à la fois le type de minéral et les interactions de la MO dans les études sur le cycle du Fe.

Afin d'explorer plus en détail l'impact de variables environnementales supplémentaires, l'étude (2) a examiné comment le mode de sorption du phosphate (P), adsorption versus coprécipitation (P/Fe 0, 0,01 et 0,1 mol:mol), influence les propriétés et la réactivité des

composites alginate-Fh (C/Fe 0 et 1,0). Les coprécipités P-OM-Fe ont montré la plus grande réductibilité microbienne et chimique. Une charge élevée en P, quel que soit le mode de sorption, a presque complètement stabilisé le Fh contre la transformation en phases plus cristallines — plus efficacement que l'alginate seul. Notamment, le P et l'OM coprécipités ensemble ont conféré une résistance accrue à la transformation minérale après la réduction biotique. Ces résultats soulignent l'importance de prendre en compte à la fois l'OM et le P, et la façon dont le P est incorporé, lors de l'évaluation de la stabilité environnementale et de la réactivité des minéraux Fe, avec des implications pour la fertilité des sols, la mobilité des contaminants et le cycle des nutriments.

Enfin, l'étude (3) a évalué l'effet de l'irradiation γ (25 kGy) comme méthode de stérilisation sur les coprécipités MO-Fe. Après irradiation, la dissolution et la réduction du Fe(III) ont augmenté avec la teneur en MO, et la taille des particules a varié en fonction du type de coprécipité minéral, tandis que la surface spécifique et la porosité ont été modifiées. La spectroscopie Mössbauer a révélé une cristallinité accrue du Fh après irradiation, bien que la minéralogie globale soit restée inchangée. Il est intéressant de noter que les taux de réduction microbienne après irradiation sont restés similaires à ceux des échantillons non traités, mais l'ampleur de la réduction du Fe(III), en particulier pour les coprécipités Fh, a augmenté jusqu'à 28 %. De légères augmentations de la bioréduction ont également été observées pour certains coprécipités Lp et Gt. Ces résultats soulignent que l'irradiation γ peut modifier les caractéristiques physiques et chimiques clés des composites Fe-MO, faussant potentiellement les mesures de biodisponibilité et de liaison des contaminants dans les échantillons stérilisés.

En résumé, ces découvertes approfondissent notre compréhension de l'influence de la matière organique, du phosphate et des traitements expérimentaux sur la réactivité environnementale et la transformation des (oxyhydr)oxydes de fer. Ces connaissances sont

essentielles pour améliorer les modèles de cycle du carbone en conditions réductrices et pour développer des stratégies de gestion de la mobilité des nutriments et des métaux dans les sols et les sédiments.

Acknowledgments

I would like to express my deepest gratitude to my supervisor Dr. Danielle Fortin for her patience, guidance, scientific support, and encouragement throughout this research. Her positive attitude made my experience a remarkable one. My sincerest thanks to Daniela Quintero, Ende Zuo, Birendra Sapkota, and Sarina Cotroneo for their friendship, and making the experience of graduate studies a special one. I'm indebted to Dr. Nimal de Silva, Smita Mohanty, and Glenn Poirier, for sharing their expertise with me throughout my studies, the plethora of knowledge they provided me with regards to analytical techniques and analytical instruments is immeasurable, I feel privileged to have been allowed to get to know and learn from them.

Throughout my studies I had the unforgettable opportunity to work with and to know many professors and technicians, i.e. Dr. Ian Clark, Dr. Tom Al, Paul Middlestead, Wendy Abdi, Kerry Klassen, Dominique Bower, Guadalupe Maldonado Sanchez, Monika Wilk, David Zal, and Jeremy Potvin. I thank them all for their support and friendship, I learned a lot and shared a great time.

Finally, I dedicate this work to the special people in my life, my wife and son, parents, brother, and sister and her husband. Thank you for your unconditional support and love.

Table of Contents

List of Tables

List of Figures

Preface

This thesis is organized as manuscripts for publication. As such, the chapters may contain some repetition of Chapter 1 of this thesis. The entire thesis was written by the candidate and all the results presented in this thesis are based on measurements performed by the candidate. The experiments carried out by the candidate include: synthesis of synthetic 2-line ferrihydrite, lepidocrocite, goethite in the presence and absence of Na-alginate, synthesis of 2-line ferrihydrite in the presence or absence of phosphate, preparation of 2-line ferrihydrite with adsorbed phosphate, chemical dissolution experiments, and all of the microbial reduction experiments. The analytical measurements and analyses using various instrumentations that were carried out by the candidate include X-ray diffraction, Scanning Electron Microscopy, FTIR-ATR, electrophoretic mobility, and N_2-adsorption desorption isotherms for the determination of BET. The candidate also performed all of the PHREEQ-C modeling along with data interpretation and statistical analyses. ICP measurements and analyses were performed by Dr. Nimal de Silva and Smita Mohanty at the University of Ottawa. Carbon content measurements and analyses were performed by the staff at the Ján Veizer Stable Isotope Laboratory at the University of Ottawa. Mössbauer spectroscopy measurements and data analyses were performed by Dr. Prachi Joshi at the University of Tuebingen in collaboration with Dr. Andreas Kappler. Sterilization by γ-irradiation was performed by the technicians at Nordion Canada Inc.

Chapter 1: General Introduction

1. Iron (oxyhydr)oxides and Organic Matter Association

1.1. Formation and occurrence

Organic matter (OM) is a heterogeneous mixture of molecular compounds formed by the decay of terrestrial organic material or produced in aquatic systems by microbiota, and it is ubiquitous in natural waters (Kleber et al., 2015; Vindedahl et al., 2016; Song et al., 2022). The key molecular characteristics that define the reactivity of OM include aromaticity; functional groups like catechol, carboxylate, and phenolic moieties; amino acid content; and O, S, N, and P composition (Kleber et al., 2015; Vindedahl et al., 2016; Song et al., 2022). These features collectively determine the hydrophobic or hydrophilic nature of OM. Among the OM constituents, humic substances—particularly humic (HA) and fulvic acids (FA)—and extracellular polymeric substances (EPS) are among the most extensively studied in relation to interactions with iron oxides (including iron(III) oxides, oxyhydroxides, and hydroxides) (Kleber et al., 2015; Vindedahl et al., 2016; Song et al., 2022). Iron oxides are also ubiquitous in aquatic and terrestrial systems and can interact with various chemical compounds in natural environments due to their unique characteristics such as large surface area and variable surface charge (Cornell and Schwertmann, 2003; Kleber et al., 2015; Vindedahl et al., 2016; Song et al., 2022). These interactions are important for transport, bioavailability, and immobilization of OM, nutrients, heavy metals, and metalloids in the environment (Cornell and Schwertmann, 2003; Kleber et al., 2015; Fabisch et al., 2016; Vindedahl et al., 2016; Song et al., 2022; Martens et al., 2023). The significance of Fe-OM interactions is supported by observed positive correlations between Fe and carbon (C) concentrations in soils and sediments (Lalonde et al., 2012; Kleber et al., 2015; Vindedahl et al., 2016; Zhao et al., 2017; Song et al., 2022; Dong et al., 2023; Li et al., 2023; Martens et al., 2023).

Furthermore, it has been proposed that Fe minerals function as a long-term "rusty sink," stabilizing organic C in sediments (Lalonde et al., 2012). This mechanism has been estimated to account for the preservation of 21.5 ± 8.6% of sedimentary organic C in the global ocean (Lalonde et al., 2012; Kleber et al., 2015; Li et al., 2023).

The interactions between OM and iron oxides form through a number of pathways that include adsorption and coprecipitation (Figure 1-1) (Eusterhues et al., 2008; Kleber et al., 2015; Vindedahl et al., 2016). Adsorption on the oxide surface occurs due to the difference in chemical and structural features of both OM and mineral surface (Kleber et al., 2015; Vindedahl et al., 2016; Song et al., 2022). This reaction typically involves the binding of OM functional groups—such as carboxyl, phenolic, and hydroxyl moieties— through electrostatic attraction, ligand exchange, and/or hydrogen bonding to the surface hydroxyl groups of the already formed iron oxides (Vindedahl et al., 2016). Recent NEXFAS spectroscopy showed that as the number of carboxyl functional groups present in simple carboxylic OM compounds increases, the number of carboxylate-Fe bonds formed between the carboxyl functional groups and the ferrihydrite particles increases, and thus the binding strength, stability and persistence of the OM associated with ferrihydrite also increases (Curti et al., 2021). For EPS, which are composed of polysaccharides and proteins, with minor amounts of nucleic acids and lipids, phosphate groups play an important role in binding to the surface of the iron oxide through the formation of innersphere Fe-phosphate complexes (Kleber et al., 2015). Time and the chemistry of the solution (e.g. pH, ionic strength, competing anions) are also important factors to consider for adsorption reactions (Kleber et al., 2015; Vindedahl et al., 2016). Typically, longer residence time often leads to a higher uptake of OM due to diffusion into the micropores of the iron oxides (Kaiser et al., 1997; Kaiser, 2003; Kaiser et al., 2007), whereas acidic conditions enhance OM adsorption, which favor the formation

of innersphere surface complexes, while at neutral to alkaline pH, weaker outersphere complexes predominate (Kleber et al., 2015; Vindedahl et al., 2016). Furthermore, new bonds may form depending on the presence of divalent cations (e.g. Ca^{2+}) in solution that may enhance the uptake of OM via surface charge modification and bridging reactions (i.e. ternary complexes) (Kleber et al., 2015; Vindedahl et al., 2016; Sowers et al., 2018; Adhikari et al., 2019).

In contrast to adsorption, the formation of Fe-OM mineral coprecipitates typically begins as OM binds hydrolyzed Fe species through ligand exchange or coordination reactions thereby forming soluble or colloidal Fe-OM complexes, and as the solution reaches a state of oversaturation the Fe-OM complexes begin to precipitate as hydroxide phases intimately associated with OM (Schwertmann et al., 2005; Eusterhues et al., 2008; Kleber et al., 2015; Li et al., 2023). Furthermore, as the iron oxide phases nucleate and continue to grow or aggregate, OM in solution can also adsorb onto the surfaces of the forming particles or become entrapped within a mineral matrix during the aggregation of the newly forming particles (Figure 1-1) (Eusterhues et al., 2008; Kleber et al., 2015; Li et al., 2023). Therefore, these reactions typically lead to a much higher uptake of OM than adsorption alone, since the extent of adsorption to pre-formed iron oxides is limited by available reactive sites on the surface of the mineral (Chen et al., 2014; Curti et al., 2021). For example, at comparable initial C/Fe molar ratios, Chen et al. (2014) reported a maximum of ratio of 17.5 in coprecipitates vs. 4.6 following adsorption. The authors attributed this difference due to the formation of insoluble Fe(III)-organic C complexes in the coprecipitates. It should be also noted that extent of Fe(III) polymerization and mineral precipitation is controlled by the concentration of OM in solution, such that high concentrations may suppress the polymerization of $Fe(O,OH)_6$ octahedra to the formation of stable Fe oligomers (Baalousha, 2009; Angelico et al., 2014; Vindedahl et al., 2016). Under such circumstances repulsion between the

negatively charged Fe-OM oligomers dominate, thereby preventing further polymerization and aggregation reactions (Baalousha, 2009; Angelico et al., 2014; Vindedahl et al., 2016).

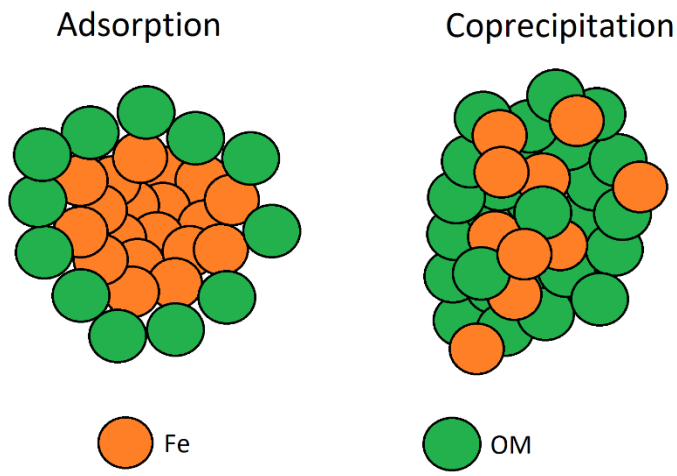

Figure 1-1: Simple illustration to differentiate and visualize adsorption and coprecipitation reactions of OM and iron oxides.

One example of Fe-OM coprecipitates is biogenic iron oxides (BIOS), which form from the metabolic activity of a diverse range of species of Fe(II)-oxidizing bacteria (FeOB) that inhabit a broad range of environments, including: pH-neutral and acidic, oxic, oxic-anoxic, anoxic, and hydrothermal settings (Figure 1-2) (Ferris et al., 2000; Ferris, 2005; Fortin and Langley, 2005; Kappler and Straub, 2005; Melton et al., 2014). Although the chemical oxidation of dissolved Fe(II) by molecular O_2 is very rapid at circumneutral pH and O_2 saturated conditions (half-life of ~5 minutes) (Stumm and Morgan, 2013), microaerophilic FeOB, such as *Gallionella* spp. and *Leptothrix* spp., are capable of competing with O_2 for Fe(II) by occupying limited oxic-anoxic zones that are characterized by elevated concentrations of Fe(II) and low pO_2 (Fortin and Langley, 2005; Hedrich et al., 2011). These conditions occur in a broad range of environments, including: hydrothermal sea vents (Kennedy et al., 2003; Langley et al., 2009e; Toner et al., 2009; Toner et al., 2012), soils (Cismasu et al., 2016), wetland plant rhizospheres (Maisch et al., 2019), lake

sediments (Fortin et al., 1993), mining impacted environments (Chan et al., 2004; Fabisch et al., 2016), and ferriferous groundwater discharge zones (Gault et al., 2011; ThomasArrigo et al., 2022). Within these environments, the formation of BIOS stems from the oxidation of Fe(II) to Fe(III), and the eventual precipitation of iron oxides. The iron oxides precipitate on or in close proximity of cell surfaces or EPS, such as twisted stalks and sheaths generated by the FeOB *Gallionella ferruginea* and *Leptothrix ochracea*, respectively (Figure 1-2) (Chan et al., 2004; Fortin and Langley, 2005; Kappler and Straub, 2005; Chan et al., 2009; Chan et al., 2011). Furthermore, the negatively charged functional groups on cell surfaces, bacteria, including non-Fe metabolizing bacteria, and extracellular surfaces act as passive heterogeneous templates for the sorption, nucleation, and precipitation of iron oxides that formed chemically in solution (Warren and Ferris, 1998; Châtellier et al., 2001; Châtellier et al., 2004; Fortin and Langley, 2005; Rancourt et al., 2005).

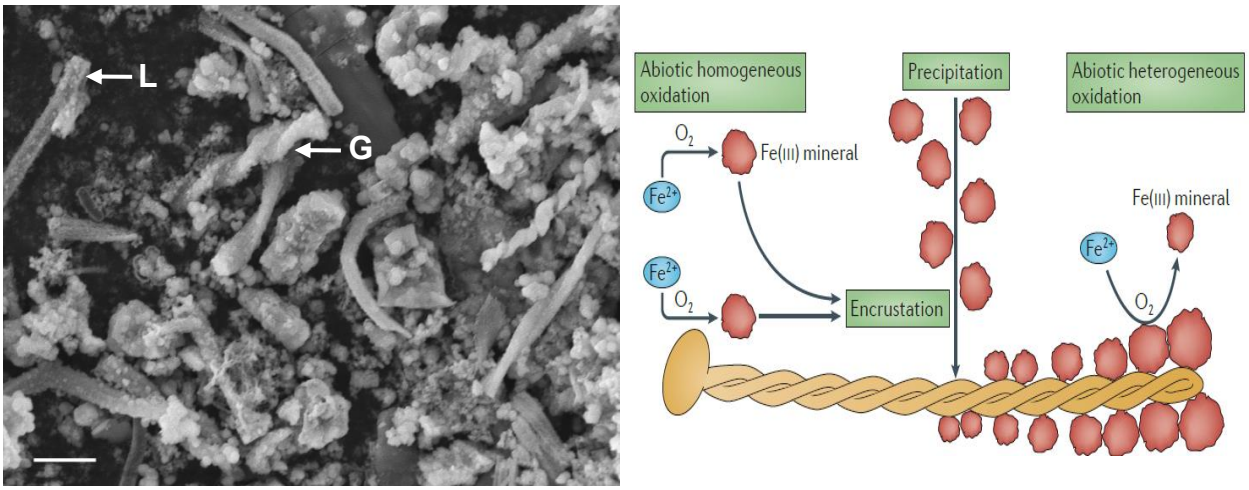

Figure 1-2: Left - scanning electron micrograph of a naturally occurring BIOS sample showing the sheaths-like structures and twisted stalks of the FeOB *Leptothrix* spp. (L) and *Gallionella* spp. (G), respectively. Right – a simple illustration showing how BIOS are formed through the activity of *Gallionella* spp. (Melton et al., 2014).

1.2. Mineralogy and environmental significance

The most common iron oxide that precipitates in close association of the cells and/or their EPS within BIOS is a short-ranged ordered phase that resembles the poorly crystalline mineral 2-line ferrihydrite ($Fe_{10}O_{14}(OH)_2$) (Langley et al., 2009b; Toner et al., 2009; Gault et al., 2011; ThomasArrigo et al., 2022). Other minerals including the crystalline iron oxides lepidocrocite (γ-FeOOH), goethite (α-FeOOH), akaganeite (β-FeOOH) or hematite (α-Fe_2O_3), were also identified comprising <30% of the total Fe (Chan et al., 2004; Hallberg and Ferris, 2004; Fortin and Langley, 2005; Chan et al., 2009; Chan et al., 2011; ThomasArrigo et al., 2022). 2-line ferrihydrite is a metastable Fe(III) mineral with a hexagonal close-packed structure of oxygen and hydroxide anions (Cornell and Schwertmann, 2003). 2-line ferrihydrite is also present in soils, sediments, and aqueous environments, and it is an environmentally important iron oxide as it is considered to be the most efficient adsorbent of nutrients (e.g., PO_4), trace metals (e.g., Cu, Co, Zn, etc.), OM, and organic and inorganic contaminants (e.g., As) (Fortin et al., 1993; Cornell and Schwertmann, 2003; Eusterhues et al., 2008; Baken et al., 2015; Baken et al., 2016; Fabisch et al., 2016). This efficiency stems from its nanometric size (1-6 nm), high specific surface area (SSA, 300-600 m^2/g), and abundance in the environment (Cornell and Schwertmann, 2003).

Adsorption of OM or foreign species to the surface of the iron oxides does not directly influence the mineral properties of the oxide such as crystallinity, crystallite size, and the identity of the mineral. However, this reaction modifies the physicochemical properties of minerals. For example, the addition of negatively charged dissolved HA to suspensions of positively charged iron oxide at near neutral pH conditions favors the aggregation of the particles as a consequence of the changes in the mineral's surface charge (Baalousha, 2009; Angelico et al., 2014; Colombo et al., 2015; Vindedahl et al., 2016). In contrast, high concentration of HA leads to steric stabilization and electrostatic repulsion among the Fe-OM particles (Angelico et al., 2014;

Vindedahl et al., 2016). Nonetheless, the adsorption of OM to the mineral surface leads to changes in the SSA of the mineral and consequently its adsorptive capacity (Chen et al., 2014; Kleber et al., 2015). OM may also inhibit anion adsorption to the mineral surface by ion complexation or through competition for reactive surface sites. Numerous studies have documented these mechanisms while examining the influence of soil OM, FA, HA, and EPS on the adsorption of Cd(II), PO_4, AsO_4, OM, and other foreign species onto iron oxides (Mikutta et al., 2014; Kleber et al., 2015; Song et al., 2022). More recent research has also indicated that the adsorption of soil OM onto mineral surfaces can protect OM from microbial degradation (Eusterhues et al., 2014b). Likewise, surface coatings of OM may shield iron oxides from microbial Fe(III) reduction (Eusterhues et al., 2014a).

In contrast to adsorption, coprecipitation alters the mineralogical characteristics as well as the physicochemical properties of an iron oxide as a consequence of Fe coordination, and distortion of octahedra during precipitation (Eusterhues et al., 2008; Kleber et al., 2015). For example, BIOS collected from various environments and those formed under laboratory conditions were observed to possess lower crystallinity and smaller particle size when compared to synthetic mineral equivalents as determined by various analytical techniques such as K-edge extended x-ray absorption fine structure and Mössbauer spectroscopy (Toner et al., 2009; Muehe et al., 2013; Vollrath et al., 2013; Cismasu et al., 2016; Sowers et al., 2017; Field et al., 2019; ThomasArrigo et al., 2022). Mössbauer spectroscopy of Fe-forest floor extract (FFE) coprecipitates revealed a mixture of mineral-organic phases and ~10% of Fe was bound in Fe(II)-organic complexes as a consequence of Fe(III) reduction by reactive functioanl groups in the FFE (Schwertmann et al., 2005). Likewise, coprecipitates of FFE of increasing C content possessed decreased ferrihydrite particle diameters and fewer lattice planes (Eusterhues et al., 2008). A similar observation was

reported for ferrihydrite coprecipitated with bacterial cells and varying concentrations of the polysaccharides polygalacturonic acid and alginic acid (Rancourt et al., 2005; Mikutta et al., 2008). Adding further to this complexity is that the extent of disruption to the crystalline structure of iron oxides was shown to vary according to the OM content of reactive functional groups such as O-alkyl, carboxyl, and amine/amide groups (Chen et al., 2018). Several studies have also reported changes in the macroscopic properties of the minerals following coprecipitation. For example, the general consensus is that ferrihydrite-OM coprecipitates (HA, FA, soil OM, and EPS) possess a lower SSA (determined by N_2 gas adsorption at 77 K) than that of pure 2-line ferrihydrite as a consequence of the low N_2-surface area of OM, pore blockage by OM, and occlusion of interparticle nanometer-sized pores (Eusterhues et al., 2008; Mikutta et al., 2008; Kleber et al., 2015; Najem et al., 2016; Poggenburg et al., 2016). Thus, increasing C content often leads to lower SSA approaching values <40 m^2/g, as compared to >300 m^2/g for pure ferrihydrite (Mikutta et al., 2008; Chen et al., 2014). Consistent with these observations, naturally occurring BIOS were also reported to possess a lower SSA than that of synthetic iron oxide equivalents (Najem et al., 2016). In contrast, the SSA increased and decreased with increasing C content in goethite-FA coprecipitates, whereas the SSA of Fe mineral coprecipitates that formed in the presence of citrate increased with increasing C content (Liu, 1999; Liu et al., 2019b). It should be noted that the exent of changes in the SSA in ferrihydrite-OM coprecipitates could depend on the type of OM. For example, at equivalent initial C/Fe molar ratios, ferrihydrite-EPS coprecipitates had lower SSA than that of ferrihydrite-soil OM coprecipitates (Poggenburg et al., 2016). This observation was attributed to the difference in the overall particle/aggregate size such that the aggregate size of a ferrihydrite-EPS coprecipitate was larger than those of ferrihydrite-soil OM coprecipitates. Other studies also reported a decrease in particle/aggregate size as the C content increased for

ferrihydrite-HA coprecipitates, which was attributed to the electrostatic replusion between the negatively charged particles that prevented aggregation of particles (Angelico et al., 2014; Adhikari et al., 2017). At a low C/Fe molar ratio of 0.5, however, ferrihydrite-HA coprecipitates formed larger aggregates than that of synthetic ferrihydrite as a consequence of charge neutralization and bridging of particles (Adhikari et al., 2017). Finally, common to all Fe-OM coprecipitates is the observation that the associated OM decreases the point of zero charge compared to that of pure mineral phases (Mikutta et al., 2008; Shimizu et al., 2013; Kleber et al., 2015).

Changes to the macroscopic and mineralogical properties of Fe-OM coprecipitates also influence the sorptive properties and bioavailability of both the OM and Fe(III) fractions. For example, microbial degradation was slowed for a polysaccharide-rich FEE and inhibited for lignin when these compounds were associated with ferrihydrite through adsorption or coprecipitation (Eusterhues et al., 2014b). Previous studies have also demonstrated the capability of BIOS to immobilize a significant amount of metal(loid)s under laboratory and natural settings, which has been attributed to the presence of the organic fraction that provides additional binding sites (Ferris et al., 2000; Langley et al., 2009d; Fabisch et al., 2016; Hao et al., 2016; Whitaker and Duckworth, 2018; Field et al., 2019). Similar conclusions were reported for iron oxide coprecipitated with EPS, citric acid, aspartic acid, cysteine, FA, or HA (Moon and Peacock, 2012; Mikutta et al., 2014; Kleber et al., 2015; Chen et al., 2018; Liu et al., 2019b). Therefore, the effectiveness of BIOS at immobilizing metal(loid)s increases with decreasing iron content, hence an increase in the relative proportion of OM (Ferris et al., 1999; Ferris et al., 2000). Hao et al. (2016) assessed the sorption and partitioning of heavy metals (Au, Cd, Cr, CrO_4^{-2}, Cu, Hg, Ni, Pd, tributyltin, and Zn) to bacteria-EPS-iron oxide aggregates formed by a pure culture of the photoautotrophic FeOB

Rhodobacter ferrooxidans strain SW2. The authors found that the heavy metals were preferentially bound by microbial cells and their EPS, and that Fe(III) and Fe(II) competed for the same sites, particularly on EPS. Eickhoff et al. (2014), however, found that synthetic 2-line ferrihydrite adsorbed a higher amount of Ni^{2+} when compared to that of biogenic ferrihydrite produced by a pure culture of the freshwater and marine photoautotrophic FeOB *Rhodobacter ferrooxidans* SW2 and *Rhodovulum iodosum*, respectively, which was attributed to the competition between Ni^{2+} and cell derived OM for sorption sites on the biogenic 2-line ferrihydrite. In contrast, Langley et al. (2009c) showed that BIOS dominated by *Leptothrix*-like sheath structures were more efficient at binding Sr^{2+} (S_{max} of 3.41μmol/g) than synthetic 2-line ferrihydrite (S_{max} of 1 μmol/g). Martinez et al. (2003) suggested that BIOS formed from the activity of microaerophilic FeOB provide heterogeneous reactive sites whereby some heavy metals preferentially bind to the mineral fraction while others preferentially bind to the organic fraction. BIOS dominated by *Gallionella*-like stalks that formed within mine water (pH 6.0) contaminated with heavy metals were found to efficiently scavenge heavy metals, Cu, in particular, was found to preferentially bind to the iron oxide fraction (Fabisch et al., 2016). Sowers et al. (2017) reported that As(III) exhibited similar sorption extents on BIOS and synthetic 2-line ferrihydrite, while As(V) sorption to BIOS was roughly three times greater than that observed for the synthetic counterpart. This efficiency was attributed to increased outersphere adsorption and possible formation of As-Fe-organic ternary complexes (Sowers et al., 2017). In contrast, BIOS produced by *Acidovorax* sp. strain BoFeN1 adsorbed ~8x As(V) less than iron-mineral-based commercial filter systems due to the repulsion between the negatively charged BIOS and As(V) (Kleinert et al., 2011). The extent of phosphate adsorption to ferrihydrite-HA coprecipitates either decreased or did not change with increasing C content, in which case the

difference in the properties of the HAs (e.g. the content of functional groups) determined this observation (Chen et al., 2018).

Collectively, these studies show that OM induced modifications of various iron oxides likely play an important role in the attenuation of different contaminants in the environment, moreover these associations have important consequences on the fate and cycling of C in the environment. However, the mobility and fate of associated contaminants and C are dependent on the redox state of Fe.

1.3. Mineral stability

2-line ferrihydrite is the least stable and most soluble iron oxide mineral and it tends to transform into more stable and crystalline iron oxide minerals including goethite, hematite, and magnetite (Cornell and Schwertmann, 2003). The kinetics of transformation, pathway, and end product strongly depend on the prevailing geochemical conditions (e.g. pH, temperature, ionic strength, redox potential) and the concentration and type of various foreign species such as cations, anions, and OM that could enhance, retard, or inhibit transformation (Cornell and Schwertmann, 2003). Transformation may proceed via two competing pathways, including: (1) dissolution of precursor ferrihydrite nanoparticles and the subsequent precipitation of goethite (dissolution-reprecipitation), or (2) dehydration-aggregation and internal rearrangement of ferrihydrite nanoparticles to form hematite (solid-state transformation) (Cornell and Schwertmann, 2003). Subsequent crystal growth may proceed through Ostwald ripening or oriented aggregation of nanoparticles (Penn and Soltis, 2014).

The transformation of a highly reactive mineral to crystalline phases has important ecological and environmental implications, as the varying properties of the iron phases influence their biogeochemical reactivity and in turn affect the mobility and fate of nutrients and

contaminants that are associated with the iron phase. Reduced SSA of the resulting crystalline minerals (e.g. goethite 8-200 m^2/g, hematite 4-100 m^2/g) leads to reduced capacity to uptake foreign species. Transformation may also lead to the desorption or the incorporation of associated foreign species. The latter is particularly desirable because crystalline iron oxides are recalcitrant to microbial Fe(III) reduction (Roden and Zachara, 1996; Hansel et al., 2003). However, the resulting crystalline iron phases with incorporated foreign species are also subject to Fe^{2+} mediated recrystallization under reducing conditions, a process that may lead to the re-release of incorporated foreign species (e.g. Co^{2+}, Ni^{2+}, Cu^{2+}) (Latta et al., 2012; Hua et al., 2023).

Foreign species adsorbed and/or incorporated by ferrihydrite often result in a concentration dependent effect on the kinetics and extent of transformation, and in turn modify the identity/proportion of the mineral products that form (Cornell and Schwertmann, 2003; Chen et al., 2015). Inhibition of transformation can proceed by either blocking dissolution sites on ferrihydrite and the nucleation of crystalline phases in solution or linking ferrihydrite nanoparticles into an immobile network thereby preventing their aggregation (Cornell and Schwertmann, 2003; Najem et al., 2016). For example, increasing the concentration of silicate (Si/Fe mol ratio 0.001-0.1) was found to progressively inhibit the transformation of ferrihydrite into goethite at 70°C and alkaline conditions (pH 11), and where transformation occurred, silicate was found to promote the formation of hematite (Cornell et al., 1987). Similarly, the degree of transformation of ferrihydrite coprecipitated or adsorbed with increasing concentrations of phosphate (P/Fe mol ratio 0-0.03) progressively diminished, and where transformation occurred, phosphate was found to promote the formation of hematite over goethite (Gálvez et al., 1999; Namayandeh et al., 2023; Namayandeh et al., 2024). Thus, innersphere binding anions promote the transformation pathway into hematite due to their ability to bind nanoparticles and promote aggregation through surface

charge changes (Gálvez et al., 1999; Namayandeh et al., 2023). OM can also stabilize 2-line ferrihydrite preventing its transformation to goethite or hematite (Cornell and Schwertmann, 2003).

For OM, complexation with aqueous Fe(III) may inhibit iron oxide nucleation, and OM can associate with the surface of the neoformed mineral nuclei and crystals to inhibit crystal growth as previously explained (Cornell and Schwertmann, 2003; Kleber et al., 2015; Zhao et al., 2022b; Zhao et al., 2022c). For example, naturally occurring ferrihydrite containing OM (C content of 10.23 %) was boiled in an alkaline solution, conditions which strongly favor the formation of goethite (Schwertmann, 1966). However, the mineralogy of natural ferrihydrite remained the same whereas synthetic ferrihydrite fully transformed into goethite (Schwertmann, 1966). Likewise, the proportion of the iron oxide minerals of BIOS as determined Fe-EXAFS did not change following storage at 4°C for ~5 years (Najem et al., 2016). Kennedy et al. (2004) coprecipitated 2-line ferrihydrite in the presence of variable amounts of non-Fe-metabolizing bacteria, *Bacillus subtilis*, and subjected the synthetic bacteria-ferrihydrite composites to aqueous heating at 80°C for 2 days. These authors found that hematite formation was progressively inhibited with increasing cell content and concluded that inhibition occurs when 50% of the total Fe was present as 2-line ferrihydrite and the remainder is bound/complexed as ferric iron. Within the same study, Kennedy et al. (2004) subjected marine BIOS formed from the activity of microaerophilic FeOB to similar conditions and found that BIOS resisted transformation into hematite. In addition to concentration, the effect of OM on the inhibition of transformation of ferrihydrite into crystalline phases is also a function of carboxylic acid functional group content. For example, Zhao et al. (2022c) found that the retardation effect of OM generally increases in the order pentanoic acid < hexanedioic acid < butane 1, 2, 4 tricarboxylic, thus with increasing carboxylic acid binding strength.

Under anoxic conditions, the transformation of ferrihydrite is accelerated by Fe^{2+} through reductive dissolution reprecipitation mechanism to form various end products such as mixed Fe(II)/Fe(III) phases (e.g. magnetite and greenrust), goethite, and hematite (Hansel et al., 2003; Hansel et al., 2005; Chen et al., 2015; Hua et al., 2023). The end product largely depends on the concentration of Fe^{2+} as well as foreign species and geochemical conditions (Hansel et al., 2003; Hansel et al., 2005). For example, Hansel et al. (2005) showed that 2-line ferrihydrite transforms into lepidocrocite and goethite at low Fe(II) loading (<1.0 mmol Fe(II)/g 2-line ferrihydrite) whereas magnetite, lepidocrocite, and goethite are the dominant products at high Fe(II) loadings (>1.0 mmol Fe(II)/g 2-line ferrihydrite), the proportions of which were also dependent on anions present in solution including Cl^-, SO_4^{-2}, and HCO_3^-. PO_4, however, inhibits the formation of goethite and magnetite by (1) binding to the surface of ferrihydrite thereby preventing either dissolution and subsequent reprecipitation or internal recrystallization of ferrihydrite, and (2) forming vivianite and aqueous complexes with Fe(II) thereby preventing Fe(III) from reaching the required surface loading threshold to form goethite or magnetite (Fredrickson et al., 1998; Cornell and Schwertmann, 2003; Hansel et al., 2003; Borch et al., 2007; Amstaetter et al., 2012). At Fe(II)/Fe(III) molar ratio of 0.3, ferrihydrite transformed into goethite whereas a ferrihydrite-PO_4 coprecipitate (P/Fe ~0.9 mol:mol) did not change (Kraal et al., 2022). Complete inhibition of transformation was observed for coprecipitates of ferrihydrite-OM (OM extracted from O horizon of an Ultisol) at C/Fe molar ratio 1.6 reacted with 0.2 mM or 2 mM Fe^{2+} (Chen et al., 2015). At lower C/Fe molar ratios, however, OM promoted the transformation into lepidocrocite over goethite (Chen et al., 2015). Under similar conditions and in contrast to OM extracted from O horizon of an Ultisol, polygalacturonic acid (PGA) promoted the transformation into goethite in ferrihydrite-PGA coprecipitates (Chen and Sparks, 2018). The type of OM also dictates the

transformation end products as determined by studies that utilized Fe^{2+} or HS^- as the reducing agents (Zhou et al., 2018; ThomasArrigo et al., 2020; Wang et al., 2023). For example, Zhou et al. (2018) found that ferrihydrite-HA coprecipitates (up to 1.6 C/Fe mol:mol) transformed into goethite following reaction with 2 mM Fe^{2+}, whereas ferrihydrite-FA coprecipitates (up to 1.6 C/Fe mol:mol) did not transform into crystalline end products. Mechanisms by which OM inhibit Fe(II) mediated transformation of ferrihydrite include the decreased Fe(II) adsorption, the surface blockage, and organic complexation of Fe(II) (Kleber et al., 2015; Zhou et al., 2018). OM may also accelerate the transformation of ferrihydrite into crystalline end products depending on the presence of redox active functional groups that reduce Fe(III) to Fe(II).

2. Dissimilatory Iron Reducing Bacteria

One of the factors that govern the impact of iron oxides on the mobility and bioavailability of associated contaminants is the exposure of iron oxides to anaerobic conditions, which favor the reductive dissolution of iron oxides that can be mediated by dissimilatory iron reducing bacteria (DIRB) or hydrogen sulfide (HS^-). Under pH-neutral and non-sulfidogenic conditions, the reductive dissolution of iron oxides is principally mediated by DIRB, such as *Geobacter* spp. and *Shewanella* spp., which couple the oxidation of organic matter or H_2 to the reduction of Fe(III) generating Fe(II), and energy required for growth and function (Lovley et al., 2004). The ability of DIRB to reduce iron oxides is dependent on the physicochemical properties of the mineral, including: surface area, aggregation state, crystallinity, morphology, and solubility of the iron phase (Roden and Zachara, 1996; Bonneville et al., 2004; Bonneville et al., 2009; Cutting et al., 2009). Typically, the rate and extent of microbial Fe(III) reduction increases with increasing surface area, therefore 2-line ferrihydrite is considered to be the most bioavailable Fe(III)-phase whereas crystalline iron oxides, such as hematite, goethite, and magnetite, are generally

recalcitrant to microbial Fe(III) reduction (Roden and Zachara, 1996). Under pH-neutral conditions, however, DIRB face the challenge of utilizing the poorly soluble iron oxides as terminal electron acceptors, because iron oxides cannot pass the cell membrane (Lovley et al., 2004). Consequently, DIRB have developed a number of strategies to transfer electrons to iron oxides, including: (1) electron transfer via direct contact between bacteria and the mineral surface mediated by outer membrane-bound proteins (c-type cytochromes) or conductive pili-like appendages called "nanowires" (Lovley et al., 2004; Gorby et al., 2006), (2) electron transfer by endogenous compounds generated by *Shewanella* spp. such as flavins that chelate Fe(III) and function as electron shuttles (Marsili et al., 2008; Von Canstein et al., 2008), and (3) electron transfer by exogenous redox-active compounds such as quinones and dissolved or solid-phase humic substances that also function as electron shuttles (Lovley et al., 2004; Roden et al., 2010). Through these processes, DIRB mediate a number of reactions that have important consequences on the environment, in particular the reductive dissolution of iron oxides may lead to the remobilization of adsorbed contaminants, which could have detrimental impacts on human health as prominently discussed for arsenic (Islam et al., 2004; Muehe et al., 2013). Consequently, research has focused on determining the factors that impact the rate and extent of Fe(III) reduction by DIRB as well as the release or sequestration of foreign species.

Research to date indicates that in addition to the physicochemical properties of the iron phase, concentration of DIRB (Roden and Zachara, 1996; O'Loughlin et al., 2010; Zegeye et al., 2010), geochemical conditions (e.g. pH, bicarbonate as buffer, etc.) (Fredrickson et al., 1998; Zachara et al., 2002), presence of oxyanions (e.g. PO_4^{-3}, MoO_4^{-2}, etc.) (Fredrickson et al., 1998; O'Loughlin et al., 2010), presence of electron shuttles (Fredrickson et al., 1998), and orientation of the incubation vessel (Dippon et al., 2015), affect the rate and extent of microbial Fe(III)

reduction. In turn, these factors affect the transformation pathways of ferrihydrite and the precipitation of secondary iron minerals. For example, vivianite, siderite, magnetite, goethite, lepidocrocite, and carbonate or sulfate substituted green rusts are common secondary iron minerals reported in literature (Fredrickson et al., 1998; Zachara et al., 2002; Kukkadapu et al., 2004; O'Loughlin et al., 2010; O'Loughlin et al., 2013; Dippon et al., 2015). The formation of secondary iron minerals have important consequences on subsurface environments as they are capable of transforming and/or sequestering the released contaminants adsorption and/or structural incorporation as was previously illustrated by a number of laboratory-based studies for Zn, Ni, Sr, Cd (Parmar et al., 2000; Tufano et al., 2008; Muehe et al., 2013).

2.1. Effects of OM on microbial Fe(III) reduction

In addition to the various factors discussed above that influence the rate and extent of microbial Fe(III) reduction, OM also plays a significant role (Table 1-1). OM can impact microbial Fe(III) reduction through several mechanisms (Kleber et al., 2015):

1. The mode of OM association with iron oxides—adsorption versus coprecipitation—can differently affect DIRB. Both adsorbed and coprecipitated OM may hinder Fe(III) reduction due to electrostatic repulsion between the negatively charged OM-Fe composites and bacterial cell surfaces.
2. The reduced crystallinity typically observed in Fe-OM coprecipitates may enhance Fe(III) reduction by making the minerals more reactive and accessible to microbes.
3. OM can complex with biogenic Fe(II), reducing surface passivation of minerals and cells, and thereby thermodynamically favouring continued Fe(III) reduction (Fredrickson et al., 1998; Kukkadapu et al., 2004).

4. By complexing Fe(II), OM can inhibit the transformation of less crystalline phases such as ferrihydrite or lepidocrocite into more crystalline and less bioavailable minerals, thus sustaining Fe(III) reduction.
5. OM-associated aggregates, whether formed through adsorption or coprecipitation, can vary in size and influence microbial access to reactive sites; the C content of the system is a key factor in determining the nature of these aggregates and, in turn, the extent of Fe(III) reduction.
6. The type of OM is also important. Certain forms, such as HAs, can function as electron shuttles, enhancing microbial Fe(III) reduction by bypassing the need for direct surface contact.

Shimizu et al. (2013) studied the effects of varying C/Fe ratios (0–4.8) in ferrihydrite-HA coprecipitates on Fe(III) reduction by *Shewanella putrefaciens* CN32. They found that low C/Fe ratios (≤ 1.8) suppressed Fe(III) reduction, while higher ratios (≥ 1.8) enhanced it—likely due to the release of HA into solution at higher concentrations, enabling electron shuttling. Similarly, Poggenburg et al. (2016) observed that ferrihydrite–EPS coprecipitates were reduced more slowly than ferrihydrite coprecipitated with OM extracted from the Oi horizon of a Cambisol or the Oa horizon of a Podzol by *Shewanella putrefaciens*. They also found that the reduction patterns differed depending on the bacterial species involved—*Shewanella putrefaciens*, which can use electron shuttles, versus *Geobacter metallireducens*, which requires direct surface contact. While these studies provided important insights into the impact of OM on the bioreducibility of ferrihydrite-OM composites, no studies have investigated the effects of coprecipitation of OM on the bioavailability of crystalline iron oxide phases.

Table 1-1: Summary of rates of Fe(III) reduction and extent of Fe(III) reduction by DIRB or chemical compounds, along with the reported secondary Fe minerals that formed following reduction extracted from selected studies. RR and RE correspond to relative rate and relative extent, respectively, which correspond to values calculated relative to the pure mineral phase or control in each study.

Iron oxide	DIRB/Chemical	RR	RE	Secondary Fe Mineral	Reference
Coprecipitation					
Fe-HA colloids (Aldrich HA)[a]	*Shewanella putrefaciens* CIP 80.40 T	8.2	4.5 (10 hours)	N/A	Pedrot et al. (2011)
Fh-NOM (Oi horizon)[b]	*Shewanella putrefaciens* (DSM-6067)	15	2.3	Vivianite	Poggenburg et al. 2016
Fh-NOM (Oi horizon)	*Geobacter metallireducens* (DSM-7210)	0.5	0.6	Vivianite	Poggenburg et al. 2016
Fh-NOM (Oa horizon)	*Shewanella putrefaciens* (DSM-6067)	19	3.6	None	Poggenburg et al. 2016
Fh-NOM (Oa horizon)	*Geobacter metallireducens* (DSM-7210)	0.75	0.75	None	Poggenburg et al. 2016
Fh-EPS (*Bacillus subtilis*)	*Shewanella putrefaciens* (DSM-6067)	5	1.8	Vivianite	Poggenburg et al. 2016
Fh-EPS (*Bacillus subtilis*)	*Geobacter metallireducens* (DSM-7210)	0.43	0.7	None	Poggenburg et al. 2016
Fh-FFE (C/Fe 0.41 mol:mol)	*Geobacter bremensis* (DSM 12179)	1.1	1.3	Siderite	Eusterhues et al. (2014a)
Fh-FFE (C/Fe 1.06 mol:mol)	*Geobacter bremensis* (DSM 12179)	0.8	1.08	Siderite	Eusterhues et al. (2014a)
Fh-FFE (C/Fe 2.83 mol:mol)	*Geobacter bremensis* (DSM 12179)	0.7	0.65	None	Eusterhues et al. (2014a)
Fh-FFE (C/Fe 0.41 mol:mol)	Na-Dithionite	N/A	N/A	N/A	Eusterhues et al. (2014a)
Fh-FFE (C/Fe 1.06 mol:mol)	Na-Dithionite	0.20	0.77	N/A	Eusterhues et al. (2014a)
Fh-FFE (C/Fe 2.83 mol:mol)	Na-Dithionite	0.03	0.24	N/A	Eusterhues et al. (2014a)
Fh-FFE (C/Fe 0.41 mol:mol)	*Shewanella oneidensis* MR-1	1.7	1.7	Ferrihydrite	Cooper et al. (2017)
Fh-FFE (C/Fe 1.06 mol:mol)	*Shewanella oneidensis* MR-1	1.8	1.7	Ferrihydrite	Cooper et al. (2017)
Fh-FFE (C/Fe 2.83 mol:mol)	*Shewanella oneidensis* MR-1	2.3	2.0	Ferrihydrite	Cooper et al. (2017)
Fh-HA (Elliot Soil HA) (C/Fe 0.4)	*Shewanella putrefaciens* CN32	0.73	0.7	85% ferrihydrite 9% magnetite 6% green rush	Shimizu et al. (2013)

Fh-HA (Elliot Soil HA) (C/Fe 0.8)	*Shewanella putrefaciens* CN32	0.73	0.7	82% ferrihydrite 8% magnetite 10% green rush	Shimizu et al. (2013)
Fh-HA (Elliot Soil HA) (C/Fe 1.8)	*Shewanella putrefaciens* CN32	1	1.1	74% ferrihydrite 10% magnetite 16% green rush	Shimizu et al. (2013)
Fh-HA (Elliot Soil HA) (C/Fe 4.3)	*Shewanella putrefaciens* CN32	2.8	3	60% ferrihydrite 10% magnetite 30% green rush	Shimizu et al. (2013)
Fh-PGA (C/Fe 0.36 mol:mol)[c]	Siderophore desferrioxamine B, pH 7	18.3	N/A	N/A	Mikutta and Kretzschmar (2008)
Fh-PGA (C/Fe 0.65 mol:mol)	Siderophore desferrioxamine B, pH 7	48	N/A	N/A	Mikutta and Kretzschmar (2008)
Fh-PGA (C/Fe 0.9 mol:mol)	Siderophore desferrioxamine B, pH 7	40	N/A	N/A	Mikutta and Kretzschmar (2008)
Fh-PGA (C/Fe 1.25 mol:mol)	Siderophore desferrioxamine B, pH 7	170	N/A	N/A	Mikutta and Kretzschmar (2008)
Fh-Alg (C/Fe 1.18 mol:mol)[d]	Siderophore desferrioxamine B, pH 7	183	N/A	N/A	Mikutta and Kretzschmar (2008)
Fh-NOM (Oi horizon)	Siderophore desferrioxamine B, pH 7	8.5	1	N/A	Poggenburg et al. (2018)
Fh-NOM (Oa horizon)	Siderophore desferrioxamine B, pH 7	61	4.6	N/A	Poggenburg et al. (2018)
Fh-EPS (*Bacillus subtilis*)	Siderophore desferrioxamine B, pH 7	35	1	N/A	Poggenburg et al. (2018)
BIOS	*Shewanella putrefaciens* CN32	1.66	1.07	Vivianite	Langley et al. (2009b)
BIOS	*Shewanella putrefaciens* CN32	3.33	1.2	Vivianite	Langley et al. (2009b)
BIOS	*Shewanella putrefaciens* CN32	2.9	1.2	Vivianite	Langley et al. (2009b)
Adsorption					
Fh-FFE (C/Fe 0.39 mol:mol)	*Geobacter bremensis* (DSM 12179)	0.85	1.01	Siderite	Eusterhues et al. (2014a)
Fh-FFE (C/Fe 1.04 mol:mol)	*Geobacter bremensis* (DSM 12179)	0.55	0.7	None	Eusterhues et al. (2014a)
Fh-FFE (C/Fe 2.46 mol:mol)	*Geobacter bremensis* (DSM 12179)	0.5	0.6	None	Eusterhues et al. (2014a)
Fh-FFE (C/Fe 0.39 mol:mol)	Na-Dithionite	0.3	0.75	N/A	Eusterhues et al. (2014a)
Fh-FFE (C/Fe 1.04 mol:mol)	Na-Dithionite	0.14	0.36	N/A	Eusterhues et al. (2014a)
Fh-FFE (C/Fe 2.46 mol:mol)	Na-Dithionite	0.13	0.29	N/A	Eusterhues et al. (2014a)

Fh-FFE (C/Fe 0.41 mol:mol)	*Shewanella oneidensis* MR-1	1.45	1.5	Ferrihydrite	Cooper et al. (2017)
Fh-FFE (C/Fe 1.06 mol:mol)	*Shewanella oneidensis* MR-1	1.72	1.4	Ferrihydrite	Cooper et al. (2017)
Fh-FFE (C/Fe 2.83 mol:mol)	*Shewanella oneidensis* MR-1	1.86	1.6	Ferrihydrite	Cooper et al. (2017)
Fh-NOM (Oi horizon 5 mgC/g)	Siderophore desferrioxamine B, pH 7	1.5	1.8	N/A	Poggenburg et al. (2018)
Fh-NOM (Oi horizon 10 mgC/g)	Siderophore desferrioxamine B, pH 7	1.64	1.5	N/A	Poggenburg et al. (2018)
Fh-NOM (Oi horizon 20 mgC/g)	Siderophore desferrioxamine B, pH 7	1.64	1.2	N/A	Poggenburg et al. (2018)
Fh-NOM (Oi horizon 40 mgC/g)	Siderophore desferrioxamine B, pH 7	1.8	0.7	N/A	Poggenburg et al. (2018)
Fh-NOM (Oa horizon 5 mgC/g)	Siderophore desferrioxamine B, pH 7	2.7	2.3	N/A	Poggenburg et al. (2018)
Fh-NOM (Oa horizon 10 mgC/g)	Siderophore desferrioxamine B, pH 7	2.6	2	N/A	Poggenburg et al. (2018)
Fh-NOM (Oa horizon 20 mgC/g)	Siderophore desferrioxamine B, pH 7	1.22	0.7	N/A	Poggenburg et al. (2018)
Fh-EPS (*Bacillus subtilis* 5 mgC/g)	Siderophore desferrioxamine B, pH 7	4.12	2	N/A	Poggenburg et al. (2018)
Fh-EPS (*Bacillus subtilis* 10 mgC/g)	Siderophore desferrioxamine B, pH 7	3.46	1.5	N/A	Poggenburg et al. (2018)
Fh-EPS (*Bacillus subtilis* 20 mgC/g)	Siderophore desferrioxamine B, pH 7	1.2	0.7	N/A	Poggenburg et al. (2018)
Addition					
Lp (0.5 mM citrate)[e]	*Shewanella putrefaciens* CN32	0.11	1.8	Green rust	O'Loughlin et al. (2010)
Lp (0.5 mM Oxalate)	*Shewanella putrefaciens* CN32	1	1	Magnetite, ferrous hydroxy carbonate	O'Loughlin et al. (2010)
Lp (5 mM Oxalate)	*Shewanella putrefaciens* CN32	1	1.3	Magnetite, ferrous hydroxy carbonate	O'Loughlin et al. (2010)
Lp (20 mg/L Elliot soil HA)	*Shewanella putrefaciens* CN32	0.1	1.8	Green rust	O'Loughlin et al. (2010)
Lp (20 mg/L Leonardite HA)	*Shewanella putrefaciens* CN32	0.1	1.8	Green rust	O'Loughlin et al. (2010)
Lp (20 mg/L Pony Lake FA)	*Shewanella putrefaciens* CN32	1.2	1	Magnetite, ferrous hydroxy carbonate	O'Loughlin et al. (2010)

Lp (20 mg/L Suwannee River FA)	*Shewanella putrefaciens* CN32	0.08	1.8	Green rust	O'Loughlin et al. (2010)
Lp (20 mg/L Suwannee River HA)	*Shewanella putrefaciens* CN32	0.1	1.8	Green rust	O'Loughlin et al. (2010)
Lp (100 mg/L EPS from *Shewanella putrefaciens* CN32)	*Shewanella putrefaciens* CN32	0.1	1.8	Green rust	O'Loughlin et al. (2010)
Fh-HA (Pahokee Peat HA) 50 mg/L (5 mM Fe)	*Shewanella oneidensis* MR-1	1.4	0.8	Vivianite	Amstaetter et al. (2012)
Fh-HA (Pahokee Peat HA) 100 mg/L (5 mM Fe)	*Shewanella oneidensis* MR-1	2.1	N/A	Vivianite	Amstaetter et al. (2012)
Fh-HA (Pahokee Peat HA) 200 mg/L (5 mM Fe)	*Shewanella oneidensis* MR-1	3.3	0.87	Vivianite	Amstaetter et al. (2012)
Fh-HA (Pahokee Peat HA) 400 mg/L (5 mM Fe)	*Shewanella oneidensis* MR-1	3.3	1	Vivianite	Amstaetter et al. (2012)
Fh-HA (Pahokee Peat HA) 50 mg/L (30 mM Fe)	*Shewanella oneidensis* MR-1	1.2	1.1 (6 days)	Magnetite	Amstaetter et al. (2012)
Fh-HA (Pahokee Peat HA) 100 mg/L (30 mM Fe)	*Shewanella oneidensis* MR-1	0.57	1 (6 days)	N/A	Amstaetter et al. (2012)
Fh-HA (Pahokee Peat HA) 200 mg/L (30 mM Fe)	*Shewanella oneidensis* MR-1	0.5	0.7 (6 days)	Magnetite	Amstaetter et al. (2012)
Fh-HA (Pahokee Peat HA) 400 mg/L (30 mM Fe)	*Shewanella oneidensis* MR-1	0.47	0.55 (6 days)	N/A	Amstaetter et al. (2012)

[a] – Fh corresponds to 2-line ferrihydrite
[b] – NOM corresponds to natural organic matter
[c] – PGA corresponds to polygalacturonic acid
[d] – Alg corresponds to alginate
e – Lp corresponds to lepidocrocite

2.2. Effects of phosphate on microbial Fe(III) reduction

Phosphate (PO_4) is an important limiting nutrient in the environment that plays an important role in the eutrophication of aquatic environments. Like OM, the mobility and fate of

PO_4 under oxic conditions is also strongly affected by reactions with iron oxides in the environment, and these reactions include innersphere surface adsorption, surface precipitation, and coprecipitation (Rose et al., 1997; Kaegi et al., 2010; Voegelin et al., 2013; Senn et al., 2015; Kraal et al., 2019; Voegelin et al., 2019). The sorption of PO_4 leads to concentration dependent alteration of the physicochemical properties of the oxide, including surface charge, SSA, and colloidal/aggregation stability in solution (Kaegi et al., 2010; Voegelin et al., 2010; Voegelin et al., 2013; Santoro et al., 2019). Moreover, as with OM, the sorption mode of PO_4 differently impacts the structure, composition, and stability of iron oxides, such that coprecipitation also alters the crystallinity and the formation pathways of an iron oxide (Rose et al., 1997; Voegelin et al., 2013; Senn et al., 2015; Kraal et al., 2019). By means of EXAFS, it was proposed that the presence of PO_4 disrupts Fe-Fe bond formation through bridging Fe single corner sharing or PO_4-Fe linkages of pre-existing units (Rose et al., 1997; Voegelin et al., 2010; Voegelin et al., 2013; Senn et al., 2015; van der Grift et al., 2016). In aqueous near-neutral pH solutions with various concentrations of PO_4 (initial molar P/Fe ratio of up to 2) in the presence of Ca and/or Si, the structure of Fe(III)-precipitates formed by the oxidation of Fe(II) was rationalized in terms of mixtures of three main endmembers, including poorly-crystalline lepidocrocite, Si-containing ferrihydrite, and amorphous Fe(III)-PO_4 (Kaegi et al., 2010; Voegelin et al., 2010; Voegelin et al., 2013; Senn et al., 2015; Voegelin et al., 2019). The proportion of each endmember largely depended on the concentration of the surrounding constituents (Voegelin et al., 2013; Senn et al., 2015; Voegelin et al., 2019). Under similar conditions, goethite formation was inhibited during the oxidation of Fe(II) in the presence of PO_4 even at a molar P/Fe ratio of 0.02 (Châtellier et al., 2013). Likewise, PO_4 disrupted the structure of the resulting iron oxide minerals from the oxidation of Fe(II) more so than bacterial cells (Châtellier et al., 2004).

As with OM, the impact of PO_4 on the microbial Fe(III) reduction of iron oxides is complex as evidenced by the varying findings in the literature (Table 1-2). Past research investigated the impact of PO_4 on DIR to determine the factors that affect the release and fate of PO_4 under anoxic conditions. PO_4 may be released following DIR, however more recent research indicated that PO_4 is prone to release under sulfate-reducing conditions (Kraal et al., 2022; Bronner et al., 2023) Nonetheless, PO_4 can either promote or inhibit the rate and extent of Fe(III) reduction by DIRB. Several mechanisms may explain the enhancement of Fe(III) reduction in the presence of PO_4:

1. PO_4 may stimulate DIRB growth,
2. PO_4 may form complexes with biogenic Fe(II), reducing mineral and cell surface passivation by Fe(II),
3. PO_4 may stabilize thermodynamically unstable iron oxides, preventing their transformation,
4. PO_4 adsorption onto iron oxide surfaces may alter aggregation and flocculation, increasing surface accessibility to DIRB.

Conversely, PO_4 may inhibit Fe(III) reduction by adsorbing to iron oxide surfaces and blocking access of DIRB to reactive sites (Borch et al., 2007). While past studies investigated the effects of added PO_4 or pre-adsorbed PO_4 on the DIR of various iron oxides, few have explored the impact of coprecipitated PO_4 on the reactivity of iron oxides to DIRB. These few studies found that, relative to pure ferrihydrite and coprecipitates, at equivalent PO_4 loading (P/Fe 0.05 and P/Fe 0.09 mol:mol), pre-adsorption of PO_4 was reported to hinder the dissolution kinetics and release of Fe by 0.01 M HCl and ~0.1 M ascorbate (Kraal et al., 2019). Within the same study, it was reported that coprecipitates of ferrihydrite-PO_4 exhibited the highest dissolution rates (Kraal et al.,

2019). Similarly, O'Loughlin et al. (2013) found that the rate of chemical dissolution of lepidocrocite-PO_4 coprecipitates (0.007 – 0.1 P/Fe mol:mol) by 0.01 M ascorbate increased with increasing PO_4 content, relative to that of PO_4-free lepidocrocite. Yet, within the same study, the presence of PO_4 reduced the rate of Fe(III) reduction by *Shewanella putrefaciens* CN32 but enhanced the extent of Fe(III) reduction relative to that of PO_4-free lepidocrocite. In contrast, a ferrihydrite-PO_4 coprecipitate (P/Fe 0.1 mol:mol) produced from a Fe(III) solution was reduced at a slower rate by Na-dithionite relative to pure ferrihydrite and ferrihydrite with pre-adsorbed PO_4 (P/Fe 0.07 mol:mol) (Wen et al., 2023). While these studies provided important insights into the impact of the sorption mode of PO_4 on the reactivity of different iron oxides, no studies have investigated the effects of coprecipitation of PO_4 on the bioavailability of ferrihydrite. Moreover, past studies have mainly focused on the impact of PO_4 as a single entity on the physicochemical properties and bioavailability of iron oxides, whereas very few studies considered the effects of additional entities such as OM (Wen et al., 2023). Finally, as with OM, PO_4 plays an important role in controlling the secondary iron products that form due to mechanisms similar to those described for OM (Table 1-2).

Table 1-2: Summary of rates of Fe(III) reduction and extent of Fe(III) reduction by DIRB or chemical compounds, along with the reported secondary Fe minerals that formed following reduction extracted from selected studies. RR and RE correspond to relative rate and relative extent, respectively, which correspond to values calculated relative to the pure mineral phase or control in each study.

Iron oxide	DIRB/Chemical	RR	RE	Secondary Fe Mineral	Reference
Coprecipitation					
Lp (0.0045 P/Fe mol:mol)	*Shewanella putrefaciens* CN32	0.2	1.6	Green rust, ferrous hydroxy carbonate	O'Loughlin et al. (2013)
Lp (0.0074 P/Fe mol:mol)	*Shewanella putrefaciens* CN32	0.15	2	Green rust, ferrous hydroxy carbonate	O'Loughlin et al. (2013)
Lp (0.0208 P/Fe mol:mol)	*Shewanella putrefaciens* CN32	0.15	2	Green rust, ferrous hydroxy carbonate	O'Loughlin et al. (2013)

Lp (0.1026 P/Fe mol:mol)	*Shewanella putrefaciens* CN32	0.33	2	Green rust, ferrous hydroxy carbonate, vivianite	O'Loughlin et al. (2013)
Lp (0.0045 P/Fe mol:mol)	Ascorbic acid	0.4	N/A	N/A	O'Loughlin et al. (2013)
Lp (0.0074 P/Fe mol:mol)	Ascorbic acid	0.7	N/A	N/A	O'Loughlin et al. (2013)
Lp (0.0208 P/Fe mol:mol)	Ascorbic acid	4.8	N/A	N/A	O'Loughlin et al. (2013)
Lp (0.1026 P/Fe mol:mol)	Ascorbic acid	10	N/A	N/A	O'Loughlin et al. (2013)
Fh (P/Fe 0.05 mol:mol)	Ascorbic acid	1.7	N/A	N/A	Kraal et al. (2019)
Fh (P/Fe 0.1 mol:mol)	Ascorbic acid	3.1	N/A	N/A	Kraal et al. (2019)
Fh (P/Fe 0.05 mol:mol)	0.01 mol/L HCl	1.4	N/A	N/A	Kraal et al. (2019)
Fh (P/Fe 0.1 mol:mol)	0.01 mol/L HCl	2.5	N/A	N/A	Kraal et al. (2019)
Fh (P/Fe 0.1 mol:mol)	Na-dithionite	0.1	0.9	N/A	Wen et al. (2023)
Fh-OM (P/Fe 0.1 mol:mol, C/Fe 2 mol:mol Algae-derived OM)	Na-dithionite	0.05	0.7	N/A	Wen et al. (2023)
Fh-HA (P/Fe 0.1 mol:mol, C/Fe 2 mol:mol standard HA)	Na-dithionite	0.05	0.7	N/A	Wen et al. (2023)
Adsorption					
Fh (50% surface coverage phosphate)	*Shewanella putrefaciens* CN32	N/A	0.6	7% Magnetite 12% Green rust	Borch et al. (2007)
Fh (100% surface coverage phosphate)	*Shewanella putrefaciens* CN32	N/A	0.2	5% Green rust	Borch et al. (2007)
Fh (P/Fe 0.05 mol:mol)	Ascorbic acid	0.65	N/A	N/A	Kraal et al. (2019)
Fh (P/Fe 0.1 mol:mol)	Ascorbic acid	0.84	N/A	N/A	Kraal et al. (2019)
Fh (P/Fe 0.05 mol:mol)	0.01 mol/L HCl	0.65	N/A	N/A	Kraal et al. (2019)
Fh (P/Fe 0.1 mol:mol)	0.01 mol/L HCl	1	N/A	N/A	Kraal et al. (2019)
Schwertmannite (80 µmole PO_4/g)	Natural consortium	N/A	1.4	Goethite	Schoepfer et al. (2017)

Schwertmannite (400 µmole PO_4/g)	Natural consortium	N/A	0.6	Goethite (minor)	Schoepfer et al. (2017)
Schwertmannite (800 µmole PO_4/g)	Natural consortium	N/A	0.1	Goethite (minor)	Schoepfer et al. (2017)
Fh (P/Fe 0.07 mol:mol)	Na-dithionite	0.45	1	N/A	Wen et al. (2023)
Fh with ads PO_4 and OM (P/Fe 0.07 mol:mol, C/Fe 0.05 mol:mol Algae derived OM)	Na-dithionite	0.3	1	N/A	Wen et al. (2023)
Fh with ads PO_4 and OM (P/Fe 0.07 mol:mol, C/Fe 0.05 mol:mol standard HA)	Na-dithionite	0.6	1	N/A	Wen et al. (2023)
Addition					
Lp (0.5 mM PO_4)	*Shewanella putrefaciens* CN32	0.13	2.4	Green rust	O'Loughlin et al. (2010)
Fh (5 mM Fe, 0.8 mM PO_4)	*Shewanella oneidensis* MR-1	0.5	0.8	None	Amstaetter et al. (2012)
Fh (30 mM Fe, 0.8 mM PO_4)	*Shewanella oneidensis* MR-1	0.8	0.9	Magnetite	Amstaetter et al. (2012)

3. Alginate

The OM selected for this research is sodium alginate $(C_6H_7NaO_6)_n$, which is a polysaccharide that is abundant in nature and occurs as a structural component in marine brown algae (*phaeophyceae*). Alginate is a linear copolymer consisting of (1→4)-linked α-L-guluronic acid (G) and β-D-mannuronic acid (M) residues arranged in varying sequences (Figure 1-3). The specific arrangement of these G and M units depends on the species from which the alginate is derived (Cardenas-Jiron et al., 2011; Hecht and Srebnik, 2016; Wang et al., 2019). Typically, the polymer chains contain random sequences of M- and G-blocks, interspersed with alternating MG regions (Hecht and Srebnik, 2016; Wang et al., 2019). Alginates are generally stiff molecules due to the rigidity of the six-membered sugar rings and the limited rotational flexibility around the glycosidic bonds (Hecht and Srebnik, 2016; Wang et al., 2019).

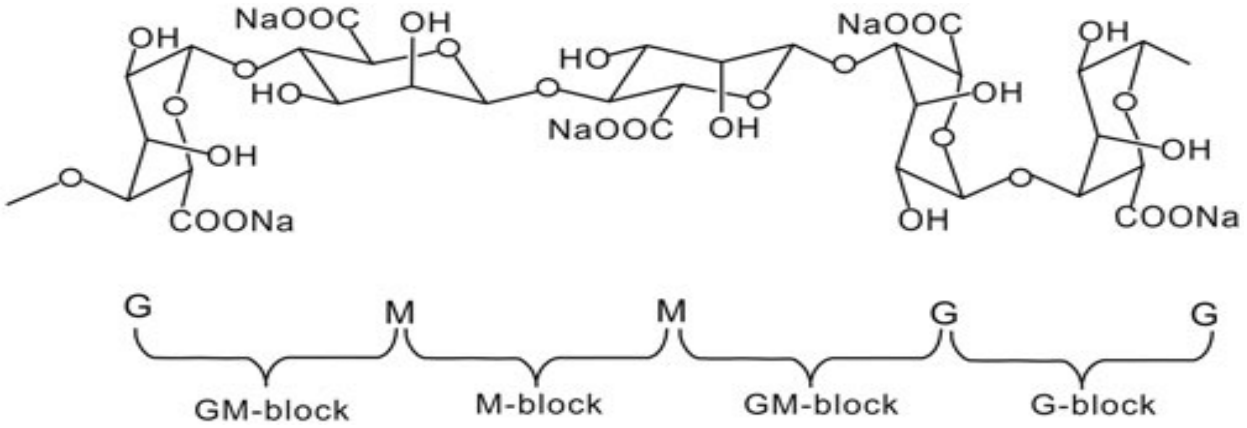

Figure 1-3: Molecular structure of Na-alginate (Wang et al., 2018).

The environmental relevance of alginate is supported by Chan et al. (2009), who characterized BIOS using analytical techniques such as scanning transmission X-ray microscopy, micro-X-ray fluorescence microscopy, and high-resolution transmission electron microscopy. Their findings identified microbial polymers (sheaths and twisted stalks) as acidic polysaccharides containing carboxyl functional groups, with compositional similarities to alginate. This resemblance reinforces the selection of alginate as a representative OM in studies of microbial and geochemical interactions.

4. Gamma (γ)-irradiation

Studies conducted to date to determine the reactivity of BIOS, in particular BIOS that formed from the activity of microaerophilic FeOB, have been carried out utilizing naturally occurring BIOS, necessitating the need to sterilize the samples in order to prevent reactions mediated by the native microbial communities during storage and experimental duration (Langley et al., 2009b; Langley et al., 2009d; Langley et al., 2009e). From the range of available sterilization methods reported in the literature, apparently all come with a disadvantage. Autoclaving, for instance, can significantly alter the physicochemical properties of natural samples, including a decrease of surface area as a consequence of heat induced transformation of poorly crystalline Fe

oxyhydroxide minerals into crystalline iron oxides as well as particle aggregation (Berns et al., 2008; Radloff et al., 2008; Otte et al., 2018; Zhao et al., 2021), and release of nutrients and organic matter (Salonius et al., 1967; Lotrario et al., 1995; McNamara et al., 2003; Berns et al., 2008; Buessecker et al., 2019). On the other hand, the application of chemical agents was reported to result in the increase of extractable of Fe(II) and Fe(III) (Buessecker et al., 2019; Layglon et al., 2020), as well as the chemical alteration of organic matter properties and trace metal behaviour (Wolf et al., 1989; Buessecker et al., 2019; Retelletti Brogi et al., 2019; Layglon et al., 2020). Moreover, the application of chemical agents may hinder the inoculation of sterilized samples with model microorganisms (Langley et al., 2009b; Langley et al., 2009d; Langley et al., 2009e).

Although autoclaving tends to be more commonly used due to its lower cost and ease of accessibility, sterilization by gamma(γ)-irradiation has been determined to be the most appropriate method by several studies (McNamara et al., 2003; Herbert et al., 2005; Berns et al., 2008; Borisover et al., 2016; Lees et al., 2018; Buessecker et al., 2019). Sterilization by γ-irradiation proceeds either directly or indirectly. Directly, the ionizing energy causes direct damage to cell DNA. Indirectly, sterilization proceeds by reactive radical species that form from the radiolysis of cellular H_2O (e.g. $^{\bullet}OH$, $^{\bullet}e_{aq}^-$, $^{\bullet}H$, H_2O_2, $^{\bullet}O_2^-$), which may react with proteins, nucleic acids, and lipids causing cleavage of carbon-carbon bonds leading to the depolymerization of complex organic matter ultimately leading to cell death (McNamara et al., 2003; Yakabuskie et al., 2011; Brown et al., 2015). The efficiency of γ-irradiation as a sterilization and minimally invasive technique has been compared with a number of other sterilization techniques such as autoclaving, and the application of poisons and fumigants (e.g. sodium azide, chloroform, mercuric chloride) (McNamara et al., 2003). While some studies identify γ-irradiation as an effective and minimally invasive technique, others suggest otherwise indicating that irradiation driven alteration of the

physicochemical properties of soils/sediments may be related to the properties, mineralogy and OM content of the soil/sediment (McNamara et al., 2003; Schaller et al., 2011).

One of the most common changes observed for soils/sediments following γ-irradiation is the increase in dissolved organic C, likely originating from radiation induced depolymerization of complex OM (including microorganisms) within the sample (Salonius et al., 1967; Tuominen et al., 1994; McNamara et al., 2003; Bank et al., 2008; Schaller et al., 2011). In contrast, the effects of γ-irradiation on the physical properties of soils/sediments are variable. Wolf et al. (1989) γ-sterilized a number of different soils (dosage of 50-60 kGy) and observed no significant changes in their surface area. Similarly, Herbert et al. (2005) found no significant changes in the mineralogy and surface area of mine tailings following irradiation to a final dose of 10 or 25 kGy. In contrast, Lotrario et al. (1995) observed a 16% decline in soil surface area following γ-irradiation (10 kGy). More recently, Schaller et al. (2011) found that γ-irradiation (4x 15kGy) of sediments with high organic C content (9.5%) led to a significantly higher remobilization of arsenic and uranium into solution when compared to non-sterilized sediments. Bank et al. (2008) found that γ-irradiated sediments (final dose of 20 kGy) adsorbed a significantly higher amount of U(VI) than non-sterilized sediments which was attributed to irradiation induced alteration of the cation exchange capacity of the sediment and the partial reduction of goethite to Fe(II). Berns et al. (2008) found that γ-irradiation (36 kGy) altered the aggregation state of soil and in turn increased the surface area. In contrast, the exposure of various clay minerals to a high dosage of γ-irradiation (1.1 MGy) slightly altered the surface area of select minerals, whereas in other minerals (e.g. smectite) irradiation induced reduction of Fe(III) to Fe(II) leading to an overall decline in cation exchange capacity (Plötze et al., 2003). On the other hand, the exposure of synthetic 2-line ferrihydrite and hematite to a similar dose (1 MGy) was found to alter their crystalline structure and enhance their

bioavailability to microbial Fe(III) reduction by *Shewanella oneidensis* MR-1 in the presence of an electron shuttle (Brown et al., 2014). Even at lower doses (0.6 and 38.6 kGy), however, γ-irradiation may have enhanced the bioavailability of Fe(III) in sediments to microbial reduction by *Geobacter sulfurreducens* (Brown et al., 2015). Thus, radiation driven alteration of the physicochemical properties and oxidation state of iron may lead to an over-or under-estimation of their reactivity and may in turn influence the secondary iron products that form during microbial Fe(III) reduction.

Thus far, we have highlighted the importance of physicochemical and mineralogical properties as well as OM content/type in modulating the reactivity of Fe-OM coprecipitates. Therefore, given sensitivity in reactivity of iron oxides to changes in crystallinity and OM content, determining the extent of impact of γ-radiation on the reactivity of Fe-OM coprecipitates is important for future studies employing this technique to natural samples.

5. Statistics

Data comparison was carried out using either one-way ANOVA or two-tailed t-test at the 95% confidence interval as previously done in past studies (Langley et al., 2009a; Najem et al., 2016). One-way ANOVA was carried out for Chapters 2 and 3 for sample inter-comparisons paired with Tukey's post hoc test to determine which specific pairs of group means are significantly different from each other after a significant result in an ANOVA test. This approach also eliminates Type 1 error. For Chapter 4, two-tailed t-test were performed as opposed to ANOVA, because comparisons were carried out between a native and an irradiated sample and no inter-comparisons were performed among samples. Finally, statistical analyses were carried out in SigmaPlot version 12.3.

6. Objectives and Hypotheses

The objectives of this thesis are:

1. To investigate the effects of varying concentrations of OM on the physicochemical and mineralogical properties, as well as the reactivity of various iron oxide-OM coprecipitates including ferrihydrite, lepidocrocite, and goethite. Because coprecipitation modifies the physicochemical and mineralogical properties of the iron oxides studied, as observed for BIOS, it is hypothesized that the reactivity, assessed with chemical dissolution and bioavailability, will increase with increasing C content.
2. To investigate the cooperative impact of PO_4 and OM on the physicochemical properties, abiotic dissolution mediated through reduction (ascorbic acid), and bioavailability (*Shewanella putrefaciens* CN32) of 2-line ferrihydrite. The concentrations of PO_4 (0.01 and 0.1 P/Fe mol:mol) and OM (C/Fe 1.0 mol:mol) chosen for this study correspond to those encountered in the environment (Fortin et al., 1993; Chen et al., 2014; Baken et al., 2015; Zhao et al., 2016; van der Grift et al., 2018). It is hypothesized that the sorption mode of PO_4 will play an important role in dictating the reactivity of ferrihydrite, whereas in binary systems (OM and PO_4) it is expected that the constituents would diminish the reactivity of ferrihydrite due to the expected modifications of the physicochemical properties of the oxide including SSA, aggregation, and surface charge as determined by past studies (Wen et al., 2023).
3. To investigate the impact of γ-irradiation at a dose of 25 kGy on the physicochemical and mineralogical properties, as well as the bioavailability of various iron oxides (ferrihydrite, lepidocrocite, and goethite) coprecipitated with various concentrations of OM (C/Fe 0, 0.5, 1.0, and 1.5 mol:mol). Based on past research, it is hypothesized that γ-irradiation at 25

kGy will impact the physicochemical and mineralogical properties of the iron oxides studied, and such impact is likely to increase with increasing OM content. Changes in the physicochemical and mineralogical properties of the iron oxides studies will also likely influence their bioavailability to *Shewanella putrefaciens* CN32.

References

Adhikari, D., Poulson, S. R., Sumaila, S., Dynes, J. J., McBeth, J. M. and Yang, Y., 2016. Asynchronous reductive release of iron and organic carbon from hematite–humic acid complexes. Chem. Geol. 430: 13-20.

Adhikari, D., Sowers, T., Stuckey, J. W., Wang, X., Sparks, D. L. and Yang, Y., 2019. Formation and redox reactivity of ferrihydrite-organic carbon-calcium co-precipitates. Geochim. Cosmochim. Acta 244: 86-98.

Adhikari, D., Zhao, Q., Das, K., Mejia, J., Huang, R., Wang, X., Poulson, S. R., Tang, Y., Roden, E. E. and Yang, Y., 2017. Dynamics of ferrihydrite-bound organic carbon during microbial Fe reduction. Geochim. Cosmochim. Acta 212: 221-233.

Amstaetter, K., Borch, T. and Kappler, A., 2012. Influence of humic acid imposed changes of ferrihydrite aggregation on microbial Fe (III) reduction. Geochim. Cosmochim. Acta 85: 326-341.

Angelico, R., Ceglie, A., He, J.-Z., Liu, Y.-R., Palumbo, G. and Colombo, C., 2014. Particle size, charge and colloidal stability of humic acids coprecipitated with ferrihydrite. Chemosphere 99: 239-247.

Baalousha, M., 2009. Aggregation and disaggregation of iron oxide nanoparticles: Influence of particle concentration, pH and natural organic matter. Sci. Total Environ. 407(6): 2093-2101.

Baken, S., Moens, C., van der Grift, B. and Smolders, E., 2016. Phosphate binding by natural iron-rich colloids in streams. Water Res. 98: 326-333.

Baken, S., Verbeeck, M., Verheyen, D., Diels, J. and Smolders, E., 2015. Phosphorus losses from agricultural land to natural waters are reduced by immobilization in iron-rich sediments of drainage ditches. Water Res. 71: 160-170.

Bank, T. L., Kukkadapu, R. K., Madden, A. S., Ginder-Vogel, M. A., Baldwin, M. E. and Jardine, P. M., 2008. Effects of gamma-sterilization on the physico-chemical properties of natural sediments. Chem. Geol. 251(1-4): 1-7.

Berns, A. E., Philipp, H., Narres, H. D., Burauel, P., Vereecken, H. and Tappe, W., 2008. Effect of gamma-sterilization and autoclaving on soil organic matter structure as studied by solid state NMR, UV and fluorescence spectroscopy. Eur. J. Soil Sci. 59(3): 540-550.

Bonneville, S., Behrends, T. and Van Cappellen, P., 2009. Solubility and dissimilatory reduction kinetics of iron (III) oxyhydroxides: A linear free energy relationship. Geochim. Cosmochim. Acta 73(18): 5273-5282.

Bonneville, S., Van Cappellen, P. and Behrends, T., 2004. Microbial reduction of iron (III) oxyhydroxides: effects of mineral solubility and availability. Chem. Geol. 212(3-4): 255-268.

Borch, T., Masue, Y., Kukkadapu, R. K. and Fendorf, S., 2007. Phosphate imposed limitations on biological reduction and alteration of ferrihydrite. Environ. Sci. Technol. 41(1): 166-172.

Borisover, M., Keren, Y., Usyskin, A. and Bukhanovsky, N., 2016. Effects of gamma-irradiation of original and organic matter-amended soils on the sorption of triclosan and diuron from aqueous solutions. Chemosphere 152: 62-70.

Bronner, R., Thompson, K., Dreher, C., Runge, E., Voggenreiter, E., Shuster, J., Wan, B., Joshi, P., Fischer, S. and Duda, J., 2023. Co-reduction of Fe (III) and S0 drives Fe-S biomineral formation and phosphate mobilisation. Geochemical Perspectives Letters 24: 27-32.

Brown, A. R., Boothman, C., Pimblott, S. M. and Lloyd, J. R., 2015. The impact of gamma radiation on sediment microbial processes. Appl. Environ. Microbiol. 81(12): 4014-4025.
Brown, A. R., Wincott, P. L., LaVerne, J. A., Small, J. S., Vaughan, D. J., Pimblott, S. M. and Lloyd, J. R., 2014. The impact of gamma radiation on the bioavailability of Fe(III) minerals for microbial respiration. Environ. Sci. Technol. 48(18): 10672-10680.
Buessecker, S., Tylor, K., Nye, J., Holbert, K. E., Urquiza Muñoz, J. D., Glass, J. B., Hartnett, H. E. and Cadillo-Quiroz, H., 2019. Effects of sterilization techniques on chemodenitrification and N_2O production in tropical peat soil microcosms. Biogeosciences 16(23): 4601-4612.
Byrne, J. M. and Kappler, A., 2021. A revised analysis of ferrihydrite at liquid helium temperature using Mössbauer spectroscopy. American Mineralogist In press.
Cardenas-Jiron, G., Leal, D., Matsuhiro, B. and Osorio-Roman, I. O., 2011. Vibrational spectroscopy and density functional theory calculations of poly-D-mannuronate and heteropolymeric fractions from sodium alginate. J. Raman Spectrosc. 42(4): 870-878.
Chan, C. S., De Stasio, G., Welch, S. A., Girasole, M., Frazer, B. H., Nesterova, M. V., Fakra, S. and Banfield, J. F., 2004. Microbial polysaccharides template assembly of nanocrystal fibers. Science 303(5664): 1656-1658.
Chan, C. S., Fakra, S. C., Edwards, D. C., Emerson, D. and Banfield, J. F., 2009. Iron oxyhydroxide mineralization on microbial extracellular polysaccharides. Geochim. Cosmochim. Acta 73(13): 3807-3818.
Chan, C. S., Fakra, S. C., Emerson, D., Fleming, E. J. and Edwards, K. J., 2011. Lithotrophic iron-oxidizing bacteria produce organic stalks to control mineral growth: implications for biosignature formation. The ISME journal 5(4): 717-727.
Chandıa, N., Matsuhiro, B. and Vásquez, A., 2001. Alginic acids in Lessonia trabeculata: characterization by formic acid hydrolysis and FT-IR spectroscopy. Carbohydr. Polym. 46(1): 81-87.
Châtellier, X., Fortin, D., West, M. M., Leppard, G. G. and Ferris, F. G., 2001. Effect of the presence of bacterial surfaces during the synthesis of Fe oxides by oxidation of ferrous ions. European Journal of Mineralogy 13(4): 705-714.
Châtellier, X., Grybos, M., Abdelmoula, M., Kemner, K. M., Leppard, G. G., Mustin, C., West, M. M. and Paktunc, D., 2013. Immobilization of P by oxidation of Fe (II) ions leading to nanoparticle formation and aggregation. Appl. Geochem. 35: 325-339.
Châtellier, X., West, M. M., Rose, J., Fortin, D., Leppard, G. G. and Ferris, F. G., 2004. Characterization of iron-oxides formed by oxidation of ferrous ions in the presence of various bacterial species and inorganic ligands. Geomicrobiol. J. 21(2): 99-112.
Chen, C., Dynes, J. J., Wang, J. and Sparks, D. L., 2014. Properties of Fe-organic matter associations via coprecipitation versus adsorption. Environ. Sci. Technol. 48(23): 13751-13759.
Chen, C., Kukkadapu, R. and Sparks, D. L., 2015. Influence of Coprecipitated Organic Matter on Fe^{2+}(aq)-Catalyzed Transformation of Ferrihydrite: Implications for Carbon Dynamics. Environ. Sci. Technol. 49(18): 10927-10936.
Chen, C. and Sparks, D. L., 2018. Fe (II)-induced mineral transformation of ferrihydrite–organic matter adsorption and co-precipitation complexes in the absence and presence of As (III). ACS Earth Space Chem. 2(11): 1095-1101.

Chen, K.-Y., Hsu, L.-C., Chan, Y.-T., Cho, Y.-L., Tsao, F.-Y., Tzou, Y.-M., Hsieh, Y.-C. and Liu, Y.-T., 2018. Phosphate removal in relation to structural development of humic acid-iron coprecipitates. Sci. Rep. 8(1): 10363.

Cismasu, A. C., Michel, F. M., Tcaciuc, A. P., Tyliszczak, T. and Brown, J. G. E., 2011. Composition and structural aspects of naturally occurring ferrihydrite. Comptes Rendus Geoscience 343(2-3): 210-218.

Cismasu, A. C., Williams, K. H. and Nico, P. S., 2016. Iron and Carbon Dynamics during Aging and Reductive Transformation of Biogenic Ferrihydrite. Environ. Sci. Technol. 50(1): 25-35.

Colombo, C., Palumbo, G., Sellitto, V. M., Cho, H. G., Amalfitano, C. and Adamo, P., 2015. Stability of coprecipitated natural humic acid and ferrous iron under oxidative conditions. Journal of Geochemical Exploration 151: 50-56.

Cooper, R. E., Eusterhues, K., Wegner, C.-E., Totsche, K. U. and Küsel, K., 2017. Ferrihydrite-associated organic matter (OM) stimulates reduction by Shewanella oneidensis MR-1 and a complex microbial consortia. Biogeosciences 14(22): 5171-5188.

Cornell, R., Giovanoli, R. and Schindler, P., 1987. Effect of silicate species on the transformation of ferrihydrite into goethite and hematite in alkaline media. Clays Clay Miner. 35(1): 21-28.

Cornell, R. M. and Schwertmann, U., 2003. The iron oxides: structure, properties, reactions, occurrences, and uses, Wiley-vch Weinheim.

Curti, L., Moore, O. W., Babakhani, P., Xiao, K.-Q., Woulds, C., Bray, A. W., Fisher, B. J., Kazemian, M., Kaulich, B. and Peacock, C. L., 2021. Carboxyl-richness controls organic carbon preservation during coprecipitation with iron (oxyhydr)oxides in the natural environment. Commun. Earth Environ. 2(1).

Cutting, R., Coker, V., Fellowes, J., Lloyd, J. and Vaughan, D., 2009. Mineralogical and morphological constraints on the reduction of Fe (III) minerals by Geobacter sulfurreducens. Geochim. Cosmochim. Acta 73(14): 4004-4022.

Dippon, U., Schmidt, C., Behrens, S. and Kappler, A., 2015. Secondary mineral formation during ferrihydrite reduction by Shewanella oneidensis MR-1 depends on incubation vessel orientation and resulting gradients of cells, Fe^{2+} and Fe minerals. Geomicrobiol. J. 32(10): 878-889.

Dong, H., Huang, L., Zhao, L., Zeng, Q., Liu, X., Sheng, Y., Shi, L., Wu, G., Jiang, H., Li, F., Zhang, L., Guo, D., Li, G., Hou, W. and Chen, H., 2022. A critical review of mineral–microbe interaction and co-evolution: mechanisms and applications. National Science Review 9(10).

Dong, H., Zeng, Q., Sheng, Y., Chen, C., Yu, G. and Kappler, A., 2023. Coupled iron cycling and organic matter transformation across redox interfaces. Nature Reviews Earth & Environment 4(9): 659-673.

Eickhoff, M., Obst, M., Schröder, C., Hitchcock, A. P., Tyliszczak, T., Martinez, R. E., Robbins, L. J., Konhauser, K. O. and Kappler, A., 2014. Nickel partitioning in biogenic and abiogenic ferrihydrite: the influence of silica and implications for ancient environments. Geochim. Cosmochim. Acta 140: 65-79.

Ekstrom, E. B., Learman, D. R., Madden, A. S. and Hansel, C. M., 2010. Contrasting effects of Al substitution on microbial reduction of Fe (III)(hydr) oxides. Geochim. Cosmochim. Acta 74(24): 7086-7099.

Eusterhues, K., Hädrich, A., Neidhardt, J., Küsel, K., Keller, T., Jandt, K. and Totsche, K., 2014a. Reduction of ferrihydrite with adsorbed and coprecipitated organic matter: microbial reduction by Geobacter bremensis vs. abiotic reduction by Na-dithionite. Biogeosciences 11(18): 4953-4966.

Eusterhues, K., Neidhardt, J., Hädrich, A., Küsel, K. and Totsche, K. U., 2014b. Biodegradation of ferrihydrite-associated organic matter. Biogeochemistry 119: 45-50.

Eusterhues, K., Wagner, F. E., Häusler, W., Hanzlik, M., Knicker, H., Totsche, K. U., Kögel-Knabner, I. and Schwertmann, U., 2008. Characterization of ferrihydrite-soil organic matter coprecipitates by X-ray diffraction and Mossbauer spectroscopy. Environ. Sci. Technol. 42(21): 7891-7897.

Fabisch, M., Freyer, G., Johnson, C. A., Buchel, G., Akob, D. M., Neu, T. R. and Kusel, K., 2016. Dominance of 'Gallionella capsiferriformans' and heavy metal association with Gallionella-like stalks in metal-rich pH 6 mine water discharge. Geobiology 14(1): 68-90.

Falkeborg, M., Cheong, L.-Z., Gianfico, C., Sztukiel, K. M., Kristensen, K., Glasius, M., Xu, X. and Guo, Z., 2014. Alginate oligosaccharides: Enzymatic preparation and antioxidant property evaluation. Food Chem. 164: 185-194.

Ferris, F., 2005. Biogeochemical properties of bacteriogenic iron oxides. Geomicrobiol. J. 22(3-4): 79-85.

Ferris, F., Hallberg, R., Lyvén, B. and Pedersen, K., 2000. Retention of strontium, cesium, lead and uranium by bacterial iron oxides from a subterranean environment. Appl. Geochem. 15(7): 1035-1042.

Field, H. R., Whitaker, A. H., Henson, J. A. and Duckworth, O. W., 2019. Sorption of copper and phosphate to diverse biogenic iron (oxyhydr) oxide deposits. Sci. Total Environ. 697: 134111.

Fortin, D. and Langley, S., 2005. Formation and occurrence of biogenic iron-rich minerals. Earth-Sci. Rev. 72(1-2): 1-19.

Fortin, D., Leppard, G. G. and Tessier, A., 1993. Characteristics of lacustrine diagenetic iron oxyhydroxides. Geochim. Cosmochim. Acta 57(18): 4391-4404.

Fredrickson, J. K., Zachara, J. M., Kennedy, D. W., Dong, H., Onstott, T. C., Hinman, N. W. and Li, S.-m., 1998. Biogenic iron mineralization accompanying the dissimilatory reduction of hydrous ferric oxide by a groundwater bacterium. Geochim. Cosmochim. Acta 62(19-20): 3239-3257.

Gálvez, N., Barrón, V. and Torrent, J., 1999. Effect of phosphate on the crystallization of hematite, goethite, and lepidocrocite from ferrihydrite. Clays Clay Miner. 47(3): 304-311.

Gault, A. G., Ibrahim, A., Langley, S., Renaud, R., Takahashi, Y., Boothman, C., Lloyd, J. R., Clark, I. D., Ferris, F. G. and Fortin, D., 2011. Microbial and geochemical features suggest iron redox cycling within bacteriogenic iron oxide-rich sediments. Chem. Geol. 281(1-2): 41-51.

Glasauer, S., Weidler, P. G., Langley, S. and Beveridge, T. J., 2003. Controls on Fe reduction and mineral formation by a subsurface bacterium. Geochim. Cosmochim. Acta 67(7): 1277-1288.

Gorby, Y. A., Yanina, S., McLean, J. S., Rosso, K. M., Moyles, D., Dohnalkova, A., Beveridge, T. J., Chang, I. S., Kim, B. H. and Kim, K. S., 2006. Electrically conductive bacterial nanowires produced by Shewanella oneidensis strain MR-1 and other microorganisms. Proc. Natl. Acad. Sci. 103(30): 11358-11363.

Grybos, M., Davranche, M., Gruau, G. and Petitjean, P., 2007. Is trace metal release in wetland soils controlled by organic matter mobility or Fe-oxyhydroxides reduction? J. Colloid Interface Sci. 314(2): 490-501.
Hallberg, R. and Ferris, F. G., 2004. Biomineralization by gallionella. Geomicrobiol. J. 21(5): 325-330.
Han, L., Sun, K., Keiluweit, M., Yang, Y., Yang, Y., Jin, J., Sun, H., Wu, F. and Xing, B., 2019. Mobilization of ferrihydrite-associated organic carbon during Fe reduction: Adsorption versus coprecipitation. Chem. Geol. 503: 61-68.
Hansel, C. M., Benner, S. G. and Fendorf, S., 2005. Competing Fe (II)-induced mineralization pathways of ferrihydrite. Environ. Sci. Technol. 39(18): 7147-7153.
Hansel, C. M., Benner, S. G., Neiss, J., Dohnalkova, A., Kukkadapu, R. K. and Fendorf, S., 2003. Secondary mineralization pathways induced by dissimilatory iron reduction of ferrihydrite under advective flow. Geochim. Cosmochim. Acta 67(16): 2977-2992.
Hao, L., Guo, Y., Byrne, J. M., Zeitvogel, F., Schmid, G., Ingino, P., Li, J., Neu, T. R., Swanner, E. D., Kappler, A. and Obst, M., 2016. Binding of heavy metal ions in aggregates of microbial cells, EPS and biogenic iron minerals measured in-situ using metal- and glycoconjugates-specific fluorophores. Geochim. Cosmochim. Acta 180: 66-96.
Hecht, H. and Srebnik, S., 2016. Structural characterization of sodium alginate and calcium alginate. Biomacromolecules 17(6): 2160-2167.
Hedrich, S., Schlömann, M. and Johnson, D. B., 2011. The iron-oxidizing proteobacteria. Microbiology 157(6): 1551-1564.
Henneberry, Y. K., Kraus, T. E. C., Nico, P. S. and Horwath, W. R., 2012. Structural stability of coprecipitated natural organic matter and ferric iron under reducing conditions. Org. Geochem. 48: 81-89.
Herbert, R. B., Malmström, M., Ebenå, G., Salmon, U., Ferrow, E. and Fuchs, M., 2005. Quantification of abiotic reaction rates in mine tailings: evaluation of treatment methods for eliminating iron-and sulfur-oxidizing bacteria. Environ. Sci. Technol. 39(3): 770-777.
Hofmann, A., Pelletier, M., Michot, L., Stradner, A., Schurtenberger, P. and Kretzschmar, R., 2004. Characterization of the pores in hydrous ferric oxide aggregates formed by freezing and thawing. J. Colloid Interface Sci. 271(1): 163-173.
Hua, J., Sun, J., Chen, M., Liu, C. and Wu, F., 2023. Aqueous Fe (II)-catalyzed iron oxide recrystallization: Fe redox cycling and atom exchange, mineralogical recrystallization and contributing factor. Reviews in Environmental Science and Bio/Technology 22(1): 55-78.
Hyacinthe, C., Bonneville, S. and Van Cappellen, P., 2006. Reactive iron(III) in sediments: Chemical versus microbial extractions. Geochim. Cosmochim. Acta 70(16): 4166-4180.
Hyacinthe, C. and Van Cappellen, P., 2004. An authigenic iron phosphate phase in estuarine sediments: composition, formation and chemical reactivity. Mar. Chem. 91(1-4): 227-251.
Islam, F. S., Gault, A. G., Boothman, C., Polya, D. A., Charnock, J. M., Chatterjee, D. and Lloyd, J. R., 2004. Role of metal-reducing bacteria in arsenic release from Bengal delta sediments. Nature 430(6995): 68-71.
Jones, A. M., Collins, R. N., Rose, J. and Waite, T. D., 2009. The effect of silica and natural organic matter on the Fe (II)-catalysed transformation and reactivity of Fe (III) minerals. Geochim. Cosmochim. Acta 73(15): 4409-4422.

Kaegi, R., Voegelin, A., Folini, D. and Hug, S. J., 2010. Effect of phosphate, silicate, and Ca on the morphology, structure and elemental composition of Fe (III)-precipitates formed in aerated Fe (II) and As (III) containing water. Geochim. Cosmochim. Acta 74(20): 5798-5816.

Kaiser, K., 2003. Sorption of natural organic matter fractions to goethite (α-FeOOH): effect of chemical composition as revealed by liquid-state ^{13}C NMR and wet-chemical analysis. Org. Geochem. 34(11): 1569-1579.

Kaiser, K., Guggenberger, G., Haumaier, L. and Zech, W., 1997. Dissolved organic matter sorption on sub soils and minerals studied by ^{13}C-NMR and DRIFT spectroscopy. Eur. J. Soil Sci. 48(2): 301-310.

Kaiser, K., Mikutta, R. and Guggenberger, G., 2007. Increased stability of organic matter sorbed to ferrihydrite and goethite on aging. Soil Sci. Soc. Am. J. 71(3): 711-719.

Kappler, A. and Straub, K. L., 2005. Geomicrobiological cycling of iron. Reviews in Mineralogy and Geochemistry 59(1): 85-108.

Kennedy, C., Scott, S. and Ferris, F., 2003. Characterization of bacteriogenic iron oxide deposits from Axial Volcano, Juan de Fuca Ridge, northeast Pacific Ocean. Geomicrobiol. J. 20(3): 199-214.

Kennedy, C., Scott, S. and Ferris, F., 2004. Hydrothermal phase stabilization of 2-line ferrihydrite by bacteria. Chem. Geol. 212(3-4): 269-277.

Kleber, M., Eusterhues, K., Keiluweit, M., Mikutta, C., Mikutta, R. and Nico, P. S., 2015. Mineral–Organic Associations: Formation, Properties, and Relevance in Soil Environments. 130: 1-140.

Kleinert, S., Muehe, E. M., Posth, N. R., Dippon, U., Daus, B. and Kappler, A., 2011. Biogenic Fe (III) minerals lower the efficiency of iron-mineral-based commercial filter systems for arsenic removal. Environ. Sci. Technol. 45(17): 7533-7541.

Kostka, J. E. and Luther, G. W., 1994. Partitioning and speciation of solid phase iron in saltmarsh sediments. Geochim. Cosmochim. Acta 58(7): 1701-1710.

Kraal, P., Van Genuchten, C. M. and Behrends, T., 2022. Phosphate coprecipitation affects reactivity of iron (oxyhydr) oxides towards dissolved iron and sulfide. Geochim. Cosmochim. Acta 321: 311-328.

Kraal, P., van Genuchten, C. M., Behrends, T. and Rose, A. L., 2019. Sorption of phosphate and silicate alters dissolution kinetics of poorly crystalline iron (oxyhydr) oxide. Chemosphere 234: 690-701.

Kukkadapu, R. K., Zachara, J. M., Fredrickson, J. K. and Kennedy, D. W., 2004. Biotransformation of two-line silica-ferrihydrite by a dissimilatory Fe (III)-reducing bacterium: formation of carbonate green rust in the presence of phosphate. Geochim. Cosmochim. Acta 68(13): 2799-2814.

Lagarec, K. and Rancourt, D. G., 1997. Extended Voigt-based analytic lineshape method for determining N-dimensional correlated hyperfine parameter distributions in Mössbauer spectroscopy. Nuclear Instruments and Methods in Physics Research Section B: Beam Interactions with Materials and Atoms 129(2): 266-280.

Lalonde, K., Mucci, A., Ouellet, A. and Gélinas, Y., 2012. Preservation of organic matter in sediments promoted by iron. Nature 483(7388): 198-200.

Langley, S., Gault, A., Ibrahim, A., Renaud, R., Fortin, D., Clark, I. D. and Ferris, F. G., 2009a. A Comparison of the Rates of Fe(III) Reduction in Synthetic and Bacteriogenic Iron Oxides by Shewanella putrefaciens CN32. Geomicrobiology Journal 26(2): 57-70.

Langley, S., Gault, A., Ibrahim, A., Renaud, R., Fortin, D., Clark, I. D. and Ferris, F. G., 2009b. A Comparison of the Rates of Fe(III) Reduction in Synthetic and Bacteriogenic Iron Oxides byShewanella putrefaciensCN32. Geomicrobiol. J. 26(2): 57-70.
Langley, S., Gault, A. G., Ibrahim, A., Takahashi, Y., Renaud, R., Fortin, D., Clark, I. D. and Ferris, F. G., 2009c. Sorption of strontium onto bacteriogenic iron oxides. Environ. Sci. Technol. 43(4): 1008-1014.
Langley, S., Gault, A. G., Ibrahim, A., Takahashi, Y., Renaud, R., Fortin, D., Clark, I. D. and Ferris, F. G., 2009d. Strontium desorption from bacteriogenic iron oxides (BIOS) subjected to microbial Fe(III) reduction. Chem. Geol. 262(3-4): 217-228.
Langley, S., Igric, P., Takahashi, Y., Sakai, Y., Fortin, D., Hannington, M. D. and Schwarz-Schampera, U., 2009e. Preliminary characterization and biological reduction of putative biogenic iron oxides (BIOS) from the Tonga-Kermadec Arc, southwest Pacific Ocean. Geobiology 7(1): 35-49.
Latta, D. E., Gorski, C. A. and Scherer, M. M., 2012. Influence of Fe2+-catalysed iron oxide recrystallization on metal cycling. Biochem. Soc. Trans. 40(6): 1191-1197.
Layglon, N., Misson, B., Mounier, S., Lenoble, V., Omanovic, D. and Garnier, C., 2020. Have decades of abiotic studies in sediments been misinterpreted? Sci. Total Environ. 707: 135949.
Leal, D., Matsuhiro, B., Rossi, M. and Caruso, F., 2008. FT-IR spectra of alginic acid block fractions in three species of brown seaweeds. Carbohydr Res 343(2): 308-316.
Lees, K., Fitzsimons, M., Snape, J., Tappin, A. and Comber, S., 2018. Soil sterilisation methods for use in OECD 106: How effective are they? Chemosphere 209: 61-67.
Li, Q., Hu, W., Li, L. and Li, Y., 2023. Interactions between organic matter and Fe oxides at soil micro-interfaces: Quantification, associations, and influencing factors. Sci. Total Environ. 855: 158710.
Liu, C., 1999. Surface chemistry of iron oxide minerals formed in different ionic environments.
Liu, Q., Li, X., Tang, J., Zhou, Y., Lin, Q., Xiao, R. and Zhang, M., 2019. Characterization of goethite-fulvic acid composites and their impact on the immobility of Pb/Cd in soil. Chemosphere 222: 556-563.
Lotrario, J., Stuart, B., Lam, T., Arands, R., O'Connor, O. and Kosson, D., 1995. Effects of sterilization methods on the physical characteristics of soil: implications for sorption isotherm analyses. Bull. Environ. Contam. Toxicol. 54: 668-675.
Lovley, D. R., Holmes, D. E. and Nevin, K. P., 2004. Dissimilatory fe (iii) and mn (iv) reduction. Adv. Microb. Physiol. 49(2): 219-286.
Maisch, M., Lueder, U., Kappler, A. and Schmidt, C., 2019. Iron lung: how rice roots induce iron redox changes in the rhizosphere and create niches for microaerophilic Fe (II)-oxidizing bacteria. Environmental Science & Technology Letters 6(10): 600-605.
Marsili, E., Baron, D. B., Shikhare, I. D., Coursolle, D., Gralnick, J. A. and Bond, D. R., 2008. Shewanella secretes flavins that mediate extracellular electron transfer. Proc. Natl. Acad. Sci. 105(10): 3968-3973.
Martens, J., Mueller, C. W., Joshi, P., Rosinger, C., Maisch, M., Kappler, A., Bonkowski, M., Schwamborn, G., Schirrmeister, L. and Rethemeyer, J., 2023. Stabilization of mineral-associated organic carbon in Pleistocene permafrost. Nat Commun 14(1): 2120.
Martinez, R. E., Smith, D. S., Pedersen, K. and Ferris, F. G., 2003. Surface chemical heterogeneity of bacteriogenic iron oxides from a subterranean environment. Environ. Sci. Technol. 37(24): 5671-5677.

McNamara, N. P., Black, H. I. J., Beresford, N. A. and Parekh, N. R., 2003. Effects of acute gamma irradiation on chemical, physical and biological properties of soils. Appl. Soil Ecol. 24(2): 117-132.
Mejia, J., He, S., Yang, Y., Ginder-Vogel, M. and Roden, E. E., 2018. Stability of Ferrihydrite-Humic Acid Coprecipitates under Iron-Reducing Conditions. Environ. Sci. Technol. 52(22): 13174-13183.
Melton, E. D., Swanner, E. D., Behrens, S., Schmidt, C. and Kappler, A., 2014. The interplay of microbially mediated and abiotic reactions in the biogeochemical Fe cycle. Nature Reviews Microbiology 12(12): 797-808.
Mikutta, C. and Kretzschmar, R., 2008. Synthetic coprecipitates of exopolysaccharides and ferrihydrite. Part II: Siderophore-promoted dissolution. Geochim. Cosmochim. Acta 72(4): 1128-1142.
Mikutta, C., Mikutta, R., Bonneville, S., Wagner, F., Voegelin, A., Christl, I. and Kretzschmar, R., 2008. Synthetic coprecipitates of exopolysaccharides and ferrihydrite. Part I: Characterization. Geochim. Cosmochim. Acta 72(4): 1111-1127.
Mikutta, R., Lorenz, D., Guggenberger, G., Haumaier, L. and Freund, A., 2014. Properties and reactivity of Fe-organic matter associations formed by coprecipitation versus adsorption: Clues from arsenate batch adsorption. Geochim. Cosmochim. Acta 144: 258-276.
Moon, E. M. and Peacock, C. L., 2012. Adsorption of Cu (II) to ferrihydrite and ferrihydrite–bacteria composites: Importance of the carboxyl group for Cu mobility in natural environments. Geochim. Cosmochim. Acta 92: 203-219.
Muehe, E. M., Scheer, L., Daus, B. and Kappler, A., 2013. Fate of arsenic during microbial reduction of biogenic versus abiogenic As–Fe (III)–mineral coprecipitates. Environ. Sci. Technol. 47(15): 8297-8307.
Najem, T., Langley, S. and Fortin, D., 2016. A comparison of Fe(III) reduction rates between fresh and aged biogenic iron oxides (BIOS) by Shewanella putrefaciens CN32. Chem. Geol. 439: 1-12.
Namayandeh, A., Borkiewicz, O. J., Bompoti, N. M., Watson, S. K., Kubicki, J. D., Chrysochoou, M. and Michel, F. M., 2023. Effects of Oxyanion Surface Loading on the Rate and Pathway of Ferrihydrite Transformation. ACS Earth Space Chem. 7(10): 2154-2165.
Namayandeh, A., Zhang, W., Watson, S. K., Borkiewicz, O. J., Bompoti, N. M., Chrysochoou, M., Penn, R. L. and Michel, F. M., 2024. Goethite and Hematite Nucleation and Growth from Ferrihydrite: Effects of Oxyanion Surface Complexes. Environ. Sci. Technol. 58(13): 5952-5962.
O'Loughlin, E. J., Boyanov, M. I., Flynn, T. M., Gorski, C. A., Hofmann, S. M., McCormick, M. L., Scherer, M. M. and Kemner, K. M., 2013. Effects of bound phosphate on the bioreduction of lepidocrocite (γ-FeOOH) and maghemite (γ-Fe2O3) and formation of secondary minerals. Environ. Sci. Technol. 47(16): 9157-9166.
O'Loughlin, E. J., Gorski, C. A., Scherer, M. M., Boyanov, M. I. and Kemner, K. M., 2010. Effects of oxyanions, natural organic matter, and bacterial cell numbers on the bioreduction of lepidocrocite (γ-FeOOH) and the formation of secondary mineralization products. Environ. Sci. Technol. 44(12): 4570-4576.
Otte, J. M., Blackwell, N., Soos, V., Rughoft, S., Maisch, M., Kappler, A., Kleindienst, S. and Schmidt, C., 2018. Sterilization impacts on marine sediment---Are we able to inactivate microorganisms in environmental samples? FEMS Microbiol. Ecol. 94(12).

Parmar, N., Warren, L. A., Roden, E. E. and Ferris, F. G., 2000. Solid phase capture of strontium by the iron reducing bacteria Shewanella alga strain BrY. Chem. Geol. 169(3-4): 281-288.
Patzner, M. S., Logan, M., McKenna, A. M., Young, R. B., Zhou, Z., Joss, H., Mueller, C. W., Hoeschen, C., Scholten, T., Straub, D., Kleindienst, S., Borch, T., Kappler, A. and Bryce, C., 2022. Microbial iron cycling during palsa hillslope collapse promotes greenhouse gas emissions before complete permafrost thaw. Commun. Earth Environ. 3(1).
Pedrot, M., Le Boudec, A., Davranche, M., Dia, A. and Henin, O., 2011. How does organic matter constrain the nature, size and availability of Fe nanoparticles for biological reduction? J. Colloid Interface Sci. 359(1): 75-85.
Penn, R. L. and Soltis, J. A., 2014. Characterizing crystal growth by oriented aggregation. CrystEngComm 16(8): 1409-1418.
Piepenbrock, A., Schröder, C. and Kappler, A., 2014. Electron transfer from humic substances to biogenic and abiogenic Fe (III) oxyhydroxide minerals. Environ. Sci. Technol. 48(3): 1656-1664.
Plötze, M., Kahr, G. and Hermanns Stengele, R., 2003. Alteration of clay minerals—gamma-irradiation effects on physicochemical properties. Applied Clay Science 23(1-4): 195-202.
Poggenburg, C., Mikutta, R., Sander, M., Schippers, A., Marchanka, A., Dohrmann, R. and Guggenberger, G., 2016. Microbial reduction of ferrihydrite-organic matter coprecipitates by Shewanella putrefaciens and Geobacter metallireducens in comparison to mediated electrochemical reduction. Chem. Geol. 447: 133-147.
Poggenburg, C., Mikutta, R., Schippers, A., Dohrmann, R. and Guggenberger, G., 2018. Impact of natural organic matter coatings on the microbial reduction of iron oxides. Geochim. Cosmochim. Acta 224: 223-248.
Possinger, A. R., Zachman, M. J., Dynes, J. J., Regier, T. Z., Kourkoutis, L. F. and Lehmann, J., 2021. Co-precipitation induces changes to iron and carbon chemistry and spatial distribution at the nanometer scale. Geochim. Cosmochim. Acta 314: 1-15.
Radloff, K. A., Manning, A. R., Mailloux, B., Zheng, Y., Rahman, M. M., Huq, M. R., Ahmed, K. M. and van Geen, A., 2008. Considerations for conducting incubations to study the mechanisms of As release in reducing groundwater aquifers. Appl. Geochem. 23(11): 3224-3235.
Rancourt, D. G., Thibault, P.-J., Mavrocordatos, D. and Lamarche, G., 2005. Hydrous ferric oxide precipitation in the presence of nonmetabolizing bacteria: Constraints on the mechanism of a biotic effect. Geochim. Cosmochim. Acta 69(3): 553-577.
Retelletti Brogi, S., Derrien, M. and Hur, J., 2019. In-Depth Assessment of the Effect of Sodium Azide on the Optical Properties of Dissolved Organic Matter. J Fluoresc 29(4): 877-885.
Riedel, T., Zak, D., Biester, H. and Dittmar, T., 2013. Iron traps terrestrially derived dissolved organic matter at redox interfaces. Proc. Natl. Acad. Sci. 110(25): 10101-10105.
Roden, E. E., 2003. Fe (III) oxide reactivity toward biological versus chemical reduction. Environ. Sci. Technol. 37(7): 1319-1324.
Roden, E. E., Kappler, A., Bauer, I., Jiang, J., Paul, A., Stoesser, R., Konishi, H. and Xu, H., 2010. Extracellular electron transfer through microbial reduction of solid-phase humic substances. Nature geoscience 3(6): 417-421.
Roden, E. E. and Urrutia, M. M., 2002. Influence of biogenic Fe (II) on bacterial crystalline Fe (III) oxide reduction. Geomicrobiol. J. 19(2): 209-251.

Roden, E. E. and Zachara, J. M., 1996. Microbial reduction of crystalline iron (III) oxides: influence of oxide surface area and potential for cell growth. Environ. Sci. Technol. 30(5): 1618-1628.
Rose, J., Flank, A.-M., Masion, A., Bottero, J.-Y. and Elmerich, P., 1997. Nucleation and growth mechanisms of Fe oxyhydroxide in the presence of PO4 ions. 2. P K-edge EXAFS study. Langmuir 13(6): 1827-1834.
Rouquerol, J., Llewellyn, P. and Rouquerol, F., 2007. Is the BET equation applicable to microporous adsorbents. Stud. Surf. Sci. Catal 160(07): 49-56.
Rouquerol, J., Rouquerol, F., Llewellyn, P., Maurin, G. and Sing, K., 2013. Adsorption by powders and porous solids: principles, methodology and applications, Academic press.
Salonius, P., Robinson, J. and Chase, F., 1967. A comparison of autoclaved and gamma-irradiated soils as media for microbial colonization experiments. Plant Soil 27(2): 239-248.
Santoro, V., Martin, M., Persson, P., Lerda, C., Said-Pullicino, D., Magnacca, G. and Celi, L., 2019. Inorganic and organic P retention by coprecipitation during ferrous iron oxidation. Geoderma 348: 168-180.
Sartori, C., Finch, D. S., Ralph, B. and Gilding, K., 1997. Determination of the cation content of alginate thin films by FTIR spectroscopy. Polymer 38(1): 43-51.
Schaller, J., Weiske, A. and Dudel, E. G., 2011. Effects of gamma-sterilization on DOC, uranium and arsenic remobilization from organic and microbial rich stream sediments. Sci. Total Environ. 409(17): 3211-3214.
Schoepfer, V. A., Burton, E. D., Johnston, S. G. and Kraal, P., 2017. Phosphate-imposed constraints on schwertmannite stability under reducing conditions. Environ. Sci. Technol. 51(17): 9739-9746.
Schwertmann, U., 1966. Inhibitory effect of soil organic matter on the crystallization of amorphous ferric hydroxide. Nature 212(5062): 645-646.
Schwertmann, U. and Cornell, R. M., 2008. Iron oxides in the laboratory: preparation and characterization, John Wiley & Sons.
Schwertmann, U., Wagner, F. and Knicker, H., 2005. Ferrihydrite–Humic Associations. Soil Sci. Soc. Am. J. 69(4): 1009-1015.
Senn, A.-C., Kaegi, R., Hug, S. J., Hering, J. G., Mangold, S. and Voegelin, A., 2015. Composition and structure of Fe (III)-precipitates formed by Fe (II) oxidation in water at near-neutral pH: Interdependent effects of phosphate, silicate and Ca. Geochim. Cosmochim. Acta 162: 220-246.
Shimizu, M., Zhou, J., Schroder, C., Obst, M., Kappler, A. and Borch, T., 2013. Dissimilatory reduction and transformation of ferrihydrite-humic acid coprecipitates. Environ. Sci. Technol. 47(23): 13375-13384.
Song, X., Wang, P., Van Zwieten, L., Bolan, N., Wang, H., Li, X., Cheng, K., Yang, Y., Wang, M. and Liu, T., 2022. Towards a better understanding of the role of Fe cycling in soil for carbon stabilization and degradation. Carbon Research 1(1): 5.
Sowers, T. D., Harrington, J. M., Polizzotto, M. L. and Duckworth, O. W., 2017. Sorption of arsenic to biogenic iron (oxyhydr) oxides produced in circumneutral environments. Geochim. Cosmochim. Acta 198: 194-207.
Sowers, T. D., Stuckey, J. W. and Sparks, D. L., 2018. The synergistic effect of calcium on organic carbon sequestration to ferrihydrite. Geochemical transactions 19: 1-11.

Stookey, L. L., 1970. Ferrozine---a new spectrophotometric reagent for iron. Analytical Chemistry 42(7): 779-781.
Stumm, W. and Morgan, J. J., 2013. Aquatic chemistry: chemical equilibria and rates in natural waters, John Wiley & Sons.
ThomasArrigo, L. K., Bouchet, S., Kaegi, R. and Kretzschmar, R., 2020. Organic matter influences transformation products of ferrihydrite exposed to sulfide. Environmental Science: Nano 7(11): 3405-3418.
ThomasArrigo, L. K., Notini, L., Shuster, J., Nydegger, T., Vontobel, S., Fischer, S., Kappler, A. and Kretzschmar, R., 2022. Mineral characterization and composition of Fe-rich flocs from wetlands of Iceland: Implications for Fe, C and trace element export. Sci. Total Environ. 816: 151567.
Toner, B. M., Marcus, M. A., Edwards, K. J., Rouxel, O. and German, C. R., 2012. Measuring the form of iron in hydrothermal plume particles. Oceanography 25(1): 209-212.
Toner, B. M., Santelli, C. M., Marcus, M. A., Wirth, R., Chan, C. S., McCollom, T., Bach, W. and Edwards, K. J., 2009. Biogenic iron oxyhydroxide formation at mid-ocean ridge hydrothermal vents: Juan de Fuca Ridge. Geochim. Cosmochim. Acta 73(2): 388-403.
Tufano, K. J., Reyes, C., Saltikov, C. W. and Fendorf, S., 2008. Reductive processes controlling arsenic retention: revealing the relative importance of iron and arsenic reduction. Environ. Sci. Technol. 42(22): 8283-8289.
Tuominen, L., Kairesalo, T. and Hartikainen, H., 1994. Comparison of methods for inhibiting bacterial activity in sediment. Appl. Environ. Microbiol. 60(9): 3454-3457.
van der Grift, B., Behrends, T., Osté, L., Schot, P., Wassen, M. and Griffioen, J., 2016. Fe hydroxyphosphate precipitation and Fe (II) oxidation kinetics upon aeration of Fe (II) and phosphate-containing synthetic and natural solutions. Geochim. Cosmochim. Acta 186: 71-90.
van der Grift, B., Osté, L., Schot, P., Kratz, A., van Popta, E., Wassen, M. and Griffioen, J., 2018. Forms of phosphorus in suspended particulate matter in agriculture-dominated lowland catchments: Iron as phosphorus carrier. Sci. Total Environ. 631: 115-129.
Vindedahl, A. M., Strehlau, J. H., Arnold, W. A. and Penn, R. L., 2016. Organic matter and iron oxide nanoparticles: aggregation, interactions, and reactivity. Environmental Science: Nano 3(3): 494-505.
Viollier, E., Inglett, P. W., Hunter, K., Roychoudhury, A. N. and Van Cappellen, P., 2000. The ferrozine method revisited: Fe(II)/Fe(III) determination in natural waters. Applied Geochemistry 15(6): 785-790.
Voegelin, A., Kaegi, R., Frommer, J., Vantelon, D. and Hug, S. J., 2010. Effect of phosphate, silicate, and Ca on Fe (III)-precipitates formed in aerated Fe (II)-and As (III)-containing water studied by X-ray absorption spectroscopy. Geochim. Cosmochim. Acta 74(1): 164-186.
Voegelin, A., Senn, A.-C., Kaegi, R. and Hug, S. J., 2019. Reductive dissolution of As (V)-bearing Fe (III)-precipitates formed by Fe (II) oxidation in aqueous solutions. Geochemical transactions 20: 1-13.
Voegelin, A., Senn, A.-C., Kaegi, R., Hug, S. J. and Mangold, S., 2013. Dynamic Fe-precipitate formation induced by Fe (II) oxidation in aerated phosphate-containing water. Geochim. Cosmochim. Acta 117: 216-231.

Vollrath, S., Behrends, T., Koch, C. B. and Van Cappellen, P., 2013. Effects of temperature on rates and mineral products of microbial Fe (II) oxidation by Leptothrix cholodnii at microaerobic conditions. Geochim. Cosmochim. Acta 108: 107-124.
Von Canstein, H., Ogawa, J., Shimizu, S. and Lloyd, J. R., 2008. Secretion of flavins by Shewanella species and their role in extracellular electron transfer. Appl. Environ. Microbiol. 74(3): 615-623.
Wagai, R. and Mayer, L. M., 2007. Sorptive stabilization of organic matter in soils by hydrous iron oxides. Geochim. Cosmochim. Acta 71(1): 25-35.
Wang, B., Wan, Y., Zheng, Y., Lee, X., Liu, T., Yu, Z., Huang, J., Ok, Y. S., Chen, J. and Gao, B., 2019. Alginate-based composites for environmental applications: a critical review. Crit. Rev. Environ. Sci. Technol. 49(4): 318-356.
Wang, Q., Wang, J., Wang, X., Kumar, N., Pan, Z., Peiffer, S. and Wang, Z., 2023. Transformations of ferrihydrite–extracellular polymeric substance coprecipitates driven by dissolved sulfide: interrelated effects of carbon and sulfur loadings. Environ. Sci. Technol. 57(10): 4342-4353.
Warren, L. A. and Ferris, F. G., 1998. Continuum between sorption and precipitation of Fe (III) on microbial surfaces. Environ. Sci. Technol. 32(15): 2331-2337.
Weihe, S. H., Mangayayam, M., Sand, K. K. and Tobler, D. J., 2019. Hematite crystallization in the presence of organic matter: impact on crystal properties and bacterial dissolution. ACS Earth Space Chem. 3(4): 510-518.
Wen, S., Lu, Y., Dai, J., Huang, X., An, S., Liu, J., Liu, Z., Du, Y. and Zhang, Y., 2023. Stability of organic matter-iron-phosphate associations during abiotic reduction of iron. J. Hazard. Mater. 449: 131016.
Whitaker, A. H. and Duckworth, O. W., 2018. Cu, Pb, and Zn sorption to biogenic iron (oxyhydr) oxides formed in circumneutral environments. Soil syst. 2(2): 18.
Wolf, D., Dao, T., Scott, H. and Lavy, T., 1989. Influence of sterilization methods on selected soil microbiological, physical, and chemical properties, Wiley Online Library.
Xue, Q., Ran, Y., Tan, Y., Peacock, C. L. and Du, H., 2019. Arsenite and arsenate binding to ferrihydrite organo-mineral coprecipitate: Implications for arsenic mobility and fate in natural environments. Chemosphere 224: 103-110.
Yakabuskie, P. A., Joseph, J. M., Keech, P., Botton, G. A., Guzonas, D. and Wren, J. C., 2011. Iron oxyhydroxide colloid formation by gamma-radiolysis. Phys Chem Chem Phys 13(15): 7198-7206.
Zachara, J. M., Fredrickson, J. K., Li, S.-M., Kennedy, D. W., Smith, S. C. and Gassman, P. L., 1998. Bacterial reduction of crystalline Fe3+ oxides in single phase suspensions and subsurface materials. American Mineralogist 83(11): 1426-1443.
Zachara, J. M., Kukkadapu, R. K., Fredrickson, J. K., Gorby, Y. A. and Smith, S. C., 2002. Biomineralization of poorly crystalline Fe (III) oxides by dissimilatory metal reducing bacteria (DMRB). Geomicrobiol. J. 19(2): 179-207.
Zegeye, A., Mustin, C. and Jorand, F., 2010. Bacterial and iron oxide aggregates mediate secondary iron mineral formation: green rust versus magnetite. Geobiology 8(3): 209-222.
Zeng, Q., Huang, L., Ma, J., Zhu, Z., He, C., Shi, Q., Liu, W., Wang, X., Xia, Q. and Dong, H., 2020. Bio-reduction of ferrihydrite-montmorillonite-organic matter complexes: Effect of montmorillonite and fate of organic matter. Geochim. Cosmochim. Acta 276: 327-344.

Zhao, Q., Adhikari, D., Huang, R., Patel, A., Wang, X., Tang, Y., Obrist, D., Roden, E. E. and Yang, Y., 2017. Coupled dynamics of iron and iron-bound organic carbon in forest soils during anaerobic reduction. Chem. Geol. 464: 118-126.

Zhao, Q., Kobayashi, T., Saito, T. and Sasaki, T., 2021. Gamma-irradiation-induced molecular-weight distribution and complexation affinity of humic acid with Cs(+), Sr(2+), and Eu(3). J. Hazard. Mater. 411: 125071.

Zhao, Q., Poulson, S. R., Obrist, D., Sumaila, S., Dynes, J. J., McBeth, J. M. and Yang, Y., 2016. Iron-bound organic carbon in forest soils: quantification and characterization. Biogeosciences 13(16): 4777-4788.

Zhao, X., Yuan, Z., Wang, S., Pan, Y., Chen, N., Tunc, A., Cheung, K., Alparov, A., Chen, W. and Deevsalar, R., 2022a. Iron (II)-activated phase transformation of Cd-bearing ferrihydrite: Implications for cadmium mobility and fate under anaerobic conditions. Sci. Total Environ. 848: 157719.

Zhao, Y., Moore, O. W., Xiao, K.-Q., Curti, L., Fariña, A. O., Banwart, S. A. and Peacock, C. L., 2022b. The role and fate of organic carbon during aging of ferrihydrite. Geochim. Cosmochim. Acta 335: 339-355.

Zhou, Z., Latta, D. E., Noor, N., Thompson, A., Borch, T. and Scherer, M. M., 2018. Fe(II)-Catalyzed Transformation of Organic Matter–Ferrihydrite Coprecipitates: A Closer Look Using Fe Isotopes. Environ. Sci. Technol. 52(19): 11142-11150.

Chapter 2: Physicochemical properties and bioavailability of synthetic coprecipitates of Fe (oxy)hydroxides and Na-alginate

Tarek Najem[a] and Danielle Fortin[a*]

[a] Department of Earth and Environmental Sciences, University of Ottawa, Ottawa, Ontario, Canada

* Corresponding author: dfortin@uottawa.ca

To be submitted to a journal

Abstract

Microbial dissimilatory iron reduction (DIR) is a common process in anoxic environments that plays an important role in the cycling of Fe and C, ultimately influencing the distribution of nutrients, contaminants, and trace metals in the environment. Extensive research has explored this process, focusing on Fe(III)-reducing bacterial strains, the chemical composition of the surrounding medium, and the type of Fe substrate serving as the electron acceptor. More recently, research has shifted to explore the impact of organic matter (OM) on the DIR rates and extent of Fe(III) reduction of Fe substrates that are closely associated with OM through adsorption and/or coprecipitation processes. However, much of this work had focused on ferrihydrite-OM associations, overlooking lepidocrocite- and goethite-OM associations despite their widespread presence in soils, sediments, and wetlands. Here, we examined the influence of Na-alginate, an analogue to polysaccharides on the physicochemical properties and reactivity of 2-line ferrihydrite (Fh), lepidocrocite (Lp), and goethite (Gt). The minerals were synthesized by forced hydrolysis of Fe^{3+} (Fh)- and oxidation of Fe^{2+} (Lp and Gt)-solutions in the presence of varying concentrations of alginate (C/Fe 0, 0.5, 1.0, and 1.5 mol:mol) that are relevant to environmental conditions. Characterization of the minerals was performed by conventional analytical techniques (XRD, ATR-FTIR, BET, ζ-potential, and particle size), whereas their reactivity was assessed using chemical extractants (0.5 M HCl, and ascorbate) and the model Fe-reducing bacterium, *Shewanella putrefaciens* CN32. As the alginate content increased, the crystallinity of the minerals notably decreased due to alginate-mediated inhibition of crystal growth. This was accompanied by a decrease and increase in the specific surface area for the Fh and Gt coprecipitates, and lepidocrocite, respectively. Electrophoretic mobility measurements showed a decrease in the isoelectric point across all coprecipitates, while changes in particle or aggregate size varied

between the different mineral types. When exposed to chemical extractants, alginate at its highest concentration had only a minor impact on the extractability of Fh. In contrast, the extractability of the Lp and Gt coprecipitates significantly increased with increasing alginate content, suggesting an increase in the proportion of a poorly crystalline Fe phase. Despite these significant changes in crystallinity and physicochemical properties, the alginate content did not significantly affect microbial Fe(III) reduction rates compared to pure minerals. However, the maximum amount of Fe reduced from the Fh coprecipitates was ~15% lower than that of pure Fh. For Lp and Gt coprecipitates, the extent of Fe reduction increased by ~7% and ~4%, respectively, at a C/Fe ratio of 1.0 and 1.5. Overall, this study highlights that OM interactions with Fe minerals can significantly alter their crystallinity, surface properties, and chemical extractability, yet these changes do not always translate directly to differences in microbial Fe(III) reduction rates, which appear to be influenced more by the mineral type and extent of OM association. These are important considerations for predicting DIR processes and the cycling/release of associated nutrients, contaminants, and C in natural settings, as well as for the potential application of DIR in bioremediation strategies and other environmental management practices.

Keywords
Na-Alginate, Organic matter, Coprecipitation, Ferrihydrite, Goethite, Lepidocrocite, Bioavailability, *Shewanella putrefaciens*

1. Introduction

Iron oxides (referring to iron oxides, hydroxides, and oxyhydroxides) are ubiquitous in terrestrial and aquatic environments, and due to their unique physicochemical properties, such as large surface area and variable surface charge, they play a key role in controlling the transport and bioavailability of nutrients, heavy metals, and metalloids. Iron oxides also exhibit high reactivity towards organic matter (OM), encompassing humic acids, fulvic acids, and polysaccharides. Consequently, iron oxides are closely associated with OM in aquatic and terrestrial environments that arise from a range of chemical and physical processes. These processes include the adsorption of OM to the surface of preformed- and the coprecipitation of OM with neoformed- mineral phases where the latter comprises several interlinked complex processes (Kaiser et al., 1997; Kaiser, 2003; Schwertmann et al., 2005; Wagai and Mayer, 2007; Mikutta et al., 2008; Pedrot et al., 2011; Chen et al., 2014; Kleber et al., 2015; Curti et al., 2021; Possinger et al., 2021; Li et al., 2023). Such processes are abundant in the environment, and they occur within the porewaters of soils and sediments (Wagai and Mayer, 2007; Cismasu et al., 2011; Lalonde et al., 2012; Zhao et al., 2016), oxic-anoxic transition zones where Fe(II)-bearing anoxic solutions contact atmospheric O_2 (Riedel et al., 2013), and industrial coagulation water treatment landfills (Henneberry et al., 2012).

The impact of OM on the mineralogy, crystallinity, stability, and physicochemical properties of iron oxides during precipitation is well documented in the literature and has been described in laboratory-based studies and naturally occurring samples (Langley et al., 2009e; Vollrath et al., 2013; Chen et al., 2015; Liu et al., 2019b; ThomasArrigo et al., 2022). These organo-mineral coprecipitates are characterized by small crystal size, defective crystallographic structure as well as distinct specific surface area, aggregation state, and surface charge (Eusterhues et al., 2008; Mikutta et al., 2008; Toner et al., 2009; ThomasArrigo et al., 2022). Because of these

properties, organo-mineral coprecipitates have been a subject of intense research to determine their role in the environment towards contaminant, nutrient, and trace metal mobility (Grybos et al., 2007; Mikutta et al., 2014; Fabisch et al., 2016; Hao et al., 2016; Sowers et al., 2017; Chen et al., 2018; Field et al., 2019; Xue et al., 2019; Dong et al., 2022), C storage (Lalonde et al., 2012; Han et al., 2019; Patzner et al., 2022; Martens et al., 2023), long term stability (Kaiser et al., 2007; Cismasu et al., 2016; Najem et al., 2016; Zhao et al., 2022c), well as susceptibility to abiotic reductants (e.g. sulfide) (Wang et al., 2023). Past and ongoing research also focused on examining the bioavailability of organo-mineral coprecipitates to dissimilatory iron reducing bacteria (DIR) to determine reaction rates as well as the fate of C and associated nutrients/trace metals/contaminants (Langley et al., 2009b; Pedrot et al., 2011; Amstaetter et al., 2012; Shimizu et al., 2013; Eusterhues et al., 2014a; Adhikari et al., 2016; Poggenburg et al., 2016; Adhikari et al., 2017; Cooper et al., 2017; Zhao et al., 2017; Mejia et al., 2018; Poggenburg et al., 2018; Han et al., 2019; Zeng et al., 2020; Dong et al., 2023). Within this context, past research highlighted the importance of the physicochemical and mineralogical properties as well as OM content/type in modulating the reactivity of these composites. For example, the rate and extent of DIR of ferrihydrite (Fh)-humic acid composites by *Shewanella putrefaciens* CN32 depended on the C/Fe ratio such that DIR was hindered and enhanced at low (≤0.8) and high (≥1.8) C/Fe ratios, respectively (Shimizu et al., 2013). DIR of Fh coprecipitated with various types of OM (C/Fe 1.0) by the same strain of bacteria was also influenced by the amount of available electron shuttling molecules provided by the OM, with Fh-exopolysaccharides composites exhibiting the least bioavailability in comparison to other Fh-OM composites (Poggenburg et al., 2016; Poggenburg et al., 2018). In contrast, DIR of the same composites by *Geobacter metallireducens* was influenced by particle size and OM-induced aggregation (Poggenburg et al., 2016).

While the effects of OM on DIR have been studied for Fh-OM associations, information on how other iron oxides are affected is sparse. Lepidocrocite (Lp) and goethite (Gt), for example, exhibit different thermodynamic stability than Fh under typical near surface temperature and pH conditions (Cornell and Schwertmann, 2003). These minerals are also abundant in soils and sediments, and they have been described in the literature to form in close association of exopolysaccharides produced by Fe(II)-oxidizing bacteria in the environment and under laboratory conditions (Kleinert et al., 2011; Muehe et al., 2013; Vollrath et al., 2013; Najem et al., 2016; ThomasArrigo et al., 2022). To the best of our knowledge, few studies have investigated how OM coprecipitated with Lp and Gt affects DIR processes. Muehe et al. (2013) reported that the rate of DIR by *S. oneidensis* MR-1 of a biogenic iron oxide, a mixture of mainly Gt and 13 ± 5% Fh, formed by the Fe(II)-oxidizer *Acidovorax* sp. BoFeN1 was equivalent to and higher than that of synthetic Fh and Gt, respectively. Piepenbrock et al. (2014) also reported a higher reduction of biogenic Gt by humic substances than that of a synthetic equivalent. Likewise, Fe-humic acid nanoparticulate coprecipitates formed from the oxidation of Fe(II) in the presence of OM were reduced by *S. putrefaciens* CIP 80.40 T 8x faster than in the case of nano-lepidocrocite (Pedrot et al., 2011). More recently, Weihe et al. (2019) reported that alginate-hematite coprecipitates (C/Fe 0.1 and 1.0) exhibited a 30-50% lower DIR rate by *S. oneidensis* MR-1 but a slightly higher Fe(III) reduction extent than pure hematite. Therefore, it is clear that OM has variable impact on the bioavailability of iron oxides.

The objectives of this study are to: (i) identify the physicochemical and mineralogical characteristics of Fh-, Lp-, and Gt-OM coprecipitates; (ii) determine the susceptibility of the coprecipitates to chemical dissolution; and (iii) determine the bioavailability of the coprecipitates to DIR by a model iron reducing bacteria *Shewanella putrefaciens* CN32. To this end, Fh, Lp, and

Gt were synthesized in the presence of varying concentrations of Na-alginate at C/Fe ratios that are relevant to those found in the environment. Alginate was chosen as the organic compound due to its chemical resemblance to algae derived OM and to the twisted stalks and sheaths produced by the Fe(II)-oxidizing bacteria *Gallionella* spp. and *Leptothrix* spp., respectively (Chan et al., 2004; Chan et al., 2009; Wen et al., 2023). Polysaccharides are also important components of plant root exudates, contributing up to ~10% of the total organic matter pool in soils and sediments (Kleber et al., 2015). The synthetic minerals used for this research were previously characterized in terms of physicochemical and mineralogical properties, and bioavailability against their γ-irradiated counterparts (Najem et al., 2025). For this research, we focus on analyzing differences among the minerals to differentiate the effects of OM content on mineralogy and bioavailability. Therefore, results from this research adds to the understanding of the influence of OM on DIR processes and the biogeochemical cycling of Fe and C in natural environments.

2. Materials and methods

2.1. Synthesis of coprecipitates

Prior to mineral syntheses, all necessary glassware and components were initially submerged in 10% HNO_3 bath for a minimum duration of 24 hours then washed 3x with ultrapure water (UPW) (18 MΩ•cm). The glassware was then baked in a muffle-furnace at 450 ºC for a duration of 8 hours to remove any residual organic matter and then sterilized by autoclaving. Prior to use, Na-alginate was sterilized by spreading the dry powder on the base of a beaker or Pyrex bottle followed by irradiation with an ultraviolet light source (UVA) for a period of 1 hour. Potential UVA induced structural changes of alginate was assessed via FTIR-ATR, which revealed no observable changes (data not shown). To ensure sterility, all working solutions were prepared aseptically by using autoclaved UPW or by filtering (0.22 μm pore size).

Pure 2-line ferrihydrite (Fh) was synthesized by the rapid addition of 1 M NaOH to a solution of 80 mmol $FeCl_3 \bullet 6H_2O$ under vigorous stirring to a final pH of 7.0 (Langley et al., 2009b). The ferrihydrite-alginate coprecipitates were synthesized in a similar fashion to pure Fh from the point of NaOH addition to the Fe(III) solution as previously described (Mikutta et al., 2008). For the synthesis, an appropriate amount of Na-alginate powder was initially dissolved in 450 mL of sterile UPW for a period of 24 hours in the dark. Subsequently, the pH of the alginate-solution was adjusted to ~2.5 with 6 M trace metal grade HCl using a sterile pH probe while vigorously mixing. Following pH adjustment, the alginate solution obtained a homogenous milky appearance at which point 200 mL of $FeCl_3 \bullet 6H_2O$ solution of appropriate concentration was added to the alginate solution while vigorously mixing. At this point the pH of the mixture dropped to 1.4-1.8 and had an orange-milky appearance. 1 M NaOH was then added rapidly as described with Fh until a red-brown precipitate had formed. The pH of the final solution was ~7.00, which was monitored and adjusted for at least 20 minutes until fluctuation had ceased. Washing of the precipitate proceeded by centrifugation/vertexing and washing with sterile UPW until the conductivity of the supernatant decreased to <25 µS/cm.

Pure lepidocrocite (Lp) was synthesized following the method outlined in Schwertmann and Cornell (2008). Briefly, 11.93 g of $FeCl_2 \bullet 4H_2O$ (60 mmol) was dissolved in 100 mL UPW and filtered (Cytiva polyethersulfone membrane, 0.22µm) to sterilize and to remove any oxidized products directly into sterile 200 mL UPW while stirring. Subsequently, the pH of the acidic solution was rapidly adjusted to 6.7 with 1 M NaOH, at which point filtered compressed air was introduced at a rate of 100-115 mL/min. During the oxidation process, the pH of the solution was manually adjusted (6.7 – 6.9) by the addition of base until fluctuation had stabilised for at least 30 minutes. Synthesis of lepidocrocite-alginate coprecipitates proceeded in the same manner

described for Lp with some modifications. Initially, an appropriate amount of Na-alginate was dissolved in 300 mL of sterile UPW in the dark for a duration of 24 hours. After the pH adjustment of the alginate solution to 2.5, synthesis and pH adjustment proceeded as described with Lp. However, it was noted that the synthesis time of Lp increased with increasing organic matter content, in which case the time increased from 3 hours (pure Lp) to 6-8 hours (C/Fe 1.0 and 1.5). Consequently, minor amounts of goethite had formed likely as a result of the long exposure time of the solution to CO_2 (HCO_3^-) from the compressed air. Therefore, in order to eliminate such contamination, lepidocrocite-alginate coprecipitates (C/Fe of 1.0 and 1.5) were synthesized by bubbling with pure O_2 at a rate of ~25 mL/min. Such approach was successful in eliminating goethite and it also reduced the synthesis time to ~3 hours. Washing of the Lp precipitates proceeded as described for Fh.

Pure goethite (Gt) was synthesized via the oxidation of a Fe(II) solution following the method outlined in Schwertmann and Cornell (2008). Prior to synthesis, deoxygenated sterile UPW was prepared by sparging with filtered N_2 for 1 hour, and then transferred into a Coy Labs anaerobic chamber operating with an atmosphere of 95:5 N_2:H_2. Inside the anaerobic chamber, 15 g of $FeCl_2$•$4H_2O$ (75.45mmol) was dissolved into 150 mL of the deoxygenated UPW and then filtered (Cytiva polyethersulfone membrane, 0.22 μm) directly into 850 mL of deoxygenated UPW water in a 2 L Pyrex glass bottle and stirred. Outside the anaerobic chamber, 170 mL of a freshly prepared and filter sterilized solution of 1 M $NaHCO_3$ was aseptically added to the Fe(II) solution while stirring. This final mixture was then sparged with compressed air at a rate of 30-40 mL/min for a duration of 48 hours in the dark. Goethite-alginate coprecipitates were prepared by dissolving an appropriate amount of alginate into 500 mL of deoxygenated UPW for 24 hours in the dark. Under anaerobic conditions, 150 mL of 75.45 mmol of Fe(II) solution was then filtered directly

into the alginate solution while vigorously stirring, and then topped off with deoxygenated UPW to a final volume of 1 L. Subsequent synthesis proceeded as described for pure Gt. The final Gt precipitates were allowed to settle for up to 1 week prior to washing as described above.

2.2. Characterization of the Iron Oxides

2.2.1. ^{57}Fe Mössbauer spectroscopy

Samples for Mössbauer analyses were handled and dried under anaerobic conditions (95:5 N_2:H_2). The powdered samples were loaded into Plexiglas holders (area 1 cm^2), forming a disc. These samples were kept in airtight jars at -20 °C until measurement. Holders were inserted into a closed-cycle exchange gas cryostat (Janis cryogenics) under a backflow of He to minimize exposure to air. Spectra were collected at 77 K and 5 K using a constant acceleration drive system (WissEL) in transmission mode with a ^{57}Co/Rh source. All spectra were calibrated against a 7 μm thick α-^{57}Fe foil that was measured at room temperature. Analysis was carried out using Recoil (University of Ottawa) and the extended Voigt Based Fitting (VBF) routine (Lagarec and Rancourt, 1997). The half width at half maximum (HWHM) was constrained to 0.123 mm/s during fitting.

2.2.2. Powder X-ray Diffraction

The bulk mineralogy of the iron oxides was determined by X-ray diffraction (XRD). Air-dried samples were thoroughly ground to fine powders with an agate mortar and pestle and analysed with a Rigaku Ultima IV diffractometer using a Cu-Kα X-ray source, operating at 45 kV and 40 mA. Continuous scans were run from 10–80° 2Θ using a step size of 0.02° at a rate of 0.7 °/minute.

2.2.3. Specific Surface Area

Surface area measurements on duplicate samples prepared in the same manner as XRD were carried out using a Quantachrome Autosorb-1. Approximately, 100-300 mg of a sample was initially degassed under vacuum at a temperature of 50 °C for 24 h using a 9 mm cell. After the determination of degassing stability and final dry mass, 33 N_2 adsorption and 19 desorption points were recorded at 77 K in the partial pressure region $5x10^{-3}$- 0.99 P/P_0. The SSA was determined by applying the BET equation on the standard partial pressure region (0.05 – 0.3 P/P_0) or by applying the criteria established by Rouquerol et al. (2007) where deemed necessary. The micropore volume was determined by applying the Dubinin-Radushkevich (DR) method to adsorption points below 0.01 P/P_0, whereas the mesopore volume (2-50 nm) was determined by applying the Barrett-Joyner-Halenda (BJH) method as determined by the accompanying Autosorb-1 software (Mikutta et al., 2008; Poggenburg et al., 2016). Total pore volume was determined from the last point of the N_2 adsorption isotherm (0.99 P/P_0). Lastly, the mineral SSA and pore volumes were corrected for the weight of retained alginate content as described in Mikutta et al. (2008).

2.2.4. Fourier Transform Infrared Spectroscopy

Powdered samples were analysed with Fourier transform infrared spectroscopy (FTIR) using a *Nicolet 6700* spectrophotometer (ThermoFisher Scientific) equipped with a deuterated triglycine sulfate (*DTGS)* detector and a diamond crystal coated with ZnSe in attenuated total reflectance (ATR) mode. Prior to analyses, the powdered samples were dried under vacuum in an Oxoid™ Anaerobic Jar (~27 inHg below atmosphere) at 50 °C for a period of 24 hours to minimize the contribution of surface adsorbed H_2O to the spectra. While at 50 °C, the samples were flushed with pure nitrogen (GR4.5) and allowed to cool in a desiccator until analyses. Four individual measurements were made on each sample in order to determine the homogeneity of sample in

terms of particle size and composition together with instrumental reproducibility. For each sample, spectra were acquired from 500 to 4000 cm^{-1} at 4 cm^{-1} resolution, with 128 scans averaged per spectrum. Subsequently, the spectra were processed using the OMNIC software package (Thermo Fisher Scientific, version 9) where the spectra were averaged, automatically baseline corrected, and normalized to the maximum absorbance value.

2.2.5. Iron and Carbon Content

The pseudo-total iron content of dry powdered or wet samples was determined by suspending a known amount into 6 mL of UPW and fully digested by the addition of 4 mL trace metal grade 30 % H_2O_2 and 2 mL trace metal grade HNO_3 followed by heating at 75 °C for 24 hours. After dilution with 1% HNO_3 (v/v), the Fe content was determined via inductively coupled plasma ─ optical emission spectroscopy using a Varian Vista-PRO CCD Simultaneous ICP-OES, operating under standard conditions. All digestions were carried out in duplicates (powdered samples) or triplicates (wet samples). For carbon content determination, approximately 10 mg of a dry powdered sample was weighed into a tin capsule. The prepared samples were then analysed for carbon content at the University of Ottawa at the Jan Veizer Stable Isotope Laboratory using the Elementar Vario Isotope Cube.

2.2.6. Non-sequential Chemical Extractions

To determine the fraction of amorphous Fe non-sequential chemical extractions were carried out in triplicates following the methods outlined in Kostka and Luther (1994). Briefly, ~20 mg of wet sample was accurately weighed into 20 mL scintillation vials followed by the addition of either HCl (0.5 M) or ascorbate (pH 8.0). The HCl extraction proceeded under oxic conditions for a duration of 1 hour, whereas the ascorbate extraction proceeded under anoxic conditions for a

duration of 24 hours in the dark. Following extraction with HCl (0.5 M), the digests were filtered (Cytiva polyethersulfone membrane, 0.22 μm) and an aliquot was analysed with the ferrozine assay to determine the Fe(II) content ($HCl_{Fe(II)}$), and another aliquot was reduced with 0.28 M ClH_4NO in 0.28 M HCl for a duration of 30 minutes to determine total Fe ($HCl_{totalFe}$) concentration following determination with the ferrozine assay (Stookey, 1970; Kostka and Luther, 1994; Viollier et al., 2000). The 0.5 M HCl extractable Fe was calculated as $HCl_{Fe(III)} = HCl_{totalFe} - HCl_{Fe(II)}$. For the ascorbate extraction, the digests were filtered (Cytiva polyethersulfone membrane, 0.22 μm) under anoxic conditions and the filtrates were analysed using the ferrozine assay. To determine the fraction of amorphous Fe in the precipitates, the concentration of Fe extracted by ascorbate or HCl was normalized by the total Fe concentration (*Section 2.2.5.*).

2.2.7. Electrophoretic Mobility and Particle Size

The electrophoretic mobility (EM) and particle size of the iron oxides was measured in a filtered (Sartorius polyethersulfone membrane, 0.22 μm) 10 mM $NaNO_3$ solution using a Zetasizer Nano-ZS (Malvern, Instruments) at 25 °C. Initially, the iron oxides were dispersed by adding a wet sample (equivalent to 25-30 mg of dry solid per litre) to 500 mL of background electrolyte and stirred for 1 hour. Subsequently, the pH of 50 mL aliquots was adjusted with filtered 10 mM NaOH or HNO_3 to a constant desired value between pH 3 – 9. The EM measurements were determined from the average of 5 runs comprising of 10 cycles each. Particle size of the suspensions was determined from the average of two individual measurements at pH ~6 in automatic mode.

2.3. Bioavailability

2.3.1. Microbial Medium and Preparation of Cultures

Microbial Fe reduction experiments were carried out with a well characterized, facultative, dissimilarity Fe(III)-reducing bacterium, *Shewanella putrefaciens* strain CN32 (*S. putrefaciens* CN32). Microcosm reduction experiments were carried out in a chemically defined medium (CDM) (pH ~6.7) composed of 20 mM sodium lactate as the electron donor, 4 mM 1,4-piperazinediethanesulfonic acid (PIPES) buffer, mineral salts solution, and trace metals solution (Zachara et al., 1998; Glasauer et al., 2003; Langley et al., 2009a). For transfer into CDM, *S. putrefaciens* CN32 was initially revived from a glycerol stock solution by streaking onto tryptic soy agar (TSA) plates at room temperature (~22 °C). For inoculation, the bacteria were prepared according to the protocols of Glasauer et al. (2003) and Langley et al. (2009a). Briefly, cells were prepared by aseptically inoculating 50 mL of TSB with a colony of *S. putrefaciens* CN32 from TSA plates, and kept on a stir plate (125 rpm) for 24 hours at 22 °C. Subsequently, 0.5 mL of the culture was transferred into 50 mL of 50:50 CDM:TSB mixtures. After 24 hours, the passaging procedure was repeated with 95:5 CDM:TSB containing 100 μM phosphate, and continued by transferring into 99:1 CDM:TSB containing 200 μM phosphate for a period of 30 hours. The final step involved growing the bacteria in 100 % CDM containing 400 μM phosphate for a period of 36 hours. The concentration of phosphate was progressively increased to acclimate the bacteria to depleted nutrients and microcosm conditions (Glasauer et al., 2003; Langley et al., 2009b). Following the acclimation period, the bacteria were harvested by centrifugation at 4000 rpm and the cell pellet was re-suspended into 2 mL of fresh, sterile CDM. Finally, the BioRad Protein Assay II dye reagent was used to standardize the concentrated cell suspension in order for the microcosms to contain a cell density of ~10^7 CFU/mL (Glasauer et al., 2003; Langley et al., 2009b).

The experimental setup consisted of 500 mL acid-washed Pyrex bottles (microcosms) containing 450 mL of sterile CDM amended with 4 mM Fe in the form of iron oxide, and 400 μM

of sodium phosphate. The experiments were conducted in triplicates and controls to which no bacteria were added were included. Prior to inoculation with *S. putrefaciens* CN32, the microcosms were wrapped in aluminium foil in order to avoid potential photochemical reactions and then transferred into an anaerobic chamber where inoculation proceeded. Throughout the paper, we refer to the microcosms to which cells were added as "biotic" microcosms, whereas controls to which no bacteria were added are referred to as "control" microcosms.

2.3.2. Sampling and Analyses

Sampling of each system was performed immediately following the addition of the cells (time 0) and then periodically at selected time points. Sampling was carried out by vigorously shaking the microcosms to suspend the iron oxides into solution. Immediately, 20 mL of the suspension was poured into a sterile 20 mL scintillation vial from which all sub-sampling proceeded to minimize the potential contamination of the microcosms (Langley et al., 2009a). The sub-sampled suspensions were analysed for pH, cell viability (at the start and end of the experiment), total and dissolved Fe(II), and total Fe. pH was monitored utilizing standard calibrated laboratory meters and probes, whereas cell viability was determined by colony counts on TSA plates (Glasauer et al., 2003; Langley et al., 2009a). Fe(II) associated with the solid phase (total Fe(II)) was determined by dispensing 1 mL of unfiltered iron oxide suspension into 1 mL of trace metal grade 6 M HCl (final concentration of 3 M) and allowed to digest for at least 24 hours under anoxic conditions prior to dilution and analysis via the ferrozine assay (Stookey, 1970; Viollier et al., 2000). Dissolved Fe(II) was determined by filtering (0.22 μm) 6 mL of the suspension into an acid-washed 20 mL scintillation vial, and immediately dispensing 0.5 mL of the filtrate into 4.5 mL of trace metal grade 0.5 M HCl. Digestion proceeded for at least 24 hours under anoxic conditions prior to analysis by the ferrozine assay. To determine total Fe, 2 mL of

the unfiltered iron oxide suspensions were digested with 2 mL of trace metal grade 12 M HCl for a period of 24 hours. Following dilution, Fe determination proceeded by dispensing 100 µL aliquot of the digest into 900 µL of 0.28 M ClH_4NO in 0.28 M HCl for a duration of 30 minutes and then determining the concentration of Fe^{2+} using the ferrozine assay.

2.3.3. Biogenic solids

At the end of the experimental period, post-reduction minerals were collected by centrifugation (3000 rpm), washed 3x with anaerobic UPW, and dried under anaerobic conditions. The powdered precipitates were analysed by XRD as described above, using an air sensitive sample holder in order to prevent the oxidation of potential Fe(II)-bearing minerals.

3. Results and Discussion

3.1. Physicochemical properties of solids

3.1.1. Chemical characterization of solids

Table 1 summarizes the chemical composition of the synthetic samples. At the same initial C/Fe ratio, the C/Fe content followed the trend Fh >> Lp ≥ Gt (Table 1). This suggests that synthesis via rapid neutralization of an acidic Fe(III) solution led to greater OM incorporation, likely due to OM entrapment during the rapid aggregation and condensation of Fh nanoparticles (Baalousha, 2009; Pedrot et al., 2011; Angelico et al., 2014; Colombo et al., 2015). In contrast, during Lp and Gt synthesis via Fe^{2+} oxidation in the presence of OM, stable, negatively charged Fe(III)-OM complexes likely form as Fe^{2+} oxidizes, preventing the aggregation and condensation of the resulting iron oxide due to electrostatic repulsion (Baalousha, 2009; Pedrot et al., 2011). Baalousha (2009) reported that high concentrations of OM (HA/Fe ratio >0.5) could either induce or inhibit the aggregation of Fe nanoparticles according to the prevailing physicochemical

conditions. During the oxidation of a Fe^{2+} solution in the presence of humic acid, Pedrot et al. (2011) suggested that OM affect the oxidation-hydrolysis of Fe(II) by (i) reducing and slowing down Fe(II) oxidation partly by complexation-mediated sequestration of 'truly' dissolved Fe within OM and (ii) inhibiting the development and aggregation of Fe particles. Additionally, for Gt coprecipitates, the added HCO_3^- likely competed with OM and Fe(III)-OM complexes for adsorption sites. Thus, these factors likely contributed to the lower OM uptake within the solid phase under the conditions used in this study. Further characterization of the supernatants from Lp and Gt coprecipitates confirmed detectable concentrations of dissolved organic carbon and Fe(III), with minor Fe(II) levels, indicative of the presence of stable Fe(III)-OM complexes and potentially Fe(II)-Fe(III)-OM complexes that resist oxidation (Figure S1). In contrast, the supernatant from Fh coprecipitated at C/Fe 0.5 contained no detectable DOC, Fe(III), or Fe(II).

Table 1 also presents Fe extracted using 0.5 M HCl and ascorbate, along with their respective proportions of total Fe. It also includes the fraction of Fe(II) relative to total Fe. Ascorbate and 0.5 M HCl were chosen due to their well-established selectivity to dissolve poorly crystalline Fe phases, whereas oxalate was omitted due to its tendency to overestimate the Fe fraction associated with poorly crystalline Fe phases in the presence of Fe(II) (Kostka and Luther, 1994; Hyacinthe and Van Cappellen, 2004; Hyacinthe et al., 2006). Both 0.5 M HCl and ascorbate fully dissolved pure Fh and Fh coprecipitates with C/Fe of 0.5 and 1.0, while for Fh with C/Fe of 1.5, ~95% of Fe was dissolved, suggesting alginate may offer some protection against dissolution (Table 1). In contrast, 0.5 M HCl extracted ~7% and ~2% of Fe from pure Lp and Gt, respectively, likely including poorly ordered oxidation by-products. For Lp coprecipitates, HCl-extractable Fe remained ~7% at C/Fe 0.5 but increased to ~33% and ~40% at C/Fe 1.0 and 1.5 ($P<0.05$). Similarly, for Gt coprecipitates, HCl-extractable Fe increased to ~4%, 6%, and 11% at C/Fe 0.5,

1.0, and 1.5 ($P<0.05$). Ascorbate extracted ~51% of Fe from pure Lp, increasing to ~70% at C/Fe 1.0 ($P<0.05$), with no further rise at C/Fe 1.5. For Gt, ascorbate extraction rose from ~8% (pure) to ~14% and 17% at C/Fe 0.5 and 1.0 ($P<0.05$), stabilizing at C/Fe 1.5. In comparison to the 0.5 M HCl extraction, ascorbate extracted 1.7-8x more Fe from a corresponding Lp or Gt precipitate, although the difference between the extractants appeared to decrease with increasing OM content (Table 1). The higher amount of Fe extracted from the ascorbate treatment than that of proton-promoted dissolution (0.5 M HCl) can be attributed to the duration of extraction and the formation of easily detachable complexes of reduced Fe(II) and ligands at the particle surface (Kostka and Luther, 1994; Kraal et al., 2019). All components of citrate-bicarbonate-ascorbic acid solution used can contribute to surface complex detachment (Kostka and Luther, 1994; Kraal et al., 2019). Nonetheless, data from both extractants indicate an increased proportion of a poorly crystalline Fe phase as the C/Fe content increases (Table 1).

Table 1: Chemical extractions of the solid and wet iron phases. The fractions of poorly crystalline Fe containing phases as determined by 0.5 M HCl (H) and ascorbate (A) are presented relative to the total Fe. The table includes the C/Fe molar ratios determined from the solid precipitates. Values for the chemical extractions correspond to the mean ± standard deviation of three replicates, whereas values for the C/Fe molar ratios correspond to the mean ± standard deviation of two replicates.

Sample	Total Fe (T)	0.5M HCl (H)	Ascorbate (A)	Fe(II)/T (%)	Poorly Crystalline Fraction (%) H/T	Poorly Crystalline Fraction (%) A/T	C/Fe (mol:mol)
Fh	64.07 (0.22)	64.9 (2.47)	62.98 (0.52)	1.69 (0.48)	101.29 (3.88)	98.3 (0.88)	0.02 (0.001)
Fh 0.5	34.91 (0.64)	34.96 (0.36)	35.04 (0.87)	2.85 (0.96)	100.14 (2.12)	100.38 (3.1)	0.54 (0.012)
Fh 1.0	13.22 (0.23)	12.99 (0.44)	13.66 (0.56)	5.04 (0.58)	98.21 (3.73)	103.33 (4.58)	0.96 (0.001)
Fh 1.5	9.32 (0.17)	8.7 (0.07)	8.83 (0.03)	4.97 (0.69)	93.42 (1.84)	94.78 (1.75)	1.44 (0.053)
Lp	56.16 (0.998)	3.69 (0.06)	28.7 (1.23)	0 (0)	6.57 (0.16)	51.11 (2.37)	0.03 (0.001)
Lp 0.5	107.58 (1.64)	7.72 (0.15)	50.24 (1.47)	0.54 (0.02)	7.18 (0.18)	46.71 (1.54)	0.24 (0.001)
Lp 1.0	67.43 (3.32)	22.19 (0.61)	47.65 (1.23)	1.23 (0.1)	32.91 (1.85)	70.67 (3.93)	0.47 (0.012)
Lp 1.5	60.59 (3.19)	24.12 (1.89)	46.04 (0.57)	1.24 (0.31)	39.81 (3.76)	75.98 (4.1)	0.64 (0.002)
Gt	121.79 (2.04)	2.95 (0.18)	10.09 (1.18)	0.34 (0.03)	2.42 (0.15)	8.28 (0.98)	0.05 (0.003)
Gt 0.5	147.01 (1.07)	6.23 (0.08)	21.16 (1.85)	0.54 (0.05)	4.24 (0.06)	14.39 (1.26)	0.24 (0.003)
Gt 1.0	135.09 (4.6)	8.15 (0.48)	22.93 (0.58)	0.66 (0.07)	6.03 (0.41)	16.98 (0.72)	0.35 (0.007)
Gt 1.5	111.85 (1.24)	12.02 (0.38)	20.16 (0.22)	0.86 (0.18)	10.75 (0.36)	18.03 (0.28)	0.44 (0.003)

* Significant difference between values at the 95% confidence interval ($P<0.05$, two-tailed t-test)

3.1.2. Electrophoretic mobility: ζ-potential and particle size

Plots of ζ-potential vs. pH of the iron oxides are presented in Figure 1, whereas the particle size is presented in Figure 2. For the pure Fh, Lp, and Gt, the isoelectric point, pH_{iep}, was estimated at 7.2, 7.3, and 7.6, respectively, which were within the range of the point of zero charge (PZC) reported in the literature (Cornell and Schwertmann, 2003; Mikutta et al., 2008). Coprecipitation with alginate led to the reduction of the pH_{iep} in agreement with Mikutta et al. (2008) (Figure 1). In comparison to pure Fh, the pH_{iep} of the coprecipitates with C/Fe of 0.5, 1.0, and 1.5 was ~6.5, >2, and <2, respectively (Figure 1). Despite possessing lower C/Fe content than Fh coprecipitates, the Lp and Gt coprecipitates exhibited reduced pH_{iep} (Figure 1). For the Lp coprecipitates with C/Fe 0.5, 1.0, and 1.5, the pH_{iep} was >2, <2, and <2, respectively, whereas for the Gt coprecipitates with C/Fe 0.5, 1.0, and 1.5, the pH_{iep} was ~3.4, ~2.7, and ~2.7, respectively (Figure 1). Therefore, the reduced pH_{iep} characteristics deduced from electrophoretic mobility measurements confirmed the prevalence of alginate on the surface of the coprecipitates, an observation that is consistent with the literature for iron oxides coprecipitated with various types of OM (Mikutta et al., 2008; Shimizu et al., 2013; Mikutta et al., 2014; Poggenburg et al., 2016).

Coprecipitation with alginate also affected the particle size of the iron oxides studied as depicted in Figure 2 The particle size of the Fhs exhibited an increasing trend with increasing C/Fe content, although there was large variability between measurements (Figure 2). In contrast to the Fh coprecipitates, and in comparison to pure Lp, the particle size of the Lp coprecipitates initially decreased as C/Fe increased to 0.5, then increased as the C/Fe increased to 1.0 and 1.5 (Figure 2). Likewise, changes in the particle size of the Gts exhibited the same overall trends as those observed for the Lps (Figure 2). As shown in previous studies (Amstaetter et al., 2012; Angelico et al., 2014; Poggenburg et al., 2016; Adhikari et al., 2017), OM can affect the particle size and aggregation of

iron oxides by increasing repulsion between particles or acting as bridging materials. For humic acid-Fh coprecipitates Adhikari et al. (2017) reported an average particle size of 1862, 2362, 1833, and 170 nm, for coprecipitates with C/Fe ratio of 0.7, 0.9, 1.8, and 3.7, respectively, compared to 92 nm for Fh. Poggenburg et al. (2017) observed that particle size is also affected by the type of OM, presumably due to differences in functional groups, such that at an equivalent initial C/Fe ratio particle size increased from ~2 μm for Fh, to 3-4.2 μm for Fh-soil OM coprecipitates, and ~6 μm for Fh-exopolysaccharide coprecipitate. The particle size of Fhs from this study is within range of those previously published, and the large variability can be attributed to broad size distributions (Angelico et al., 2014). The extent of aggregation could be also influenced by the synthesis method, such that during the synthesis of Fh coprecipitates the initial pH drops to ~1.5 which may have led to the flocculation and aggregation of alginate (Angelico et al., 2014; Poggenburg et al., 2016). As discussed above, rapid neutralization leads to the aggregation, flocculation, and entrapment of Fh nanoparticles and alginate thereby forming large aggregates (Figure 2). In contrast, the precipitation of Lp and Gt does not occur rapidly and as the pH is raised to near neutral, the extended time of synthesis allows for alginate aggregates initially formed in acidic conditions to disperse as well as the repulsion between particles and complexes to take place thereby forming smaller aggregates.

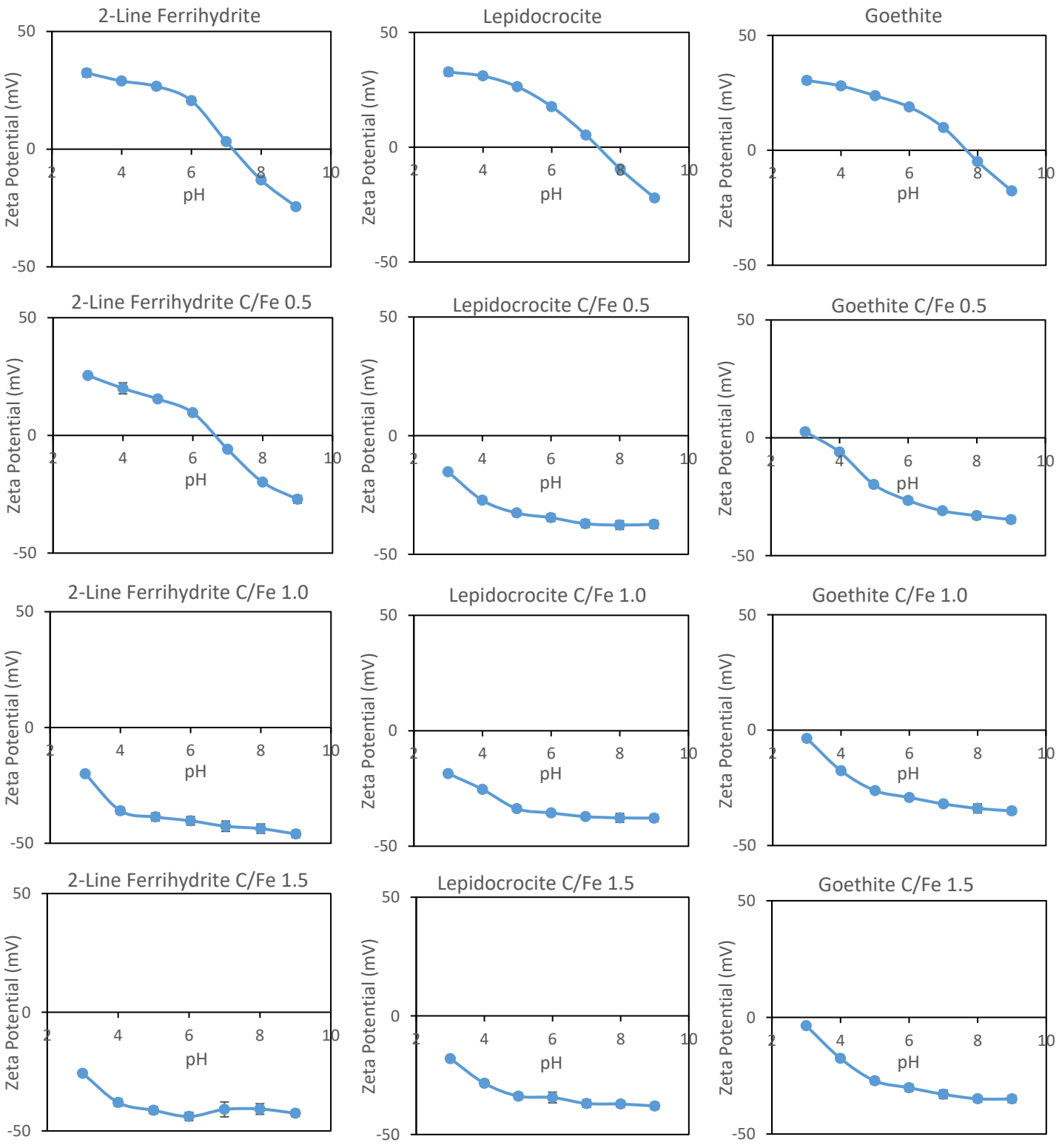

Figure 1: Plot of the zeta potential versus pH for the various iron oxides coprecipitated with alginate (C/Fe 0, 0.5, 1.0, and 1.5 mol:mol). Data markers represent mean ± standard deviation derived from 5 electrophoretic mobility measurements.

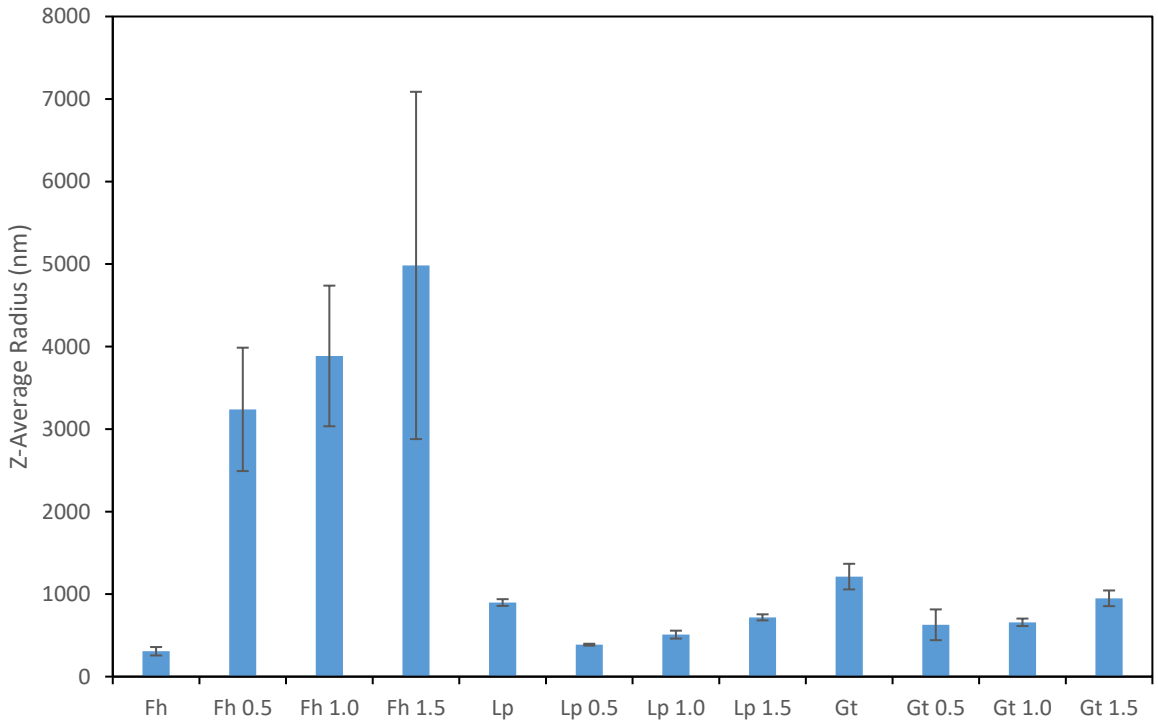

Figure 2: Size of particles (Z-average) measured for the iron oxides studied. Data represents the mean ± standard deviation of 2 individual replicates. Fh, Lp, and Gt correspond to 2-line ferrihydrite, lepidocrocite, and goethite, respectively.

3.1.3. Specific surface area and porosity

The N_2-adsorption desorption isotherms of the various iron oxides studied are presented in Figures S2-S4, and the derived specific surface area (SSA) as well as the micropore- (MIV), mesopore- (MEV), and total pore- volumes (TPV) are presented in Figure 3. The pure Fh and Fh coprecipitated with C/Fe 0.5 or 1.0 exhibited a reversible Type I(a) isotherm, typical of microporous solids (Figure S2). Unfortunately, a full N_2 adsorption-desorption isotherm for Fh coprecipitated with C/Fe 1.5 could not be obtained, therefore only the SSA and MIV values are reported for this solid. The SSA of ~431 m^2/g determined for pure Fh accords well with published data (Cornell and Schwertmann, 2003; Mikutta et al., 2008; Poggenburg et al., 2016), and the MIV determined for pure Fh occupied ~55% of the TPV, which is also in excellent agreement with that reported by other studies (Hofmann et al., 2004; Mikutta et al., 2008). Alginate, however, significantly affected the porosity and SSA of the Fh coprecipitates ($P<0.05$). It was observed that the MIV, MEV, and TPV inversely correlated with the C/Fe content, such that the porosity of the coprecipitates decreased with increasing C/Fe content (Mikutta et al., 2008). Compared to pure Fh, the MIV decreased by ~30 and 70% as the C/Fe content increased by 0.5 and 1.0, respectively, and became undetectable as the C/Fe content increased to 1.5. Likewise, in comparison to pure Fh, both MEV and TPV decreased by ~20 and 60% as the C/Fe content increased by 0.5 and 1.0, respectively (Figure 3). Concomitant with reduced porosity, the SSA of the coprecipitates also decreased by ~30, 70, and 98% as the C/Fe content increased by 0.5, 1.0, and 1.5, respectively, when compared to the SSA of pure Fh (Figure 3). The observed trends align with previous studies examining Fh-OM coprecipitates with similar C/Fe ratios and utilizing various types of OM (Mikutta et al., 2008; Shimizu et al., 2013; Eusterhues et al., 2014a; Poggenburg et al., 2016). The reduced SSA has been attributed to significant particle aggregation and the blockage of pore sites

by OM preventing adsorption of N_2 (Mikutta et al., 2008; Eusterhues et al., 2014a; Kleber et al., 2015). Surface blockage of pore sites is in agreement with surface associated alginate as deduced from electrophoretic mobility measurements.

Pure Lp and Lp coprecipitates exhibited a non-reversible Type II isotherm (Figure S3). The non-reversible nature of the isotherms was highlighted by hysteresis in the desorption branch, which became more prominent as the C/Fe content increased and shifting into Type H4 as the C/Fe content reached a maximum (Figure S3) (Rouquerol et al., 2013). Significant uptake of N_2 was also observed in the lower partial pressure region ($<P/P_0$ 0.1) of the isotherms, which also became more apparent as the C/Fe increased (Figure S3). Such changes in the isotherms of the Lp coprecipitates imply the development of mesopores as indicated by hysteresis, and the development of micropores as indicated by N_2 micropore filling in the lower partial pressure region (Rouquerol et al., 2007; Rouquerol et al., 2013). The SSA of pure Lp reached ~110 m^2/g, which falls within the range of previously reported values (Schwertmann and Cornell, 2008). Consistent with the low SSA, MIV and MEV of the pure Lp accounted for ~5 and 50% of the TPV, respectively. Apart from TPV, alginate also significantly affected the MIV, MEV, and the SSA of the Lp coprecipitates ($P<0.05$). In comparison to pure Lp, the MIV of the Lp coprecipitates increased by ~2x and 3x as the C/Fe content increased by 0.5 and 1.0, respectively, with no further increase observed as the C/Fe increased to 1.5 (Figure 3). Similarly, MEV also increased within the Lp coprecipitates when compared to that of pure Lp, whereby the MEV increased by a maximum of ~2x as the C/Fe content increased to 0.5 or 1.0, but only increased by ~1.6x as the C/Fe content increased to 1.5 (Figure 3). In contrast to MIV and MEV, the TPV of the Lps did not exhibit a specific trend and in contrast to pure LP, TPV remained comparable to that determined for the Lp coprecipitates with C/Fe of 0.5 and 1.0 but appeared to decline as the C/Fe content

increased to 1.5 (Figure 3). Consistent with the observed increase in MIV and MEV, the SSA of the Lp coprecipitates increased by ~1.6x as the C/Fe content increased to 0.5 and by a maximum of ~2.5x as the C/Fe content increased by 1.0 or 1.5, when compared to the SSA of pure Lp (Figure 3). Therefore, the overall trend in MIV, MEV, TPV, and SSA were opposite to those observed for Fh coprecipitates, despite Lp coprecipitates possessing surface associated alginate (Figures 1 and 3). The change in surface area is likely a consequence of a number of factors as discussed below, including particle size, morphology, crystallinity, and/or presence of poorly crystalline Fe phases. Similar observations were reported for iron oxides synthesized from the oxidation of Fe(II) solutions containing increasing concentration of low molecular weight ligands (e.g., citrate or tartrate) (Liu, 1999). Likewise, the SSA of Lp-aluminum and Lp-phosphate coprecipitates formed from the oxidation of Fe(II) solutions increased with increasing concentrations of aluminum or phosphate as observed in this study suggesting a common mechanism among the different foreign species (Ekstrom et al., 2010; O'Loughlin et al., 2013).

Pure Gt and Gt coprecipitates also exhibited a non-reversible Type II isotherm (Rouquerol et al., 2013). The isotherms exhibited a clear hysteresis loop and significant N_2 uptake in the lower partial pressure region ($<P/P_0$ 0.1) (Figure S4). Therefore, the Gt precipitates possessed both meso- and micro-pores. The SSA for pure Gt was determined to be ~380 m^2/g which was higher than previously reported values (Cornell and Schwertmann, 2003; Schwertmann and Cornell, 2008). Such discrepancy may be attributed to differences in the synthesis conditions including concentration of Fe(II) and the rate of mixing. Furthermore, the MIV and MEV for pure Gt accounted for ~15 and 90% of the TPV, respectively, which may explain the high surface area determined for this solid. The effects of alginate on the shape of the isotherms of the Gt coprecipitates were not as apparent as those observed for the Lp coprecipitates. Nonetheless,

alginate had a significant effect on the porosity and SSA of the Gt coprecipitates ($P<0.05$). The MIV exhibited a declining trend with increasing C/Fe content (Figure 3). However, Tucky's post hoc analyses only revealed a significant difference in the MIV between pure Gt and Gt coprecipitated with a C/Fe content of 1.5 ($P<0.05$). In comparison to pure Gt, the MEV decreased by ~30% as the C/Fe content increased to 0.5 or 1.0, which further decreased by ~50% as the C/Fe content increased to 1.5 (Figure 3). Consistent with the decreasing MIV and MEV, the TPV of the Gt coprecipitates decreased by ~15, 30, and 45% as the C/Fe content increased by 0.5, 1.0, and 1.5, respectively, when compared to the TPV of pure Gt (Figure 3). Concomitant with reduced porosity, the SSA of the Gt coprecipitates decreased by ~15% as the C/Fe content increased to 0.5 or 1.0, and by ~25% as the C/Fe content reached a maximum when compared to the SSA of pure Gt (Figure 3). Thus, the SSA and porosity of the Gt coprecipitates exhibited an opposite trend compared to the Lp coprecipitates, despite similarities in their synthesis pathway (i.e., Fe(II) oxidation), and variations in the proportion of poorly extractable crystalline Fe phases as well as in particle size. The reason for this difference is unknown and warrants further investigation. In contrast to our results, the SSA of Gt-fulvic acid coprecipitates synthesized from the neutralization of Fe(III)-solutions increased with increasing OM content up to 5%, at which point SSA decreased as the OM content increased to 15% (Liu et al., 2019b). Initial increase in SSA was associated with the development of micropores and dispersion of Gt particles, whereas the decrease in SSA was associated with reduced MIV as a consequence from the aggregation of Gt particles and pore blockage by OM (Liu et al., 2019b).

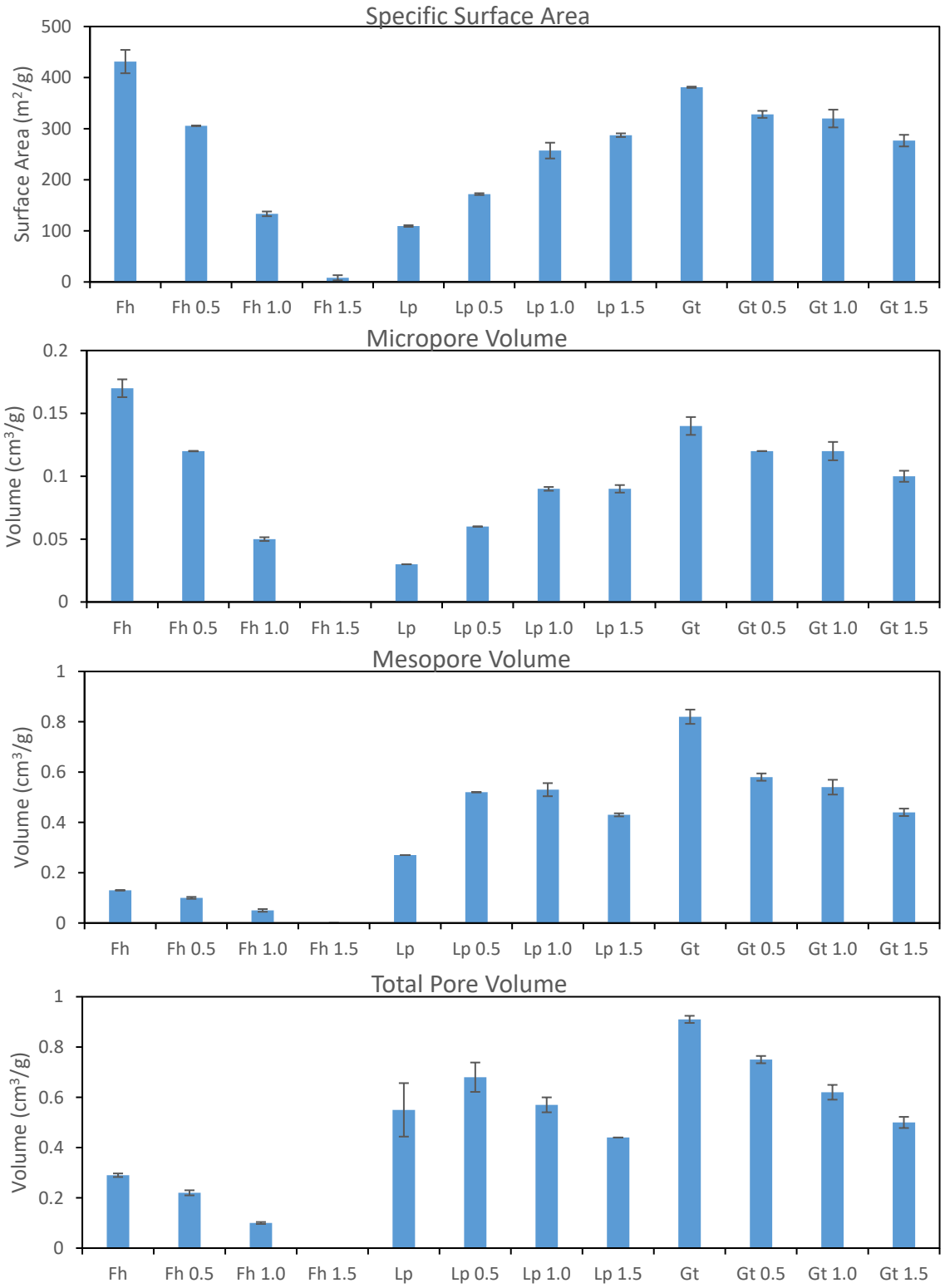

Figure 3: Specific surface area, micropore volume, mesopore volume, and total pore volume values of the iron oxides studied. Data points represent the mean ± standard deviation of two replicates. Data extracted from the N_2 adsorption-desorption isotherms provided in Figure S2-S4. Fh, Lp, and Gt correspond to 2-line ferrihydrite, lepidocrocite, and goethite, respectively.

3.2. Mineralogy

3.2.1. ^{57}Fe Mössbauer spectroscopy

The Mössbauer spectra of the Fhs are shown in Figure 4, and the derived Mössbauer parameters are given in Table 2. At 77 K, 2-line ferrihydrite exhibits a doublet with the parameter values of center shift (CS): 0.35 – 0.5 mm/s and quadrupole split (QS): 0.7 – 0.85 mm/s. At 5 K, ferrihydrite is magnetically ordered, evidenced by splitting of the doublet into a sextet. The 5 K spectrum of ferrihydrite is best fit with two sextets: sextet A with approximate parameters of CS = 0.48 mm/s, QS = 0 mm/s, hyperfine field (H) = 50 T, and sextet B with approximate parameters of CS = 0.42 mm/s, QS = -0.03 mm/s, hyperfine field (H) = 45 T (Byrne and Kappler, 2021). All the Fhs spectra exhibited a Fe(III) doublet at 77 K and two magnetic sextets at 5 K indicative of ferrihydrite (Figure 4). The magnitude of the hyperfine fields and quadrupole splitting of our samples agree well with values previously found for 2-line ferrihydrite, and the similarity among the samples indicate alginate hardly affected interparticle magnetic exchange interaction of ferrihydrite (Table 2). We did however observe slight broadening at the base and lack of separation of the doublet peaks as the C/Fe ratio increased to 1.0 and 1.5 (Figure 4). This could indicate slightly reduced particle size and crystallinity of the Fh-coprecipitates compared to pure Fh (Mikutta et al., 2008). In agreement with our observations, Mikutta et al. (2008) also found slight OM induced structural changes of Fh coprecipitated with various types of polysaccharides as determined by Mössbauer spectroscopy and EXAFS. The authors further suggested that limited magnetic super-exchange between Fh particles in the coprecipitates may arise from magnetic dilution by the polysaccharides.

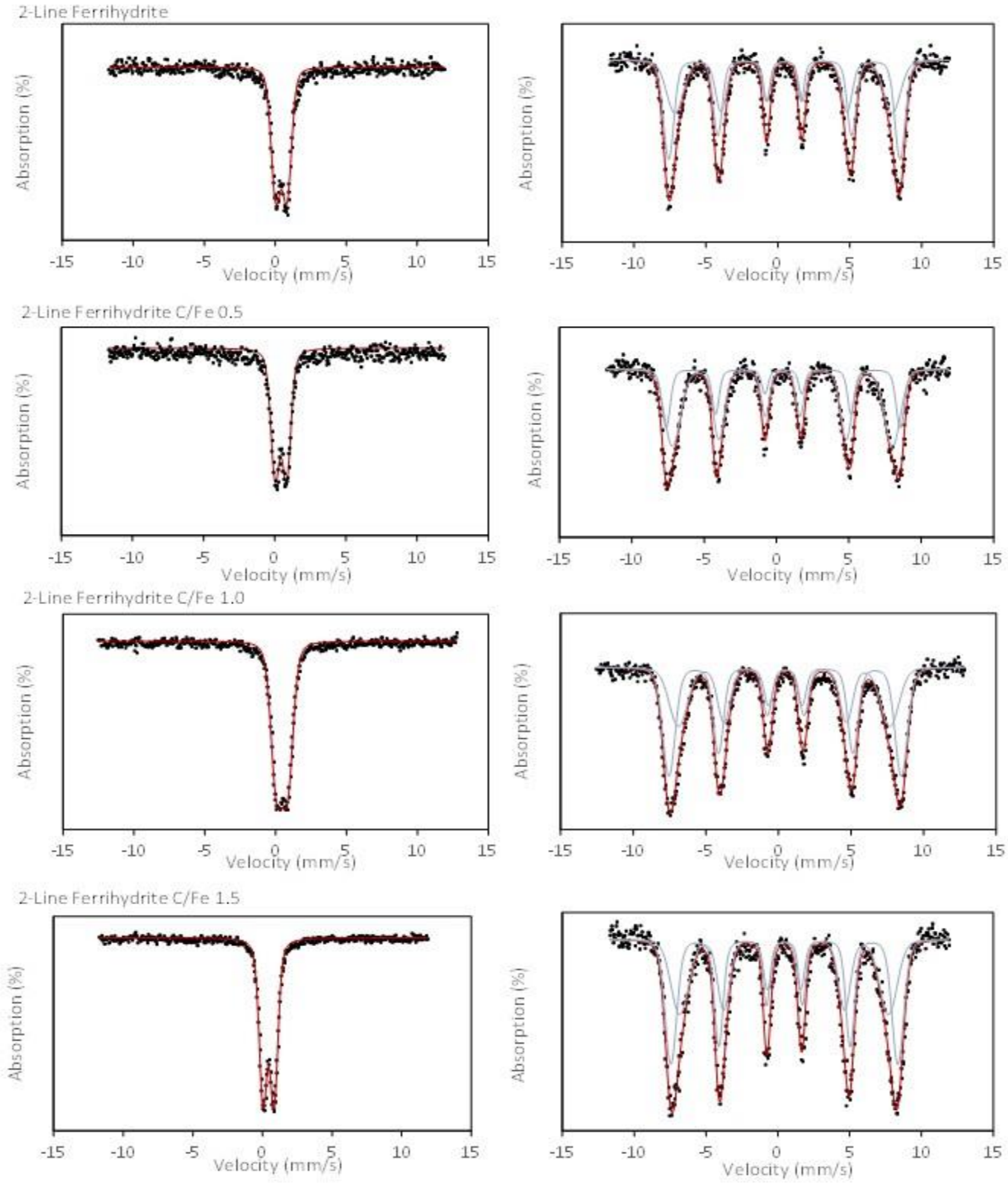

Figure 4: Mössbauer spectra of the Fh coprecipitated with alginate (C/Fe ratios of 0, 0.5, 1.0, and 1.5 mol:mol), taken at liquid nitrogen (77 K, left) and liquid helium temperature (5 K, right). Symbols show experimental data and lines represent their fit.

Table 2: Mössbauer parameters for 2-line ferrihydrite and coprecipitates (C/Fe 0.5, 1.0, and 1.5) determined from spectra collected at liquid nitrogen (77 K) and liquid helium temperature (5 K).

Sample	T (K)	Site	CS (mm/s)	QS (mm/s)	H (T)	Relative area (%)	χ^2
Fh	77	Fe(III)	0.43	0.79		100	0.76
	5	Ferrihydrite A	0.46	-0.01	49.9	55.0	0.68
		Ferrihydrite B	0.44	-0.01	46.8	45.0	
Fh C/Fe 0.5	77	Fe(III)	0.43	0.81		100	1.24
	5	Ferrihydrite A	0.48	0.0	50.2	30.0	0.70
		Ferrihydrite B	0.42	-0.01	47.1	70.0	
Fh C/Fe 1.0	77	Fe(III)	0.44	0.79		100	1.33
	5	Ferrihydrite A	0.48	-0.02	49.6	57.0	0.76
		Ferrihydrite B	0.42	-0.04	45.1	43.0	
Fh C/Fe 1.5	77	Fe(III)	0.43	0.79		100	1.01
	5	Ferrihydrite A	0.45	0.00	49.1	54.0	0.68
		Ferrihydrite B	0.43	0.00	45.1	46.0	

3.2.2. X-ray diffraction and FTIR-ATR

Figure 5 shows the x-ray diffraction patterns of the different iron oxide phases. Reflections indicative of 2-line ferrihydrite, lepidocrocite, and goethite were identified in the diffractograms, and they corresponded closely with those published in the literature (Cornell and Schwertmann, 2003). Substantial differences between the diffractograms of the Fhs as a function of the C/Fe content were not evident (Figure 5). Although the reflections at ~35 and 62° appeared to slightly broaden with increasing C/Fe content, which may be indicative of reduced particle size and crystallinity in agreement with Mössbauer spectroscopy (Figures 4 and 5). The effects of alginate on the diffraction reflections of Lp were more apparent and they varied as a function of C/Fe content (Figure 5). With increasing C/Fe content, the (200), (210), (301), (020), (511), and (321) reflections (14, 27, 36, 47, 52, 60°, respectively) considerably broadened, whereas the reflections of lower intensity completely disappeared (Figure 5). Minor amounts of Gt were also detected within the Lp coprecipitates as determined by the reflections centred at ~21, 33, 34°, which became difficult to resolve as the C/Fe content reached a maximum (Figure 5). In contrast to Lp, the effects

of alginate on the crystallinity of Gt were less apparent, although the Gt reflections slightly broadened with increasing C/Fe content (Figure 5).

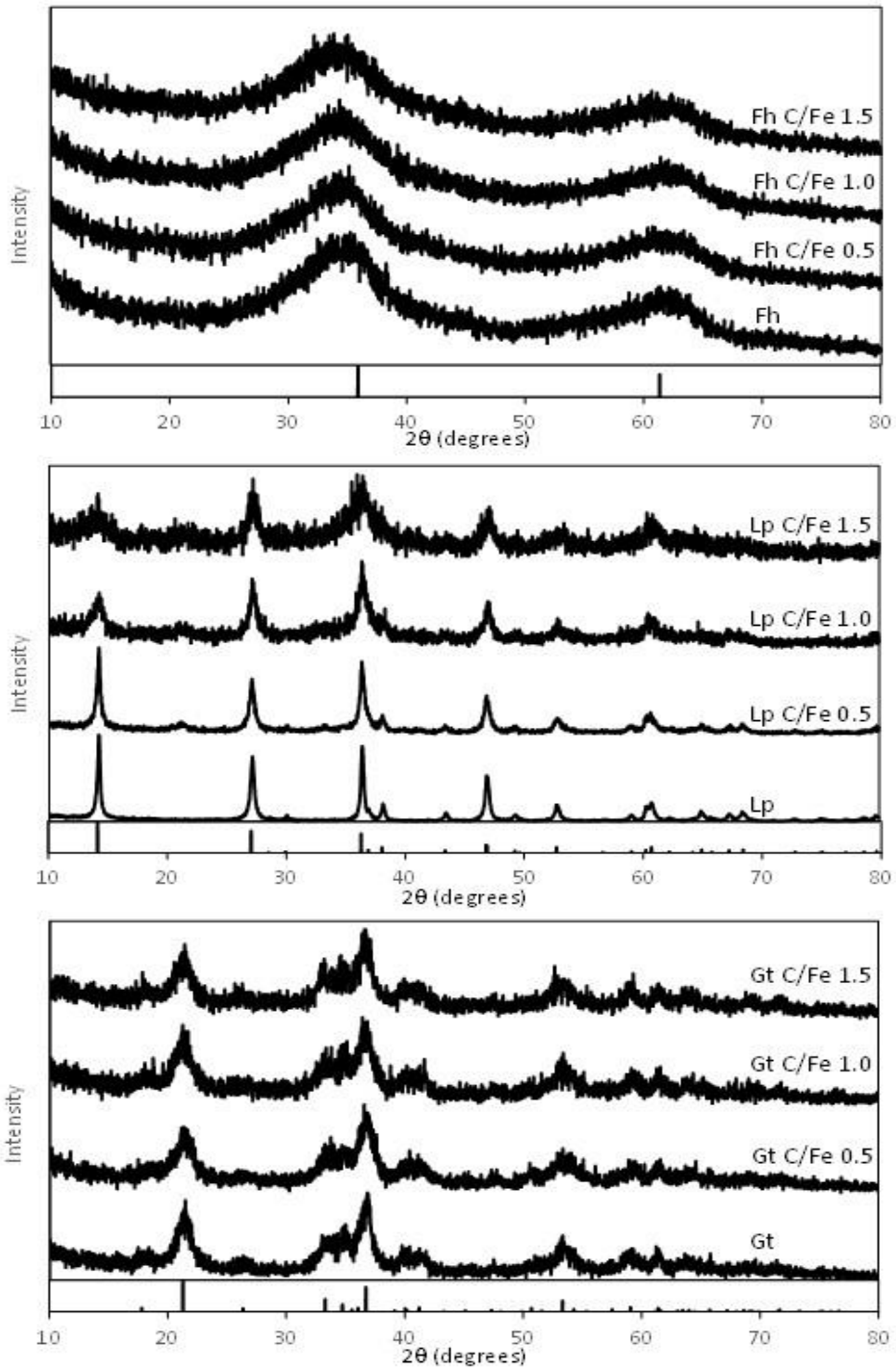

Figure 5: Powder x-ray diffractograms of the iron oxides studied compared to the standard reference lines. For clarity, all patterns have been vertically separated on an arbitrary y-axis. Fh, Lp, and Gt correspond to 2-line ferrihydrite, lepidocrocite, and goethite, respectively.

Additional information about the chemical composition, functional groups, and degree of crystallinity was obtained with IR spectroscopy. The FTIR spectra of the iron oxides studied are presented in (Figure 6) and the assignments of the most characteristic vibrational modes are summarized in Tables S1-S4 as determined by theory and the literature (Sartori et al., 1997; Chandıa et al., 2001; Cornell and Schwertmann, 2003; Leal et al., 2008; Schwertmann and Cornell, 2008; Cardenas-Jiron et al., 2011). For pure Fh, the spectrum was characterized by 3 regions including (Figure 6): (1) a broad band centred at ~3291 cm^{-1} corresponding to the ν(O-H) related to superposition of stretching vibrations of structural OH^- groups and adsorbed H_2O molecules, (2) broad bands within 1700 - 1300 cm^{-1} region corresponding to δ(O-H) vibrations from adsorbed H_2O centred at ~1627 cm^{-1}, and stretching vibrations ν_{asym} and ν_{sym} of C-O bonds from adsorbed carbonate centred at ~1469 and ~1378 cm^{-1}, respectively, and (3) a weak broad band centred at ~565 cm^{-1} attributed to the stretching vibration of Fe-O in the Fh lattice. The IR spectra of the Fh coprecipitates were characterized by additional bands belonging to alginate in the 1700 – 800 cm^{-1} region, which appeared to increase in intensity as the C/Fe increased (Figure 6). Within this region the bands belonging to adsorbed carbonate were difficult to discern suggesting that alginate may have outcompeted carbonate for adsorption sites (Figure 6). In comparison to pure Fh and Na-alginate, it was observed that the centre of ν(O-H) shifted to lower wavenumbers as the C/Fe content increased suggesting a possible increase in the strength of the hydrogen bonds (Figure 6). Also, the intensity of the Fe-O stretching vibration band was found to decrease with increasing C/Fe content, which could be attributed to a dilution effect or a decrease in the crystallinity of the Fh as was observed by XRD and Mössbauer spectroscopy.

The FTIR spectra of pure Lp and Lp coprecipitates are presented in Figure 6 and their band assignments are given in Table S3. For pure Lp, the broad band of weak intensity centred at ~1630

cm^{-1} attributed to δ(O-H) suggests minor contribution of adsorbed H_2O to the spectrum. Therefore, the broad band centred at ~3015 cm^{-1} was assigned to ν(O-H) vibration related to the structural OH^- of the mineral. Broad bands of weak intensity corresponding to the stretching vibrations of adsorbed atmospheric carbonate were also observed (Figure 6). Bands characteristic of Lp centred at ~1155 and 1020, 753, and 597 cm^{-1} were assigned to in-plane δ(O-H) vibrations, out-of-plane bending (γ(O-H)) vibrations, and twisting or displacement vibrations of structural O^{2-} (τ(O)), respectively (Figure 6). For the Lp coprecipitates, bands corresponding to alginate were observed in the 1700 – 800 cm^{-1} region and their intensity increased with increasing C/Fe content (Figure 6). The IR spectra of the Lp coprecipitates revealed alginate induced changes to the intensity, shapes, and positions of the bands characteristic of Lp (Figure 6). In comparison to pure Lp: (1) a broad band appeared at ~3450 cm^{-1} likely corresponding to the ν(O-H) vibration from adsorbed H_2O, and this band increased in intensity with increasing C/Fe content suggesting enhanced uptake of H_2O (Figure 6), (2) the intensity of the ν(O-H) stretch decreased and its position shifted towards higher wavenumbers as the C/Fe content increased, (3) the bands centred at ~1155, 753, and 597 cm^{-1} shifted towards lower wavenumbers and eventually disappeared as the C/Fe content increased, and (4) the intensity of the band centred at ~1020 cm^{-1} considerably decreased and slightly shifted towards higher wavenumbers with increasing C/Fe content until it became difficult to resolve due to band overlap (Figure 6). The observed alginate induced band changes suggest a weakening of the hydrogen bonding between the zig-zag sheets of $Fe(O,OH)_6$ octahedra due to a decrease in crystallinity, in agreement with the results obtained by XRD (Cornell and Schwertmann, 2003). Contamination due to Gt formation was clearly observed in the FTIR spectrum of the Lp coprecipitated with the lowest alginate content (C/Fe 0.5) as indicated by the band centred at ~883 cm^{-1} (in plane δ(O-H)) and shoulder band centred at ~793 cm^{-1} (out of plane

γ(O-H)) (Figure 6). The persistence of the shoulder band at ~793 cm^{-1} within the spectra for Lp coprecipitated with higher content of alginate (C/Fe 1.0 and 1.5) confirms the presence of minor amounts of Gt within these precipitates (Figure 6).

The FTIR spectra of Gt and Gt coprecipitates are presented in (Figure 6) and their band assignments are given in Table S4. For pure Gt, contribution due to adsorbed H_2O was evidenced by the ν(O-H) and δ(O-H) bands centred at ~3450 and 1636 cm^{-1}, respectively (Figure 6). Broad bands centred at ~1507 and 1321 cm^{-1} were assigned to ν_{asym} and ν_{sym}, respectively, of C-O bonds originating from the bound carbonate added during synthesis (Figure 6). The broad band centred at ~3166 cm^{-1} was assigned to the structural OH^- groups of the mineral, whereas the broad bands characteristic for Gt centred at ~888, 793, and 605 cm^{-1} were assigned to in-plane δ(O-H) vibration, out-of-plane γ(O-H) vibration, and ν_{sym} vibration of the lattice Fe-O bonds, respectively (Figure 6). For the Gt coprecipitates, bands corresponding to alginate as well as carbonate were observed in the 1700 – 1000 cm^{-1} region and the intensity of the alginate bands increased with increasing C/Fe content (Figure 6). In contrast to the XRD, the effects of alginate on the crystallinity of Gt coprecipitates were more apparent by FTIR. As was observed for Lp coprecipitates, alginate also affected the intensity, shape, and position of the bands characteristic of Gt (Figure 6). In comparison to pure Gt: (1) the intensity of the broad band centred at ~3450 cm^{-1} increased as the C/Fe content increased suggesting enhanced uptake of H_2O, (2) the intensity of the ν(O-H) band decreased and shifted towards higher wavenumbers, (3) the intensity of the δ(O-H), γ(O-H), and ν_{sym}(Fe-O) bands decreased with increasing C/Fe content, (4) the δ(O-H) and γ(O-H) bands appeared to broaden with increasing C/Fe content, and (5) the positions of δ(O-H) and γ(O-H) bands shifted towards lower wavenumbers as the C/Fe content increased to 1.0 with no further change observed as the C/Fe reached 1.5. The position of δ(O-H) band was noticeably more

affected than that of γ(O-H) and the difference in position between these bands decreased from ~95 cm^{-1} for pure Gt to ~89, 86.5, and 86.4 cm^{-1} for Gt coprecipitated with C/Fe ratio of 0.5, 1.0, and 1.5, respectively. The position of ν_{sym}(Fe-O) band is also influenced by crystallinity and particle morphology (Cornell and Schwertmann, 2003). However, for the Gt coprecipitates, shifting of this band did not exhibit a specific trend such that as the C/Fe content increased to 1.0 the position of this band shifted towards higher wavenumbers but shifted back towards lower wavenumbers as the C/Fe content increased to 1.5. Nonetheless, the observed alginate induced changes to the IR bands of Gt suggest a weakening of the hydrogen bonds as a consequence of decreasing crystallinity (Cornell and Schwertmann, 2003).

The overall results are consistent with those reported in the literature reaffirming the impact of various types of OM on the crystallinity of the iron oxides studied (Jones et al., 2009; Pedrot et al., 2011; Vollrath et al., 2013; Eusterhues et al., 2014a; Kleber et al., 2015; Najem et al., 2016; Liu et al., 2019b). OM can inhibit or "poison" the crystal growth of iron oxides by binding to reactive surfaces or interfering with nucleation and aggregation reactions (Liu, 1999; Chan et al., 2009; Piepenbrock et al., 2014; ThomasArrigo et al., 2022). Low molecular weight organic ligands (e.g., citrate, oxalate, tartrate) or natural organic matter can adsorb onto growing iron oxide surfaces, blocking active growth sites and leading to the formation of smaller, less crystalline, and, in some cases, more porous particles with higher SSA (Liu, 1999; Chan et al., 2009; Liu et al., 2019b). This interference alters morphology and precipitation pathways of the resulting iron oxides, which may lead to the precipitation of poorly ordered Fe phases as we determined through chemical extractions from Lp and Gt coprecipitates (Kleber et al., 2015; Liu et al., 2019b).

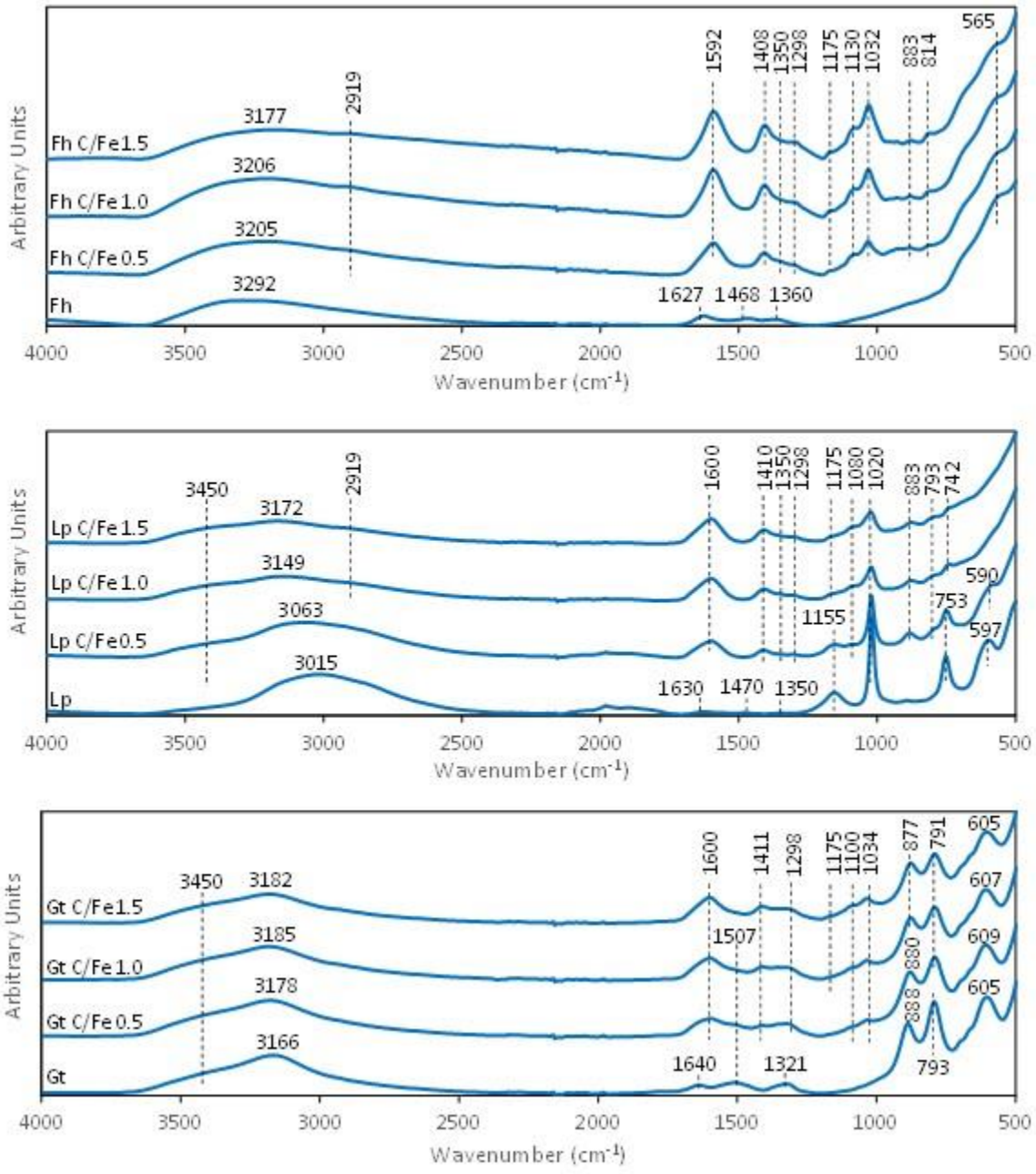

Figure 6: FTIR spectra of iron oxides studied. Band assignments are presented in Tables S1-S4 including the one for alginate powder for comparison.

3.3. Bioavailability

In addition to the analytical techniques employed in this study, microbial Fe(III) reduction experiments were carried out to further probe the impact of alginate on the bioavailability (rate and extent of Fe(III) reduction) of the various iron oxides studied. Enzymatic Fe(III) reduction curves of the iron oxides are presented in Figure S5, which show the increase of total Fe(II) and dissolved Fe(II) relative to total Fe throughout the experimental period (up to 25 days). The rates of Fe reduction by *S. putrefaciens* CN32 were calculated by linear regression of selected time points that corresponded to the period of maximum accumulation of total Fe(II) relative to total Fe. The extent of Fe reduction was determined from the maximum amount of total Fe(II) relative to total Fe, which equated to the concentrations measured on the last 3 sampling points of the experiment (Figure S5). A summary of the regression data and the maximum amount of Fe(III) reduced for the studied iron oxides are presented in Table 3. Control experiments showed no significant changes in the concentration of Fe(II), pH, or mineralogy throughout the experimental period, and their sterility was confirmed at the start and end of the experimental period (data not shown).

3.3.1. Pure iron oxides

As previously observed, the more crystalline iron oxides, Lp and Gt, were reduced at a slower rate than the poorly crystalline iron oxide Fh (Roden and Zachara, 1996; Fredrickson et al., 1998; Zachara et al., 1998; Cutting et al., 2009; Ekstrom et al., 2010; Poggenburg et al., 2018). The initial Fe reduction rates of pure Fh was ~2x and 3x faster than the rates determined for pure Lp and Gt, respectively (Table 3). The faster rate of Fe(III) reduction for Fh resulted in a higher amount reduced. After 25 days of incubation, ~62% of the pure Fh was reduced compared with ~34% and ~31% for Lp and Gt, respectively (Table 3).

3.3.2. Iron oxide-alginate coprecipitates

Alginate coprecipitation had a variable effect on the microbial Fe(III) reduction of Fh, Gt and Lp. Three stages corresponding to the accumulation of Fe(II) were observed during the microbial reduction of the Fhs: 1. an initial stage corresponding to the maximum accumulation of Fe(II) occurring during the first 5-6 days, 2. a second stage corresponding to a lower rate of Fe(II) accumulation starting at day 8 and ending at day 14, and 3. a third stage corresponding to either the plateau of Fe(II) accumulation or the very slow rate of accumulation of Fe(II) starting at day 15 until termination of the experiment (Figure S5). We did not observed a significant difference in the rate of Fe(III) reduction as a function of C/Fe ($P>0.05$, Table 3). Alginate, however, had a negative effect on the extent of microbial Fe(III) reduction. In contrast to pure Fh, only ~43% and ~45% of Fh coprecipitated with C/Fe of 0.5 and C/Fe 1.0 or C/Fe 1.5, respectively, was reduced (Table 3). Therefore, in comparison to pure Fh, the amount of Fe(III) reduced from the Fh coprecipitates was on average ~30% lower (Table 3). As was observed for Fh, microbial Fe(III) reduction did not significantly vary with increasing C/Fe ratio for either Lp or Gt. We did not observed a significant difference in the rate of Fe(III) reduction as a function of C/Fe within either Lp or Gt mineral groupings ($P>0.05$, Table 3). Thus, despite the observed effects of alginate on the chemical Fe extractability, SSA, particle size, and crystallinity of the iron oxides studied, the rates of Fe(III) reduction remained comparable. The maximum Fe(III) reduction reached ~35%, 39%, and 42% for Lp coprecipitated with C/Fe ratios of 0.5, 1.0, and 1.5, respectively (Table 2). No significant difference was observed between pure Lp and Lp with C/Fe 0.5 ($P>0.05$), but alginate significantly enhanced Fe(III) reduction at higher C/Fe ratios (1.0 and 1.5), where the extent plateaued ($P>0.05$). Overall, alginate increased Fe(III) reduction by ~7% on average compared to pure Lp at higher C/Fe ratios (Table 3). Fe(III) reduction in Gt coprecipitates followed

a similar trend to Lp, reaching ~30%, 36%, and 34% for C/Fe ratios of 0.5, 1.0, and 1.5, respectively (Table 2). No significant difference was observed between pure Gt and Gt with C/Fe 0.5 ($P>0.05$), but Fe(III) reduction was significantly higher at C/Fe 1.0 and 1.5 ($P<0.05$), with no significant difference between these two ($P>0.05$). Overall, alginate enhanced Fe(III) reduction by ~4% on average compared to pure Gt at higher C/Fe ratios (Table 3). Across all experiments (Lp and Gt), microbial reduction was terminated at ~25 days, although mineral reduction is ongoing for the pure and coprecipitated phases (Figure S5). Across all biotic experiments, the majority of Fe(II) produced remained in the aqueous phase comprising 50-60% of the total Fe(II) at the later stages of the experimental reduction period (Figure S5). Moreover, the concentration of dissolved Fe(II) did not vary as a function of C content highlighting the lack of contribution of alginate to complex Fe(II) within these systems (Figure S5).

Table 3: Linear Fe(III) reduction rates and maximum percentage of total Fe reduced for the various iron oxides studied. The values represent the mean ± standard deviation of 3 replicate experiments for each precipitate.

Sample	Rate (day^{-1})	Maximum Fe reduced (%)
Fh	0.042±0.003 (R^2 = 0.995)	61.72±3.03*
Fh 0.5	0.044±0.008 (R^2 = 0.976)	43.22±1.24*
Fh 1.0	0.047±0.009 (R^2 = 0.976)	45.83±1.13*
Fh 1.5	0.050±0.008 (R^2 = 0.981)	44.75±2.00*
Lp	0.018±0.002 (R^2 = 0.987)	33.58±5.14*
Lp 0.5	0.016±0.004 (R^2 = 0.962)	34.85±2.18
Lp 1.0	0.024±0.004 (R^2 = 0.975)	39.12±2.95*
Lp 1.5	0.028±0.007 (R^2 = 0.963)	42.46±2.53
Gt	0.013±0.002 (R^2 = 0.985)	30.57±2.71*
Gt 0.5	0.013±0.003 (R^2 = 0.960)	30.09±2.92
Gt 1.0	0.015±0.002 (R^2 = 0.993)	35.81±3.06*
Gt 1.5	0.017±0.002 (R^2 = 0.986)	34.03±2.97

* Represents significant difference at the 95% confidence interval level.

Several factors influence the bioavailability of iron oxides, including SSA, solubility, morphology, particle size, and crystallinity (Roden and Zachara, 1996; Roden, 2003; Bonneville et al., 2004; Bonneville et al., 2009; Cutting et al., 2009). Here we do not observe a direct

significant relationship between SSA (P>0.05) or particle size (P>0.05) and the rates of Fe(III) reduction (Figure 7). The results are in line with several studies who also identified SSA as a poor predictor of Fe(III) reduction rates, especially where OM is closely associated with the iron oxide (Mikutta and Kretzschmar, 2008; Mikutta et al., 2008; Shimizu et al., 2013; Eusterhues et al., 2014a; Poggenburg et al., 2016; Poggenburg et al., 2018). For example, a synthetic Fh-exopolysaccharide coprecipitate and naturally occurring biogenic iron oxides, predominantly Fh, were reduced more rapidly and to a greater extent by *S. putrefaciens* CN32 than pure Fh despite possessing much lower SSA (Langley et al., 2009b; Langley et al., 2009e; Poggenburg et al., 2016). Similarly, abiotic dissolution rates by the siderophore desferrioxamine B of synthetic Fh-polygalacturonic acid (C/Fe 0.36, 0.65, 0.90, 1.25) and Fh-alginate (C/Fe 1.18) coprecipitates were significantly higher than that of pure Fh (Mikutta and Kretzschmar, 2008). Likewise, we also observed a higher reduction rate of Fh-alginate (C/Fe 1.0) by ascorbate than that of pure Fh (data not shown). In contrast, the rates of Fe(III) reduction by dithionite and *Geobacter bremensis* decreased with increasing OM (forest-floor extract) content (C/Fe 0, 0.4, 1.0, and 2.8 mol:mol) (Eusterhues et al., 2014a). Particle size and the extent of aggregation were also reported to impact the rate of reduction, although these factors also depended on the strain of iron reducing bacteria (Amstaetter et al., 2012; Poggenburg et al., 2016). Large aggregates of humic acid-Fh associations were less bioavailable whereas particle size was a poor or an excellent predictor of bioavailability for a range of Fh-OM coprecipitates to *S. putrefaciens* or *Geobacter metallireducens*, respectively (Amstaetter et al., 2012; Poggenburg et al., 2016). Along these lines surface charge was suggested to play an inhibitory role on the bioreduction of Fh-OM associations, whereby negatively charged OM would block or repel negative charged bacteria from directly accessing the surface of the oxide for DIR (Amstaetter et al., 2012; Shimizu et al., 2013; Poggenburg et al., 2016; Adhikari et al.,

2017). Yet, OM may enhance the biotic or abiotic reduction/dissolution of iron oxide-OM coprecipitates by modifying the crystallinity of the iron oxide (i.e. poisoning the crystal growth of the iron oxide during precipitation), coupled with OM-induced alterations in the dispersion of the particles (Mikutta and Kretzschmar, 2008; Eusterhues et al., 2014a; Poggenburg et al., 2016). Consequently, increased repulsion between particles may facilitate the access of the reducing agent to the reactive iron sites.

OM may also form complexes with biogenic Fe(II) reducing the potential of Fe(II) to block surfaces of the oxide, however we found that the dissolved Fe(II)/total Fe fraction was similar among the biotic microcosms indicative of the absence of this mechanism. This is in line with the findings that alginate poorly forms complexes with Fe(II) (Falkeborg et al., 2014). Depending on the OM type, OM may act as electron shuttles for iron reducing bacteria alleviating the requirement for direct surface contact between bacteria and the oxide surface (Adhikari et al., 2016; Poggenburg et al., 2016; Cooper et al., 2017; Poggenburg et al., 2018). In our case, alginate does not possess the necessary functional groups that facilitate electron transfer processes (Poggenburg et al., 2016; Weihe et al., 2019). Therefore, it is likely that mineralogy and macroscopic properties are the main controlling factors of bioavailability of the iron oxides studied. For the coprecipitates, we observed reduced crystallinity, yet the size of the aggregates varied with increasing C/Fe content. This could suggest simultaneous competing factors (crystallinity vs. aggregate size) contributing to the enhancement and inhibition of Fe(III) reduction. However, it is also possible that as the reduction proceeds alginate may be released into solution and may re-adsorb to the surface of the oxide retarding further Fe(III) reduction. This mechanism would be speculated to contribute to the observed decrease in the amount of Fe(III) reduced in the coprecipitates in comparison to pure Fh, as well as the small difference between the pure Lp and Gt and the

corresponding coprecipitates. Moreover, Fe(II) may adsorb on the surface of the oxide further contributing to this inhibiting effect (Roden and Zachara, 1996; Fredrickson et al., 1998; Roden and Urrutia, 2002; Hansel et al., 2003).

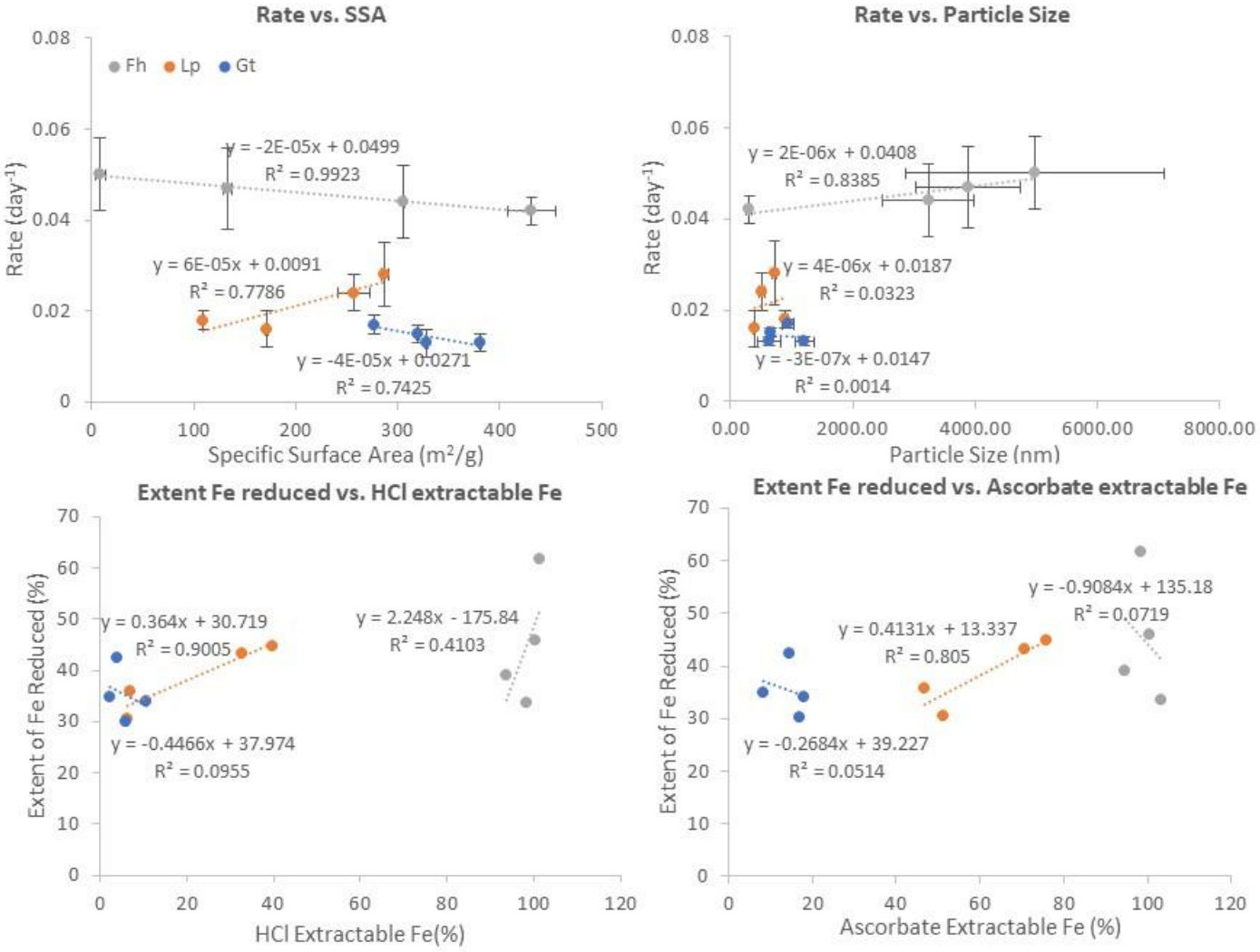

Figure 7: Relationship between the microbial rate of Fe(III) reduction and specific surface area (SSA) or particle size. Regression analysis determined that the correlation between the variables was not significant (P>0.05) at the 95% confidence interval. Also shown is the relationship between the extent of Fe(III) reduced by *S. putrefaciens* CN32 and 0.5 M HCl extractable Fe or ascorbate extractable Fe. For both cases, regression analysis showed that the correlation is significant (P<0.05) at the 95% confidence interval for the lepidocrocites.

3.3.2. Biogenic solids

X-ray diffractograms of the post-reduction minerals are shown in Figure 8. Broad reflections corresponding to residual 2-line ferrihydrite were detected in the biogenic solids following the microbial reduction of the Fhs (Figure 8). In contrast to the reduced Fh coprecipitates, Fe reduction led to the transformation of the pure Fh into 2-line ferrihydrite with a "higher" crystallinity as judged by the slightly "sharper" reflections at 35 and 62° (Figure 8). However, mineral phases corresponding to iron oxides of higher crystallinity such as goethite, lepidocrocite, or magnetite were not detected in any of the biogenic solids following the microbial reduction of the Fhs (Figure 8). The lack of transformation of the studied Fhs into more crystalline phases stems from the stabilizing effects of the added phosphate and, for the coprecipitates, alginate (Borch et al., 2007; Amstaetter et al., 2012; Shimizu et al., 2013). Nonetheless, it is also possible that minerals of higher crystallinity may have formed to levels that were below the bulk detection limit of the XRD (~5% by weight). The addition of phosphate to the media as a nutrient (400 μM) led to the precipitation of vivianite ($Fe_3(PO_4)_2$•8H2O) (Zachara et al., 2002; Glasauer et al., 2003), which was detected in the biogenic solids following the microbial reduction of the pure Fh consistent with past studies (Figure 8). Vivianite, however, was not detected in any of the biogenic solids following the microbial reduction of the Fh coprecipitates (Figure 8). This can be attributed to the adsorption and retention of phosphate to the mineral surfaces preventing the precipitation of vivianite. Following the microbial reduction of the Lps and Gts, the biogenic solids consisted mainly of the residual Lp or Gt, respectively, together with vivianite, and no other differences could be distinguished (Figure 8). Interestingly, vivianite could not be detected by XRD within the biogenic solids following the microbial reduction of the Gt coprecipitated with C/Fe of 0.5 (Figure 8).

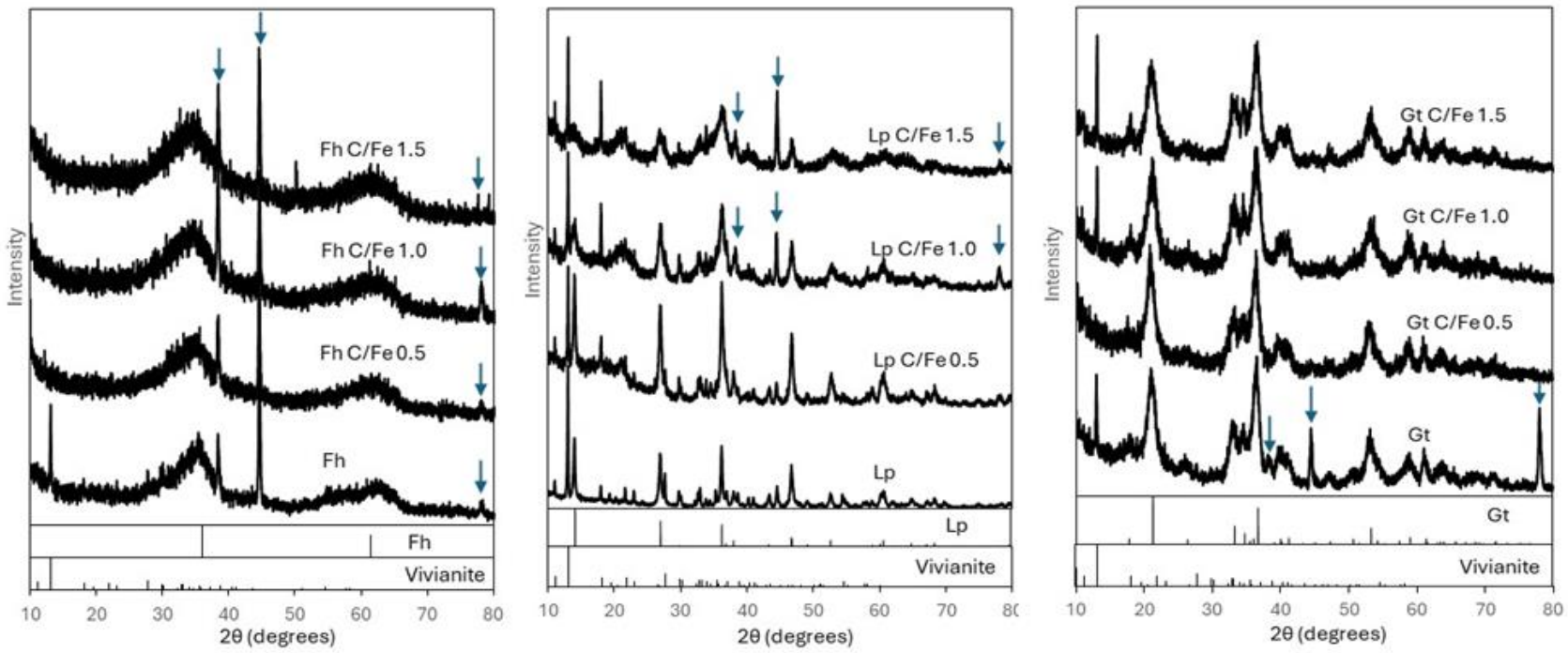

Figure 8: Powder x-ray diffraction of the iron oxides studied post reduction by S. putrefaciens CN32 (~25 days of incubation) compared to reference lines from Fh, Lp, Gt, and vivianite. Blue arrows point to additional reflections originating from the sample holder. All patterns have been vertically separated on an arbitrary y-axis. Fh, Lp, and Gt correspond to 2-line ferrihydrite, lepidocrocite, and goethite, respectively.

3.4. Chemical extractions vs. microbial Fe(III) reduction

As previously mentioned, the 0.5 M HCl-extractable and ascorbate-extractable Fe fractions reflect the fraction that is "bioavailable" (Hyacinthe et al., 2006). Although both extractants fully dissolved/reduced all of the Fhs, the extent of Fe(III) reduced by *S. putrefaciens* CN32 was considerably lower. Hyacinthe et al. (2006) attributed this difference to the smaller size of the reducing agent (ascorbate) than bacteria, which is able to reach reactive Fe(III) sites within tight pore spaces. For the Lp and Gt coprecipitates, the extent of Fe(III) reduced correlated with the amount of Fe extracted by 0.5 M HCl and ascorbate (Figure 7). Therefore, the higher amount of Fe(III) reduced as the C/Fe increases can be attributed to the higher proportion of a poorly crystalline Fe fraction.

4. Conclusions

To better constrain C and Fe biogeochemical processes in soils and sediments, this study aimed to assess, first, the effect of OM on the physicochemical and mineralogical properties of various iron oxides and, second, how the formed OM–iron oxide coprecipitates then interact with the iron reducing bacteria. This was performed here with a case study on the effects of variable concentration of alginate on Fh, Lp, and Gt formation, followed by abiotic and biotic reduction/dissolution assessment of these composites. The presence of increasing initial C/Fe ratio of alginate impacted the minerals in several ways: particle size, surface charge, SSA, crystallinity, and the proportion of chemically extractable poorly crystalline Fe fraction. Exposure of these alginate-iron oxide coprecipitates to the dissimilatory iron-reducing bacteria *S. putrefaciens* CN32 showed variable results that did not depend on SSA nor particle size. Despite the apparent significant alginate-induced changes at the mineralogical and macroscopic scale, the rates of Fe(III) reduction remained comparable to the alginate-free iron oxides. The results from this study

contradicts the findings of others that reported significant differences in reactivity between biogenic iron oxides and synthetic equivalents, which has been attributed to differences in their crystallinity (Muehe et al., 2013; Piepenbrock et al., 2014). However, the type of OM studied must be also considered as has been highlighted in the past, as it can mask or override expected mineral-based trends in microbial reducibility (Kleber et al., 2015; Poggenburg et al., 2016; Poggenburg et al., 2018). Moreover, differences among Fh, Lp, and Gt highlight that mineral identity must also be considered when evaluating the impact of OM on Fe bioavailability. Overall, this study highlights that OM-induced changes to the structural and surface properties of iron oxides do not always translate into predictable shifts in microbial Fe(III) reduction behavior. These findings have important implications for biogeochemical models, particularly in natural environments where complex mixtures of minerals and OM coexist. Accurately predicting DIR rates and their contributions to Fe and C cycling in soils and sediments requires a nuanced understanding of not only mineralogical characteristics but also the nature and role of associated OM.

Declaration of competing interest

The authors declare that they have no known competing financial interests or personal relationships that could have appeared to influence the work reported in this paper.

Acknowledgements

The present research was entirely funded by a NSERC Discovery grant to D. Fortin. We would like to thank Nimal DeSilva and Smita Mohanty (University of Ottawa) for their expertise and analyzing our samples with the ICP-OES, the Ján *V*eizer Stable Isotope Lab (University of Ottawa) for their expertise and analysis of DOC and carbon content, and Dr. Javier Giorgi (University of Ottawa) for providing the access and training to use the Autosorb-1 for sample analysis.

Appendix A. Supplementary data

Supplementary material

References

Adhikari, D., Poulson, S. R., Sumaila, S., Dynes, J. J., McBeth, J. M. and Yang, Y., 2016. Asynchronous reductive release of iron and organic carbon from hematite–humic acid complexes. Chem. Geol. 430: 13-20.

Adhikari, D., Zhao, Q., Das, K., Mejia, J., Huang, R., Wang, X., Poulson, S. R., Tang, Y., Roden, E. E. and Yang, Y., 2017. Dynamics of ferrihydrite-bound organic carbon during microbial Fe reduction. Geochim. Cosmochim. Acta 212: 221-233.

Amstaetter, K., Borch, T. and Kappler, A., 2012. Influence of humic acid imposed changes of ferrihydrite aggregation on microbial Fe (III) reduction. Geochim. Cosmochim. Acta 85: 326-341.

Angelico, R., Ceglie, A., He, J.-Z., Liu, Y.-R., Palumbo, G. and Colombo, C., 2014. Particle size, charge and colloidal stability of humic acids coprecipitated with ferrihydrite. Chemosphere 99: 239-247.

Baalousha, M., 2009. Aggregation and disaggregation of iron oxide nanoparticles: Influence of particle concentration, pH and natural organic matter. Sci. Total Environ. 407(6): 2093-2101.

Bonneville, S., Behrends, T. and Van Cappellen, P., 2009. Solubility and dissimilatory reduction kinetics of iron (III) oxyhydroxides: A linear free energy relationship. Geochim. Cosmochim. Acta 73(18): 5273-5282.

Bonneville, S., Van Cappellen, P. and Behrends, T., 2004. Microbial reduction of iron (III) oxyhydroxides: effects of mineral solubility and availability. Chem. Geol. 212(3-4): 255-268.

Borch, T., Masue, Y., Kukkadapu, R. K. and Fendorf, S., 2007. Phosphate imposed limitations on biological reduction and alteration of ferrihydrite. Environ. Sci. Technol. 41(1): 166-172.

Byrne, J. M. and Kappler, A., 2021. A revised analysis of ferrihydrite at liquid helium temperature using Mössbauer spectroscopy. American Mineralogist In press.

Cardenas-Jiron, G., Leal, D., Matsuhiro, B. and Osorio-Roman, I. O., 2011. Vibrational spectroscopy and density functional theory calculations of poly-D-mannuronate and heteropolymeric fractions from sodium alginate. J. Raman Spectrosc. 42(4): 870-878.

Chan, C. S., De Stasio, G., Welch, S. A., Girasole, M., Frazer, B. H., Nesterova, M. V., Fakra, S. and Banfield, J. F., 2004. Microbial polysaccharides template assembly of nanocrystal fibers. Science 303(5664): 1656-1658.

Chan, C. S., Fakra, S. C., Edwards, D. C., Emerson, D. and Banfield, J. F., 2009. Iron oxyhydroxide mineralization on microbial extracellular polysaccharides. Geochim. Cosmochim. Acta 73(13): 3807-3818.

Chandıa, N., Matsuhiro, B. and Vásquez, A., 2001. Alginic acids in Lessonia trabeculata: characterization by formic acid hydrolysis and FT-IR spectroscopy. Carbohydr. Polym. 46(1): 81-87.

Chen, C., Dynes, J. J., Wang, J. and Sparks, D. L., 2014. Properties of Fe-organic matter associations via coprecipitation versus adsorption. Environ. Sci. Technol. 48(23): 13751-13759.

Chen, C., Kukkadapu, R. and Sparks, D. L., 2015. Influence of Coprecipitated Organic Matter on Fe^{2+}(aq)-Catalyzed Transformation of Ferrihydrite: Implications for Carbon Dynamics. Environ. Sci. Technol. 49(18): 10927-10936.

Chen, K.-Y., Hsu, L.-C., Chan, Y.-T., Cho, Y.-L., Tsao, F.-Y., Tzou, Y.-M., Hsieh, Y.-C. and Liu, Y.-T., 2018. Phosphate removal in relation to structural development of humic acid-iron coprecipitates. Sci. Rep. 8(1): 10363.

Cismasu, A. C., Michel, F. M., Tcaciuc, A. P., Tyliszczak, T. and Brown, J. G. E., 2011. Composition and structural aspects of naturally occurring ferrihydrite. Comptes Rendus Geoscience 343(2-3): 210-218.

Cismasu, A. C., Williams, K. H. and Nico, P. S., 2016. Iron and Carbon Dynamics during Aging and Reductive Transformation of Biogenic Ferrihydrite. Environ. Sci. Technol. 50(1): 25-35.

Colombo, C., Palumbo, G., Sellitto, V. M., Cho, H. G., Amalfitano, C. and Adamo, P., 2015. Stability of coprecipitated natural humic acid and ferrous iron under oxidative conditions. Journal of Geochemical Exploration 151: 50-56.

Cooper, R. E., Eusterhues, K., Wegner, C.-E., Totsche, K. U. and Küsel, K., 2017. Ferrihydrite-associated organic matter (OM) stimulates reduction by Shewanella oneidensis MR-1 and a complex microbial consortia. Biogeosciences 14(22): 5171-5188.

Cornell, R. M. and Schwertmann, U., 2003. The iron oxides: structure, properties, reactions, occurrences, and uses, Wiley-vch Weinheim.

Curti, L., Moore, O. W., Babakhani, P., Xiao, K.-Q., Woulds, C., Bray, A. W., Fisher, B. J., Kazemian, M., Kaulich, B. and Peacock, C. L., 2021. Carboxyl-richness controls organic carbon preservation during coprecipitation with iron (oxyhydr)oxides in the natural environment. Commun. Earth Environ. 2(1).

Cutting, R., Coker, V., Fellowes, J., Lloyd, J. and Vaughan, D., 2009. Mineralogical and morphological constraints on the reduction of Fe (III) minerals by Geobacter sulfurreducens. Geochim. Cosmochim. Acta 73(14): 4004-4022.

Dong, H., Huang, L., Zhao, L., Zeng, Q., Liu, X., Sheng, Y., Shi, L., Wu, G., Jiang, H., Li, F., Zhang, L., Guo, D., Li, G., Hou, W. and Chen, H., 2022. A critical review of mineral–microbe interaction and co-evolution: mechanisms and applications. National Science Review 9(10).

Dong, H., Zeng, Q., Sheng, Y., Chen, C., Yu, G. and Kappler, A., 2023. Coupled iron cycling and organic matter transformation across redox interfaces. Nature Reviews Earth & Environment 4(9): 659-673.

Ekstrom, E. B., Learman, D. R., Madden, A. S. and Hansel, C. M., 2010. Contrasting effects of Al substitution on microbial reduction of Fe (III)(hydr) oxides. Geochim. Cosmochim. Acta 74(24): 7086-7099.

Eusterhues, K., Hädrich, A., Neidhardt, J., Küsel, K., Keller, T., Jandt, K. and Totsche, K., 2014. Reduction of ferrihydrite with adsorbed and coprecipitated organic matter: microbial reduction by Geobacter bremensis vs. abiotic reduction by Na-dithionite. Biogeosciences 11(18): 4953-4966.

Eusterhues, K., Wagner, F. E., Häusler, W., Hanzlik, M., Knicker, H., Totsche, K. U., Kögel-Knabner, I. and Schwertmann, U., 2008. Characterization of ferrihydrite-soil organic matter coprecipitates by X-ray diffraction and Mossbauer spectroscopy. Environ. Sci. Technol. 42(21): 7891-7897.

Fabisch, M., Freyer, G., Johnson, C. A., Buchel, G., Akob, D. M., Neu, T. R. and Kusel, K., 2016. Dominance of 'Gallionella capsiferriformans' and heavy metal association with Gallionella-like stalks in metal-rich pH 6 mine water discharge. Geobiology 14(1): 68-90.

Falkeborg, M., Cheong, L.-Z., Gianfico, C., Sztukiel, K. M., Kristensen, K., Glasius, M., Xu, X. and Guo, Z., 2014. Alginate oligosaccharides: Enzymatic preparation and antioxidant property evaluation. Food Chem. 164: 185-194.

Field, H. R., Whitaker, A. H., Henson, J. A. and Duckworth, O. W., 2019. Sorption of copper and phosphate to diverse biogenic iron (oxyhydr) oxide deposits. Sci. Total Environ. 697: 134111.

Fredrickson, J. K., Zachara, J. M., Kennedy, D. W., Dong, H., Onstott, T. C., Hinman, N. W. and Li, S.-m., 1998. Biogenic iron mineralization accompanying the dissimilatory reduction of hydrous ferric oxide by a groundwater bacterium. Geochim. Cosmochim. Acta 62(19-20): 3239-3257.

Glasauer, S., Weidler, P. G., Langley, S. and Beveridge, T. J., 2003. Controls on Fe reduction and mineral formation by a subsurface bacterium. Geochim. Cosmochim. Acta 67(7): 1277-1288.

Grybos, M., Davranche, M., Gruau, G. and Petitjean, P., 2007. Is trace metal release in wetland soils controlled by organic matter mobility or Fe-oxyhydroxides reduction? J. Colloid Interface Sci. 314(2): 490-501.

Han, L., Sun, K., Keiluweit, M., Yang, Y., Yang, Y., Jin, J., Sun, H., Wu, F. and Xing, B., 2019. Mobilization of ferrihydrite-associated organic carbon during Fe reduction: Adsorption versus coprecipitation. Chem. Geol. 503: 61-68.

Hansel, C. M., Benner, S. G., Neiss, J., Dohnalkova, A., Kukkadapu, R. K. and Fendorf, S., 2003. Secondary mineralization pathways induced by dissimilatory iron reduction of ferrihydrite under advective flow. Geochim. Cosmochim. Acta 67(16): 2977-2992.

Hao, L., Guo, Y., Byrne, J. M., Zeitvogel, F., Schmid, G., Ingino, P., Li, J., Neu, T. R., Swanner, E. D., Kappler, A. and Obst, M., 2016. Binding of heavy metal ions in aggregates of microbial cells, EPS and biogenic iron minerals measured in-situ using metal- and glycoconjugates-specific fluorophores. Geochim. Cosmochim. Acta 180: 66-96.

Henneberry, Y. K., Kraus, T. E. C., Nico, P. S. and Horwath, W. R., 2012. Structural stability of coprecipitated natural organic matter and ferric iron under reducing conditions. Org. Geochem. 48: 81-89.

Hofmann, A., Pelletier, M., Michot, L., Stradner, A., Schurtenberger, P. and Kretzschmar, R., 2004. Characterization of the pores in hydrous ferric oxide aggregates formed by freezing and thawing. J. Colloid Interface Sci. 271(1): 163-173.

Hyacinthe, C., Bonneville, S. and Van Cappellen, P., 2006. Reactive iron(III) in sediments: Chemical versus microbial extractions. Geochim. Cosmochim. Acta 70(16): 4166-4180.

Hyacinthe, C. and Van Cappellen, P., 2004. An authigenic iron phosphate phase in estuarine sediments: composition, formation and chemical reactivity. Mar. Chem. 91(1-4): 227-251.

Jones, A. M., Collins, R. N., Rose, J. and Waite, T. D., 2009. The effect of silica and natural organic matter on the Fe (II)-catalysed transformation and reactivity of Fe (III) minerals. Geochim. Cosmochim. Acta 73(15): 4409-4422.

Kaiser, K., 2003. Sorption of natural organic matter fractions to goethite (α-FeOOH): effect of chemical composition as revealed by liquid-state ^{13}C NMR and wet-chemical analysis. Org. Geochem. 34(11): 1569-1579.

Kaiser, K., Guggenberger, G., Haumaier, L. and Zech, W., 1997. Dissolved organic matter sorption on sub soils and minerals studied by ^{13}C-NMR and DRIFT spectroscopy. Eur. J. Soil Sci. 48(2): 301-310.

Kaiser, K., Mikutta, R. and Guggenberger, G., 2007. Increased stability of organic matter sorbed to ferrihydrite and goethite on aging. Soil Sci. Soc. Am. J. 71(3): 711-719.
Kleber, M., Eusterhues, K., Keiluweit, M., Mikutta, C., Mikutta, R. and Nico, P. S., 2015. Mineral–Organic Associations: Formation, Properties, and Relevance in Soil Environments. 130: 1-140.
Kleinert, S., Muehe, E. M., Posth, N. R., Dippon, U., Daus, B. and Kappler, A., 2011. Biogenic Fe (III) minerals lower the efficiency of iron-mineral-based commercial filter systems for arsenic removal. Environ. Sci. Technol. 45(17): 7533-7541.
Kostka, J. E. and Luther, G. W., 1994. Partitioning and speciation of solid phase iron in saltmarsh sediments. Geochim. Cosmochim. Acta 58(7): 1701-1710.
Kraal, P., van Genuchten, C. M., Behrends, T. and Rose, A. L., 2019. Sorption of phosphate and silicate alters dissolution kinetics of poorly crystalline iron (oxyhydr) oxide. Chemosphere 234: 690-701.
Lagarec, K. and Rancourt, D. G., 1997. Extended Voigt-based analytic lineshape method for determining N-dimensional correlated hyperfine parameter distributions in Mössbauer spectroscopy. Nuclear Instruments and Methods in Physics Research Section B: Beam Interactions with Materials and Atoms 129(2): 266-280.
Lalonde, K., Mucci, A., Ouellet, A. and Gélinas, Y., 2012. Preservation of organic matter in sediments promoted by iron. Nature 483(7388): 198-200.
Langley, S., Gault, A., Ibrahim, A., Renaud, R., Fortin, D., Clark, I. D. and Ferris, F. G., 2009a. A Comparison of the Rates of Fe(III) Reduction in Synthetic and Bacteriogenic Iron Oxides by Shewanella putrefaciens CN32. Geomicrobiology Journal 26(2): 57-70.
Langley, S., Gault, A., Ibrahim, A., Renaud, R., Fortin, D., Clark, I. D. and Ferris, F. G., 2009b. A Comparison of the Rates of Fe(III) Reduction in Synthetic and Bacteriogenic Iron Oxides byShewanella putrefaciensCN32. Geomicrobiol. J. 26(2): 57-70.
Langley, S., Igric, P., Takahashi, Y., Sakai, Y., Fortin, D., Hannington, M. D. and Schwarz-Schampera, U., 2009c. Preliminary characterization and biological reduction of putative biogenic iron oxides (BIOS) from the Tonga-Kermadec Arc, southwest Pacific Ocean. Geobiology 7(1): 35-49.
Leal, D., Matsuhiro, B., Rossi, M. and Caruso, F., 2008. FT-IR spectra of alginic acid block fractions in three species of brown seaweeds. Carbohydr Res 343(2): 308-316.
Li, Q., Hu, W., Li, L. and Li, Y., 2023. Interactions between organic matter and Fe oxides at soil micro-interfaces: Quantification, associations, and influencing factors. Sci. Total Environ. 855: 158710.
Liu, C., 1999. Surface chemistry of iron oxide minerals formed in different ionic environments.
Liu, Q., Li, X., Tang, J., Zhou, Y., Lin, Q., Xiao, R. and Zhang, M., 2019. Characterization of goethite-fulvic acid composites and their impact on the immobility of Pb/Cd in soil. Chemosphere 222: 556-563.
Martens, J., Mueller, C. W., Joshi, P., Rosinger, C., Maisch, M., Kappler, A., Bonkowski, M., Schwamborn, G., Schirrmeister, L. and Rethemeyer, J., 2023. Stabilization of mineral-associated organic carbon in Pleistocene permafrost. Nat Commun 14(1): 2120.
Mejia, J., He, S., Yang, Y., Ginder-Vogel, M. and Roden, E. E., 2018. Stability of Ferrihydrite-Humic Acid Coprecipitates under Iron-Reducing Conditions. Environ. Sci. Technol. 52(22): 13174-13183.

Mikutta, C. and Kretzschmar, R., 2008. Synthetic coprecipitates of exopolysaccharides and ferrihydrite. Part II: Siderophore-promoted dissolution. Geochim. Cosmochim. Acta 72(4): 1128-1142.
Mikutta, C., Mikutta, R., Bonneville, S., Wagner, F., Voegelin, A., Christl, I. and Kretzschmar, R., 2008. Synthetic coprecipitates of exopolysaccharides and ferrihydrite. Part I: Characterization. Geochim. Cosmochim. Acta 72(4): 1111-1127.
Mikutta, R., Lorenz, D., Guggenberger, G., Haumaier, L. and Freund, A., 2014. Properties and reactivity of Fe-organic matter associations formed by coprecipitation versus adsorption: Clues from arsenate batch adsorption. Geochim. Cosmochim. Acta 144: 258-276.
Muehe, E. M., Scheer, L., Daus, B. and Kappler, A., 2013. Fate of arsenic during microbial reduction of biogenic versus abiogenic As–Fe (III)–mineral coprecipitates. Environ. Sci. Technol. 47(15): 8297-8307.
Najem, T., Langley, S. and Fortin, D., 2016. A comparison of Fe(III) reduction rates between fresh and aged biogenic iron oxides (BIOS) by Shewanella putrefaciens CN32. Chem. Geol. 439: 1-12.
O'Loughlin, E. J., Boyanov, M. I., Flynn, T. M., Gorski, C. A., Hofmann, S. M., McCormick, M. L., Scherer, M. M. and Kemner, K. M., 2013. Effects of bound phosphate on the bioreduction of lepidocrocite (γ-FeOOH) and maghemite (γ-Fe2O3) and formation of secondary minerals. Environ. Sci. Technol. 47(16): 9157-9166.
Patzner, M. S., Logan, M., McKenna, A. M., Young, R. B., Zhou, Z., Joss, H., Mueller, C. W., Hoeschen, C., Scholten, T., Straub, D., Kleindienst, S., Borch, T., Kappler, A. and Bryce, C., 2022. Microbial iron cycling during palsa hillslope collapse promotes greenhouse gas emissions before complete permafrost thaw. Commun. Earth Environ. 3(1).
Pedrot, M., Le Boudec, A., Davranche, M., Dia, A. and Henin, O., 2011. How does organic matter constrain the nature, size and availability of Fe nanoparticles for biological reduction? J. Colloid Interface Sci. 359(1): 75-85.
Piepenbrock, A., Schröder, C. and Kappler, A., 2014. Electron transfer from humic substances to biogenic and abiogenic Fe (III) oxyhydroxide minerals. Environ. Sci. Technol. 48(3): 1656-1664.
Poggenburg, C., Mikutta, R., Sander, M., Schippers, A., Marchanka, A., Dohrmann, R. and Guggenberger, G., 2016. Microbial reduction of ferrihydrite-organic matter coprecipitates by Shewanella putrefaciens and Geobacter metallireducens in comparison to mediated electrochemical reduction. Chem. Geol. 447: 133-147.
Poggenburg, C., Mikutta, R., Schippers, A., Dohrmann, R. and Guggenberger, G., 2018. Impact of natural organic matter coatings on the microbial reduction of iron oxides. Geochim. Cosmochim. Acta 224: 223-248.
Possinger, A. R., Zachman, M. J., Dynes, J. J., Regier, T. Z., Kourkoutis, L. F. and Lehmann, J., 2021. Co-precipitation induces changes to iron and carbon chemistry and spatial distribution at the nanometer scale. Geochim. Cosmochim. Acta 314: 1-15.
Riedel, T., Zak, D., Biester, H. and Dittmar, T., 2013. Iron traps terrestrially derived dissolved organic matter at redox interfaces. Proc. Natl. Acad. Sci. 110(25): 10101-10105.
Roden, E. E., 2003. Fe (III) oxide reactivity toward biological versus chemical reduction. Environ. Sci. Technol. 37(7): 1319-1324.
Roden, E. E. and Urrutia, M. M., 2002. Influence of biogenic Fe (II) on bacterial crystalline Fe (III) oxide reduction. Geomicrobiol. J. 19(2): 209-251.

Roden, E. E. and Zachara, J. M., 1996. Microbial reduction of crystalline iron (III) oxides: influence of oxide surface area and potential for cell growth. Environ. Sci. Technol. 30(5): 1618-1628.
Rouquerol, J., Llewellyn, P. and Rouquerol, F., 2007. Is the BET equation applicable to microporous adsorbents. Stud. Surf. Sci. Catal 160(07): 49-56.
Rouquerol, J., Rouquerol, F., Llewellyn, P., Maurin, G. and Sing, K., 2013. Adsorption by powders and porous solids: principles, methodology and applications, Academic press.
Sartori, C., Finch, D. S., Ralph, B. and Gilding, K., 1997. Determination of the cation content of alginate thin films by FTIR spectroscopy. Polymer 38(1): 43-51.
Schwertmann, U. and Cornell, R. M., 2008. Iron oxides in the laboratory: preparation and characterization, John Wiley & Sons.
Schwertmann, U., Wagner, F. and Knicker, H., 2005. Ferrihydrite–Humic Associations. Soil Sci. Soc. Am. J. 69(4): 1009-1015.
Shimizu, M., Zhou, J., Schroder, C., Obst, M., Kappler, A. and Borch, T., 2013. Dissimilatory reduction and transformation of ferrihydrite-humic acid coprecipitates. Environ. Sci. Technol. 47(23): 13375-13384.
Sowers, T. D., Harrington, J. M., Polizzotto, M. L. and Duckworth, O. W., 2017. Sorption of arsenic to biogenic iron (oxyhydr) oxides produced in circumneutral environments. Geochim. Cosmochim. Acta 198: 194-207.
Stookey, L. L., 1970. Ferrozine---a new spectrophotometric reagent for iron. Analytical Chemistry 42(7): 779-781.
ThomasArrigo, L. K., Notini, L., Shuster, J., Nydegger, T., Vontobel, S., Fischer, S., Kappler, A. and Kretzschmar, R., 2022. Mineral characterization and composition of Fe-rich flocs from wetlands of Iceland: Implications for Fe, C and trace element export. Sci. Total Environ. 816: 151567.
Toner, B. M., Santelli, C. M., Marcus, M. A., Wirth, R., Chan, C. S., McCollom, T., Bach, W. and Edwards, K. J., 2009. Biogenic iron oxyhydroxide formation at mid-ocean ridge hydrothermal vents: Juan de Fuca Ridge. Geochim. Cosmochim. Acta 73(2): 388-403.
Viollier, E., Inglett, P. W., Hunter, K., Roychoudhury, A. N. and Van Cappellen, P., 2000. The ferrozine method revisited: Fe(II)/Fe(III) determination in natural waters. Applied Geochemistry 15(6): 785-790.
Vollrath, S., Behrends, T., Koch, C. B. and Van Cappellen, P., 2013. Effects of temperature on rates and mineral products of microbial Fe (II) oxidation by Leptothrix cholodnii at microaerobic conditions. Geochim. Cosmochim. Acta 108: 107-124.
Wagai, R. and Mayer, L. M., 2007. Sorptive stabilization of organic matter in soils by hydrous iron oxides. Geochim. Cosmochim. Acta 71(1): 25-35.
Wang, Q., Wang, J., Wang, X., Kumar, N., Pan, Z., Peiffer, S. and Wang, Z., 2023. Transformations of ferrihydrite–extracellular polymeric substance coprecipitates driven by dissolved sulfide: interrelated effects of carbon and sulfur loadings. Environ. Sci. Technol. 57(10): 4342-4353.
Weihe, S. H., Mangayayam, M., Sand, K. K. and Tobler, D. J., 2019. Hematite crystallization in the presence of organic matter: impact on crystal properties and bacterial dissolution. ACS Earth Space Chem. 3(4): 510-518.
Wen, S., Lu, Y., Dai, J., Huang, X., An, S., Liu, J., Liu, Z., Du, Y. and Zhang, Y., 2023. Stability of organic matter-iron-phosphate associations during abiotic reduction of iron. J. Hazard. Mater. 449: 131016.

Xue, Q., Ran, Y., Tan, Y., Peacock, C. L. and Du, H., 2019. Arsenite and arsenate binding to ferrihydrite organo-mineral coprecipitate: Implications for arsenic mobility and fate in natural environments. Chemosphere 224: 103-110.

Zachara, J. M., Fredrickson, J. K., Li, S.-M., Kennedy, D. W., Smith, S. C. and Gassman, P. L., 1998. Bacterial reduction of crystalline Fe3+ oxides in single phase suspensions and subsurface materials. American Mineralogist 83(11): 1426-1443.

Zachara, J. M., Kukkadapu, R. K., Fredrickson, J. K., Gorby, Y. A. and Smith, S. C., 2002. Biomineralization of poorly crystalline Fe (III) oxides by dissimilatory metal reducing bacteria (DMRB). Geomicrobiol. J. 19(2): 179-207.

Zeng, Q., Huang, L., Ma, J., Zhu, Z., He, C., Shi, Q., Liu, W., Wang, X., Xia, Q. and Dong, H., 2020. Bio-reduction of ferrihydrite-montmorillonite-organic matter complexes: Effect of montmorillonite and fate of organic matter. Geochim. Cosmochim. Acta 276: 327-344.

Zhao, Q., Adhikari, D., Huang, R., Patel, A., Wang, X., Tang, Y., Obrist, D., Roden, E. E. and Yang, Y., 2017. Coupled dynamics of iron and iron-bound organic carbon in forest soils during anaerobic reduction. Chem. Geol. 464: 118-126.

Zhao, Q., Poulson, S. R., Obrist, D., Sumaila, S., Dynes, J. J., McBeth, J. M. and Yang, Y., 2016. Iron-bound organic carbon in forest soils: quantification and characterization. Biogeosciences 13(16): 4777-4788.

Zhao, Y., Moore, O. W., Xiao, K.-Q., Curti, L., Fariña, A. O., Banwart, S. A. and Peacock, C. L., 2022. The role and fate of organic carbon during aging of ferrihydrite. Geochim. Cosmochim. Acta 335: 339-355.

Supplementary Material For

Physicochemical properties and bioavailability of synthetic coprecipitates of Fe (oxy)hydroxides and Na-alginate

Tarek Najem[a] and Danielle Fortin[a*]

[a] Department of Earth and Environmental Sciences, University of Ottawa, 75 Laurier Ave. East,

K1N5N6, Ottawa, Ontario, Canada

*Corresponding Author:
Email address: dfortin@uottawa.ca

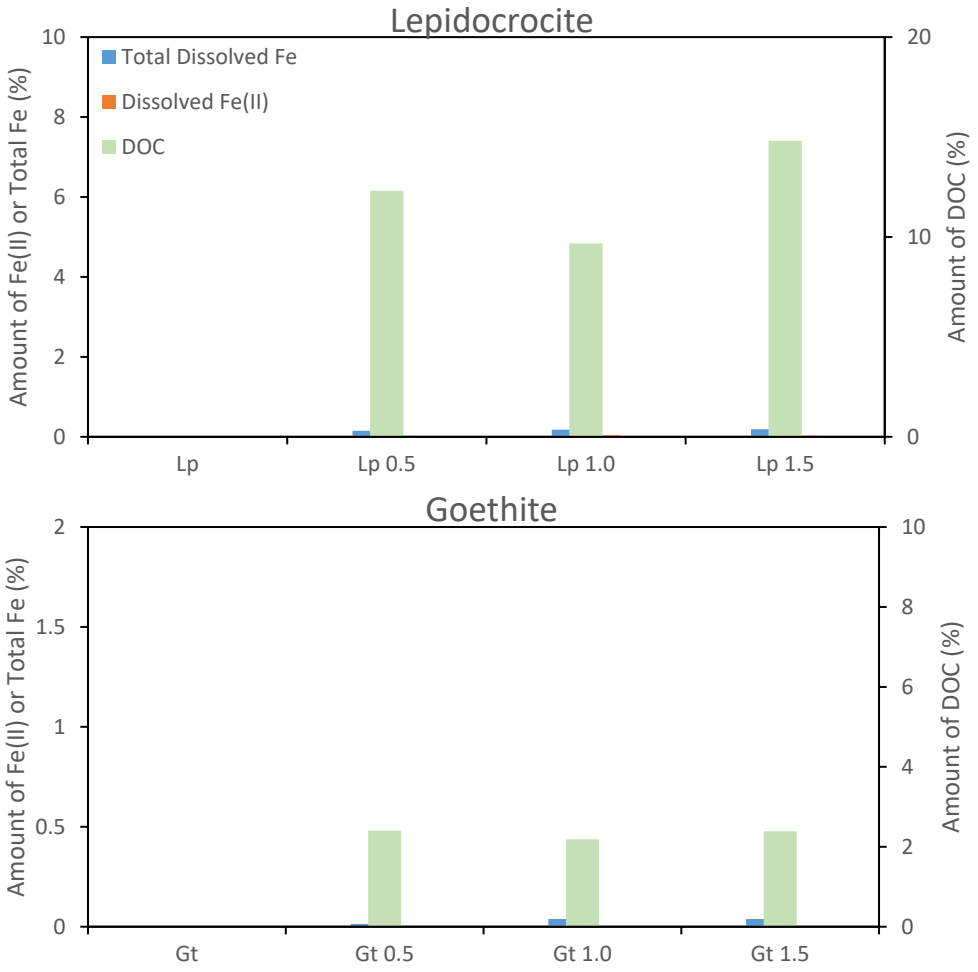

Figure S1: Amount of dissolved Fe(II), total Fe, and organic carbon (DOC) measured in the filtered (0.22 µm) aqueous supernatants collected following the centrifugation of the iron oxyhydroxides. The amounts are reported relative to the total initial amount in the jars. The data represents the mean ± standard deviation of two measurements from each supernatant collected. Note the scale for the Gt (goethite) precipitates.

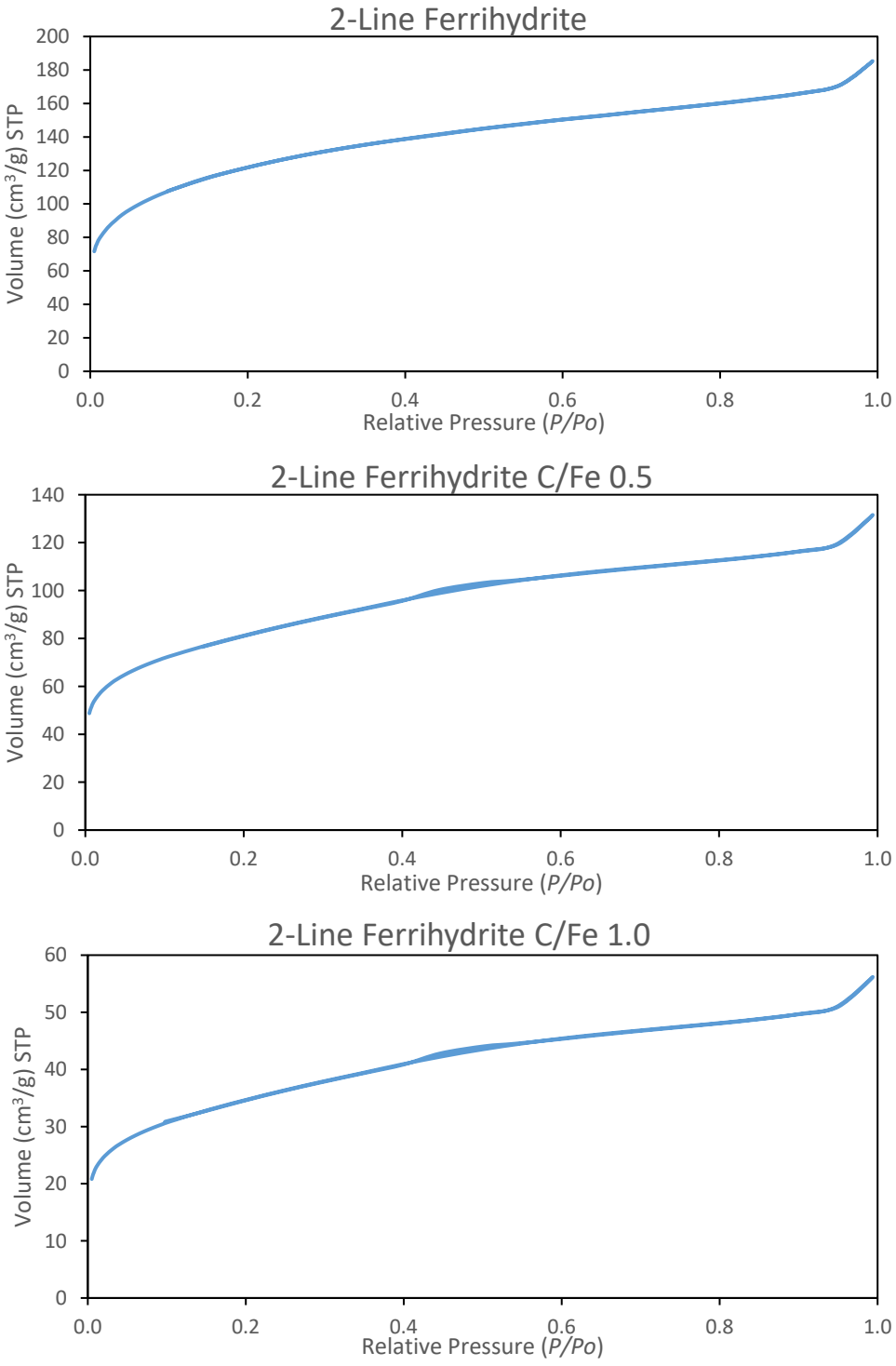

Figure S2: N_2-adsorption-desorption isotherms of the various 2-line ferrihydrite-alginate coprecipitates (C/Fe 0, 0.5, and 1.0 mol:mol). Data points represent the average of two measurements. Note the difference in the Y-axes scales.

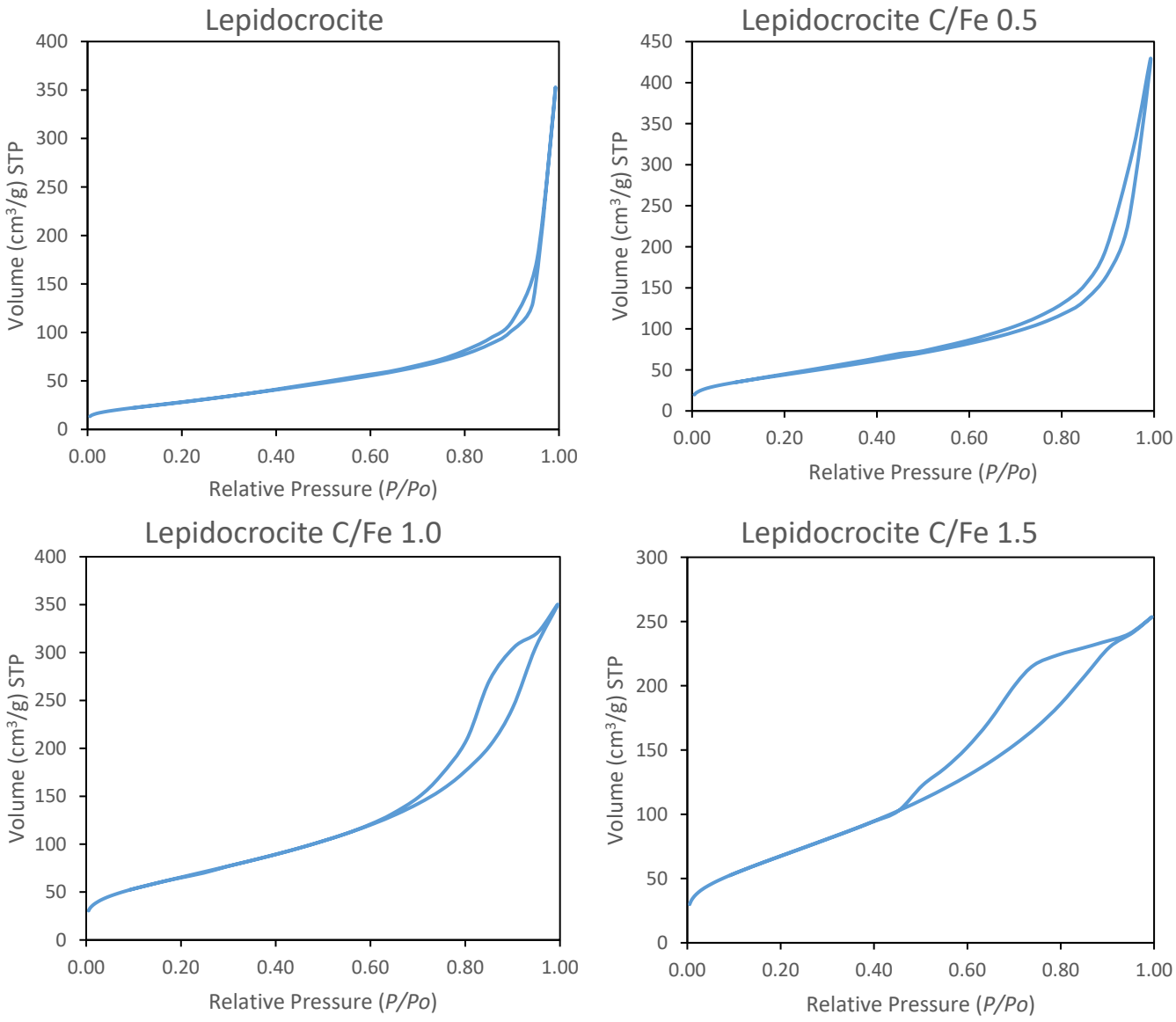

Figure S3: N_2-adsorption-desorption isotherms of the various lepidocrocite-alginate coprecipitates (C/Fe 0, 0.5, 1.0, and 1.5 mol:mol). Data points represent the average of two measurements. Note the difference in the Y-axes scales.

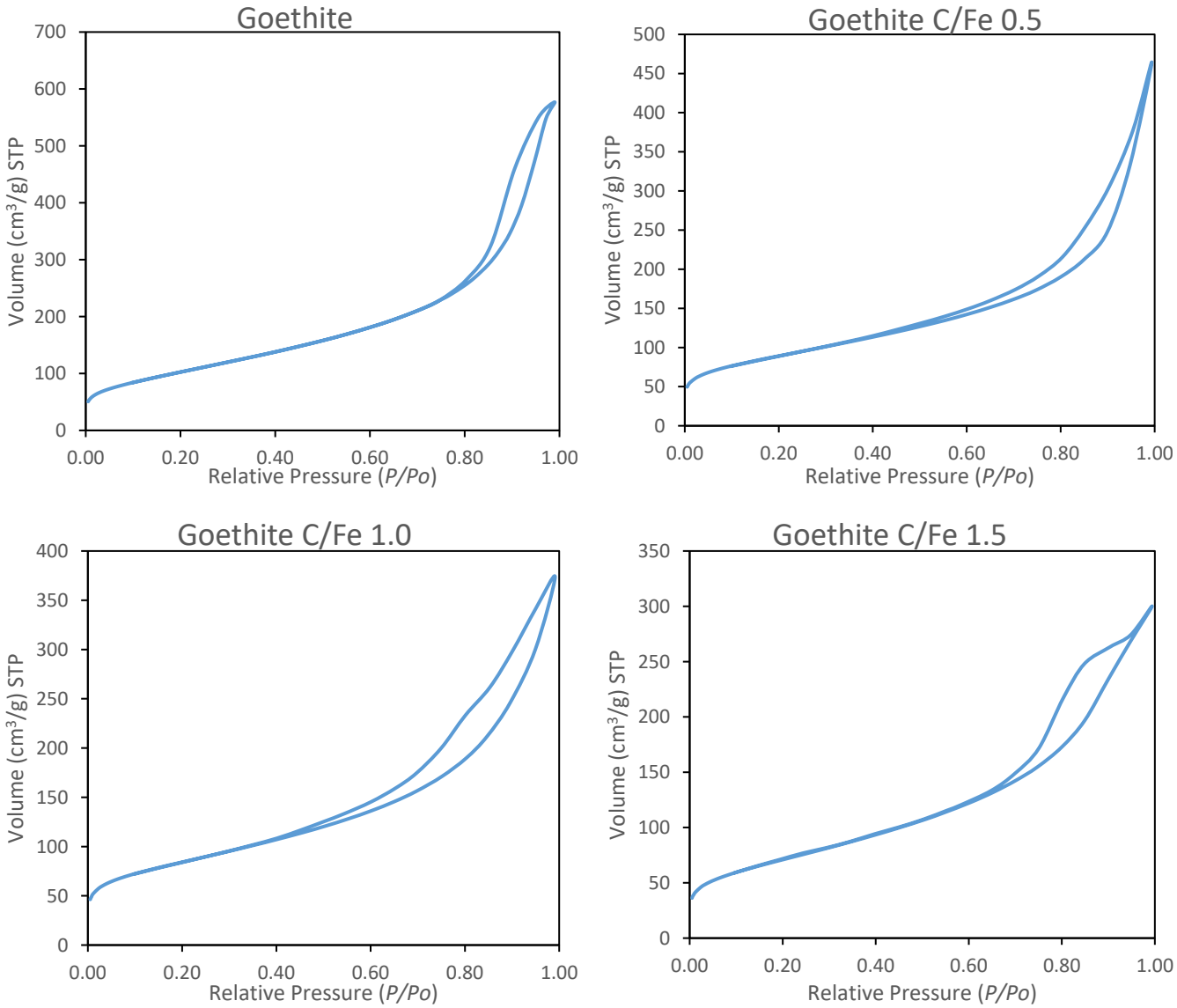

Figure S4: N_2-adsorption-desorption isotherms of the various goethite-alginate coprecipitates (C/Fe 0, 0.5, 1.0, and 1.5 mol:mol). Data points represent the average of two measurements. Note the difference in the Y-axes scales.

Table S1: IR band assignments for pure Na-alginate. Italicized wavenumber values correspond to bands obtained from the Savitsky-Golay secondary derivative with 19 points of smoothing.

Wavenumbers (cm^{-1})	**Assignment**
3226	ν(O-H)
2919	ν(C-H)
1596	ν_{asym}(C-O-O) carboxylate
1408, 1405	ν_{sym}(C-O-O) carboxylate
1298	δ(C-H)
1175	ν_{sym}(C-O) of glycosidic linkage
1130	ν(C-O) of pyranose ring
	ν(C-C) of pyranose ring
	δ(C-C-C) of pyranose ring
1087, 1080	ν(C-O-C) of pyranose ring
	ν(C-C) of pyranose ring
	ν_{asym}(C-O-C) of glycosidic linkage
1028, 1025	Vibrations due to mannuronic and guluronic acid residues:
	ν_{asym}(C-O-C) of glycosidic linkage
	ν(C-O) of pyranose ring
	ν(C-C)
	ν(C-O) of secondary alcohols
998	ν(C-O) of pyranose ring
	ν(C-C) of pyranose ring
	δ(C-C-C) of pyranose ring
952, 950	Vibrations due to mannuronic acid residues:
	ν(C-C)
	δ(C-C-H)
935	ν(C-C) of mannuronic acid residues
883	δ(C1-H) β-mannuronic acid residues
814	Vibrations due to mannuronic acid residues:
	δ(C-O-C) of glycosidic linkage
	δ(C-C-C) of pyranose ring
	δ(O-C-C) of pyranose ring
	δ(C-C-H)
779	α-L-guluronic acid residues
725	Ring breathing

Band identification acquired from: Sartori et al. (1997); Chandıa et al. (2001); Leal et al. (2008); Cardenas-Jiron et al. (2011).

Table S2: IR band assignments for ferrihydrites coprecipitated with and without Na-alginate (C/Fe 0, 0.5, 1.0, and 1.5 mol:mol).

Wavenumbers (cm^{-1})	**Assignment**
3292-3177	ν(O-H)
2919	ν(C-H)
1627	δ(O-H)
1468, 1360	2-line ferrihydrite: ν_{asym}(C-O), ν_{sym}(C-O) adsorbed carbonate
1592-1589	ν_{asym}(C-O-O) carboxylate
1408-1406	ν_{sym}(C-O-O) carboxylate
1298	δ(C-H)
1175	ν_{sym}(C-O) of glycosidic linkage
1080	ν(C-O-C) of pyranose ring
	ν(C-C) of pyranose ring
1033	Vibrations due to mannuronic and guluronic acid residues:
	ν_{asym}(C-O-C) of glycosidic linkage
	ν(C-O) of pyranose ring
	ν(C-C)
	ν(C-O) of secondary alcohols
883	δ(C1-H) β-mannuronic acid residues
814	Vibrations due to mannuronic acid residues:
	δ(C-O-C) of glycosidic linkage
	δ(C-C-C) of pyranose ring
	δ(O-C-C) of pyranose ring
	δ(C-C-H)
565	2-line ferrihydrite: ν(Fe-O)

Table S3: IR band assignments for lepidocrocite coprecipitated with and without Na-alginate (C/Fe 0, 0.5, 1.0, and 1.5 mol:mol).

Wavenumbers (cm^{-1})	**Assignment**
3450	ν(O-H) of adsorbed H_2O
3172-3015	ν(O-H) structural
2919	ν(C-H)
1630	δ(O-H) of adsorbed H_2O
1607-1600	ν_{asym}(C-O-O) carboxylate
1411-1409	ν_{sym}(C-O-O) carboxylate
1298	δ(C-H)
1175	ν_{sym}(C-O) of glycosidic linkage
1080	ν(C-O-C) of pyranose ring
	ν(C-C) of pyranose ring
1155	Lepidocrocite: In-plane δ(O-H)
1020-1024	Lepidocrocite: In-plane δ(O-H)
	Vibrations due to mannuronic and guluronic acid residues:
	ν_{asym}(C-O-C) of glycosidic linkage
	ν(C-O) of pyranose ring
	ν(C-C)
883-877	δ(C1-H) β-mannuronic acid residues
	Goethite (possible): δ(O-H) in plane
793	Goethite (possible): γ(O-H) out of plane
753-741	Lepidocrocite: γ(O-H) out of plane
597-590	Lepidocrocite: τ(O) out of plane (twisting)

Table S4: IR band assignments goethite coprecipitated with and without Na-alginate (C/Fe 0, 0.5, 1.0, and 1.5 mol:mol).

Wavenumbers (cm^{-1})	**Assignment**
3450	ν(O-H) of adsorbed H_2O
3185-3166	ν(O-H) structural
1640	δ(O-H) of adsorbed H_2O
1507, 1321	ν_{asym}(C-O), ν_{sym}(C-O) bound carbonate
1600	ν_{asym}(C-O-O) carboxylate
1411-1410	ν_{sym}(C-O-O) carboxylate
1298	δ(C-H)
1175	ν_{sym}(C-O) of glycosidic linkage
1080	ν(C-O-C) of pyranose ring
	ν(C-C) of pyranose ring
1033	Vibrations due to mannuronic and guluronic acid residues:
	ν_{asym}(C-O-C) of glycosidic linkage
	ν(C-O) of pyranose ring
	ν(C-C)
	ν(C-O) of secondary alcohols
888-877	Goethite: In-plane δ(O-H)
793-791	Goethite: Out-of-plane γ (O-H)
609-604	Goethite: ν_{sym}(Fe-O)

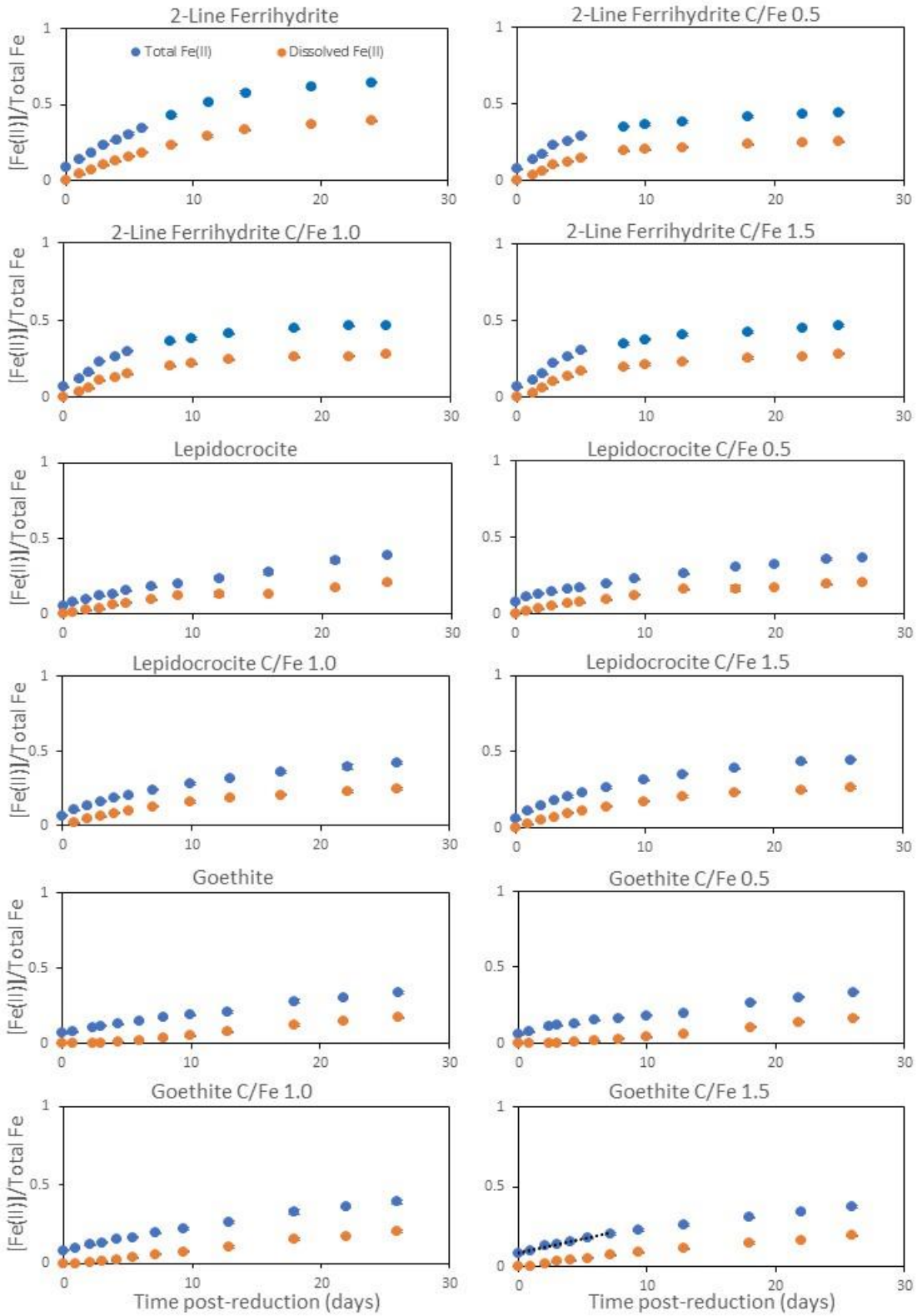

Figure S5: Changes in total and dissolved Fe(II) relative to total Fe during anaerobic Fe reduction by *S. putrefaciens* CN32. Data markers represent mean ± standard deviation derived from three experimental replicates of each system.

References

Cardenas-Jiron, G., Leal, D., Matsuhiro, B. and Osorio-Roman, I. O., 2011. Vibrational spectroscopy and density functional theory calculations of poly-D-mannuronate and heteropolymeric fractions from sodium alginate. J. Raman Spectrosc. 42(4): 870-878.

Chandıa, N., Matsuhiro, B. and Vásquez, A., 2001. Alginic acids in Lessonia trabeculata: characterization by formic acid hydrolysis and FT-IR spectroscopy. Carbohydr. Polym. 46(1): 81-87.

Leal, D., Matsuhiro, B., Rossi, M. and Caruso, F., 2008. FT-IR spectra of alginic acid block fractions in three species of brown seaweeds. Carbohydr Res 343(2): 308-316.

Sartori, C., Finch, D. S., Ralph, B. and Gilding, K., 1997. Determination of the cation content of alginate thin films by FTIR spectroscopy. Polymer 38(1): 43-51.

Chapter 3: Stability of P-OM-ferrihydrite composites: Fe(III) dissolution kinetics and fate of phosphate under abiotic and biotic conditions

Tarek Najem[a] and Danielle Fortin[a*]

[a] Department of Earth and Environmental Sciences, University of Ottawa, Ottawa, Ontario, Canada

* Corresponding author: dfortin@uottawa.ca

Submitted to Chemical Geology

Abstract

Naturally occurring iron (Fe) (oxyhydr)oxides are often associated with impurities such as phosphate (P) and organic matter (OM) that can considerably influence their reactivity towards abiotically and biotically mediated Fe(III) reductive and non-reductive dissolution. Therefore, the stability of these composites (P-OM-Fe) has an important impact on the migration and sequestration of C and P in the environment. Here, we examined the influence of Na-alginate, an analogue to microbial polysaccharides, and P on the physicochemical properties and reactivity of 2-line ferrihydrite (Fh). Synthetic Fhs with pre-adsorbed or coprecipitated P (P/Fe 0, 0.01, and 0.1 mol:mol) were prepared by base titration of Fe(III) solutions in the absence or presence of Na-alginate (C/Fe 0, and 1 mol:mol) at concentrations of environmental relevance. The minerals were characterized by conventional analytical techniques (XRD, ATR-FTIR, BET, and ζ-potential), whereas their reactivity was assessed under abiotic (excess bicarbonate-citrate-ascorbic acid solution at pH 8.0) and biotic (*Shewanella putrefaciens* CN32) conditions. At the highest loading, P and alginate coprecipitation had only a "subtle" impact on the mineral structure of Fh, whereas the simultaneous coprecipitation with both P and alginate may have additively affected the mineral structure of Fh. Despite these subtle effects, Fhs coprecipitated with P showed greater reactivity towards abiotic and biotic reductive dissolution compared to those with pre-adsorbed P, especially at the highest loading (P/Fe 0.1 mol:mol). Fhs coprecipitated with alginate were also generally more reactive in both abiotic and biotic reductive dissolution than alginate-free Fhs, with the P-alginate-Fh composite exhibiting the highest reactivity overall. Both P, even at a molar ratio of 0.01 P/Fe, and alginate influenced the extent of biotic Fe reduction, and consequently the composition and proportion of the biogenic secondary Fe minerals that formed. Moreover, regardless of the sorption mode, P, at the highest loading, nearly-completely stabilized Fh against

transformation into crystalline phases, more-so than alginate alone. However, P and alginate cooperatively stabilized Fh against transformation following the biotic reduction of P-alginate-Fh coprecipitates. In sum, this research emphasizes the importance of considering both P and OM, and the sorption mode of P when evaluating the environmental behavior and lifespan of Fe (oxyhydr)oxides, which has implications for soil fertility, water quality, and contaminant remediation.

Keywords

Na-Alginate, Organic matter, Adsorption, Coprecipitation, Ferrihydrite, Phosphate, Bioavailability, *Shewanella putrefaciens*

1. Introduction

Phosphorus is an essential nutrient that limits growth in the environment. In agricultural settings, high crop yields and food production are achieved through the use of phosphate-rich fertilizers. The release of phosphate from agricultural soils into the environment is a major contributor to eutrophication and the degradation of aquatic ecosystems (Smith et al., 1999; Conley et al., 2009). However, the association of inorganic phosphate (P) through interactions with mineral phases significantly impacts its fate and, consequently, its chemical and biological cycling in the environment (Fortin et al., 1993; Zeng et al., 2004; Baken et al., 2015; Baken et al., 2016; Chen et al., 2018; van der Grift et al., 2018). In particular, the widespread nature of iron (Fe) (oxyhydr)oxides possessing an abundance of reactive sites limit the release and mobility of P in the environment through adsorption and coprecipitation reactions (Mayer and Jarrell, 1995; Gunnars et al., 2002; Cornell and Schwertmann, 2003; Hyacinthe and Van Cappellen, 2004; Khare

et al., 2007; Kaegi et al., 2010; Voegelin et al., 2010; Voegelin et al., 2013). Consequently, the fate of P is intertwined with the redox cycling of Fe.

The sorption of P leads to concentration dependent alteration of the physicochemical properties of the oxide, including surface charge, specific surface area (SSA), and colloidal/aggregation stability in solution (Kaegi et al., 2010; Voegelin et al., 2010; Voegelin et al., 2013; Santoro et al., 2019). Moreover, the sorption mode of P differently impacts the structure, composition, and stability of Fe (oxyhydr)oxides. For instance, coprecipitation differs from adsorption in that foreign moieties interfere with the polymerization of Fe(III) octahedra by occupying crystal growth sites (Rose et al., 1997; Kaegi et al., 2010; Voegelin et al., 2010; Châtellier et al., 2013; Voegelin et al., 2013; Kleber et al., 2015; Kraal et al., 2019). By means of EXAFS, it was proposed that the presence of P disrupts Fe-Fe bond formation through bridging Fe single corner sharing or PO_4-Fe linkages of pre-existing units (Rose et al., 1997; Voegelin et al., 2010; Voegelin et al., 2013; Senn et al., 2015; van der Grift et al., 2016). In aqueous near-neutral pH solutions with various concentrations of P (initial molar P/Fe ratio of up to 2) in the presence of Ca and/or Si, the structure of Fe(III)-precipitates formed by the oxidation of Fe(II) was rationalized in terms of mixtures of three main endmembers, including poorly-crystalline lepidocrocite, Si-containing ferrihydrite, and amorphous Fe(III)-P (Kaegi et al., 2010; Voegelin et al., 2010; Voegelin et al., 2013; Senn et al., 2015; Voegelin et al., 2019). The proportion of each endmember largely depended on the concentration of the surrounding constituents (Voegelin et al., 2013; Senn et al., 2015; Voegelin et al., 2019). Under similar conditions, goethite formation was inhibited during the oxidation of Fe(II) in the presence of P even at a molar P/Fe ratio of 0.02 (Châtellier et al., 2013). The addition of P or Si (0 – 2 mol% relative to Fe) to initial solutions of Fe(III) reduced the particle size and inhibited particle growth of α-FeOOH and β-FeOOH, and led

to increased SSA (Kandori et al., 1992). The extent of impact was dependent on the anion type and concentration together with synthesis conditions. In addition to modulating the pathway and the resulting Fe endmembers, sorbed P also alters the transformation pathway of the thermodynamically unstable mineral, 2-line ferrihydrite (Fh), when exposed to elevated temperature, pH, or Fe(II), which in turn affect the stability and fate of associated P (Paige et al., 1997; Gálvez et al., 1999; Cornell and Schwertmann, 2003; Kraal et al., 2022; Namayandeh et al., 2023; Chi et al., 2024; Namayandeh et al., 2024).

A consequence of these differing impacts on the structure and mineralogy of Fe (oxyhydr)oxides is that the sorption mode of P also differently affects their reactivity towards dissolution mediated reductively by Fe-reducing bacteria (FeRB), or chemically (e.g. low molecular weight organic molecules, sulfur, etc…) (Fredrickson et al., 1998; Glasauer et al., 2003; Borch et al., 2007; Kraal et al., 2019; Kraal et al., 2022; Ahmed et al., 2024). In batch studies, the addition of P promoted microbial Fe(III) reduction by functioning as a nutrient thereby stimulating the growth and activity of FeRB (Fredrickson et al., 1998; Glasauer et al., 2003; Kukkadapu et al., 2004). In contrast, an inhibitory effect on the microbial redution of Fe was observed in studies where P was added as a nutrient or pre-adsorbed on the oxide surface (Borch et al., 2007; O'Loughlin et al., 2010; Amstaetter et al., 2012; Schoepfer et al., 2017). Relative to pure Fh and coprecipitates, at equivalent P loading (P/Fe 0.05 and P/Fe 0.09 mol:mol), pre-adsorption of P was reported to hinder the dissolution kinetics and release of Fe by 0.01 M HCl and ~0.1 M ascorbate (Kraal et al., 2019). Within the same study, it was reported that coprecipitates of Fh-P exhibited the highest dissolution rates (Kraal et al., 2019). Similarly, O'Loughlin et al. (2013) found that the rate of chemical dissolution of P-lepidocrocite coprecipitates (0.007 – 0.1 P/Fe mol:mol) by 1 M HCl or 0.01 M ascorbate increased with increasing P content, relative to that of P-free

lepidocrocite. Yet, within the same study, the presence of P reduced the rate of Fe(III) reduction by *Shewanella putrefaciens* CN32, but enhanced the extent of Fe(III) reduction relative to that of P-free lepidocrocite. In contrast, a P-Fh coprecipitate (P/Fe 0.1 mol:mol) produced from a Fe(III) solution was reduced at a slower rate by Na-dithionite relative to pure Fh and Fh with pre-adsorbed P (P/Fe 0.07 mol:mol) (Wen et al., 2023). While these studies provided important insights into the impact of the sorption mode of P on the reactivity of different Fe (oxyhydr)oxides, no studies have investigated the effects of coprecipitation of P on the bioavailability of Fh. Moreover, past studies have mainly focused on the impact of P as a single entity on the physicochemical properties and bioavailability of Fe (oxyhydr)oxides, whereas very few studies considered the effects of additional entities such as organic matter (OM) (Wen et al., 2023).

Like P, OM interact with Fe (oxyhydr)oxides through adsorption and coprecipitation reactions, processes that occur in the environment (Kaiser et al., 1997; Kaiser, 2003; Fortin and Langley, 2005; Schwertmann et al., 2005; Wagai and Mayer, 2007; Mikutta et al., 2008; Gault et al., 2011; Mikutta et al., 2014; Kleber et al., 2015; Zhao et al., 2017; Curti et al., 2021; Possinger et al., 2021; Li et al., 2023). OM, such as humic and fulvic acids, as well as polysaccharides produced by bacteria or plants, also compete with P for similar reactive sites during adsorption to- or coprecipitation with- Fe (oxyhydr)oxides, affecting their immobilization, bioavailability, as well as the compositional fractionation of OM between the aqueous and solid phase (Li et al., 2021; Luo et al., 2021; Wen et al., 2022; Ahmed et al., 2024). Nonetheless, the association of OM with Fe (oxyhydr)oxides leads to the modification of the physicochemical and mineralogical properties of these minerals (Cornell and Schwertmann, 2003; Schwertmann et al., 2005; Eusterhues et al., 2008; Mikutta and Kretzschmar, 2008; Mikutta et al., 2008; Langley et al., 2009b; Langley et al., 2009d; Chen et al., 2014; Mikutta et al., 2014; Kleber et al., 2015).

Consequently, such associations have been a subject of intense research to determine their role in the environment towards contaminant, nutrient, and trace metal mobility (Grybos et al., 2007; Mikutta et al., 2014; Fabisch et al., 2016; Hao et al., 2016; Sowers et al., 2017; Chen et al., 2018; Field et al., 2019; Xue et al., 2019; Dong et al., 2022), C storage (Lalonde et al., 2012; Han et al., 2019; Patzner et al., 2022; Martens et al., 2023), long term stability (Kaiser et al., 2007; Cismasu et al., 2016; Najem et al., 2016; Zhao et al., 2022c), and susceptibility/bioavailability to microbial degradation (Langley et al., 2009b; Pedrot et al., 2011; Amstaetter et al., 2012; Shimizu et al., 2013; Eusterhues et al., 2014a; Adhikari et al., 2016; Poggenburg et al., 2016; Adhikari et al., 2017; Cooper et al., 2017; Zhao et al., 2017; Mejia et al., 2018; Poggenburg et al., 2018; Han et al., 2019; Zeng et al., 2020; Dong et al., 2023). For example, Fhs with pre-adsorbed OM (C/Fe 0.03 – 0.05 mol:mol) and P (P/Fe 0.07 mol:mol) were reduced at ~2x slower rate by Na-dithionite than that of Fhs with pre-adsorbed OM (C/Fe 0.08 mol:mol) (Wen et al., 2023). However, under the same conditions, coprecipitates of P-OM-Fh (C/Fe 2 mol:mol, P/Fe 0.1 mol:mol) exhibited a slightly lower reduction rate than their corresponding P-free OM-Fh coprecipitates (Wen et al., 2023). More recently, the presence of both OM and P in OM-P-Fh associations were demonstrated to cooperatively inhibit Fe(II) derived transformation of Fh into crystalline products, an effect that was determined to be more substantial than the individual inhibitory effects of P and OM (Chi et al., 2024). Clearly, P-OM-Fe coprecipitates are characterized by distinct reactivity and stability, yet there is a lack of research in determining their bioavailability to FeRB making it challenging to assess OM and P burial efficiency at the water-sediment interface.

In this study, our objectives were to investigate the cooperative impact of P and OM on the physicochemical properties, abiotic dissolution mediated through reduction (ascorbic acid), and bioavailability (*Shewanella putrefaciens* CN32) of Fh. Fh, a poorly crystalline Fe (oxyhydr)oxide

with a large surface area and positive charge, was chosen because it is widely distributed in the environment including biogenic iron oxides (BIOS) (Fortin et al., 1993; Cornell and Schwertmann, 2003; Gault et al., 2011). The concentrations of P (0.01 and 0.1 P/Fe mol:mol) and OM (C/Fe 1 mol:mol) chosen for this study correspond to those encountered in the environment (Fortin et al., 1993; Chen et al., 2014; Baken et al., 2015; Zhao et al., 2016; van der Grift et al., 2018). Moreover, alginate was chosen as the organic compound due to its chemical resemblance to algae derived OM and to the twisted stalks and sheaths produced by the Fe(II)-oxidizing bacteria *Gallionella* spp. and *Leptothrix* spp., respectively, that contribute to the formation of BIOS (Chan et al., 2004; Chan et al., 2009; Wen et al., 2023). Polysaccharides are also important components of plant root exudates, contributing up to ~10% of the total organic matter pool in soils and sediments (Kleber et al., 2015). Finally, this research aims to provide new insights into the reactivity and stability of P-OM-Fh, as well as the release of P in soils and groundwater, which contribute to the better understanding of biogeochemical processes in subsurface systems.

2. Materials and methods

All necessary glassware and components were initially submerged in 10% HNO_3 bath for a minimum duration of 24 h and then again submerged in 6 M H_2SO_4 for 24 h to remove any residual phosphate (Murphy and Riley, 1962). Subsequently, the glassware was washed 3x with ultrapure water (UPW) (18 MΩ•cm) and then baked in a muffle-furnace at 450 ºC for a duration of 8 h to remove any residual organic matter. Prior to use, the necessary glassware and components were sterilized by autoclaving. For the sterilization of Na-alginate, the dry powder was spread on the base of a beaker and then irradiated with an ultraviolet light (UV-C) source for a period of 1 h. FTIR-ATR of the irradiated alginate powder did not show any significant structural changes relative to the native alginate (data not shown).

2.1. Synthesis of alginate-2-line ferrihydrite composites

2-line ferrihydrite (Fh) was synthesized in the absence or presence of Na-alginate at C/Fe molar ratios of 0 and 1.0 according to published methodologies (Glasauer et al., 2003; Mikutta et al., 2008; Schwertmann and Cornell, 2008; Langley et al., 2009b). Briefly, the Fhs were synthesized under aseptic conditions by the rapid neutralization of a $FeCl_3$ solution ($FeCl_3 \cdot 6H_2O$, 40 mmole) in a glass beaker to a steady final pH of 7.0 using 1 M NaOH as the base (Glasauer et al., 2003; Langley et al., 2009b). The preparation of the base was carried out in sterile Nalgene bottles to minimize the contribution of Si to the systems.

Synthesis of OM-Fh composite was carried out by initially dissolving an appropriate amount of Na-alginate in UPW in 1 L glass beaker using a magnetic stirrer for a period of 24 h in the dark. Prior to synthesis, the pH of the alginate-solution was adjusted to 2.5 using 6 M trace-metal-grade HCl at which point the solution was rapidly mixed with a concentrated $FeCl_3$ solution to reach a final C/Fe molar ratio of 1.0. Fe(III) hydrolysis and neutralization proceeded as described for pure Fh.

Washing of the synthesized minerals proceeded via suspension in sterile UPW, followed by repeated centrifugation (2500 rpm) and vortexing until the electrical conductivity of the supernatants were reduced to ~25 μS/cm. Prior to use, the mineral slurries were stored up to 1 week at 4 ºC in the dark. Table S1 in the Supplementary Materials provides an overview of all the Fh samples used in this study.

2.2. Synthesis of P-alginate-2-line ferrihydrite composites

Fh and OM-Fh coprecipitates with adsorbed P were prepared by the addition of P to suspensions of Fh and OM-Fh. Separate adsorption experiments were initially conducted to

determine the maximum adsorption capacity of the slurries, and to determine whether or not a composite of P-OM-Fh with P/Fe molar ratio of 0.1 can be produced. For the preparation of the mineral composites with adsorbed P, washed slurries of Fh or OM-Fh were initially re-suspended into a sterile solution of 0.01 M NaCl in a glass beaker and their pH was adjusted to 6.8. Subsequently, a sterile solution of 0.01 M NaCl containing appropriate concentrations of $Na_2HPO_4 \cdot 7H_2O$ were slowly added to the Fh or OM-Fh slurries whilst vigorously mixing to reach final P/Fe molar ratios of 0.01 and 0.1. Throughout this process, the pH was monitored using a sterile pH probe and adjusted manually to ~6.8 using small amounts of 0.5 M HCl or 1 M NaOH. The suspensions were then allowed to mix for a total period of 48 h at 400 rpm on a magnetic stirrer in the dark, and their pH was periodically re-adjusted to ~6.8 at 1, 2, 6, 24, and 48 h. The resulting slurries were decanted, washed, and stored as described above for the Fh and OM-Fh coprecipitates. It should be noted that these slurries were used for experiments within 2 days following preparation.

Synthesis of pure Fh or OM-Fh with coprecipitated P proceeded in similar fashion as described above for the pure Fh and OM-Fh coprecipitates, with the exception of using 1 M NaOH solutions containing appropriate concentrations of P. The latter solutions were initially prepared with pre-determined amounts of $Na_2HPO_4 \cdot 7H_2O$ to yield target coprecipitates with P/Fe ratios of 0.01 or 0.1. Subsequently, the slurries were washed as described above and stored for up to 1 week at 4 ºC prior to use in experiments.

2.3. Characterization of the 2-line ferrihydrite precipitates

2.3.1. Chemical composition: Fe, C, and P content

The pseudo-total iron and P content of dry powdered or wet samples was determined by suspending a known amount into 6 mL of UPW, and fully digested by the addition of 4 mL trace

metal grade 30% H_2O_2 and 2 mL trace metal grade HNO_3 followed by heating at 75 °C for 24 h. After dilution with 1% HNO_3 (v/v), the Fe and P contents were determined via inductively coupled plasma ─ optical emission spectroscopy using a Varian Vista-PRO CCD Simultaneous ICP-OES, operating under standard conditions. All digestions were carried out in duplicates (powdered samples) or triplicates (wet samples). For the determination of C content of the P-OM-Fh composites, approximately 10 mg of a dry powdered sample was weighed into a tin capsule. The prepared samples were then analysed at the University of Ottawa at the Jan Veizer Stable Isotope Laboratory using the Elementar Vario Isotope Cube. P that is associated with the surface of the oxide (adsorbed) was determined using 0.1 M NaOH (P_{NaOH}) in duplicates. Briefly, a known amount of wet slurry into 10 mL of the base followed by mixing on an end-to-end tube rotator at 5 rpm for 16 h. The concentration of P_{NaOH} was determined spectrophotometrically using the molybdenum blue method.

2.3.2. Electrophoretic mobility: ζ-potential

The electrophoretic mobility (EM) of the Fhs was measured in a filtered (Sartorius polyethersulfone membrane, 0.22 μm) 0.01 M NaCl solution using a Zetasizer Nano-ZS (Malvern, Instruments) at 25°C. Initially, the Fhs were dispersed by adding a wet sample (equivalent to 2 mM Fe) to 50 mL of background electrolyte and stirred for 1 h in Nalgene bottles. Subsequently, the pH of the suspensions was adjusted with filtered 10 mM NaOH or HCl to ~6.8. The EM measurements were determined from the average of 5 runs comprising of 10 cycles each.

2.3.3. Powder x-ray diffraction, specific surface area, scanning electron microscopy, and attenuated total reflectance Fourier-transform infrared spectroscopy

The bulk mineralogy of the Fhs was determined by x-ray diffraction (XRD). Air-dried samples were thoroughly ground to fine powders with an agate mortar and pestle and analysed

with a Rigaku Ultima IV diffractometer using a Cu-Kα X-ray source, operating at 45 kV and 40 mA. Continuous scans were run from 10-80° 2Θ using a step size of 0.02° at a rate of 0.7°/min. Specific surface area (SSA) measurements on duplicate samples prepared in the same manner as XRD were carried out using a Micromeritics® *TriStar II Plus and analysed with MicroActive for TriStar II Plus 2.03.* Approximately, 0.3-0.5 g of a sample was initially degassed under vacuum at 50 °C for 24 h. After the determination of degassing stability and final dry mass, 48 N_2 adsorption and 26 desorption points were recorded at 77 K in the partial pressure region ~$1.4x10^{-4}$ - 0.99 P/P_0. The SSA was determined by applying the criteria established by Rouquerol et al. (2007). The micropore volume was determined by applying the Dubinin-Radushkevich (DR) method to adsorption points below 0.01 P/P_0, whereas the mesopore volume (2-50 nm) was determined by applying the Barrett-Joyner-Halenda (BJH) method as determined by the accompanying software (Mikutta et al., 2008; Poggenburg et al., 2016). Total pore volume was determined from the last point of the N_2 adsorption isotherm (0.99 P/P_0). Lastly, the mineral SSA and pore volumes were corrected for the weight of retained alginate content as described in Mikutta et al. (2008).

Powdered samples were analysed with a scanning electron microscope (SEM) to observe the morphology and elemental distribution characteristics of the P-containing minerals. SEM and EDS quantification were acquired using a JEOL JSM-6610LV microscope at the University of Ottawa with energy dispersive X-ray spectroscopy operating under high vacuum at 10-15 kV. EDS analyses with area mapping technique was completed using the accompanying EDAX APEX software. Prior to analyses, samples were prepared by placing a thin layer of dry powder on a carbon tape attached to a sample holder and then carbon coated.

Powdered samples were also analysed with Fourier Transform Infrared Spectroscopy (FTIR) using the Agilent Cary 670 equipped with a diamond crystal coated with ZnSe in attenuated

total reflectance (ATR) mode. For each sample, spectra were acquired from 4000 to 500 cm^{-1} at 2 cm^{-1} resolution, with 32 scans averaged per spectrum. Subsequently, the spectra were processed using the OMNIC software package (Thermo Fisher Scientific, version 9) where the spectra were averaged, automatically baseline corrected, and normalized to the maximum absorbance value.

2.4. Bioavailability

2.4.1. Microbial Medium and Preparation of Cultures

Microbial Fe(III) reduction experiments were carried out with a well characterized, facultative, dissimilarity Fe(III)-reducing bacterium, *Shewanella putrefaciens* strain CN32 (*S. putrefaciens* CN32). Microcosm reduction experiments were carried out in a chemically defined medium (CDM) (pH ~6.7) composed of 20 mM sodium lactate as the electron donor, 4 mM 1,4-piperazinediethanesulfonic acid (PIPES) buffer, mineral salts solution, and trace metals solution (Zachara et al., 1998; Glasauer et al., 2003; Langley et al., 2009a). For transfer into CDM, *S. putrefaciens* CN32 was initially revived from a glycerol stock solution by streaking onto tryptic soy agar (TSA) plates at room temperature (~22 °C). For inoculation, the bacteria were prepared according to the protocols of Glasauer et al. (2003) and Langley et al. (2009b). Briefly, cells were prepared by aseptically inoculating 50 mL of TSB with a colony of *S. putrefaciens* CN32 from TSA plates, and kept on a stir plate (125 rpm) for 24 h at 22 °C. Subsequently, 0.5 mL of the culture was transferred into 50 mL of 50:50 CDM:TSB mixtures. After 24 h, the passaging procedure was repeated with 95:5 CDM:TSB containing 100 μM phosphate, and continued by transferring into 99:1 CDM:TSB containing 200 μM phosphate for a period of 30 h. The final step involved growing the bacteria in 100% CDM containing 400 μM phosphate for a period of 36 h. The concentration of phosphate was progressively increased to acclimate the bacteria to depleted nutrients and microcosm conditions (Glasauer et al., 2003; Langley et al., 2009b). Following the

acclimation period, the bacteria were harvested by centrifugation at 4000 rpm and the cell pellet was washed 2x with 30 mL of fresh sterile CDM, and then re-suspended into 2 mL of CDM. Finally, the BioRad Protein Assay II dye reagent was used to standardize the concentrated cell suspension in order for the microcosms to contain a cell density of ~10^7 CFU/mL (Glasauer et al., 2003; Langley et al., 2009b).

The experimental setup consisted of 500 mL Pyrex bottles (microcosms) containing 450 mL of sterile phosphate-free CDM amended with 10 mM Fe in the form of Fh. The experiments were conducted in triplicates and controls to which no bacteria were added were included. Prior to inoculation with *S. putrefaciens* CN32, the microcosms were wrapped in aluminium foil in order to avoid potential photochemical reactions and then transferred into an anoxic chamber where inoculation proceeded. Throughout the paper, we refer to the microcosms to which cells were added as "biotic" microcosms, whereas controls to which no bacteria were added are referred to as "control" microcosms.

2.4.2. Sampling and analyses

Sampling of each system was performed immediately following the addition of the cells (time 0) and then periodically at selected time points. Sampling was carried out by vigorously shaking the microcosms to suspend the iron oxides into solution. Immediately, 20 mL of the suspension was poured into a sterile and acid washed 20 mL scintillation vial from which all sub-sampling proceeded to minimize the potential contamination of the microcosms (Langley et al., 2009a). The sub-sampled suspensions were analysed for pH, cell viability, dissolved P, total and dissolved Fe(II), and total Fe. pH was monitored utilizing standard calibrated laboratory meters and probes, whereas cell viability was determined by colony counts on TSA plates (Glasauer et al., 2003; Langley et al., 2009a). Fe(II) associated with the solid phase (total Fe(II)) was

determined by dispensing 1 mL of unfiltered Fe (oxyhydr)oxide suspension into 1 mL of trace metal grade 6 M HCl (final concentration 3 M) and allowed to digest for at least 24 h under anoxic conditions prior to dilution and analysis via the ferrozine assay (Stookey, 1970; Viollier et al., 2000). Dissolved Fe(II) was determined by filtering (0.22 µm, polyethersulfone filter) 6 mL of the suspension into an acid-washed 20 mL scintillation vial, and immediately dispensing 0.5 mL of the filtrate into 4.5 mL of trace metal grade 0.5 M HCl. Digestion proceeded for at least 24 h under anoxic conditions prior to analysis by the ferrozine assay. To determine the concentration of dissolved P, filtrates were analysed using the molybdenum blue method (Murphy and Riley, 1962). To determine total Fe, 2 mL of an unfiltered suspension was digested with 2 mL of trace metal grade 12 M HCl for a period of 24 h. Following dilution, Fe determination proceeded by dispensing 100 µL aliquot of the digest into 900 µL of 0.28 M ClH_4NO in 0.28 M HCl for a duration of 30 min and then determining the concentration of Fe^{2+} using the ferrozine assay.

2.4.3. Biogenic solids

At the end of the experimental period, post-reduction minerals were collected by centrifugation (3000 rpm), washed 3x with anoxic UPW, and dried under anoxic conditions. The powdered precipitates were analysed by XRD as described above, using an air sensitive sample holder in order to prevent the oxidation of potential Fe(II)-bearing minerals. The samples were also analysed using field emission scanning electron microscopy (FE-SEM) using the JEOL 8230 microscope, Nature Museum, Gatineau, Ontario, Canada, to identify crystalline minerals at high resolution. Prior to analyses, the preparation of the samples involved placing a thin layer of powder on carbon tape, followed by coating with a gold-palladium alloy. Elemental maps were generated using the method described in *Section 2.3.3.* to determine the distribution of P and potential P-rich

phases. Finally, the Fe and P content of the dried post-reduction powders were determined as described in *Section 2.3.1.*

2.5. Abiotic dissolution

2.5.1. Ascorbate reductive dissolution

Kinetic reductive dissolution of the Fhs was carried out in duplicates under anoxic conditions using a bicarbonate-citrate-ascorbic acid (BCA) solution at pH ~8.0 (Kostka and Luther, 1994). The BCA solution consisted of 20 g/L ascorbate, 50 g/L sodium bicarbonate, and 50 g/L sodium citrate (Kostka and Luther, 1994). Initially, sodium bicarbonate and sodium citrate were dissolved in anoxic UPW, and then mixed with L-ascorbic acid, at which point the pH was adjusted to ~8.0. Prior to the onset of dissolution, sub-samples of the slurries were suspended in 10 mL of anoxic UPW in Nalgene bottles, and stirred for 10 minutes with Teflon stir bars to homogenously disperse the minerals. Subsequently, 40 mL of the BCA solution was added to the suspension while mixing at ~300 rpm to yield a total Fe concentration of 4 mM. At select time points, sub-samples (3 mL) were filtered (0.22 μm, polyethersulfone filter) directly into acid washed 20 mL scintillation vials. The concentration of dissolved Fe(II) was determined using the ferrozine assay at two time points: 1. immediately after filtering ($Fe(II)_{initial}$), and 2. after allowing the filtrates to sit under anoxic conditions for 24 hours ($Fe(II)_{<0.22\mu m}$). The concentration of dissolved Fe(II) determined from the latter represents dissolved Fe(II) from the reduction of colloids that pass through the filter ($Fe_{<0.22\mu m}$). Thus, the colloidal Fe fraction is determined from the following formula (Kraal et al., 2019):

$$Fe_{colloidal} = Fe(II)_{<0.22\mu m} - Fe(II)_{initial}$$

The concentration of dissolved P was spectrophotometrically determined using the molybdenum blue method as previously described. Although the colour development and stability for this method is usually achieved within 10 minutes, the high concentration of citrate from the BCA solution interfered with this reaction process (Yuan and Lavkulich, 1995). Consequently, following testing using standard solutions, appropriate dilutions were carried out in order to reach a stable colour development to correctly determine the concentration of P. However, colour stability was achieved after 40 minutes of reaction.

The rate of Fe(III) reduction by excess ascorbic acid was obtained using the pseudo-first-order kinetic model, such that the release kinetics of Fe(II) can be modelled according to:

$$q_t = q_e(1 - e^{-kt})$$

Where q_t is the cumulative release ratio at time t, q_e is the equilibrium release ratio, and k represents the release rate constant (sec^{-1}). The release of Fe(II)/total Fe as a function to time were fit according to the model and the q_e and k parameters were estimated using the Scipy library in Python 3.

3. Results

3.1. Properties of the ferrihydrite precipitates

3.1.1. Physicochemical properties

3.1.1.1. Specific surface area and porosity

The N_2-adsorption desorption isotherms of the various Fhs studied are presented in Figures S1 and S2. All of the Fhs exhibited a reversible Type I(b) isotherm, characteristic of materials having pores with diameters in the upper range of micropore domain, containing both wider micropores and narrow mesopores (<2.5 nm) (Rouquerol et al., 2007) (Figures S1 and S2). With

the exception of pure Fh and FhCop 0.01, all of the minerals studied exhibited a small adsorption-desorption hysteresis in the range $0.3 < P/P_0 < 0.6$ indicative of mesopores (Figures S1 and S2) (Rouquerol et al., 2007). Thus, alginate and P appeared to promote the formation of mesopores. Figures S1 and S2 also shows the BJH pore size distributions of the Fhs. Pure Fh, FhCop 0.01, FhAlg, FhAlgAds 0.01, and FhAlgCop 0.01 exhibited a bimodal distribution of pores, peaking at 1-2 nm and 3-4 nm, whereas the remaining samples exhibited pore size distribution mainly in the range of 3-4 nm (Figures S1 and S2).

Table 1 presents the derived SSA as well as the micropore- (MIV), mesopore- (MEV), and total pore- volumes (TPV). In general, for the Fhs without alginate and relative to pure Fh, the SSA slightly increased with increasing P content, regardless of whether P was adsorbed or coprecipitated, suggesting that the mode of P interaction and the concentration of P used did not have a definitive effect on SSA. (Table 1). It was also observed that SSA followed the overall trends for MEV and TPV, whereas the slight increase in SSA corresponds with the observed increase in MIV for the Fhs with the highest P content (P/Fe 0.1) (Table 1).

Relative to alginate-free Fh, coprecipitation with alginate led to a marked decrease in N_2 adsorption, concomitant with reduced porosity and SSA (Figure S2, Table 1). Only minor variations in SSA were observed at the highest P content (P/Fe = 0.1), where values increased for FhAlgAds (~16 %) but decreased for FhAlgCop (~27 %) (Table 1). This difference suggests that the influence of P sorption mode may become more apparent in Fh-OM coprecipitates. Finally, in general, P induced changes to the SSA of FhAlg corresponded closely with those observed for the porosity parameters (Table 1).

3.1.1.2. 0.1 M NaOH extractable P and ζ-potential

Regardless of the sorption mode of P and the presence of alginate, the base treatment recovered 100% of the P that was sorbed to the Fhs (Table 1). The ζ-potential and particle size of the Fhs at pH 6.8 are given in Table 1. For alginate-free Fhs, the ζ-potential decreased with increasing P content and, at equivalent P content, the Fhs with pre-adsorbed P exhibited lower ζ-potential than that of P-Fh coprecipitates (Table 1). In contrast, all alginate-Fh coprecipitates exhibited a negative ζ-potential and the presence of P had no noticeable impact (Table 1).

3.1.2. X-ray diffraction and IR spectroscopy

Figure 1 shows the XRD patterns of the different Fh samples. Reflections characteristic of 2-line ferrihydrite were identified in the diffractograms, aligning closely with those reported in the literature (Cornell and Schwertmann, 2003). Relative to pure Fh, the reflections of FhAds 0.01, FhAds 0.1, and FhCop 0.01 exhibited similar characteristics (intensity and shape) (Figure 1). In contrast, the reflections of FhCop 0.1 decreased in intensity, and the reflection at 34° 2θ slightly shifted to a lower angle (Figure 1 A). The coprecipitation of Fh with alginate also led to slight changes in the bulk mineralogy, namely the broadening of the reflections centered at 34° and 62° 2θ (Figure 1 B). As with alginate-free Fh, only FhAlgCop 0.1 exhibited changes as judged by the additional broadening and shifting of the reflections corresponding to Fh (Figure 1).

Additional information about the chemical composition and functional groups was obtained through FTIR spectroscopy. Figure 2 (A) shows the FTIR spectra of the minerals studied within the region 1725 – 525 cm^{-1}. For pure Fh, the broad bands centred at ~1627, 1468, and 1360 cm^{-1} correspond to the δ(O-H) vibrations from adsorbed H_2O and stretching vibrations ν_{asym} and ν_{sym} of C-O bonds from adsorbed carbonate, respectively (Cornell and Schwertmann, 2003; Schwertmann and Cornell, 2008). The intensity of the latter bands decreased the highest P content

Table 1: Chemical composition, specific surface area (SSA), pore characteristics, 0.1 M NaOH extractable P, and surface charge at pH 6.8 of the studied ferrihydrites. MEV, MIV, and TPV correspond to meso-, micro-, and total- pore volume, respectively. Data represents the average ± standard deviation of 2 replicates, whereas data for ζ-potential measurements represent the average ± standard deviation of 5 measurements.

Sample ID	C/Fe mol:mol	P/Fe mol:mol	SSA (m^2/g)	MEV (cm^3/g)	MIV (cm^3/g)	TPV (cm^3/g)	Extractable P (%)	ζ-potential
Fh	--[a]	Bd[b]	319.78±3.71	0.07±0.009	0.12±0.006	0.18±0.001	0	31.8±1.7
FhAds P/Fe 0.01	--	0.01±0.002	333.76±0.11	0.11±0.001	0.13±0.001	0.21±0.002	100	26.2±1.2
FhAds P/Fe 0.1	--	0.09±0.011	343.13±3.86	0.15±0.001	0.14±0.001	0.23±0.003	100	8.1±0.4
FhCop P/Fe 0.01	--	0.01±0.001	320.44±1.27	0.08±0.001	0.13±0.003	0.18±0.001	100	31.9±1.7
FhCop P/Fe 0.1	--	0.1±0.002	346.46±0.90	0.12±0.001	0.14±0.004	0.21±0.001	100	20.8±1.1
FhAlg	0.97±0.001	Bd	86.10±4.15	0.02±0.001	0.04±0.003	0.05±0.003	0	-38.5±2.4
FhAlgAds P/Fe 0.01	0.97±0.001	0.01±0.002	93.46±0.12	0.03±0.001	0.04±0.001	0.06±0.001	100	-36.9±2.5
FhAlgAds P/Fe 0.1	0.98±0.001	0.1±0.001	102.95±0.2	0.05±0.001	0.04±0.001	0.08±0.001	100	-41.7±2.6
FhAlgCop P/Fe 0.01	0.97±0.002	0.01±0.001	86.16±0.62	0.03±0.005	0.03±0.001	0.05±0.001	100	-39.1±2.7
FhAlgCop P/Fe 0.1	0.96±0.001	0.09±0.011	62.44±0.43	0.02±0.001	0.02±0.001	0.04±0.001	100	-41.7±2.5

a – Component not measured
b – Below detection of the instrument (P = 0.0052 ppm)

(FhAds and FhCop 0.1) as a consequence of the competitive advantage of P over carbonate for reactive sites (Figure 2) (Mendez and Hiemstra, 2018). The broad band centred at ~565 cm^{-1} corresponds to the stretching vibration, ν(Fe-O), of Fe-O in the Fh lattice (Figure 2). The intensity of this band decreased with increasing P content, especially for FhCop 0.1 (Figure 2). Regardless of the sorption mode, the broad band corresponding to the stretching vibrations of ν(P-O) was centred at ~1006 cm^{-1}, suggesting similar coordination/binding environment to the Fh surface/octahedra (Figure 2). Finally, this band corresponds to 3 stretching vibrations comprised of ~1102 and 1020 cm^{-1}, and at 920 cm^{-1} as determined by Savitsky-Golay secondary derivative analyses indicative of protonated bidentate binuclear complexes (data not shown) (Arai and Sparks, 2001; Wang et al., 2013).

The FTIR spectrum for Na-alginate is presented in Figure 2 (B) and the corresponding band assignments are given in Table S2 (Chandıa et al., 2001; Leal et al., 2008; Cardenas-Jiron et al., 2011). Upon coprecipitation with Fh some changes in the functional groups of Na-alginate were observed. Relative to Na-alginate, the bands corresponding to the asymmetric (~1592 cm^{-1}, ν_{asym}(C-O-O)) and symmetric (~1408 cm^{-1}, ν_{sym}(C-O-O)) stretching vibrations of the carboxylate groups broadened, whereas the former shifted by ~4 cm^{-1} (Figure 2 B). Shifting was also observed for the band centred at ~1033 cm^{-1} by 9 cm^{-1} corresponding to a host of vibrations comprising those for mannuronic and guluronic acid residues, and ν(C-O) of secondary alcohols (Figure B). Such changes can be attributed to the changes in the coordination environment of polysaccharide functional groups as they bind to the Fh octahedra (Eusterhues et al., 2008; Chen et al., 2014; Sowers et al., 2018). P was associated with the FhAlg coprecipitates, although the exact position of the bands for P were difficult to discern due to overlapping with those belonging to alginate

(Figure 2 B). Finally, relative to Fh, the band centred at 565 cm^{-1} decreased in intensity and disappeared as the P content increased (Figure 2 B).

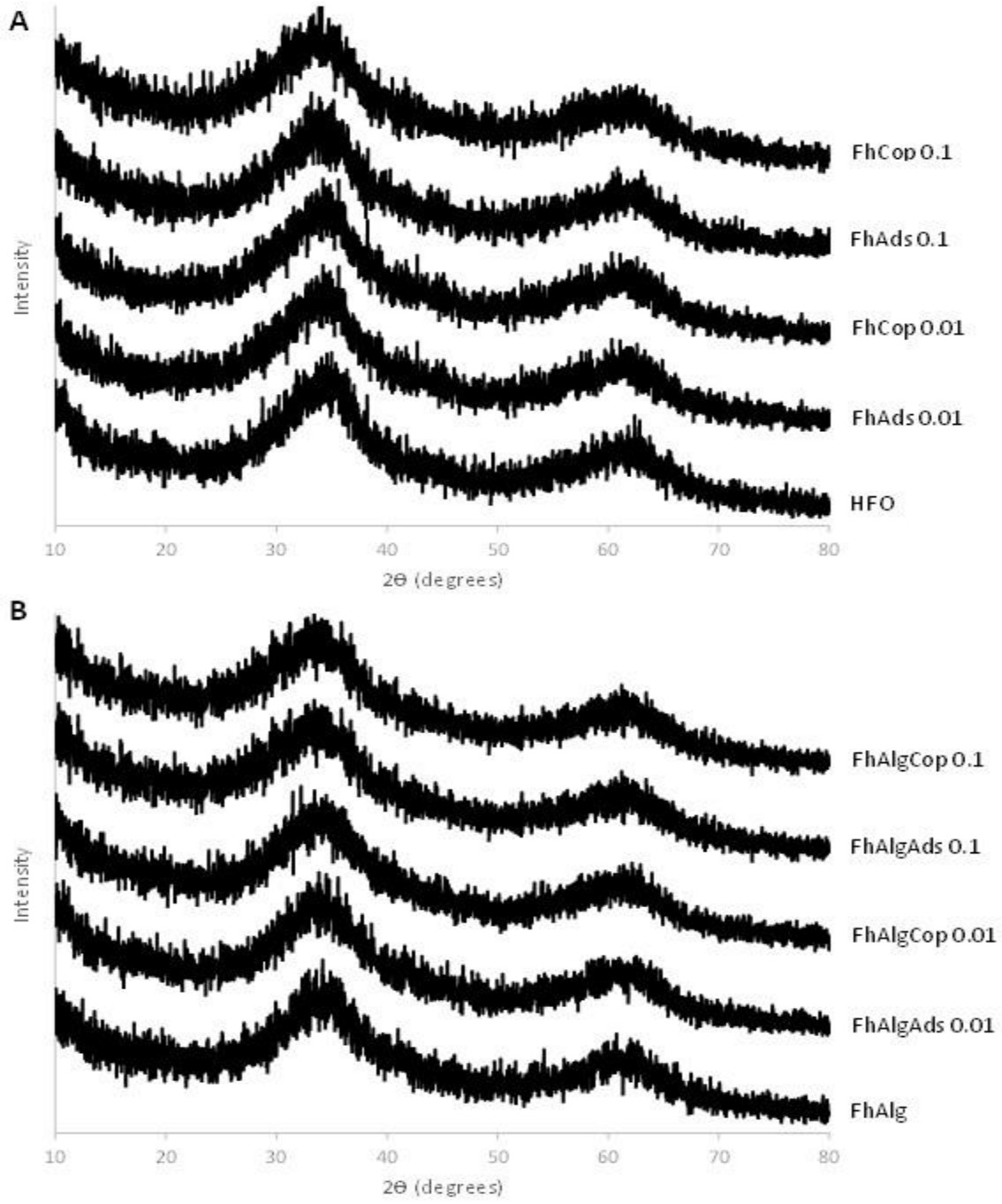

Figure 1: X-ray diffraction patterns of (A) 2-line ferrihydrite pre-adsorbed or coprecipitated with phosphate (P/Fe ratio of 0, 0.01, 0.1 mol:mol), and (B) 2-line ferrihydrite-alginate composite (C/Fe 1.0 mol:mol) with pre-adsorbed or coprecipitated phosphate (P/Fe ratio of 0, 0.01, 0.1 mol:mol).

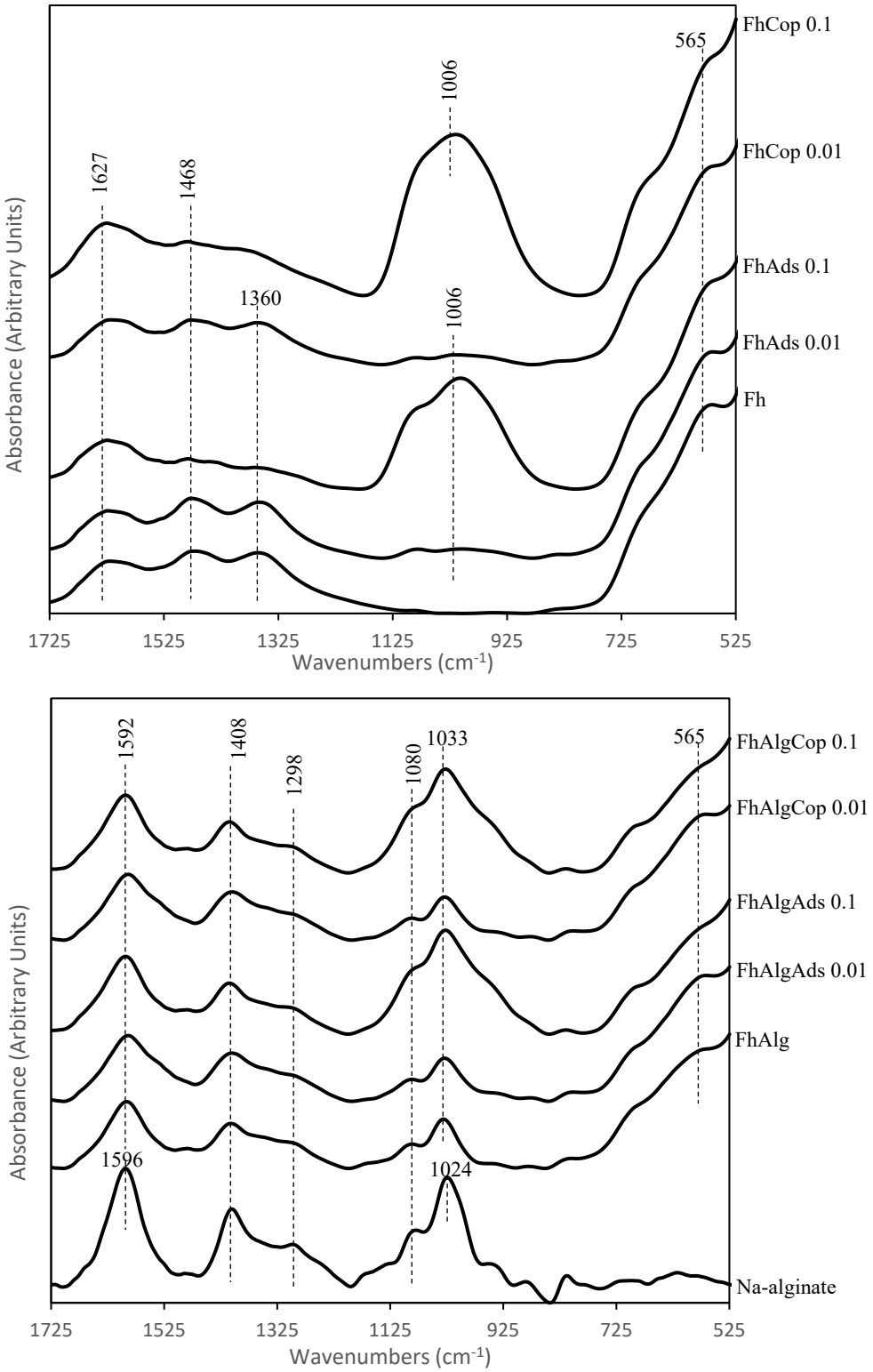

Figure 2: FTIR spectra of 2-line ferrihydrite pre-adsorbed or coprecipitated with phosphate (P/Fe ratio of 0.0, 0.01, 0.1 mol:mol) (top), and 2-line ferrihydrite-alginate composite (C/Fe 1.0 mol:mol) with pre-adsorbed or coprecipitated phosphate (P/Fe ratio of 0.0, 0.01, 0.1 mol:mol) (bottom).

3.1.3. SEM and elemental mapping

Results of the SEM analysis showed that particle sizes formed by OM-coprecipitation were larger than those formed in the absence of alginate (Figure S3). P also had no obvious effects on the morphology of the Fhs, and across all Fhs the elemental map showed that, regardless of the sorption mode, Fe and P were relatively homogeneously distributed on the surface of the associations at the micrometer scale (Figure 3 and S4).

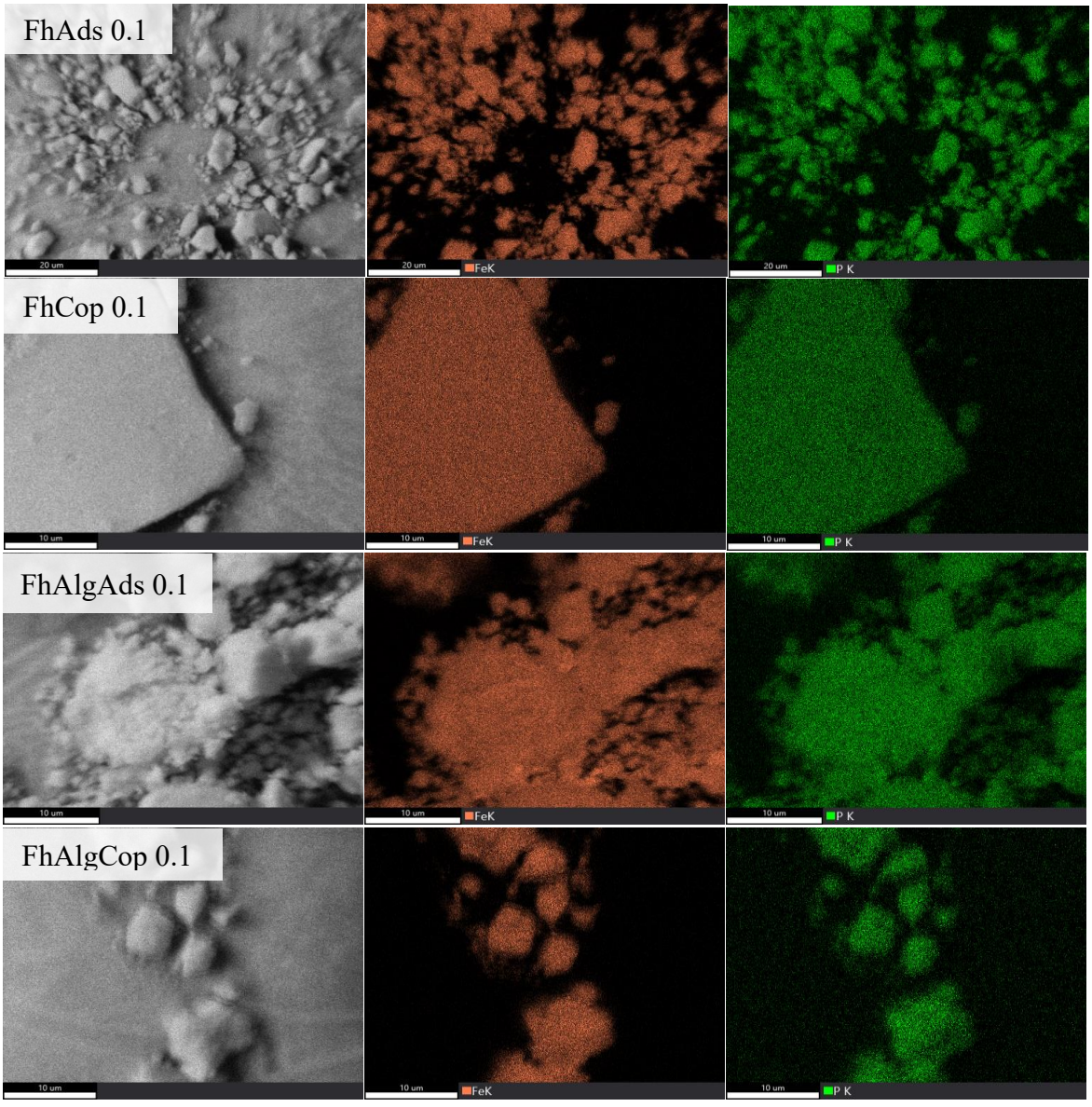

Figure 3: Elemental maps of the synthesized minerals. The maps show the strong relationship between the distribution of P and Fe indicating homogeneity.

3.2. Bioavailability

3.2.1. Control microcosms

Throughout the experiment, there were no notable changes in the measured parameters (total and dissolved Fe(II)), and no microbial growth was observed in any of the abiotic microcosms (data not shown). For all the Fhs studied, the pH more-or-less remained stable within the range of 6.7 – 6.9 (Figure S5), and dissolved P was consistently detected throughout the experimental period (Figure 4). However, dissolved P was only present in the microcosms with Fhs containing the highest P content (P/Fe 0.1), while in the microcosms with Fh coprecipitated with P/Fe 0.01 the concentration remained below the method's detection limit. The proportion of dissolved P relative to total P (P_{prop}) depended on the mode of sorption as well as the presence of alginate (Figure 4). In the case of FhAds 0.1, the P_{prop} reached a maximum of ~1% at the start of the experiment and gradually decreased to ~0.8% by the end (Figure 4). In contrast, for FhCop 0.1, the P_{prop} gradually increased reaching a maximum of ~0.18% by day 10, at which point it remained stable for the remainder of the experiment (Figure 4). P_{prop} for FhAlgAds 0.1 was comparable to that of FhAds 0.1, but did not show a specific trend (Figure 4). For FhAlgAds 0.1, P_{prop} increased from ~0.8% at the start of the experiment to ~1% at day 2, at which point it varied between these two values for the remainder of the experiment (Figure 4). In contrast, for FhAlg Cop 0.1, the P_{prop} reached ~0.5% at the start of the experiment and showed an overall increase throughout the duration of the experiment reaching a maximum of ~0.7% (Figure 4). It should also be noted that the P_{prop} for FhAlgCop 0.1 was 4-5x higher than that of FhCop 0.1 (Figure 4).

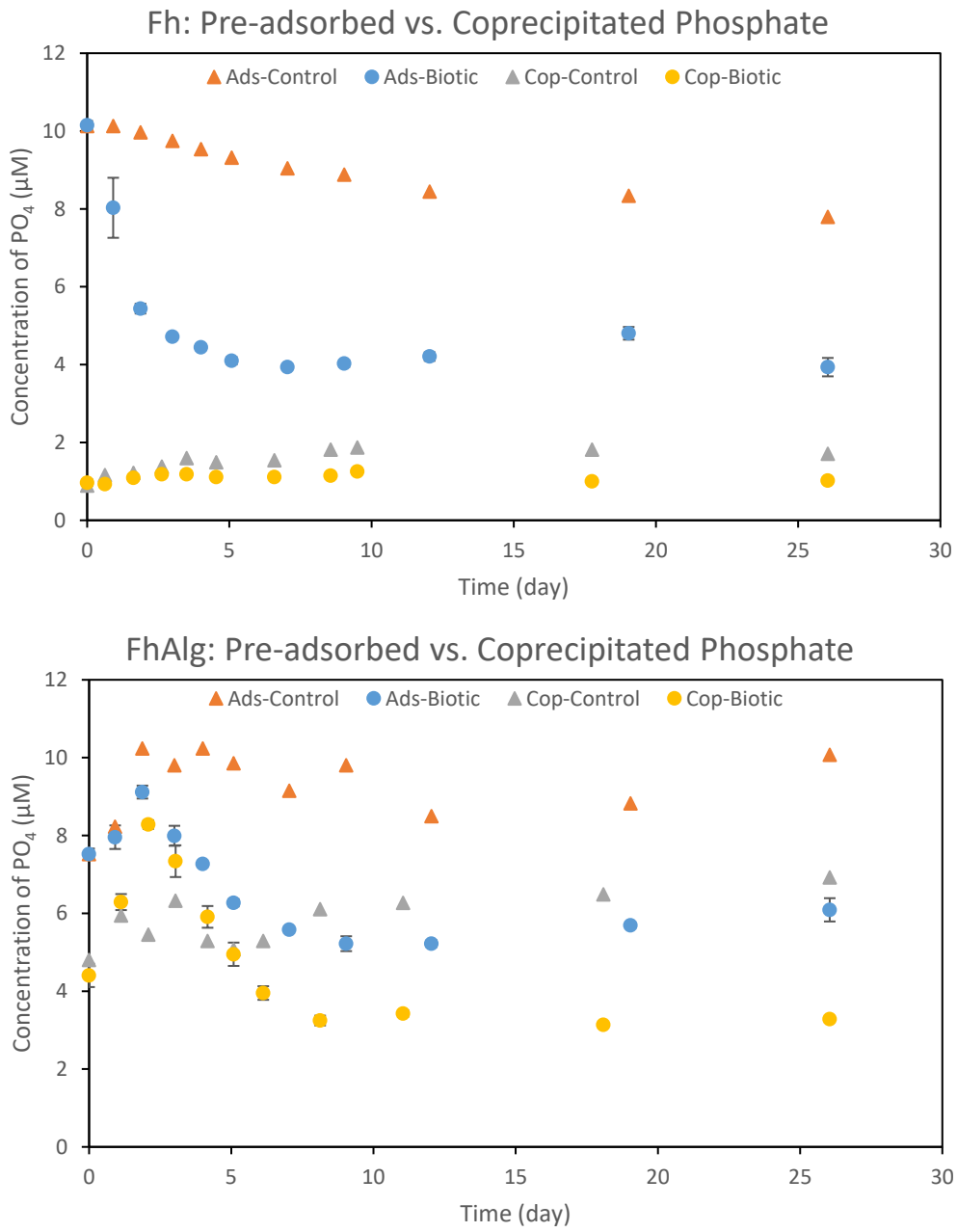

Figure 4: Changes of dissolved P concentration released from pure Fh with coprecipitated (cop) or pre-adsorbed (ads) phosphate (P/Fe molar ratio of 0.1) and Fh alginate composite (C/Fe molar ratio of 1.0) with coprecipitated or pre-adsorbed phosphate (P/Fe molar ratio of 0.1) throughout the experimental period in the presence (biotic) and absence (control) of *S. putrefaciens* CN32. The data points represent the average and standard deviation (error bars) from 3 individual replicates for the biotic experiments and 1 replicate for controls.

3.2.2. Biotic microcosms

3.2.2.1. pH and cell count

Changes in pH and cell count throughout the experimental period are presented in Figures S4. Across all biotic microcosms, pH gradually increased throughout the experimental duration reaching ~7.5 for FhAds 0.1, FhCop 0.1, and FhAlgCop 0.1, while the rest of the Fhs reached 7.2 – 7.3 at the end of the experimental period (Figure S5). Across all biotic experiments, the cell count did not exhibit a specific trend, but in general the count gradually declined throughout the experimental duration (Figure S6). In addition, cell count appeared to have declined faster for Fh-alginate coprecipitates when compared to that of alginate-free Fhs (Figure S6.).

3.2.2.2. Rate and extent of Fe(III) reduction

3.2.2.2.1. Effects of phosphate

Microbial Fe(III) reduction curves of the Fhs are presented in Figure 5, which show the increase of total Fe(II) and dissolved Fe(II) relative to total Fe throughout the experimental period (up to 25 days). The rates of Fe(III) reduction by *S. putrefaciens* CN32 were calculated by linear regression of selected time points that corresponded to the period of maximum accumulation of total Fe(II) relative to total Fe (Langley et al., 2009b; Langley et al., 2009d). The extent of Fe(III) reduction was determined from the maximum amount of total Fe(II) relative to total Fe, which equated to the last experimental measurement taken. A summary of the regression data and the maximum amount of Fe reduced for the Fhs are presented in Table 2. For alginate free Fhs, the rate of Fe(III) reduction increased with increasing P content (Table 2). Tukey's pairwise post-hoc analyses revealed a significant difference in the rates of Fe(III) reduction between pure Fh and that of P-doped Fhs (2-way ANOVA, $P<0.05$, Table 2). However, no significant difference was found in the Fe(III) reduction rate between FhAds 0.01 and FhCop 0.01 (2-way ANOVA, $P>0.05$),

whereas a significant difference was found between FhAds 0.1 and FhCop 0.1 (2-way ANOVA. $P<0.05$, Table 2). Thus, within this group FhCop 0.1 was reduced ~3x and 1.4x faster than pure Fh and FhAds 0.1, respectively (Table 2). Similar to the reduction rates, the extent of Fe(III) reduction increased with P content (Table 2). Compared to pure Fh, the extent of reduction in P-doped Fhs showed a significant difference (2-way ANOVA, $P<0.05$). Specifically, the amount of Fe(III) reduced was approximately 1.4x, 2x, 1.2x, and 1.8x higher for FhAds 0.01, FhAds 0.1, FhCop 0.01, and FhCop 0.1, respectively, relative to that of pure Fh (Table 2). Moreover, at equivalent P concentration, the amount of Fe(III) reduced was significantly higher for FhAds than that of FhCop although the difference amounted to ~5% (2-way ANOVA, $P<0.05$, Table 2).

The rates of Fe(III) reduction for Fhs-alginate coprecipitates generally followed the same trend as observed for alginate free Fhs (Table 2). However, within this group the rate of Fe(III) reduction for FhAlgAds 0.01 and FhAlgCop 0.01 did not significantly differ from that of FhAlg (2-way ANOVA, $P>0.05$, Table 2). As was observed for the alginate free Fhs, the sorption mode of P had no effect on the rate of Fe(III) for FhAlgAds 0.01 and FhAlgCop 0.01 as no significant difference was determined between the rates for these samples (2-way ANOVA, $P>0.05$). In contrast, a significant difference was determined in the rates of Fe(III) reduction between FhAlg Ads and Cop at the highest P loading (0.1 P/Fe) (2-way ANOVA, $P<0.05$, Table 2). Thus, within this group FhAlgCop 0.1 was reduced 3x and 2x faster than FhAlg and FhAds 0.1, respectively (Table 2). The overall trend and significance of the extent of Fe(III) for Fh-alginate coprecipitates was similar to what was observed for alginate free Fhs (Table 2). The amount of Fe(III) reduced was approximately 1.2x, 1.6x, 1.02x, and 1.5x higher for FhAlgAds 0.01, FhAlgAds 0.1, FhAlgCop 0.01, and FhAlgCop 0.1, respectively, relative to that of FhAlg (Table 2). Finally, as was observed for alginate free Fhs and at equivalent P concentration, the amount of Fe(III) reduced

was significantly higher for FhAlgAds than that of FhAlgCop although the difference only amounted to 2-6% (2-way ANOVA, $P<0.05$, Table 2).

3.2.2.2.2. Effects of alginate

Alginate generally enhanced the rate of Fe(III) reduction across all treatments (Table 2). Notably, at equivalent P concentration and sorption mode, there was a significant difference in Fe(III) reduction rates between alginate-free Fhs and alginate Fh coprecipitates, with the FhAlg coprecipitates reducing 1.2-1.6x faster ($P<0.05$, t-test, Table 2). The exception was between FhAds 0.1 and FhAlgAds 0.1, where the reduction rates did not significantly differ ($P>0.05$, t-test, Table 2). At equivalent P concentration and sorption mode, a significant difference was also observed in the extent of Fe(III) reduction between alginate-free Fhs and FhAlg coprecipitates ($P<0.05$, t-test, Table 2). Specifically, the amount of Fe(III) reduced from Fh-alginate coprecipitates was ~6% and 11-13% lower than that of alginate-free Fhs with P/Fe molar ratios of 0.01 and 0.1, respectively (Table 2). One exception was the pure Fh and FhAlg where the amount of Fe reduced was comparable and did not significantly differ ($P>0.05$, t-test, Table 2).

3.2.2.2.3. Dissolved phosphate

Similar to the abiotic microcosms, dissolved P was detectable in biotic microcosms only for the Fhs with the highest P content (P/Fe 0.1) (Figure 4). In the FhAds 0.1 biotic microcosms, P_{prop} decreased from 1 % to ~0.4 % by day 7, stabilizing thereafter (Figure 4). In contrast, P_{prop} in the FhCop 0.1 biotic microcosms increased from ~0.1 % to 0.12 % by day 3, which plateaued for the remainder of the experiment (Figure 4). Finally, compared to their corresponding controls, P_{prop} in both biotic microcosms was lower, with FhAds 0.1 showing higher P_{prop} than those with FhCop 0.1 (Figure 4).

For the alginate-Fh coprecipitates, the P_{prop} within the biotic microcosms of the FhAlgAds 0.1 and FhAlgCop 0.1 increased by day 2 reaching ~0.9 % and ~0.8 % respectively (Figure 4). Afterwords, the P_{prop} gradually decreased reaching ~0.6 % and 0.3 %, respectively, at the end of the experimental period (Figure 4). As with the alginate-free Fhs, P_{prop} in both biotic microcosms was lower compared to their corresponding controls, with FhAlgAds 0.1 showing higher P_{prop} than FhAlgCop 0.1 (Figure 4).

P_{prop} reached similar levels during the reduction of FhAds 0.1 and FhAlgAds 0.1, whereas the P_{rop} remained higher during the reduction of FhAlgCop 0.1 in comparison to FhCop 0.1 (Figure 4).

Table 2: Linear reduction rates and maximum amount of Fe(III) reduced by *S. putrefaciens* CN32 (biotic) and fitting parameters for Fe(III) dissolution by ascorbate (abiotic) (pH 8.0) for the various synthetic ferrihydrites studied. Data for the biotic experiments represents average ± standard deviation from 3 replicates. For all experiments, the fit had a R^2 value of >0.98.

Sample	Biotic		Abiotic	
	Rate of Reduction (day^{-1})	Fe(III) Reduced (%)	k (s^{-1})	q
Fh	0.0153±0.0016	26.78±0.28	$2.03x10^{-4}$	1.0
Fh Ads 0.01	0.0193±0.0008	38.29±1.75	$1.92x10^{-4}$	1.0
Fh Ads 0.1	0.0324±0.0011	55.05±1.12	$2.18x10^{-4}$	1.0
Fh Cop 0.01	0.0189±0.0007	33.34±1.09	$2.08x10^{-4}$	1.04
Fh Cop 0.1	0.0446±0.0029	49.32±0.58	$5.50x10^{-4}$	1.0
FhAlg	0.0244±0.0016	26.51±0.15	$2.71x10^{-4}$	1.09
FhAlg Ads 0.01	0.0251±0.0007	32.79±0.19	$2.80x10^{-4}$	1.11
FhAlg Ads 0.1	0.0336±0.0014	41.43±0.33	$3.22x10^{-4}$	1.02
FhAlg Cop 0.01	0.0249±0.0017	27.13±0.27	$3.36x10^{-4}$	1.00
FhAlg Cop 0.1	0.0721±0.0149	39.15±0.31	$6.28x10^{-4}$	1.00

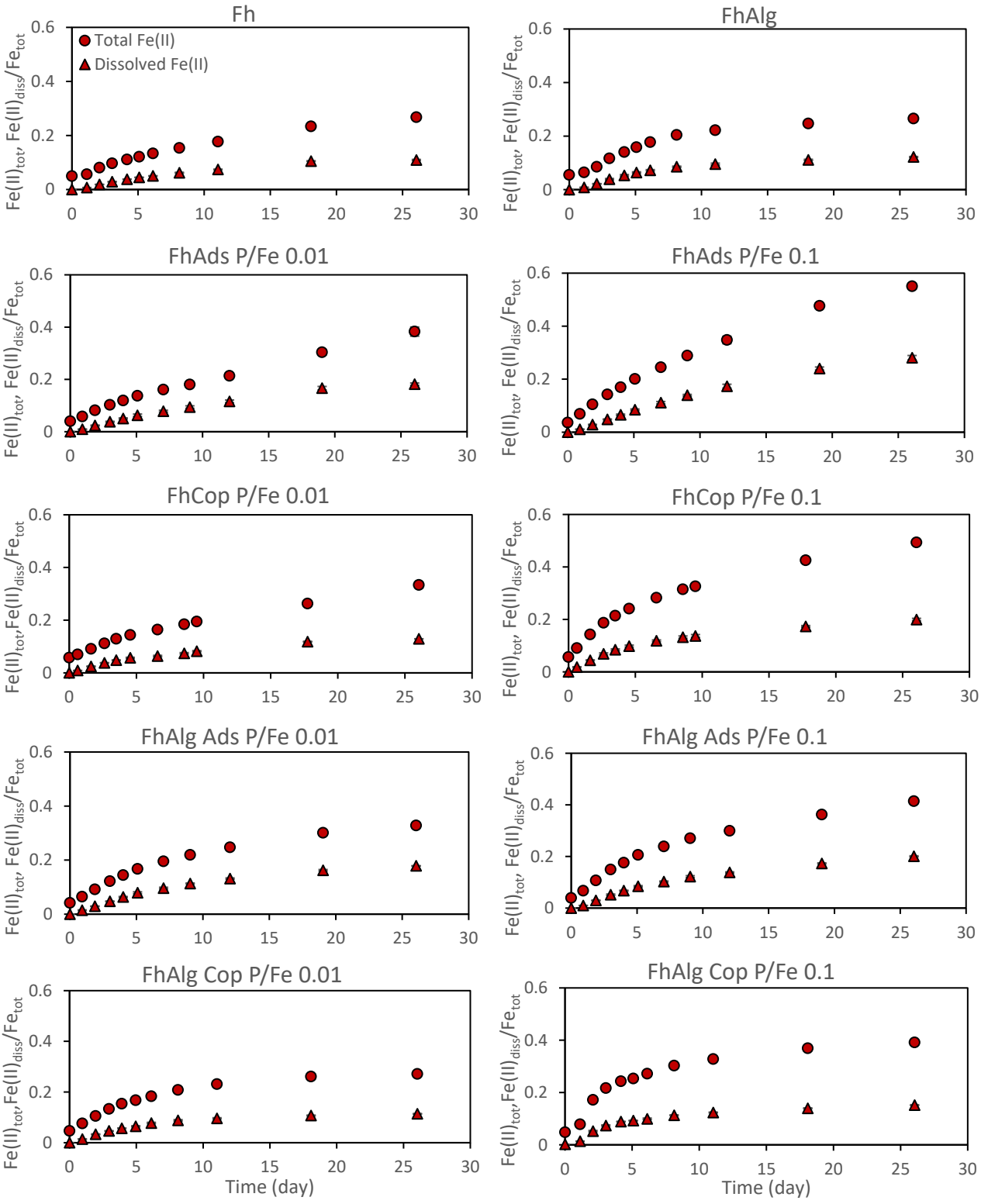

Figure 5: Changes in total (tot) and dissolved (diss) Fe(II) relative to total Fe during the microbial reduction of the studied synthetic ferrihydrites by *S. putrefaciens* CN32. Symbols represent the average and standard deviation (error bars) of 3 individual replicates.

3.2.2.3. Biogenic solids

X-ray diffractograms and electron micrographs of the post-reduction minerals are shown in Figures 6-8. For alginate-free Fhs, pure Fh transformed into a mixture of goethite and magnetite (Figure 6). However, for Fh with P/Fe 0.01 and relative to those observed for the P-free Fh, the reflections corresponding to goethite decreased in intensity, whereas the intensity of the magnetite reflection increased (Figure 6). At the highest P-content, the reflections corresponding to goethite were attenuated, whereas those corresponding to magnetite were absent (Figure 6). Nonetheless, for these precipitates the broad reflections centered at 34 and 62° 2θ appeared sharper relative to those of 2-line ferrihydrite suggesting a transformation into a ferrihydrite of higher crystallinity. Electron micrographs corroborated the XRD data, in which case morphologies pertaining to crystalline products were observed (Figure 7). For Fh and Fhs with P/Fe of 0.01, acicular goethite crystals were clearly visible (see arrows, Figure 7), whereas magnetite crystals could not be resolved suggesting the formation of nano magnetite. For Fhs with P/Fe of 0.1, crystalline products could only be resolved for FhCop, but not for FhAds (Figure 7). The former precipitates appeared to have "hedge-hog" like crystals, although the mineralogy of the "needles" could not be identified (Figure 7).

Further analyses by FTIR revealed that goethite was the dominant transformation product that formed following the reduction of Fh (Figure S7). In contrast, the intensity of the bands belonging to goethite decreased as the P content increased to P/Fe 0.01 and could not be resolved as the P content reached P/Fe 0.1 (Figure S7). Moreover, the intensity of the goethite bands for the biogenic solids formed from the reduction of FhAds 0.01 were lower than those formed from the reduction of FhCop 0.01 (Figure S7).

Goethite was the dominant product that formed following the microbial Fe(III) reduction of FhAlg and those containing P/Fe of 0.01 (Figure 6). In these precipitates, reflections corresponding to magnetite could not be resolved suggesting that alginate inhibited the formation of this mineral (Figure 6). Relative to FhAlg, the reflections pertaining to goethite in the precipitates formed from FhAlg with P/Fe of 0.01 were broader whereas the reflection centered at ~21° 2θ exhibited less intensity. For FhAlg with the highest P/Fe content, the biogenic solids were mainly composed of 2-line ferrihydrite as evident by the broad reflections centered at 34° and 62° 2θ (Figure 6). Electron micrographs also revealed acicular goethite crystals where this mineral was confirmed by XRD (Figure 8). For FhAlgAds and FhAlgCop 0.1, no crystalline products could be detected suggesting that 2-line ferrihydrite was the dominant mineral. FTIR also revealed the occurrence of goethite in agreement with XRD analyses, and as was observed for alginate-free Fhs, the intensity of the goethite bands for the biogenic solids formed from the reduction of FhAlgAds 0.01 were lower than those formed from the reduction of FhAlgCop 0.01 (Figure S7).

Across all the minerals studied, phosphate rich Fe(II) minerals such as vivianite were not detected, whereas elemental mapping showed that P and Fe remained homogenously distributed lacking any clusters of P-Fe rich regions (Figure S8). Nonetheless, geochemical modelling with PHREEQC showed that the solutions from the biotic microcosms with Fhs with P/Fe 0.1 were supersaturated with respect to vivianite ($Fe_3(PO_4)_2 \bullet 8H_2O$), therefore it may have formed at levels below the detection limit of the instruments employed in this study.

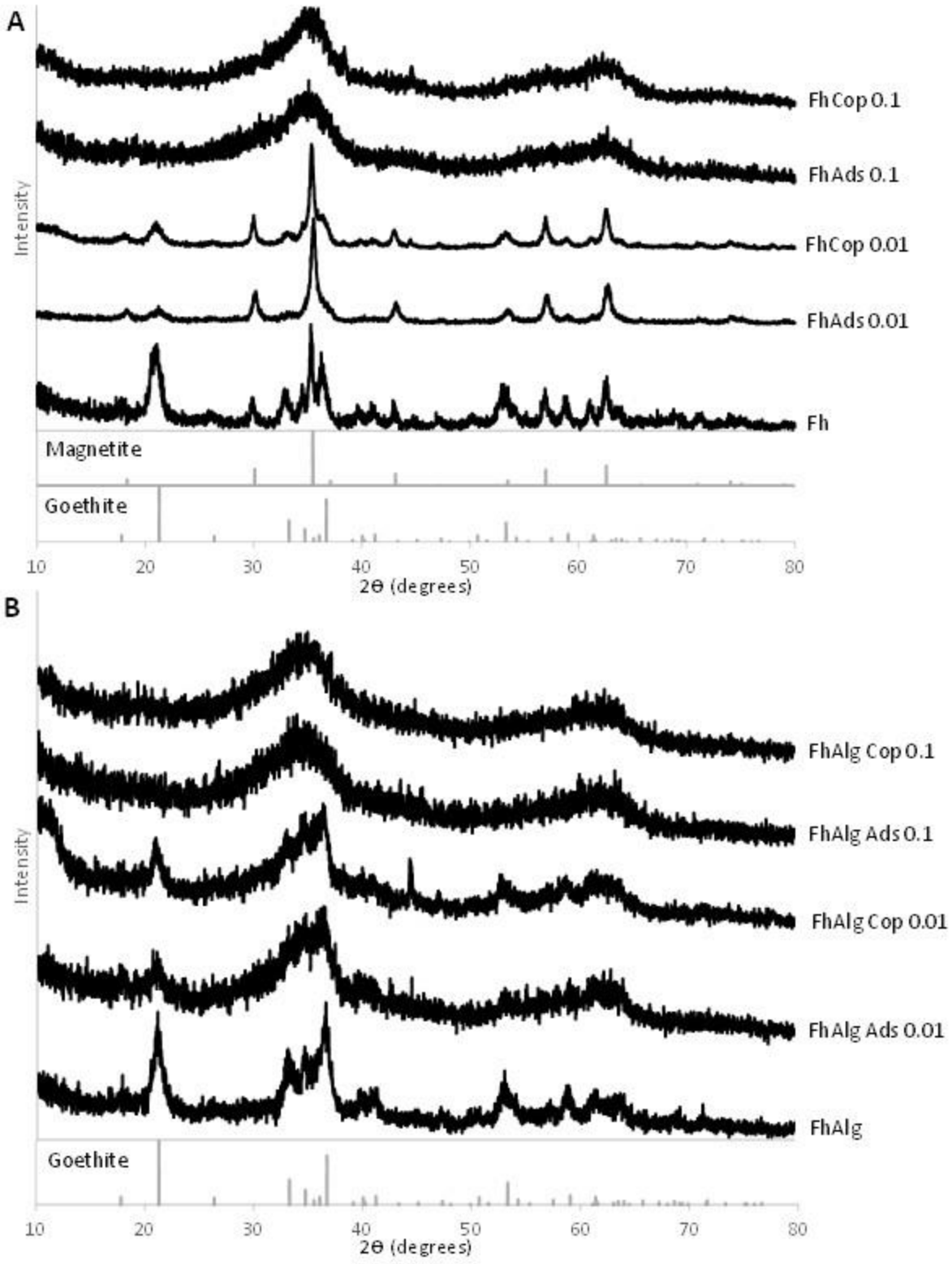

Figure 6: X-ray diffraction patterns of post Fe-reduction minerals from (A) 2-line ferrihydrite with pre-adsorbed or coprecipitated phosphate (P/Fe 0, 0.01, 0.1 mol:mol), and (B) 2-line ferrihydrite-alginate composite (C/Fe 1.0 mol:mol) with pre-adsorbed or coprecipitated phosphate (P/Fe 0, 0.01, 0.1 mol:mol).

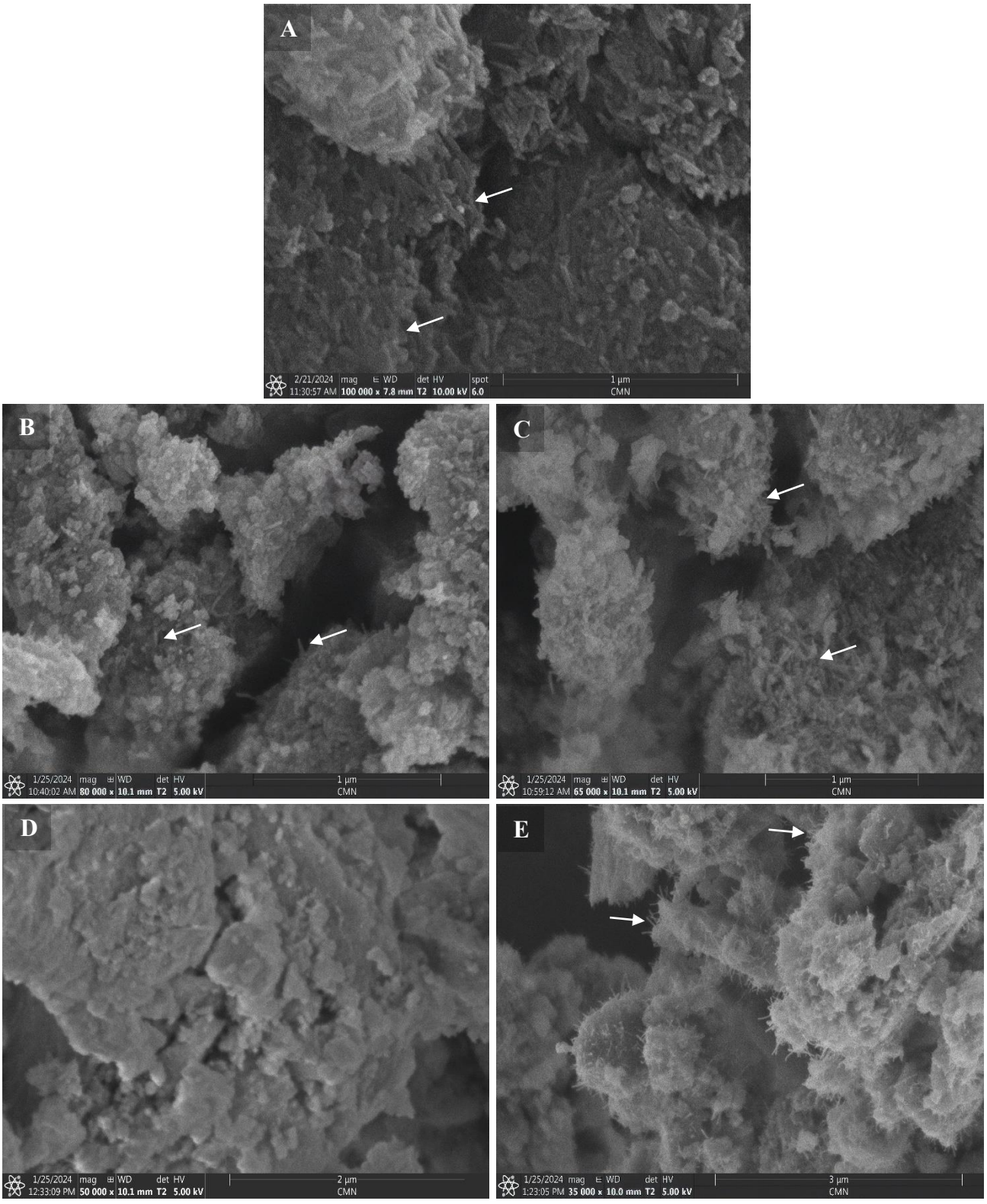

Figure 7: FESEM micrographs of the post-reduction secondary minerals produced following the microbial reduction of (A) Fh, (B) FhAds 0.01, (C) FhCop 0.01, (D) FhAds 0.1, and (E) FhCop 0.1. White arrows point to minerals with well-defined crystalline shapes.

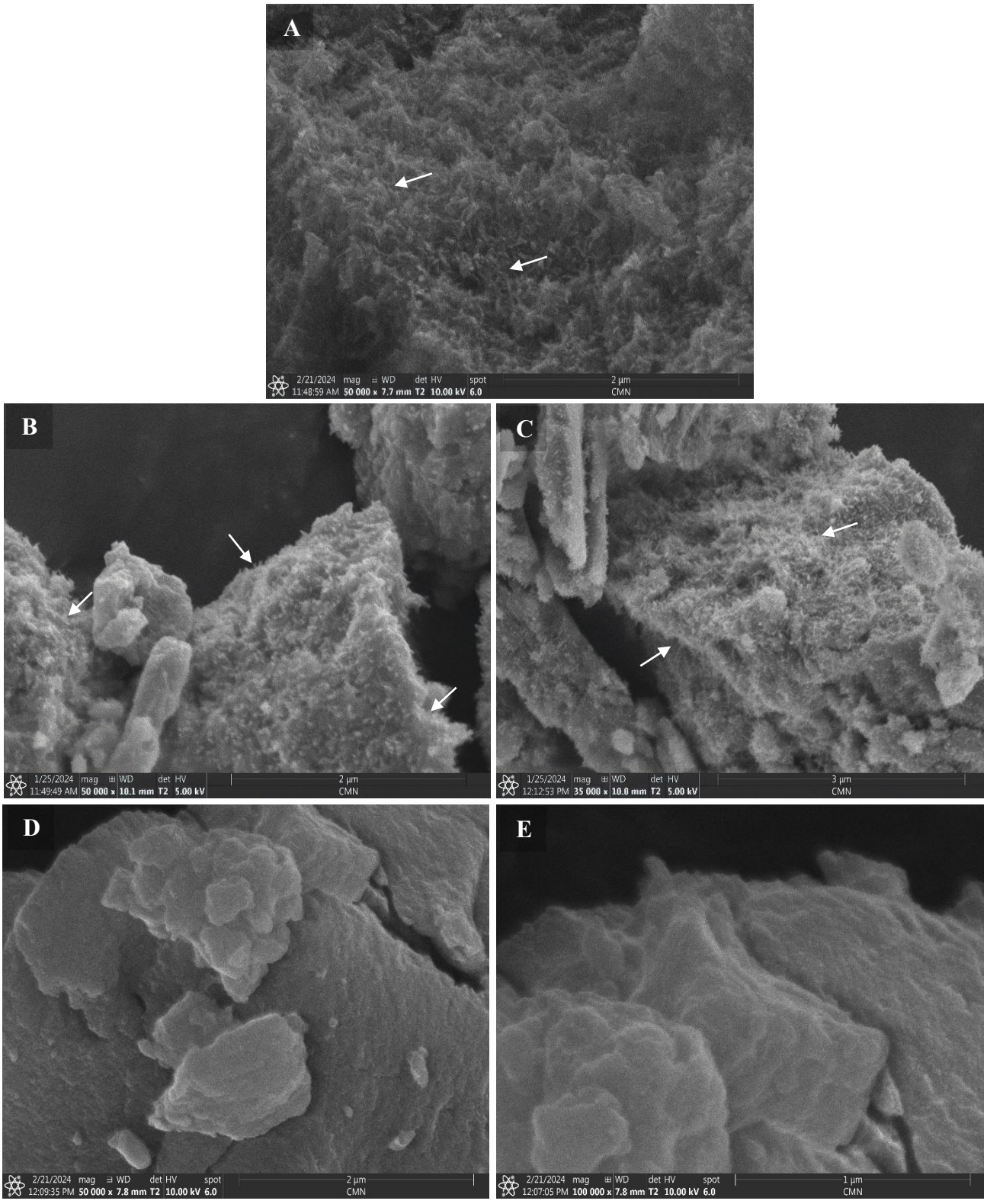

Figure 8: FESEM micrographs of the post-reduction secondary minerals produced following the microbial reduction of (A) FhAlg, (B) FhAlgAds 0.01, (C) FhAlgCop 0.01, (D) FhAlgAds 0.1, and (E) FhAlgCop 0.1. White arrows point to minerals with well defined crystalline shapes.

3.3. Chemical dissolution: ascorbate-citrate-bicarbonate

The dissolution of the Fhs was assessed from the accumulation of Fe and P in solution considering dissolved and colloidal Fe species (0.22 μm) (Figure 9). The release kinetics of Fe(II) during the reduction of the synthetic minerals fit well with the pseudo-first-order model, and the adjusted R^2 values were greater than >0.98. Among the alginate-free Fhs, FhCop 0.1 exhibited the highest dissolution rate (*k*) whereas the other Fhs were dissolved at a comparable rate (Table 2). Comparatively, at equivalent P content, alginate-Fh coprecipitates were dissolved at a faster rate than alginate-free Fhs (Table 2). One exception was the FhAlgCop 0.1, which was dissolved at a comparable rate as FhCop 0.1 (Table 2). Among the alginate-Fh coprecipitates, the rate of dissolution appeared to increase with increasing P content, and at comparable P content, the dissolution of the P containing FhAlg coprecipitates were reduced at a faster rate than their counterparts with pre-adsorbed P (Table 2). Within this group, FhAlgCop 0.1 was reduced the fastest.

$Fe_{colloid}$ showed a strong increase within the first hour of dissolution reaching a maximum of 40-60% of the total Fe across all experiments (Figure 9). Subsequently, $Fe_{colloid}$ decreased throughout the remainder of the experimental period, reaching 0% of the total Fe (Figure 9). It was also observed that $Fe_{colloid}$ accumulated the fastest during the dissolution of FhCop 0.1 and FhAlgCop 0.1 relative to the other Fhs (Figure 9).

Finally, alginate did not appear to influence the distribution of P since the release of P vs. Fe(II) $_{<0.22\mu m}$ from the alginate-free Fhs was similar to that of alginate-Fh coprecipitates, at corresponding P content (Figure 9). Similarly, alginate did not impact the release of $Fe_{colloid}$ given that the timing of release and extent were similar to what was observed for the alginate-free Fhs

(Figure 9). Across all experiments, it was also observed that the accumulation of P exceeded that of dissolved Fe(II) (Figure 9).

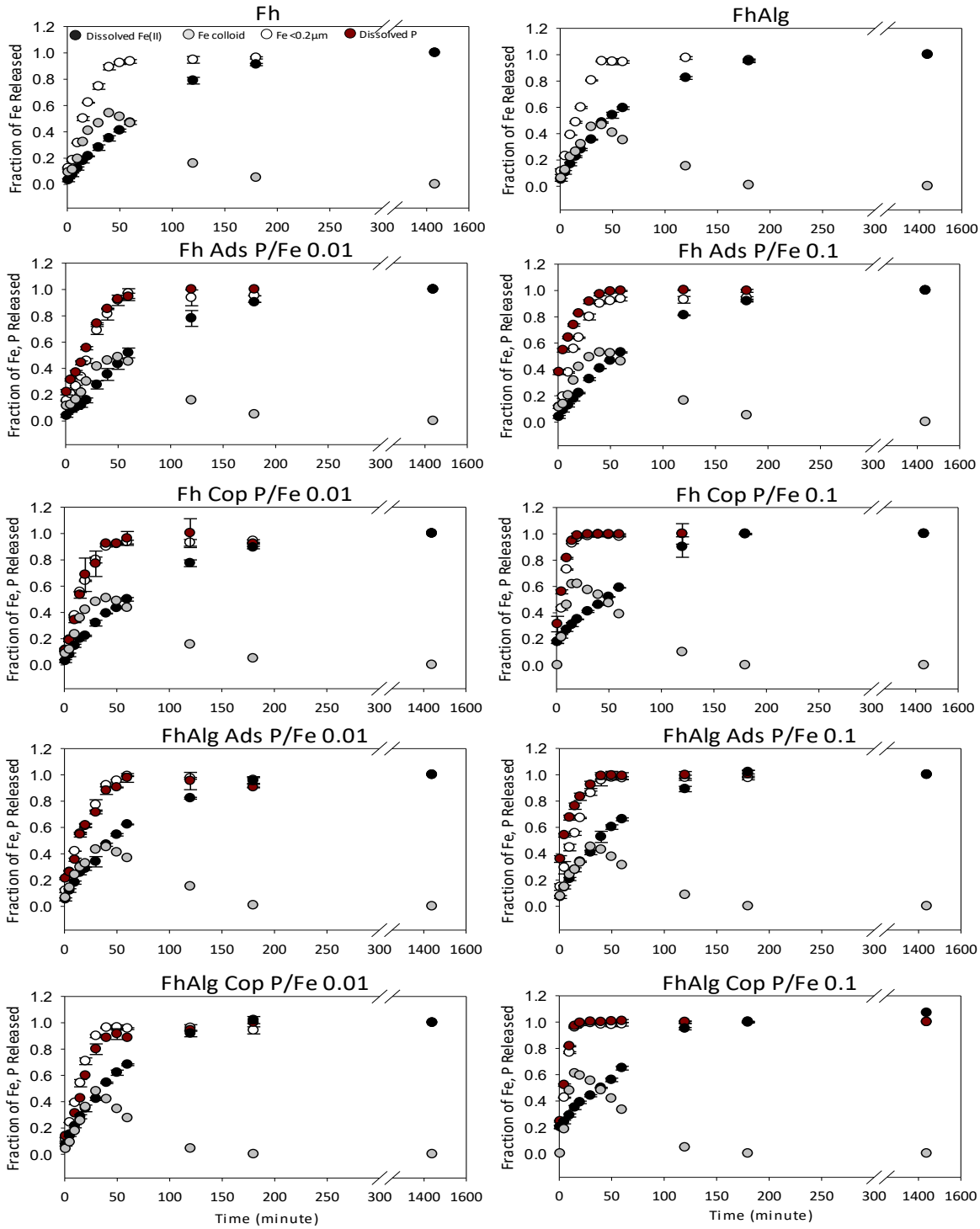

Figure 9: Kinetics of dissolved Fe(II), $Fe_{colloid}$, $Fe_{<0.2\mu m}$, and P accumulation during the reductive dissolution of the synthetic ferrihydrites studied by ascorbate (pH 8.0). Symbols represent the average and standard deviation of 2 replicates.

4. Discussion

4.1. Impact of phosphate and alginate on the physicochemical properties of the ferrihydrites

Our results show that the concentration of P used in this study (P/Fe 0.01 and 0.1) had a subtle impact on the physicochemical properties and mineralogy of the studied ferrihydrites. We observed a slight increase of SSA as the P content increased, which could be attributed to the disaggregation of the ferrihydrite nanoparticles during the drying process, allowing for N_2 to access pores not occupied by P. In contrast, the SSA decreased by ~15 and ~20 % for Fh coprecipitates containing P/Fe of 0.05 and 0.1 (mol:mol), respectively, synthesized from the aeration of Fe(II) solutions (Santoro et al., 2019). Such decrease was attributed to the aggregation induced by the negatively charged P anions and the positively charged newly formed Fe(hydr)oxide surfaces (Santoro et al., 2019). Yet, the SSA of Fe (oxyhydr)oxides formed from the oxidation of Fe(II) in the presence of P at similar P/Fe ratios used in this study increased, presumably due to the decrease in particle size (Cumplido et al., 2000; O'Loughlin et al., 2013). Likewise, the SSA of goethite synthesized from Fe(III) solutions containing P (up to 1.0 mol%) increased with increasing P content due to the formation of micropores (Kandori et al., 1992). Therefore, differences arise as a consequence of the synthesis pathway of Fe (oxyhydr)oxides.

In contrast to P, alginate had a noticeable impact on the SSA and porosity of the synthetic minerals. This observation is in line with past studies that have investigated the impact of organic substances, encompassing polysaccharides, humic acids, and fulvic acids, on the physicochemical properties of various synthetic Fe (oxyhydr)oxides, and has been attributed to pore blockage by OM (Mikutta et al., 2008; Shimizu et al., 2013; Poggenburg et al., 2016; Poggenburg et al., 2018; Liu et al., 2019b). In addition, the coprecipitation of Fh with organic P also led to reduced SSA (Santoro et al., 2019). The adsorption of P on the FhAlg coprecipitates led to the increase of SSA

presumably as a consequence of disaggregation similar to what was observed for the alginate-free Fhs. However, the coprecipitation of Fh with alginate as well as P led to reduced SSA, especially at the highest P content (P/Fe 0.1 mol:mol). This could be attributed to alginate creating a different matrix during synthesis that might interfere with the usual effect of P on ferrihydrite structure. P may promote a more dispersed structure when added without alginate, but with alginate, it could foster a denser, more compact structure with fewer exposed surfaces.

Base extraction using 0.1 M NaOH was carried out to determine the distribution of P as this extraction supposedly provides a good estimate of the amount of P adsorbed to Fe(III) oxides (Cabrera et al., 1981; O'Loughlin et al., 2013). In our study, P was fully recovered from the Fhs regardless of the sorption mode and the presence of alginate, whereas dissolution of the Fhs was insignificant (<0.1% for alginate-free Fhs and <0.35% for alginate-Fh coprecipitates). The high efficiency of P recovery with a single NaOH treatment implies that P was predominantly adsorbed onto the surface of the Fhs particles, making it more accessible to desorption. In contrast, when Fe (oxyhydr)oxides are synthesized from the oxidation of Fe(II) in the presence of P, the incorporation of P may occur through more complex structural mechanisms, potentially leading to a greater degree of occlusion within the mineral matrix (Cumplido et al., 2000; O'Loughlin et al., 2013). Occlusion of P may also occur as a consequence of ageing or transformation due to the NaOH treatment (Cabrera et al., 1981). Nonetheless, the occlusion of P hinders its release thereby requiring multiple NaOH extractions for complete recovery (O'Loughlin et al., 2013). However, ζ-potential measurements of the alginate-free Fhs suggest that not all of the P is adsorbed to the surface. Specifically, these measurements revealed differences in surface charge, which imply that for the coprecipitates a fraction of the phosphate may be bound more internally. We also expect that the occlusion of P to occur during the extraction process with NaOH as Fh is more prone to

transformation than lepidocrocite and goethite (Cornell and Schwertmann, 2003). Nonetheless, it appears that P remains accessible to desorption by excess OH^- regardless of the sorption mode and the presence of alginate. Although it is also possible that the extraction efficiency may depend on the mineral.

4.2. Mineralogy

During the hydrolysis of Fe(III), the presence of oxyanions and/or OM disrupt the mineral formation by interfering with Fe–Fe bond formation and occupying crystal growth sites thereby reducing crystallite size, structural coherence, and increasing structural strain (Rose et al., 1997; Schwertmann et al., 2005; Eusterhues et al., 2008; Chen et al., 2014; Kleber et al., 2015). This disruption is evident from various synthetic and naturally occurring Fe (oxyhydr)oxides as determined by various analytical methods including Fe-EXAFS and Mössbauer spectroscopy (Rose et al., 1997; Chan et al., 2004; Chan et al., 2009; Toner et al., 2009; Chen et al., 2018; ThomasArrigo et al., 2022). Synthetic P-Fh coprecipitates (P/Fe 0.05 and 0.09) prepared from Fe(III) solutions exhibited a decrease in the magnitude peak arising from corner-sharing Fe-Fe bonds, and, at the highest P loading, the particle size decreased from ~0.2 to 0.15 nm as determined by Fe-EXAFS and PDF (Kraal et al., 2019). Thus, coprecipitation of Fh with P, especially at a concentration of P/Fe 0.1, leads to a Fh with smaller particle size and crystallinity as we determined from XRD (Figure 1). This includes the observed shifting and broadening of the 2-line ferrihydrite reflections. Alginate appears to similarly impact Fh mineralogy, as XRD and Mössbauer data from FhAlg samples indicate slightly smaller particle size and crystallinity than pure Fh, in agreement with findings by Mikutta et al. (2008). Therefore, the coprecipitation of Fh with either alginate or P at low concentrations subtly influences Fh mineralogy. We speculate that simultaneous

coprecipitation with both alginate and P may have an additive effect on the mineral structure of Fh.

4.3. Dissolution kinetics: impact of phosphate and alginate

4.3.1. Abiotic dissolution

Reductive dissolution of the Fhs mediated by ascorbate was rapid, reaching 100% within hours. This can be attributed to citrate and ascorbate attaching to the surface thereby forming easily detachable complexes that are rapidly reduced in solution (Kraal et al., 2019; Ahmed et al., 2024). The excess concentration of the components in the BCA (bicarbonate citrate ascorbate) solution oversaturates the surface sites of the Fhs, whilst also desorbing P and preventing P from re-adsorbing back to the surface of the Fhs. This competitive ligand exchange reaction explains the rapid release of P, especially for the minerals with pre-adsorbed P. The accumulation of P exceeded that of dissolved Fe(II), as was observed by Kraal et al. (2019) (Figure 9). This is likely due to the fact that the molybdenum blue method required the use of a strong acid and an additional reducing agent (ascorbic acid), which dissolved and reduced colloidal Fe thereby releasing associated P (Kraal et al., 2019). Moreover, the extended time required to reach colour stability (40 min) further contributes to this reaction. Therefore, the release of P should be related to the release of $Fe(II)_{<0.22\mu m}$ (colloidal Fe + dissolved Fe(II)) rather than dissolved Fe(II) alone.

A comparison of the release of P and $Fe(II)_{<0.22\mu m}$ during the dissolution of the Fhs is consistent with complete or nearly complete congruency (Figure S9), suggesting a homogenous or nearly homogenous distribution of P from the surface to the centre of each particle. Deviations from unity, however, were observed particularly for FhAds 0.1 and FhAlgAds 0.1 that can be attributed to the desorption of P mediated by competing ligands as explained above. Even for the FhCop 0.1 and FhAlgCop 0.1, some deviation from unity was observed suggesting that P was

associated with the surface as well as incorporated within the Fh aggregates. These results are in agreement with the ζ-potential measurements, particularly for the alginate-free Fhs. Moreover, our results also show that coprecipitation with alginate did not impact the distribution of P within the mineral phase, since the release of P behaved similarly during dissolution between alginate-free Fhs and alginate-Fh coprecipitates (Figure 9 and S9).

The sorption mode of P and the presence of alginate clearly affected the reactivity of the Fhs to reductive dissolution, with coprecipitates (P and/or alginate) being reduced the fastest. SSA alone cannot explain our observations, because the rate of reduction of FhCop 0.1 was faster than that of FhAds 0.1 despite having a similar SSA. Moreover, the alginate-Fh coprecipitates had a lower SSA than their alginate-free counterparts, but they were reduced at a faster rate. Likewise, coprecipitation of P and/or alginate at the low initial P/Fe ratios in this study had a relatively minor impact on the Fh structure, with subtle decreases in structural coherency. Kraal et al. (2019) also found that Fhs coprecipitated with P (0.05 or 0.09 P/Fe mol:mol) or Si (0.04 or 0.09 Si/Fe mol:mol) were reduced faster than pure Fh and their corresponding Fhs with pre-adsorbed P or Si under similar conditions used in this study. Likewise, P-lepidocrocite coprecipitates formed from the oxidation of Fe(II) with P/Fe molar ratios of 0.03-0.05 completely dissolved in oxalate, while those with ratios of 0.1-0.2 mol were reduced more quickly by ascorbate than P-free poorly crystalline lepidocrocite (Cumplido et al., 2000; Voegelin et al., 2019). Abiotic dissolution rates of synthetic Fh-polygalacturonic acid coprecipitates (C/Fe 0.36–1.25) by desferrioxamine B were significantly higher than that of pure Fh and inversely correlated with SSA (229–40 m^2/g) (Mikutta and Kretzschmar, 2008). Similarly, the alginate-Fh coprecipitate (C/Fe 1.18) showed higher dissolution rates than pure Fh despite having half the SSA (Mikutta and Kretzschmar 2008). The apparent improvement in the dissolution of these coprecipitates (oxyanions or OM) was attributed

to changes in crystallinity, coupled with alterations to the macroscopic properties of the mineral, including: aggregation state, particle size, and dispersion of the mineral particles (Mikutta and Kretzschmar, 2008; Kaegi et al., 2010; Poggenburg et al., 2016). Consequently, increased repulsion between the Fh particles may facilitate the access of the reducing agent to the reactive iron sites, a process that is apparently amplified in cases where coprecipitation occurs with an oxyanion and OM. Unlike our findings, algae-derived OM-Fh coprecipitates (C/Fe 1–5 mol:mol) were reduced about ~14x slower than pure Fh by Na-dithionite (Wen et al., 2023). Under the same conditions, P-Fh (P/Fe 0.1 mol:mol) and P-algae-derived-OM-Fh (C/Fe 2 and P/Fe 0.1 mol:mol) coprecipitates were reduced 9 and 21x slower than pure Fh, respectively (Wen et al., 2023). Moreover, forest-floor OM-Fh coprecipitates (C/Fe 0.4-2.8 mol:mol) were reduced 5-29x slower than pure Fh by Na-dithionite (Eusterhues et al., 2014a). The difference in the findings between those studies and our study can be attributed to the different properties/composition of the OM used.

Pre-adsorption of P to the Fhs also affected their reducibility, such that reduction occurred at a rate equivalent to or slightly higher than P-free Fhs, but slower than P-Fh coprecipitates at corresponding P/Fe molar ratios in agreement with Kraal et al. (2019). The maximum adsorption capacity of Fh and FhAlg was determined to be ~0.21 and ~0.12 P/Fe (mol:mol), respectively. This suggests that for Fh and FhAlg, P occupied up to half or the maximum of the available reactive sites, respectively. P may hinder reduction via two mechanisms: 1. P may block the reducing agent/ligand from reaching the reactive site (Borch et al., 2007; O'Loughlin et al., 2010; O'Loughlin et al., 2013), and 2. P at the low loadings employed in this study may induce particle aggregation leading to the lower exposure of reactive sites (Kraal et al., 2019). On the other hand, adsorbed P may also facilitate reduction by preventing the aggregation of the Fh particles through

repulsive forces (Kukkadapu et al., 2004). These mechanisms likely played a role in our experiments leading to the observed results.

4.3.2. Biotic dissolution

The microbial reduction experiments with *S. putrefaciens* CN32 displayed the same overall picture of the reactivity of the Fhs as the abiotic reduction experiments. In fact, the rates of abiotic and biotic reduction were positively correlated with an R^2 value of 0.8 indicating that the mechanisms that control the abiotic rate of Fe reduction also apply to that mediated biotically (Figure S10). In contrast to our observations, Borch et al. (2009) reported that the degree of reduction of Fh-coated sand by *S. putrefaciens* CN32 significantly decreased with increasing P surface coverage (50% and 100%). Likewise, O'Loughlin et al. (2013) found that the rate of reduction of P-lepidocrocite coprecipitates (0.007 – 0.1 P/Fe mol:mol) by *S. putrefaciens* CN32 decreased relative to that of P-free lepidocrocite. The difference in the findings between those studies and this study could be attributed to the properties of the synthetic mineral and the suspension of the mineral vs. mineral coating on sand. In the latter case, aggregation and interaction of the Fh particles is limited whereas in suspension adsorbed P may impose repulsion between the Fh particles facilitating access of bacteria to reactive sites.

P was detected in the CDM and its release can be attributed to weakly bound P. P is also an important limiting nutrient for bacteria and its release into solution may have stimulated the growth of bacteria. However, cell count (CFU/mL) remained more-or-less comparable across treatments indicating that bacterial growth may have played a minor role in dictating the rate of Fe reduction (Figure S6). P may also stimulate the reduction of Fe by forming aqueous complexes with Fe(II) or a ferrous bearing P mineral thereby preventing Fe(II) from saturating the surface of the Fhs, which otherwise would block bacteria from reaching reactive sites. Indeed, across all

experiments, the P_{prop} of dissolved P decreased throughout the duration of the experiment, suggesting that P may have additionally stimulated the biotic reduction by thermodynamically driving the reaction forward (Fredrickson et al., 1998; Zachara et al., 1998; Zachara et al., 2002; Kukkadapu et al., 2004).

Alginate enhanced the rate of reduction despite forming large aggregates and possessing a negative surface charge. Past studies have shown that in the case of OM-Fe associations, the factors that control the bioavailability of Fe include: the mode of association between the mineral and OM (i.e. adsorption vs. coprecipitation) (Eusterhues et al., 2014a; Kleber et al., 2015), type and composition of OM (Poggenburg et al., 2016; Wen et al., 2023), C/Fe molar ratio (Shimizu et al., 2013; Eusterhues et al., 2014; Adhikari et al., 2017), surface charge (Amstaetter et al., 2012), and extent of OM induced aggregation (Amstaetter et al., 2012; Adhikari et al., 2016; Poggenburg et al., 2016; Poggenburg et al., 2018; Wen et al., 2023). OM may also enhance the rate of reduction by 1. acting as electron shuttles (depending on the composition of the OM and C/Fe ratio) (Shimizu et al., 2013; Adhikari et al., 2017), 2. complexing Fe(II) away from the surface of the mineral (like P) (Urrutia et al., 1999; Adhikari et al., 2017), and 3. altering the crystallinity of the mineral during coprecipitation (Eusterhues et al., 2014a; Cooper et al., 2017). Alginate lacks quinones like structures that function as electron shuttles, moreover alginate poorly complexes with Fe(II). In fact, the proportion of $Fe(II)_{dissolved}$ relative to $Fe(II)_{total}$ during the reduction of alginate-Fh coprecipitates was comparable to that of alginate-free Fhs (Figure 5). Thus, the subtle impact of alginate on the crystallinity of the Fh apparently overcomes the inhibitory effect of the negative charge and particle aggregation leading the enhancement of Fe reduction by *S.putrefaciens* CN32. In agreement with our observations, a synthetic Fh-EPS coprecipitate (C/Fe 1.0) and naturally occurring BIOS were reduced more rapidly and to a greater extent than pure Fh by *S. putrefaciens*

CN32, despite having 13x and 2.5x lower SSA, respectively (Langley et al., 2009b; Langley et al., 2009e; Poggenburg et al., 2016).

Across all experiments, P enhanced the extent of Fe reduction, whereas alginate had a negative impact. This can be attributed to the inhibiting effects of P and alginate on the Fe(II)-mediated transformation of Fh into crystalline Fe minerals that are less bioavailable than Fh (Fredrickson et al., 1998; Zachara et al., 1998; Glasauer et al., 2003; Cutting et al., 2009). Conversely, alginate may saturate the Fh surfaces as it is released during reduction thereby preventing the bacteria from reaching the reactive Fe sites. This notion is supported by the fact that the cell counts in the biotic microcosms with alginate-Fh coprecipitates decreased faster than those with alginate-free Fhs (Figure S6).

4.4. Biogenic secondary Fe minerals

It is well established in the literature that the specific identity of the biogenic minerals formed during Fe(III) reduction depends on a multitude of factors including: the stability of the iron oxide phase (Fredrickson et al., 1998; Cutting et al., 2009), Fe(II) concentration and rate of release (Fredrickson et al., 1998; Hansel et al., 2003; Amstaetter et al., 2012), solution's chemistry (e.g. selection of buffer type (organic versus HCO_3^-)) (Fredrickson et al., 1998; Zachara et al., 2002), P concentration (Borch et al., 2007), OM content (Shimizu et al., 2013; Chen et al., 2015; Poggenburg et al., 2016; Adhikari et al., 2017), and the orientation of the microcosm vessel (Dippon et al., 2015). The transformation of Fh to crystalline Fe minerals is mediated by the electron transfer from Fe(II) upon adsorption to the surface of the Fh favoring lepidocrocite and goethite formation through dissolution-precipitation reactions or magnetite through solid-state reactions (Hansel et al., 2003; Kraal et al., 2022). Mineral transformation of Fh to goethite during faster reduction or magnetite during slower reduction has been reported in several studies (Hansel

et al., 2003; Borch et al., 2007; Amstaetter et al., 2012). Conversely, decreasing formation or a complete lack of goethite and magnetite during Fe(III) reduction of Fh with increasing contents P or OM has been observed as well (Amstaetter et al., 2012; Eusterhues et al., 2014; Henneberry et al., 2012; Shimizu et al., 2013). P and OM have been reported to inhibit the transformation of Fh into more crystalline Fe minerals through various mechanisms. These include Fe(II) complexation, blocking Fe(II) binding sites on Fh, inhibiting Fe (oxyhydr)oxide polymerization, and direct electron transfer between OM and Fe(II) (Cornell and Schwertmann, 2003; Jones et al., 2009; Chen et al., 2015; Adhikari et al., 2016; Poggenburg et al., 2016; Kraal et al., 2022; Hua et al., 2023; Chi et al., 2024).

In our study, alginate favored the formation of goethite over magnetite, whereas P at low concentration (P/Fe 0.01 mol:mol) favored the formation of magnetite over goethite in line. The mode of sorption of P at the low molar ratio (0.01) used in this study also had an effect on the proportion of goethite, where pre-adsorption led to a lower proportion of goethite in comparison to the Fhs with coprecipitated P (Figure S7). This is likely due to the fact that in the former case more P is associated with the surface of Fh thereby contributing to the inhibition of Fe(II) mediated dissolution-precipitation reactions. Such notion is also applicable for the Fhs with the highest P concentration (P/Fe 0.1 mol:mol). At this concentration, the exposure of FhCop 0.1 to Fe(II) (Fe(II)/Fe(III) 0.28 or 1.6) for 6 days led to minor alteration of the short-range structure, but strongly suppressed Fe(III) crystallization as determined by Fe-EXAFS in accordance with our results (Kraal et al., 2022). In contrast, magnetite and green rust were the dominant biogenic minerals that formed following the reduction of Fh with 50% P surface coverage and OM-Fh associations (Borch et al., 2009). However, the CDM in our experiments did not contain carbonate, which was the dominant interlayer anion in the green rust phases found by Amstaetter et al. (2012),

Shimizu et al. (2013), and Borch et al. (2013). Finally, the combined presence of alginate and P led to complete inhibition of Fh transformation indicative of a cooperative inhibitory effect. In accordance with this observation, woody peat OM and P pre-adsorbed to Fh inhibited its complete transformation into crystalline phases following exposure to Fe(II) for 14 days (Chi et al., 2024).

5. Conclusions

In this study, we analyzed the stability of (P)-(OM)-Fh coprecipitates during abiotic and biotic reduction as a function of the sorption mode of P. We found that the sorption mode of P significantly impacted the reactivity of Fh towards reductive dissolution mediated abiotically and biotically, such that P-(OM)-Fh coprecipitates possessed the highest reactivity relative to (OM)-Fh with pre-adsorbed P at corresponding P content. Such enhancement was attributed to the modification of macroscopic properties of the Fhs such as aggregation state, as well as the "subtle" impacts of P and alginate on the mineralogical structure of the Fhs. P and alginate also modulated the composition of the biogenic secondary Fe minerals following the biotic reduction of the Fhs. Notably, complete stabilization of P-OM-Fh at the highest P loading (P/Fe 0.1) against transformation suggests a cooperative inhibitory effect. The study shows that even minor levels of P and/or OM impact Fh's susceptibility to reductive dissolution, especially when formed from coprecipitation. Moreover, the high reactivity of P-OM-Fh coprecipitates implies that they poorly retain nutrients under reducing conditions in the environment suggesting a rapid release of P and C, which is relevant in both natural and engineered systems for carbon and nutrient management.

Supplementary Materials

Supplementary materials and data from this manuscript are available through:

Acknowledgements

The present research was entirely funded by a NSERC Discovery grant to D. Fortin. The authors are very thankful to Nimal DeSilva and *Smita* Mohanty (University of Ottawa) for their expertise and analyzing our samples with the ICP-OES, the Ján Veizer Stable Isotope Lab (University of Ottawa) for their expertise and analysis of carbon content. We would also like to thank Glenn Poirier (University of Ottawa) for his guidance and expertise in using the SEM and FESEM.

Declaration of Competing Interest

The authors declare that they have no known competing financial interests or personal relationships that could have appeared to influence the work reported in this paper.

References

Adhikari, D., Poulson, S.R., Sumaila, S., Dynes, J.J., McBeth, J.M., Yang, Y., 2016. Asynchronous reductive release of iron and organic carbon from hematite–humic acid complexes. Chem. Geol., 430: 13-20.

Adhikari, D., Zhao, Q., Das, K., Mejia, J., Huang, R., Wang, X., Poulson, S.R., Tang, Y., Roden, E.E., Yang, Y., 2017. Dynamics of ferrihydrite-bound organic carbon during microbial Fe reduction. Geochim. Cosmochim. Acta, 212: 221-233.

Ahmed, M., Chen, K.-Y., Tsao, F.-Y., Hsieh, Y.-C., Liu, Y.-T., Tzou, Y.-M., 2024. Promotion of phosphate release from humic acid-iron hydroxide coprecipitates in the presence of citric acid. Environ. Res., 240: 117517.

Amstaetter, K., Borch, T., Kappler, A., 2012. Influence of humic acid imposed changes of ferrihydrite aggregation on microbial Fe (III) reduction. Geochim. Cosmochim. Acta, 85: 326-341.

Arai, Y., Sparks, D.L., 2001. ATR–FTIR spectroscopic investigation on phosphate adsorption mechanisms at the ferrihydrite–water interface. J. Colloid Interface Sci., 241(2): 317-326.

Baken, S., Moens, C., van der Grift, B., Smolders, E., 2016. Phosphate binding by natural iron-rich colloids in streams. Water Res., 98: 326-333.

Baken, S., Verbeeck, M., Verheyen, D., Diels, J., Smolders, E., 2015. Phosphorus losses from agricultural land to natural waters are reduced by immobilization in iron-rich sediments of drainage ditches. Water Res., 71: 160-170.

Borch, T., Masue, Y., Kukkadapu, R.K., Fendorf, S., 2007. Phosphate imposed limitations on biological reduction and alteration of ferrihydrite. Environ. Sci. Technol., 41(1): 166-172.

Cabrera, F., De Arambarri, P., Madrid, L., Toga, C., 1981. Desorption of phosphate from iron oxides in relation to equilibrium pH and porosity. Geoderma, 26(3): 203-216.

Cardenas-Jiron, G., Leal, D., Matsuhiro, B., Osorio-Roman, I.O., 2011. Vibrational spectroscopy and density functional theory calculations of poly-D-mannuronate and heteropolymeric fractions from sodium alginate. J. Raman Spectrosc., 42(4): 870-878.

Chan, C.S., De Stasio, G., Welch, S.A., Girasole, M., Frazer, B.H., Nesterova, M.V., Fakra, S., Banfield, J.F., 2004. Microbial polysaccharides template assembly of nanocrystal fibers. Science, 303(5664): 1656-8.

Chan, C.S., Fakra, S.C., Edwards, D.C., Emerson, D., Banfield, J.F., 2009. Iron oxyhydroxide mineralization on microbial extracellular polysaccharides. Geochim. Cosmochim. Acta, 73(13): 3807-3818.

Chandıa, N., Matsuhiro, B., Vásquez, A., 2001. Alginic acids in Lessonia trabeculata: characterization by formic acid hydrolysis and FT-IR spectroscopy. Carbohydr. Polym., 46(1): 81-87.

Châtellier, X., Grybos, M., Abdelmoula, M., Kemner, K.M., Leppard, G.G., Mustin, C., West, M.M., Paktunc, D., 2013. Immobilization of P by oxidation of Fe (II) ions leading to nanoparticle formation and aggregation. Appl. Geochem., 35: 325-339.

Chen, C., Dynes, J.J., Wang, J., Sparks, D.L., 2014. Properties of Fe-organic matter associations via coprecipitation versus adsorption. Environ. Sci. Technol., 48(23): 13751-9.

Chen, C., Kukkadapu, R., Sparks, D.L., 2015. Influence of Coprecipitated Organic Matter on Fe^{2+}(aq)-Catalyzed Transformation of Ferrihydrite: Implications for Carbon Dynamics. Environ. Sci. Technol., 49(18): 10927-36.

Chen, K.-Y., Hsu, L.-C., Chan, Y.-T., Cho, Y.-L., Tsao, F.-Y., Tzou, Y.-M., Hsieh, Y.-C., Liu, Y.-T., 2018. Phosphate removal in relation to structural development of humic acid-iron coprecipitates. Sci. Rep., 8(1): 10363.

Chi, J., Ou, Y., Li, F., Zhang, W., Zhai, H., Liu, T., Chen, Q., Zhou, X., Fang, L., 2024. Cooperative roles of phosphate and dissolved organic matter in inhibiting ferrihydrite transformation and their distinct fates. Sci. Total Environ., 908: 168376.

Cismasu, A.C., Williams, K.H., Nico, P.S., 2016. Iron and Carbon Dynamics during Aging and Reductive Transformation of Biogenic Ferrihydrite. Environ. Sci. Technol., 50(1): 25-35.

Conley, D.J., Carstensen, J., Vaquer-Sunyer, R., Duarte, C.M., 2009. Ecosystem thresholds with hypoxia, Eutrophication in Coastal Ecosystems: Towards better understanding and management strategies Selected Papers from the Second International Symposium on Research and Management of Eutrophication in Coastal Ecosystems, 20–23 June 2006, Nyborg, Denmark. Springer, pp. 21-29.

Cooper, R.E., Eusterhues, K., Wegner, C.-E., Totsche, K.U., Küsel, K., 2017. Ferrihydrite-associated organic matter (OM) stimulates reduction by Shewanella oneidensis MR-1 and a complex microbial consortia. Biogeosciences, 14(22): 5171-5188.

Cornell, R.M., Schwertmann, U., 2003. The iron oxides: structure, properties, reactions, occurrences, and uses, 664. Wiley-vch Weinheim.

Cumplido, J., Barrón, V., Torrent, J., 2000. Effect of phosphate on the formation of nanophase lepidocrocite from Fe (II) sulfate. Clays Clay Miner., 48(5): 503-510.

Curti, L., Moore, O.W., Babakhani, P., Xiao, K.-Q., Woulds, C., Bray, A.W., Fisher, B.J., Kazemian, M., Kaulich, B., Peacock, C.L., 2021. Carboxyl-richness controls organic carbon preservation during coprecipitation with iron (oxyhydr)oxides in the natural environment. Commun. Earth Environ., 2(1).

Cutting, R., Coker, V., Fellowes, J., Lloyd, J., Vaughan, D., 2009. Mineralogical and morphological constraints on the reduction of Fe (III) minerals by Geobacter sulfurreducens. Geochim. Cosmochim. Acta, 73(14): 4004-4022.

Dippon, U., Schmidt, C., Behrens, S., Kappler, A., 2015. Secondary mineral formation during ferrihydrite reduction by Shewanella oneidensis MR-1 depends on incubation vessel orientation and resulting gradients of cells, Fe^{2+} and Fe minerals. Geomicrobiol. J., 32(10): 878-889.

Dong, H., Huang, L., Zhao, L., Zeng, Q., Liu, X., Sheng, Y., Shi, L., Wu, G., Jiang, H., Li, F., Zhang, L., Guo, D., Li, G., Hou, W., Chen, H., 2022. A critical review of mineral–microbe interaction and co-evolution: mechanisms and applications. National Science Review, 9(10).

Dong, H., Zeng, Q., Sheng, Y., Chen, C., Yu, G., Kappler, A., 2023. Coupled iron cycling and organic matter transformation across redox interfaces. Nature Reviews Earth & Environment, 4(9): 659-673.

Eusterhues, K., Hädrich, A., Neidhardt, J., Küsel, K., Keller, T., Jandt, K., Totsche, K., 2014. Reduction of ferrihydrite with adsorbed and coprecipitated organic matter: microbial reduction by Geobacter bremensis vs. abiotic reduction by Na-dithionite. Biogeosciences, 11(18): 4953-4966.

Eusterhues, K., Wagner, F.E., Häusler, W., Hanzlik, M., Knicker, H., Totsche, K.U., Kögel-Knabner, I., Schwertmann, U., 2008. Characterization of ferrihydrite-soil organic matter coprecipitates by X-ray diffraction and Mossbauer spectroscopy. Environ. Sci. Technol., 42(21): 7891-7897.

Fabisch, M., Freyer, G., Johnson, C.A., Buchel, G., Akob, D.M., Neu, T.R., Kusel, K., 2016. Dominance of 'Gallionella capsiferriformans' and heavy metal association with Gallionella-like stalks in metal-rich pH 6 mine water discharge. Geobiology, 14(1): 68-90.

Field, H.R., Whitaker, A.H., Henson, J.A., Duckworth, O.W., 2019. Sorption of copper and phosphate to diverse biogenic iron (oxyhydr) oxide deposits. Sci. Total Environ., 697: 134111.

Fortin, D., Langley, S., 2005. Formation and occurrence of biogenic iron-rich minerals. Earth-Sci. Rev., 72(1-2): 1-19.

Fortin, D., Leppard, G.G., Tessier, A., 1993. Characteristics of lacustrine diagenetic iron oxyhydroxides. Geochim. Cosmochim. Acta, 57(18): 4391-4404.

Fredrickson, J.K., Zachara, J.M., Kennedy, D.W., Dong, H., Onstott, T.C., Hinman, N.W., Li, S.-m., 1998. Biogenic iron mineralization accompanying the dissimilatory reduction of hydrous ferric oxide by a groundwater bacterium. Geochim. Cosmochim. Acta, 62(19-20): 3239-3257.

Gálvez, N., Barrón, V., Torrent, J., 1999. Effect of phosphate on the crystallization of hematite, goethite, and lepidocrocite from ferrihydrite. Clays Clay Miner., 47(3): 304-311.

Gault, A.G., Ibrahim, A., Langley, S., Renaud, R., Takahashi, Y., Boothman, C., Lloyd, J.R., Clark, I.D., Ferris, F.G., Fortin, D., 2011. Microbial and geochemical features suggest iron redox cycling within bacteriogenic iron oxide-rich sediments. Chem. Geol., 281(1-2): 41-51.

Glasauer, S., Weidler, P.G., Langley, S., Beveridge, T.J., 2003. Controls on Fe reduction and mineral formation by a subsurface bacterium. Geochimica et Cosmochimica Acta, 67(7): 1277-1288.

Grybos, M., Davranche, M., Gruau, G., Petitjean, P., 2007. Is trace metal release in wetland soils controlled by organic matter mobility or Fe-oxyhydroxides reduction? J. Colloid Interface Sci., 314(2): 490-501.

Gunnars, A., Blomqvist, S., Johansson, P., Andersson, C., 2002. Formation of Fe (III) oxyhydroxide colloids in freshwater and brackish seawater, with incorporation of phosphate and calcium. Geochim. Cosmochim. Acta, 66(5): 745-758.

Han, L., Sun, K., Keiluweit, M., Yang, Y., Yang, Y., Jin, J., Sun, H., Wu, F., Xing, B., 2019. Mobilization of ferrihydrite-associated organic carbon during Fe reduction: Adsorption versus coprecipitation. Chem. Geol., 503: 61-68.

Hansel, C.M., Benner, S.G., Neiss, J., Dohnalkova, A., Kukkadapu, R.K., Fendorf, S., 2003. Secondary mineralization pathways induced by dissimilatory iron reduction of ferrihydrite under advective flow. Geochim. Cosmochim. Acta, 67(16): 2977-2992.

Hao, L., Guo, Y., Byrne, J.M., Zeitvogel, F., Schmid, G., Ingino, P., Li, J., Neu, T.R., Swanner, E.D., Kappler, A., Obst, M., 2016. Binding of heavy metal ions in aggregates of microbial cells, EPS and biogenic iron minerals measured in-situ using metal- and glycoconjugates-specific fluorophores. Geochim. Cosmochim. Acta, 180: 66-96.

Hua, J., Sun, J., Chen, M., Liu, C., Wu, F., 2023. Aqueous Fe (II)-catalyzed iron oxide recrystallization: Fe redox cycling and atom exchange, mineralogical recrystallization and contributing factor. Reviews in Environmental Science and Bio/Technology, 22(1): 55-78.

Hyacinthe, C., Van Cappellen, P., 2004. An authigenic iron phosphate phase in estuarine sediments: composition, formation and chemical reactivity. Mar. Chem., 91(1-4): 227-251.
Jones, A.M., Collins, R.N., Rose, J., Waite, T.D., 2009. The effect of silica and natural organic matter on the Fe (II)-catalysed transformation and reactivity of Fe (III) minerals. Geochim. Cosmochim. Acta, 73(15): 4409-4422.
Kaegi, R., Voegelin, A., Folini, D., Hug, S.J., 2010. Effect of phosphate, silicate, and Ca on the morphology, structure and elemental composition of Fe (III)-precipitates formed in aerated Fe (II) and As (III) containing water. Geochim. Cosmochim. Acta, 74(20): 5798-5816.
Kaiser, K., 2003. Sorption of natural organic matter fractions to goethite (α-FeOOH): effect of chemical composition as revealed by liquid-state ^{13}C NMR and wet-chemical analysis. Org. Geochem., 34(11): 1569-1579.
Kaiser, K., Guggenberger, G., Haumaier, L., Zech, W., 1997. Dissolved organic matter sorption on sub soils and minerals studied by ^{13}C-NMR and DRIFT spectroscopy. Eur. J. Soil Sci., 48(2): 301-310.
Kaiser, K., Mikutta, R., Guggenberger, G., 2007. Increased stability of organic matter sorbed to ferrihydrite and goethite on aging. Soil Sci. Soc. Am. J., 71(3): 711-719.
Kandori, K., Uchida, S., Kataoka, S., Ishikawa, T., 1992. Effects of silicate and phosphate ions on the formation of ferric oxide hydroxide particles. Journal of Materials Science, 27: 719-728.
Khare, N., Martin, J.D., Hesterberg, D., 2007. Phosphate bonding configuration on ferrihydrite based on molecular orbital calculations and XANES fingerprinting. Geochim. Cosmochim. Acta, 71(18): 4405-4415.
Kleber, M., Eusterhues, K., Keiluweit, M., Mikutta, C., Mikutta, R., Nico, P.S., 2015. Mineral–Organic Associations: Formation, Properties, and Relevance in Soil Environments. 130: 1-140.
Kraal, P., Van Genuchten, C.M., Behrends, T., 2022. Phosphate coprecipitation affects reactivity of iron (oxyhydr) oxides towards dissolved iron and sulfide. Geochim. Cosmochim. Acta, 321: 311-328.
Kraal, P., van Genuchten, C.M., Behrends, T., Rose, A.L., 2019. Sorption of phosphate and silicate alters dissolution kinetics of poorly crystalline iron (oxyhydr) oxide. Chemosphere, 234: 690-701.
Kukkadapu, R.K., Zachara, J.M., Fredrickson, J.K., Kennedy, D.W., 2004. Biotransformation of two-line silica-ferrihydrite by a dissimilatory Fe (III)-reducing bacterium: formation of carbonate green rust in the presence of phosphate. Geochim. Cosmochim. Acta, 68(13): 2799-2814.
Lalonde, K., Mucci, A., Ouellet, A., Gélinas, Y., 2012. Preservation of organic matter in sediments promoted by iron. Nature, 483(7388): 198-200.
Langley, S., Gault, A., Ibrahim, A., Renaud, R., Fortin, D., Clark, I.D., Ferris, F.G., 2009a. A Comparison of the Rates of Fe(III) Reduction in Synthetic and Bacteriogenic Iron Oxides by Shewanella putrefaciens CN32. Geomicrobiology Journal, 26(2): 57-70.
Langley, S., Gault, A., Ibrahim, A., Renaud, R., Fortin, D., Clark, I.D., Ferris, F.G., 2009b. A Comparison of the Rates of Fe(III) Reduction in Synthetic and Bacteriogenic Iron Oxides byShewanella putrefaciensCN32. Geomicrobiol. J., 26(2): 57-70.

Langley, S., Gault, A.G., Ibrahim, A., Takahashi, Y., Renaud, R., Fortin, D., Clark, I.D., Ferris, F.G., 2009c. Strontium desorption from bacteriogenic iron oxides (BIOS) subjected to microbial Fe(III) reduction. Chem. Geol., 262(3-4): 217-228.
Langley, S., Igric, P., Takahashi, Y., Sakai, Y., Fortin, D., Hannington, M.D., Schwarz-Schampera, U., 2009d. Preliminary characterization and biological reduction of putative biogenic iron oxides (BIOS) from the Tonga-Kermadec Arc, southwest Pacific Ocean. Geobiology, 7(1): 35-49.
Leal, D., Matsuhiro, B., Rossi, M., Caruso, F., 2008. FT-IR spectra of alginic acid block fractions in three species of brown seaweeds. Carbohydr Res, 343(2): 308-16.
Li, J., Ding, Y., Shi, Z., 2021. Binding properties of fulvic acid before and after fractionation on ferrihydrite: Effects of phosphate. ACS Earth Space Chem., 5(6): 1535-1543.
Li, Q., Hu, W., Li, L., Li, Y., 2023. Interactions between organic matter and Fe oxides at soil micro-interfaces: Quantification, associations, and influencing factors. Sci. Total Environ., 855: 158710.
Liu, Q., Li, X., Tang, J., Zhou, Y., Lin, Q., Xiao, R., Zhang, M., 2019. Characterization of goethite-fulvic acid composites and their impact on the immobility of Pb/Cd in soil. Chemosphere, 222: 556-563.
Luo, C., Wen, S., An, S., Lu, Y., Du, Y., 2021. Phosphate alters the compositional characteristics of humic acid adsorbed onto goethite. J. Soils Sed., 21: 3352-3366.
Martens, J., Mueller, C.W., Joshi, P., Rosinger, C., Maisch, M., Kappler, A., Bonkowski, M., Schwamborn, G., Schirrmeister, L., Rethemeyer, J., 2023. Stabilization of mineral-associated organic carbon in Pleistocene permafrost. Nat Commun, 14(1): 2120.
Mayer, T., Jarrell, W., 1995. Assessing colloidal forms of phosphorus and iron in the Tualatin River Basin. 0047-2425, Wiley Online Library.
Mejia, J., He, S., Yang, Y., Ginder-Vogel, M., Roden, E.E., 2018. Stability of Ferrihydrite-Humic Acid Coprecipitates under Iron-Reducing Conditions. Environ. Sci. Technol., 52(22): 13174-13183.
Mendez, J.C., Hiemstra, T., 2018. Carbonate adsorption to ferrihydrite: competitive interaction with phosphate for use in soil systems. ACS Earth Space Chem., 3(1): 129-141.
Mikutta, C., Kretzschmar, R., 2008. Synthetic coprecipitates of exopolysaccharides and ferrihydrite. Part II: Siderophore-promoted dissolution. Geochim. Cosmochim. Acta, 72(4): 1128-1142.
Mikutta, C., Mikutta, R., Bonneville, S., Wagner, F., Voegelin, A., Christl, I., Kretzschmar, R., 2008. Synthetic coprecipitates of exopolysaccharides and ferrihydrite. Part I: Characterization. Geochim. Cosmochim. Acta, 72(4): 1111-1127.
Mikutta, R., Lorenz, D., Guggenberger, G., Haumaier, L., Freund, A., 2014. Properties and reactivity of Fe-organic matter associations formed by coprecipitation versus adsorption: Clues from arsenate batch adsorption. Geochim. Cosmochim. Acta, 144: 258-276.
Murphy, J., Riley, J.P., 1962. A modified single solution method for the determination of phosphate in natural waters. Anal. Chim. Acta, 27: 31-36.
Najem, T., Langley, S., Fortin, D., 2016. A comparison of Fe(III) reduction rates between fresh and aged biogenic iron oxides (BIOS) by Shewanella putrefaciens CN32. Chem. Geol., 439: 1-12.
Namayandeh, A., Borkiewicz, O.J., Bompoti, N.M., Watson, S.K., Kubicki, J.D., Chrysochoou, M., Michel, F.M., 2023. Effects of Oxyanion Surface Loading on the Rate and Pathway of Ferrihydrite Transformation. ACS Earth Space Chem., 7(10): 2154-2165.

Namayandeh, A., Zhang, W., Watson, S.K., Borkiewicz, O.J., Bompoti, N.M., Chrysochoou, M., Penn, R.L., Michel, F.M., 2024. Goethite and Hematite Nucleation and Growth from Ferrihydrite: Effects of Oxyanion Surface Complexes. Environ. Sci. Technol., 58(13): 5952-5962.

O'Loughlin, E.J., Boyanov, M.I., Flynn, T.M., Gorski, C.A., Hofmann, S.M., McCormick, M.L., Scherer, M.M., Kemner, K.M., 2013. Effects of bound phosphate on the bioreduction of lepidocrocite (γ-FeOOH) and maghemite (γ-Fe2O3) and formation of secondary minerals. Environ. Sci. Technol., 47(16): 9157-9166.

O'Loughlin, E.J., Gorski, C.A., Scherer, M.M., Boyanov, M.I., Kemner, K.M., 2010. Effects of oxyanions, natural organic matter, and bacterial cell numbers on the bioreduction of lepidocrocite (γ-FeOOH) and the formation of secondary mineralization products. Environ. Sci. Technol., 44(12): 4570-4576.

Paige, C., Snodgrass, W., Nicholson, R.V., Scharer, J., He, Q., 1997. The effect of phosphate on the transformation of ferrihydrite into crystalline products in alkaline media. Water, Air, and Soil Pollution, 97: 397-412.

Patzner, M.S., Logan, M., McKenna, A.M., Young, R.B., Zhou, Z., Joss, H., Mueller, C.W., Hoeschen, C., Scholten, T., Straub, D., Kleindienst, S., Borch, T., Kappler, A., Bryce, C., 2022. Microbial iron cycling during palsa hillslope collapse promotes greenhouse gas emissions before complete permafrost thaw. Commun. Earth Environ., 3(1).

Pedrot, M., Le Boudec, A., Davranche, M., Dia, A., Henin, O., 2011. How does organic matter constrain the nature, size and availability of Fe nanoparticles for biological reduction? J. Colloid Interface Sci., 359(1): 75-85.

Poggenburg, C., Mikutta, R., Sander, M., Schippers, A., Marchanka, A., Dohrmann, R., Guggenberger, G., 2016. Microbial reduction of ferrihydrite-organic matter coprecipitates by Shewanella putrefaciens and Geobacter metallireducens in comparison to mediated electrochemical reduction. Chem. Geol., 447: 133-147.

Poggenburg, C., Mikutta, R., Schippers, A., Dohrmann, R., Guggenberger, G., 2018. Impact of natural organic matter coatings on the microbial reduction of iron oxides. Geochim. Cosmochim. Acta, 224: 223-248.

Possinger, A.R., Zachman, M.J., Dynes, J.J., Regier, T.Z., Kourkoutis, L.F., Lehmann, J., 2021. Co-precipitation induces changes to iron and carbon chemistry and spatial distribution at the nanometer scale. Geochim. Cosmochim. Acta, 314: 1-15.

Rose, J., Flank, A.-M., Masion, A., Bottero, J.-Y., Elmerich, P., 1997. Nucleation and growth mechanisms of Fe oxyhydroxide in the presence of PO4 ions. 2. P K-edge EXAFS study. Langmuir, 13(6): 1827-1834.

Rouquerol, J., Llewellyn, P., Rouquerol, F., 2007. Is the BET equation applicable to microporous adsorbents. Stud. Surf. Sci. Catal, 160(07): 49-56.

Santoro, V., Martin, M., Persson, P., Lerda, C., Said-Pullicino, D., Magnacca, G., Celi, L., 2019. Inorganic and organic P retention by coprecipitation during ferrous iron oxidation. Geoderma, 348: 168-180.

Schoepfer, V.A., Burton, E.D., Johnston, S.G., Kraal, P., 2017. Phosphate-imposed constraints on schwertmannite stability under reducing conditions. Environ. Sci. Technol., 51(17): 9739-9746.

Schwertmann, U., Cornell, R.M., 2008. Iron oxides in the laboratory: preparation and characterization. John Wiley & Sons.

Schwertmann, U., Wagner, F., Knicker, H., 2005. Ferrihydrite–Humic Associations. Soil Sci. Soc. Am. J., 69(4): 1009-1015.
Senn, A.-C., Kaegi, R., Hug, S.J., Hering, J.G., Mangold, S., Voegelin, A., 2015. Composition and structure of Fe (III)-precipitates formed by Fe (II) oxidation in water at near-neutral pH: Interdependent effects of phosphate, silicate and Ca. Geochim. Cosmochim. Acta, 162: 220-246.
Shimizu, M., Zhou, J., Schroder, C., Obst, M., Kappler, A., Borch, T., 2013. Dissimilatory reduction and transformation of ferrihydrite-humic acid coprecipitates. Environ. Sci. Technol., 47(23): 13375-84.
Smith, V.H., Tilman, G.D., Nekola, J.C., 1999. Eutrophication: impacts of excess nutrient inputs on freshwater, marine, and terrestrial ecosystems. Environ. Pollut., 100(1-3): 179-196.
Sowers, T.D., Harrington, J.M., Polizzotto, M.L., Duckworth, O.W., 2017. Sorption of arsenic to biogenic iron (oxyhydr) oxides produced in circumneutral environments. Geochim. Cosmochim. Acta, 198: 194-207.
Sowers, T.D., Stuckey, J.W., Sparks, D.L., 2018. The synergistic effect of calcium on organic carbon sequestration to ferrihydrite. Geochemical transactions, 19: 1-11.
Stookey, L.L., 1970. Ferrozine---a new spectrophotometric reagent for iron. Anal. Chem., 42(7): 779-781.
ThomasArrigo, L.K., Notini, L., Shuster, J., Nydegger, T., Vontobel, S., Fischer, S., Kappler, A., Kretzschmar, R., 2022. Mineral characterization and composition of Fe-rich flocs from wetlands of Iceland: Implications for Fe, C and trace element export. Sci. Total Environ., 816: 151567.
Toner, B.M., Santelli, C.M., Marcus, M.A., Wirth, R., Chan, C.S., McCollom, T., Bach, W., Edwards, K.J., 2009. Biogenic iron oxyhydroxide formation at mid-ocean ridge hydrothermal vents: Juan de Fuca Ridge. Geochim. Cosmochim. Acta, 73(2): 388-403.
Urrutia, M.M., Roden, E.E., Zachara, J.M., 1999. Influence of aqueous and solid-phase Fe (II) complexants on microbial reduction of crystalline iron (III) oxides. Environ. Sci. Technol., 33(22): 4022-4028.
van der Grift, B., Behrends, T., Osté, L., Schot, P., Wassen, M., Griffioen, J., 2016. Fe hydroxyphosphate precipitation and Fe (II) oxidation kinetics upon aeration of Fe (II) and phosphate-containing synthetic and natural solutions. Geochim. Cosmochim. Acta, 186: 71-90.
van der Grift, B., Osté, L., Schot, P., Kratz, A., van Popta, E., Wassen, M., Griffioen, J., 2018. Forms of phosphorus in suspended particulate matter in agriculture-dominated lowland catchments: Iron as phosphorus carrier. Sci. Total Environ., 631: 115-129.
Viollier, E., Inglett, P.W., Hunter, K., Roychoudhury, A.N., Van Cappellen, P., 2000. The ferrozine method revisited: Fe(II)/Fe(III) determination in natural waters. Applied Geochemistry, 15(6): 785-790.
Voegelin, A., Kaegi, R., Frommer, J., Vantelon, D., Hug, S.J., 2010. Effect of phosphate, silicate, and Ca on Fe (III)-precipitates formed in aerated Fe (II)-and As (III)-containing water studied by X-ray absorption spectroscopy. Geochim. Cosmochim. Acta, 74(1): 164-186.
Voegelin, A., Senn, A.-C., Kaegi, R., Hug, S.J., 2019. Reductive dissolution of As (V)-bearing Fe (III)-precipitates formed by Fe (II) oxidation in aqueous solutions. Geochemical transactions, 20: 1-13.

Voegelin, A., Senn, A.-C., Kaegi, R., Hug, S.J., Mangold, S., 2013. Dynamic Fe-precipitate formation induced by Fe (II) oxidation in aerated phosphate-containing water. Geochim. Cosmochim. Acta, 117: 216-231.
Wagai, R., Mayer, L.M., 2007. Sorptive stabilization of organic matter in soils by hydrous iron oxides. Geochim. Cosmochim. Acta, 71(1): 25-35.
Wang, X., Li, W., Harrington, R., Liu, F., Parise, J.B., Feng, X., Sparks, D.L., 2013. Effect of ferrihydrite crystallite size on phosphate adsorption reactivity. Environ. Sci. Technol., 47(18): 10322-10331.
Wen, S., Lu, Y., Dai, J., Huang, X., An, S., Liu, J., Liu, Z., Du, Y., Zhang, Y., 2023. Stability of organic matter-iron-phosphate associations during abiotic reduction of iron. J. Hazard. Mater., 449: 131016.
Wen, S., Lu, Y., Luo, C., An, S., Dai, J., Liu, Z., Zhong, J., Du, Y., 2022. Adsorption of humic acids to lake sediments: compositional fractionation, inhibitory effect of phosphate, and implications for lake eutrophication. J. Hazard. Mater., 433: 128791.
Xue, Q., Ran, Y., Tan, Y., Peacock, C.L., Du, H., 2019. Arsenite and arsenate binding to ferrihydrite organo-mineral coprecipitate: Implications for arsenic mobility and fate in natural environments. Chemosphere, 224: 103-110.
Yuan, G., Lavkulich, L., 1995. Colorimetric determination of phosphorus in citrate-bicarbonate-dithionite extracts of soils. Commun. Soil Sci. Plant Anal., 26(11-12): 1979-1988.
Zachara, J.M., Fredrickson, J.K., Li, S.-M., Kennedy, D.W., Smith, S.C., Gassman, P.L., 1998. Bacterial reduction of crystalline Fe3+ oxides in single phase suspensions and subsurface materials. American Mineralogist, 83(11): 1426-1443.
Zachara, J.M., Kukkadapu, R.K., Fredrickson, J.K., Gorby, Y.A., Smith, S.C., 2002. Biomineralization of poorly crystalline Fe (III) oxides by dissimilatory metal reducing bacteria (DMRB). Geomicrobiol. J., 19(2): 179-207.
Zeng, L., Li, X., Liu, J., 2004. Adsorptive removal of phosphate from aqueous solutions using iron oxide tailings. Water Res., 38(5): 1318-1326.
Zeng, Q., Huang, L., Ma, J., Zhu, Z., He, C., Shi, Q., Liu, W., Wang, X., Xia, Q., Dong, H., 2020. Bio-reduction of ferrihydrite-montmorillonite-organic matter complexes: Effect of montmorillonite and fate of organic matter. Geochim. Cosmochim. Acta, 276: 327-344.
Zhao, Q., Adhikari, D., Huang, R., Patel, A., Wang, X., Tang, Y., Obrist, D., Roden, E.E., Yang, Y., 2017. Coupled dynamics of iron and iron-bound organic carbon in forest soils during anaerobic reduction. Chem. Geol., 464: 118-126.
Zhao, Q., Poulson, S.R., Obrist, D., Sumaila, S., Dynes, J.J., McBeth, J.M., Yang, Y., 2016. Iron-bound organic carbon in forest soils: quantification and characterization. Biogeosciences, 13(16): 4777-4788.
Zhao, Y., Moore, O.W., Xiao, K.-Q., Curti, L., Fariña, A.O., Banwart, S.A., Peacock, C.L., 2022. The role and fate of organic carbon during aging of ferrihydrite. Geochim. Cosmochim. Acta, 335: 339-355.

Supplementary Material For

Stability of P-OM-ferrihydrite composites: Fe(III) dissolution kinetics and fate of phosphate under abiotic and biotic conditions

Tarek Najem[a] and Danielle Fortin[a*]

[a] Department of Earth and Environmental Sciences, University of Ottawa, Ottawa, Ontario, Canada

* Corresponding author: dfortin@uottawa.ca

Table S1: Description of the 2-line ferrihydrite minerals synthesized for this study.

Mineral	Description
Fh	Pure 2-line ferrihydrite
FhAds P/Fe 0.01	Ferrihydrite with pre-adsorbed phosphate with a P/Fe molar ratio of 0.01
FhAds P/Fe 0.1	Ferrihydrite with pre-adsorbed phosphate with a P/Fe molar ratio of 0.1
FhCop P/Fe 0.01	Ferrihydrite coprecipitated with phosphate at a P/Fe molar ratio of 0.01
FhCop P/Fe 0.1	Ferrihydrite coprecipitated with phosphate at a P/Fe molar ratio of 0.1
FhAlg	Ferrihydrite coprecipitated with alginate (C/Fe 1.00 mol:mol)
FhAlgAds P/Fe 0.01	Ferrihydrite coprecipitated with alginate (C/Fe 1.00 mol:mol) and with pre-adsorbed phosphate at a P/Fe molar ratio of 0.01
FhAlgAds P/Fe 0.1	Ferrihydrite coprecipitated with alginate (C/Fe 1.00 mol:mol) and with pre-adsorbed phosphate at a P/Fe molar ratio of 0.1
FhAlgCop P/Fe 0.01	Ferrihydrite coprecipitated with alginate (C/Fe 1.00 mol:mol) and phosphate at a P/Fe molar ratio of 0.01
FhAlgCop P/Fe 0.1	Ferrihydrite coprecipitated with alginate (C/Fe 1.00 mol:mol) and phosphate at a P/Fe molar ratio of 0.1

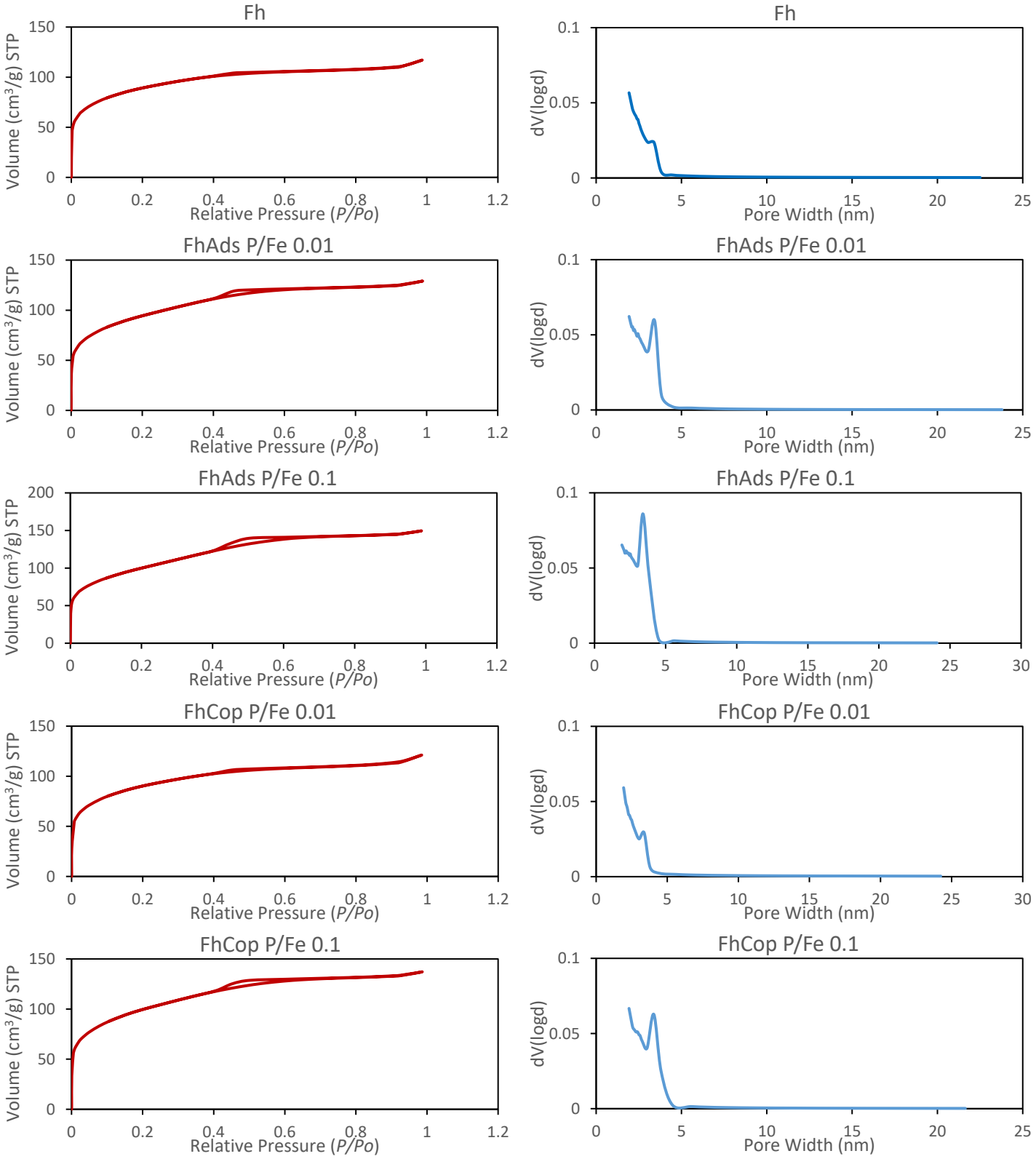

Figure S1: (a) N_2 adsorption/desorption isotherms and (b) Barett–Joyner–Halenda (BJH) distributions for the desorption branch of the isotherms of different ferrihydrite samples.

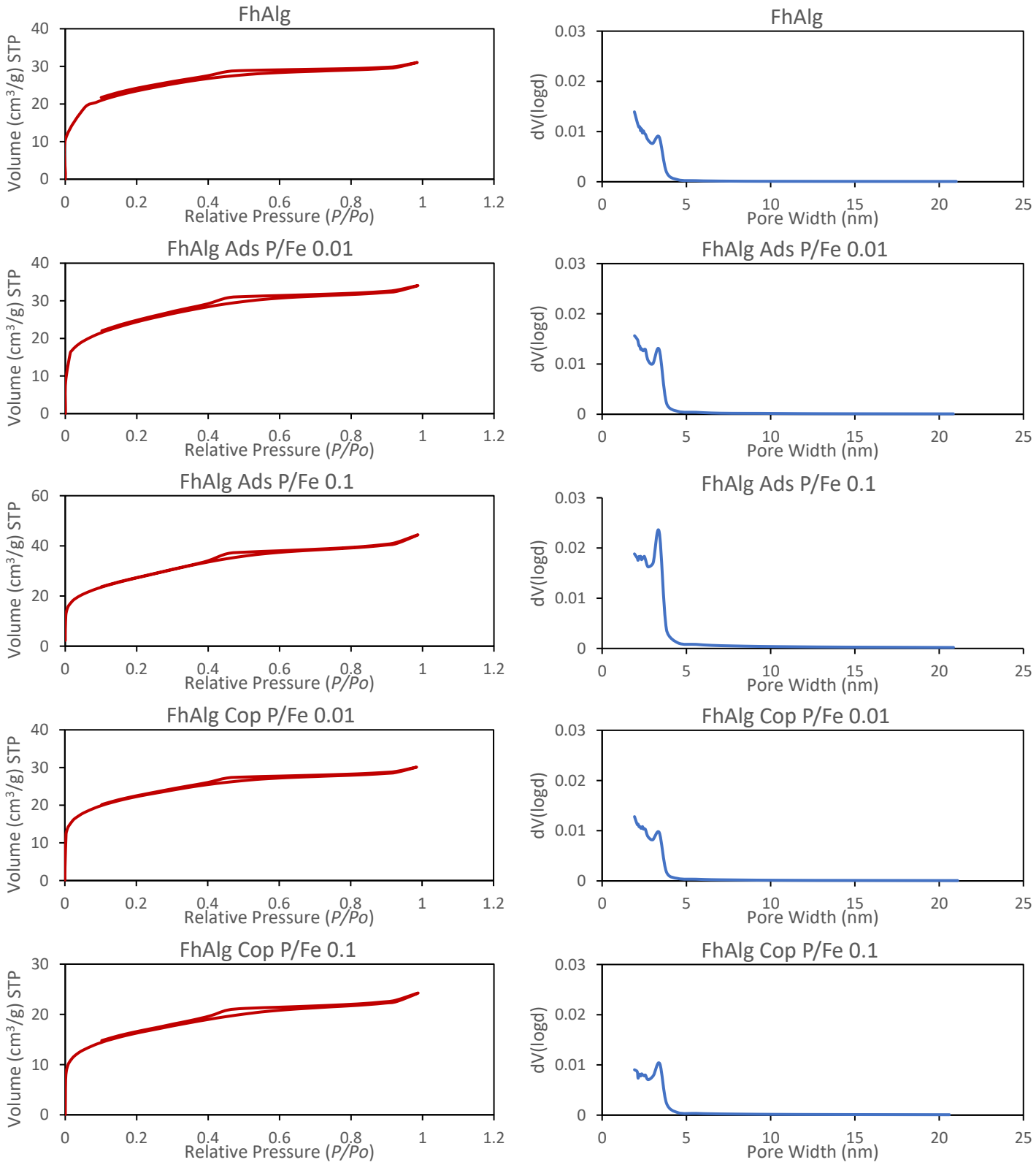

Figure S2: (a) N_2 adsorption/desorption isotherms and (b) Barett–Joyner–Halenda (BJH) distributions for the desorption branch of the isotherms of different ferrihydrite-alginate samples.

Table S2: IR band assignments for pure Na-alginate. Italicized wavenumber values correspond to bands obtained from the Savitsky-Golay secondary derivative with 19 points of smoothing.

Wavenumbers (cm^{-1})	**Assignment**
1596	ν_{asym}(C-O-O) carboxylate
1408	ν_{sym}(C-O-O) carboxylate
1298	δ(C-H)
1175	ν_{sym}(C-O) of glycosidic linkage
1130	ν(C-O) of pyranose ring
	ν(C-C) of pyranose ring
	δ(C-C-C) of pyranose ring
1080	ν(C-O-C) of pyranose ring
	ν(C-C) of pyranose ring
	ν_{asym}(C-O-C) of glycosidic linkage
1024	Vibrations due to mannuronic and guluronic acid residues:
	ν_{asym}(C-O-C) of glycosidic linkage
	ν(C-O) of pyranose ring
	ν(C-C)
	ν(C-O) of secondary alcohols
998	ν(C-O) of pyranose ring
	ν(C-C) of pyranose ring
	δ(C-C-C) of pyranose ring
950	Vibrations due to mannuronic acid residues:
	ν(C-C)
	δ(C-C-H)
935	ν(C-C) of mannuronic acid residues
883	δ(C1-H) β-mannuronic acid residues
814	Vibrations due to mannuronic acid residues:
	δ(C-O-C) of glycosidic linkage
	δ(C-C-C) of pyranose ring
	δ(O-C-C) of pyranose ring
	δ(C-C-H)
779	α-L-guluronic acid residues
725	Ring breathing

Band identification acquired from: Sartori et al. (1997); Chandıa et al. (2001); Leal et al. (2008); Cardenas-Jiron et al. (2011).

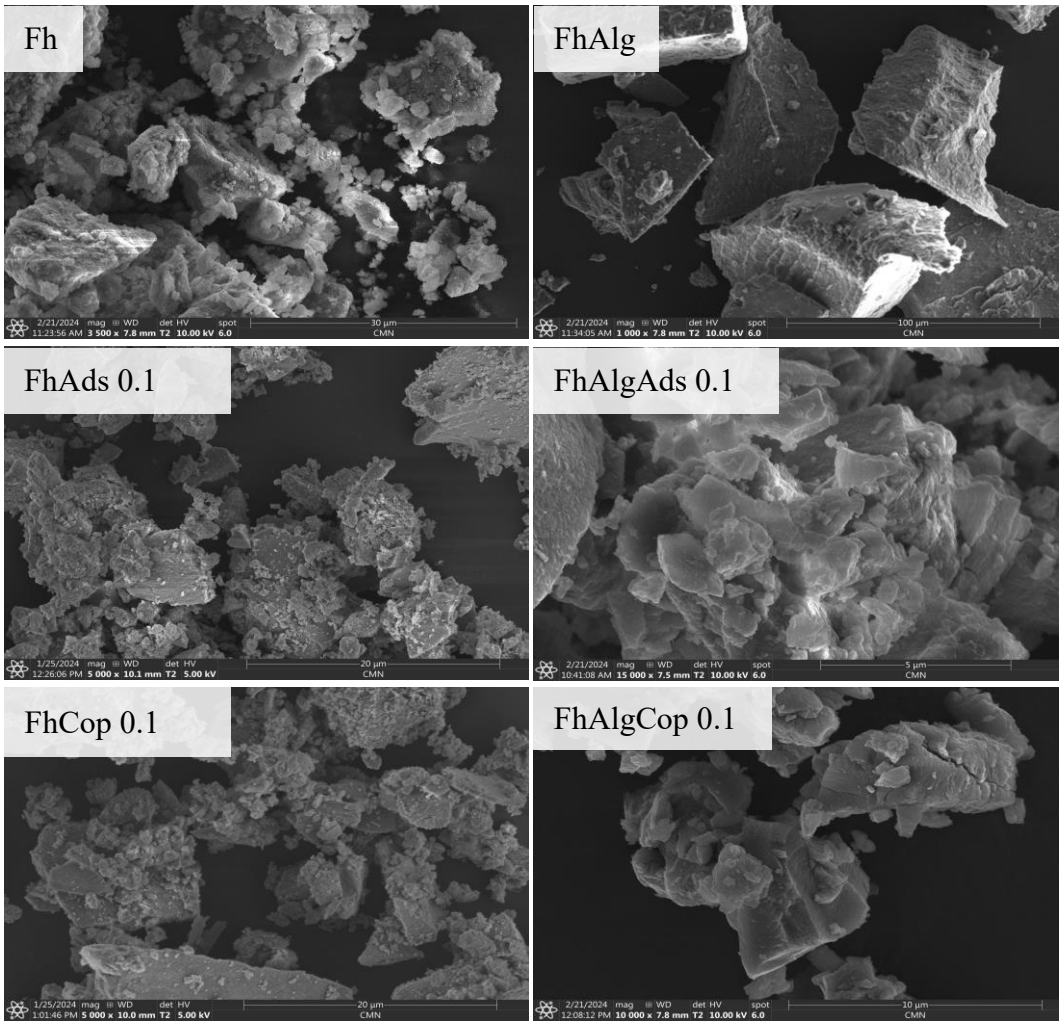

Figure S3: Electron micrographs of the ferrihydrite samples utilized for this study. They show how alginate affects the aggregate size of the minerals.

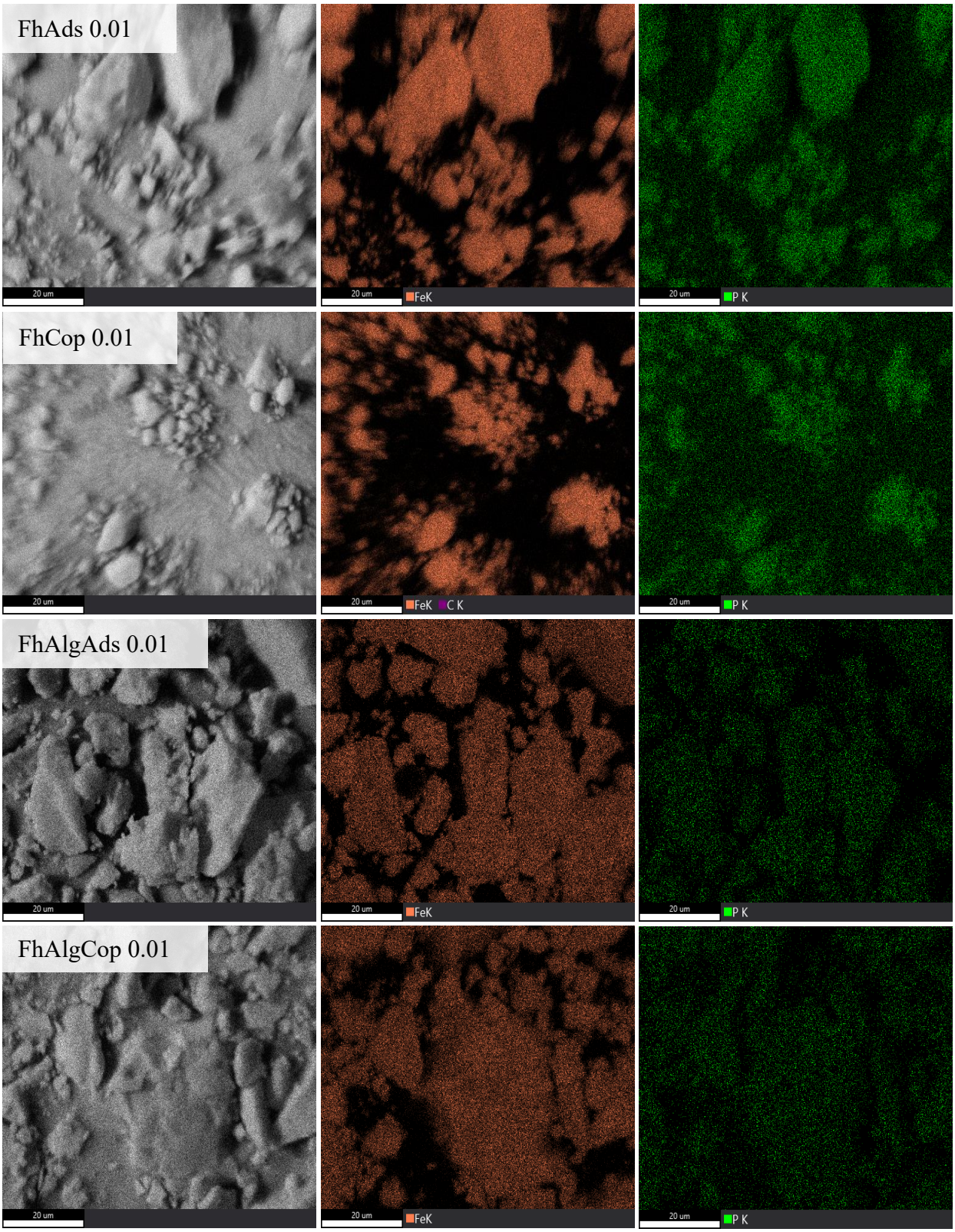

Figure S4: Elemental maps of the synthesized minerals. The maps show the strong relationship between the distribution of P and Fe indicating homogeneity.

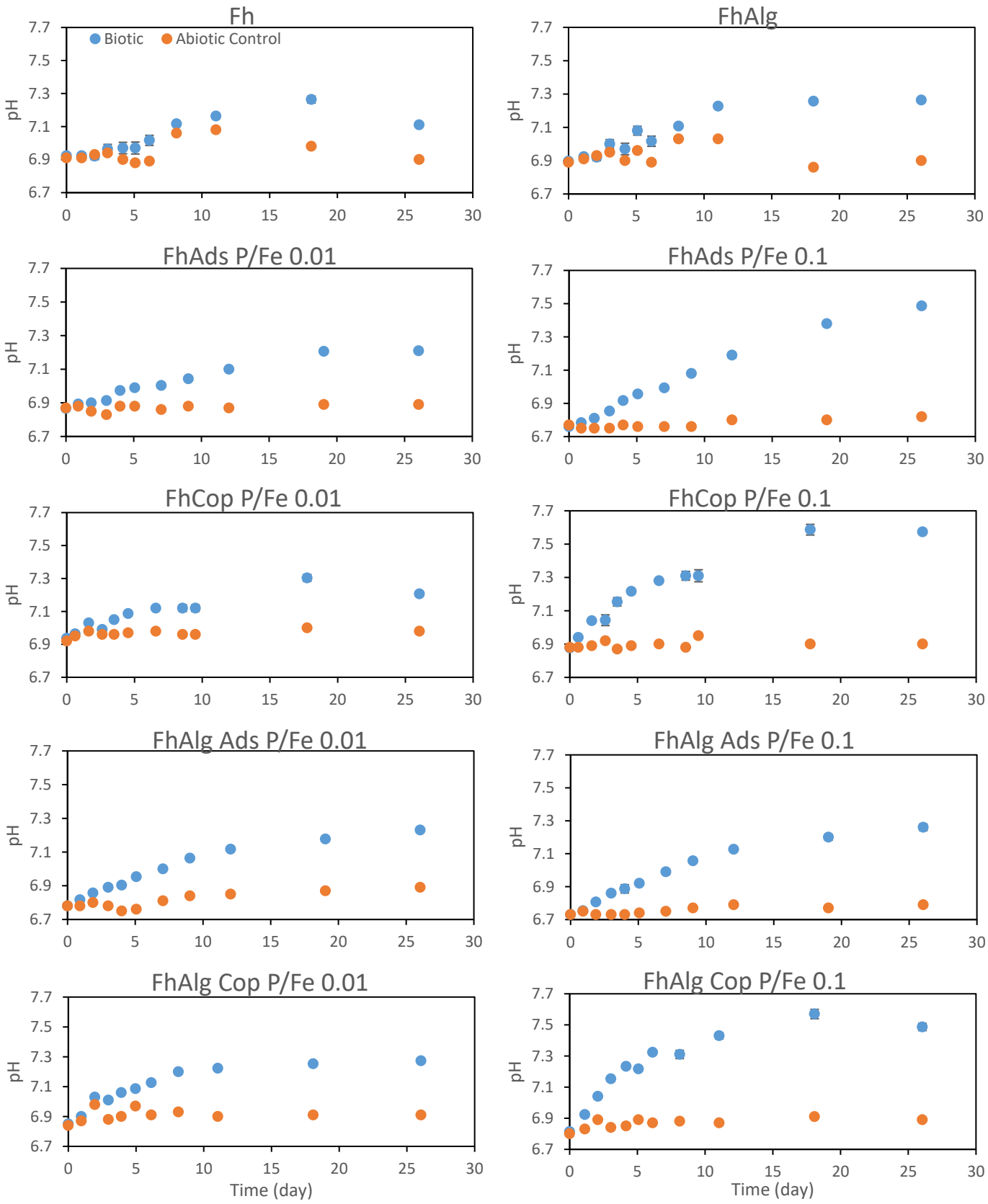

Figure S5: Changes in pH during the reduction of the various ferrihydrites studied by *S.putrefaciens* CN32.

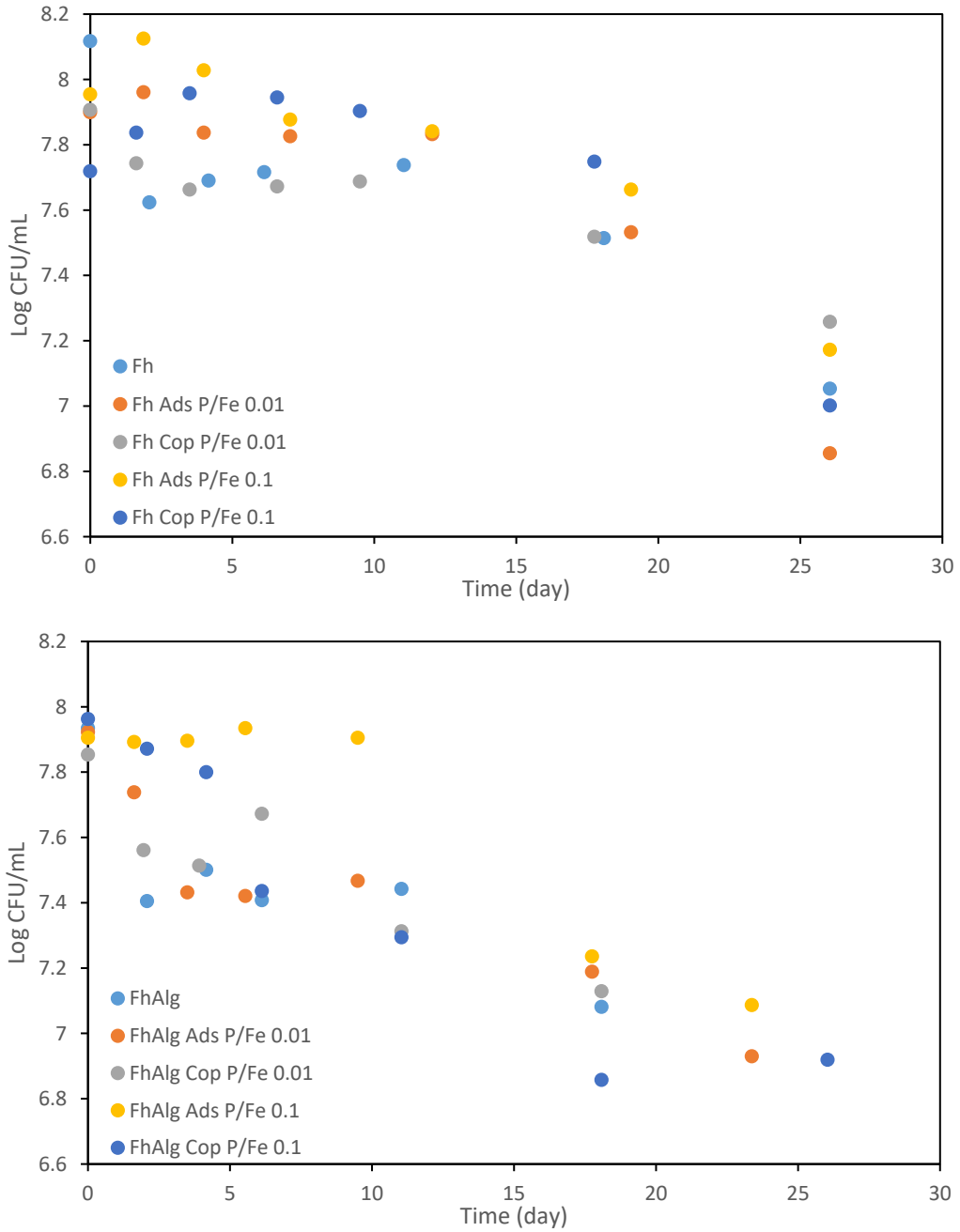

Figure S6: Changes in cell concentration of *S. putrefaciens* CN32 during the reduction of (top) 2-line ferrihydrite with adsorbed or coprecipitated phosphate (P/Fe 0.0, 0.01, 0.1 mol/mol), and (bottom) 2-line ferrihydrite-alginate composite (C/Fe 1.0 mol/mol) with adsorbed or coprecipitated phosphate (P/Fe 0.0, 0.01, 0.1 mol/mol). No growth was observed in the control microcosms. Data represents average of 3 replicates for each experiment.

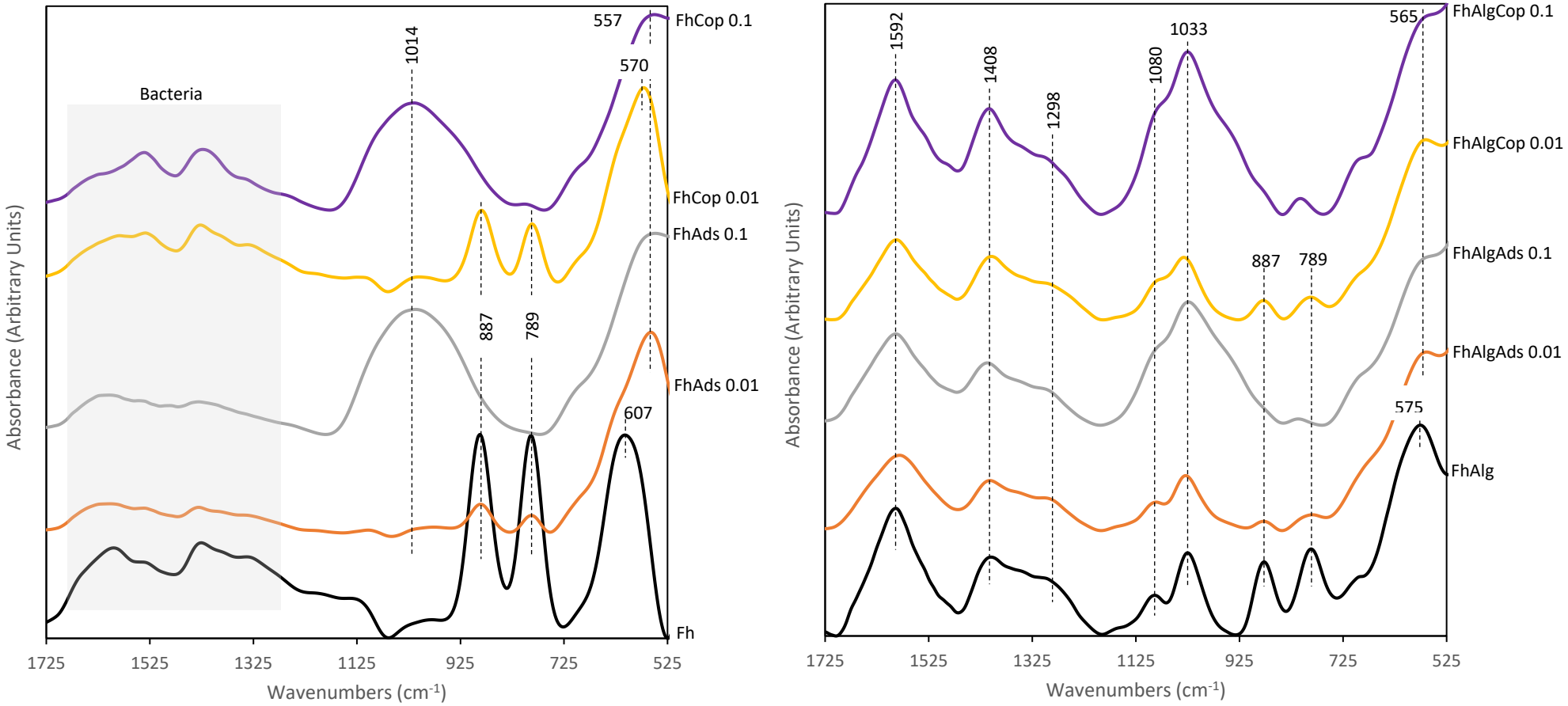

Figure S7: FTIR spectra of the biogenic secondary Fe minerals that formed following the reduction of the ferrihydrites by *S. putrefaciens* CN32. Reflections pertaining to goethite are those centered at 887, 789, and 607 cm^{-1} (Cornell and Schwertmann, 2003), while the main reflection pertaining to magnetite is centered at 570-557 cm^{-1} (Cornell and Schwertmann, 2003). The reflections in the shaded region may correspond to bacterial remnants.

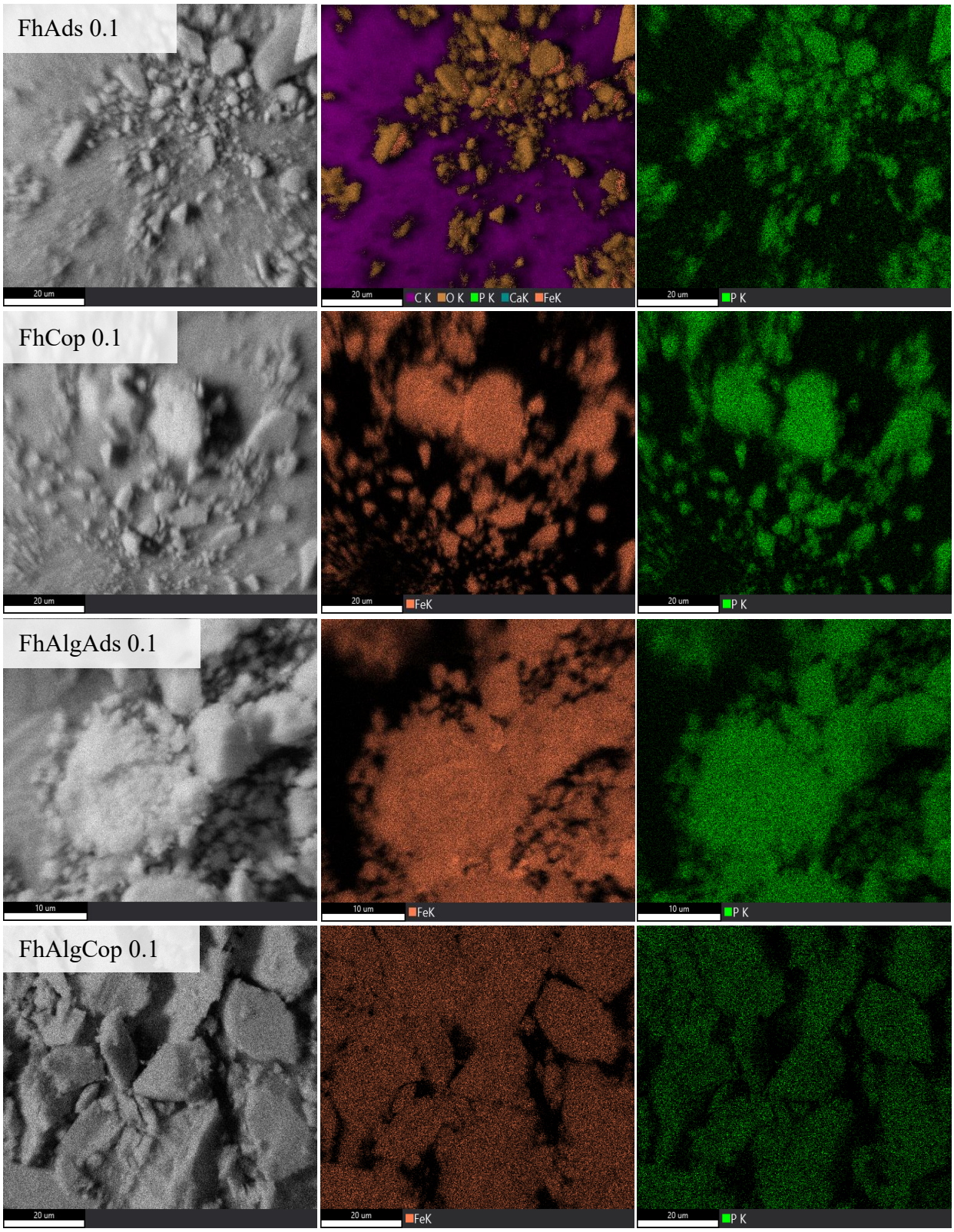

Figure S8: Elemental maps of select biogenic secondary Fe minerals that formed following the reduction of Fhs by *S. putrefaciens* CN32. The maps show the strong relationship between the distribution of P and Fe indicating homogeneity.

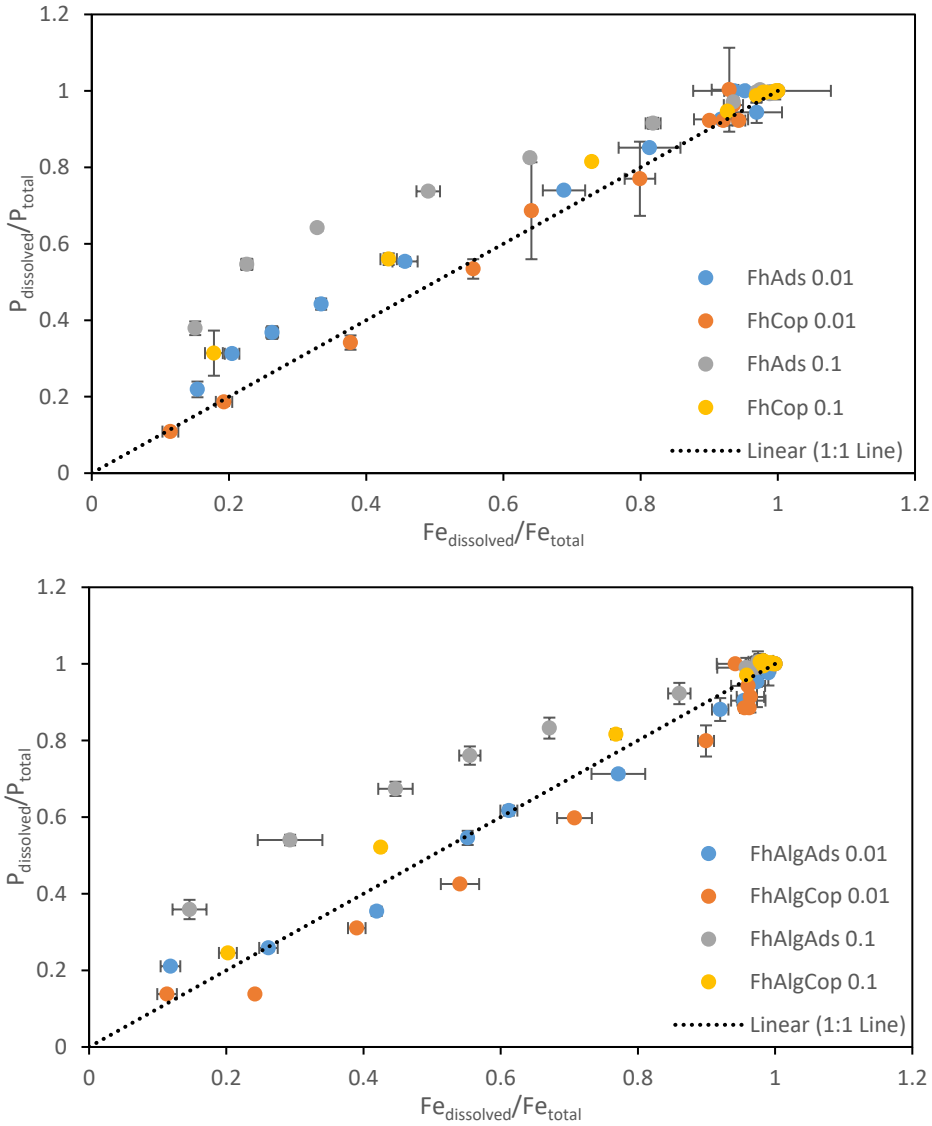

Figure S9: Fraction of dissolved P and Fe during Fh dissolution by ascorbate (pH 8.0). The dotted line indicates completely congruent dissolution. Error bars indicate the average deviation.

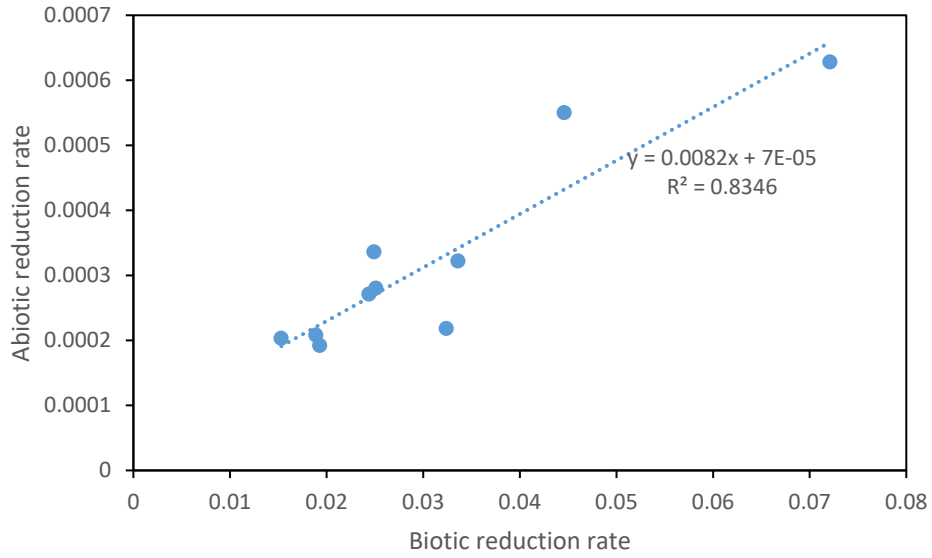

Figure S10: Relationship between the rates of reduction mediated by ascorbate (abiotic) and *S. putrefaciens* CN32 (biotic).

References

Cardenas-Jiron, G., Leal, D., Matsuhiro, B., Osorio-Roman, I.O., 2011. Vibrational spectroscopy and density functional theory calculations of poly-D-mannuronate and heteropolymeric fractions from sodium alginate. J. Raman Spectrosc., 42(4): 870-878.

Chandıa, N., Matsuhiro, B., Vásquez, A., 2001. Alginic acids in Lessonia trabeculata: characterization by formic acid hydrolysis and FT-IR spectroscopy. Carbohydr. Polym., 46(1): 81-87.

Cornell, R.M., Schwertmann, U., 2003. The iron oxides: structure, properties, reactions, occurrences, and uses, 664. Wiley-vch Weinheim.

Leal, D., Matsuhiro, B., Rossi, M., Caruso, F., 2008. FT-IR spectra of alginic acid block fractions in three species of brown seaweeds. Carbohydr Res, 343(2): 308-16.

Sartori, C., Finch, D.S., Ralph, B., Gilding, K., 1997. Determination of the cation content of alginate thin films by FTIR spectroscopy. Polymer, 38(1): 43-51.

Chapter 4: Effects of Gamma(γ)-Irradiation on the Physicochemical Properties and Bioavailability of Iron Oxyhydroxides Coprecipitated with Varying Concentrations of Na-Alginate

Tarek Najem[a], Prachi Joshi[b], Andreas Kappler[b], and Danielle Fortin[a]*

[a] Department of Earth and Environmental Sciences, University of Ottawa, 75 Laurier Ave. East, K1N5N6, Ottawa, Ontario, Canada
[b] Geomicrobiology, Department of Geoscience, University of Tuebingen, Geschwister-Scholl-Platz, 72074 Tübingen, Germany

*Corresponding Author
E-mail address: dfortin@uottawa.ca (Danielle Fortin)

Article accepted in Chemical Geology[1]

[1] Najem, T., Joshi, P., Kappler, A., & Fortin, D. (2024). Effects of gamma (γ)-irradiation on the physicochemical properties and bioavailability of iron oxyhydroxides coprecipitated with varying concentrations of Na-alginate. *Chemical Geology*, *662*, 122235.

Abstract

This study investigated the impacts of γ-radiation at a final dose of 25 kGy on the physicochemical properties of a range of wet iron oxyhydroxides (2-line ferrihydrite, lepidocrocite, and goethite) synthesized in the presence of varying concentrations of the polysaccharide Na-alginate (starting solutions containing C/Fe ratios of 0, 0.5, 1.0, and 1.5). The degree of impact to the minerals was examined by chemical extractions, and various analytical techniques including XRD, FTIR-ATR, Mössbauer spectroscopy, and N_2 adsorption-desorption isotherms, as well as by assessing their bioavailability towards the model Fe(III) reducing bacteria *Shewanella putrefaciens* CN32. Across all the coprecipitates studied, it was found that γ-irradiation led to a substantial dissolution of Fe and the concomitant release of Fe(II) and alginate into solution. Despite this observation, the bulk mineralogy and crystallinity of the studied iron oxyhydroxides, as determined by XRD and FTIR-ATR, did not appear to change. However, analyses via Mössbauer spectroscopy (77 and 5 K) revealed that the crystallinity of the 2-line ferrihydrites increased post-irradiation. Moreover, among the minerals studied, the specific surface area and porosity decreased for only the post-irradiated 2-line ferrihydrite coprecipitates with a C/Fe ratio of 0.5 or 1.0. The bioreduction rates of the studied minerals and their irradiated counterparts did not significantly differ, whereas the extent of bioreduction of post-irradiated 2-line ferrihydrite coprecipitates (C/Fe 0.5, 1.0, and 1.5) exhibited a significant increase of up to 28%. In contrast, the extent of Fe reduction for select post-irradiated lepidocrocite (C/Fe 0.5) and goethite (C/Fe 1.5) coprecipitates was slightly higher than determined for their corresponding native controls. The observed differences in bioavailability between the native and irradiated coprecipitates were attributed to irradiation induced alteration of particle aggregation and coagulation as determined by particle size analyses and visual observations. In summary, the findings suggest that even a low total dose of 25 kGy, γ-radiation

can lead to significant physicochemical changes in coprecipitates with relatively low organic matter content. Therefore, future research designed to investigate organic matter-Fe composite systems in natural samples should be cognizant of the potential effects of sterilization through γ-irradiation. These effects could potentially result in inaccurate over- or under- estimations of the bioavailability of Fe or organic matter, as well as the possible adsorption capacity of organic matter-Fe coprecipitates for contaminants.

Keywords

Iron Oxyhydroxides, Na-Alginate, Co-precipitate, γ-Irradiation, Mössbauer Spectroscopy, Bioavailability, *Shewanella putrefaciens*

1. Introduction

Sterilization of natural samples is essential for distinguishing biotic from abiotic reactions in laboratory experiments investigating the rate and extent of biogeochemical processes, and to prevent sample alteration during experimentation and storage (McNamara et al., 2003). From the range of available sterilization methods reported in the literature, apparently all come with a disadvantage. Autoclaving, for instance, can significantly alter the physicochemical properties of natural samples, including a decrease of surface area as a consequence of heat induced transformation of poorly crystalline Fe oxyhydroxide minerals into crystalline iron oxides as well as particle aggregation (Berns et al., 2008; Radloff et al., 2008; Zhao et al., 2017; Otte et al., 2018), and release of nutrients and organic matter (Salonius et al., 1967; Lotrario et al., 1995; McNamara et al., 2003; Berns et al., 2008; Buessecker et al., 2019). On the other hand, the application of chemical agents was reported to result in the increase of extractable of Fe(II) and Fe(III) (Buessecker et al., 2019; Layglon et al., 2020), as well as the chemical alteration of organic matter

properties and trace metal behaviour (Wolf et al., 1989; Buessecker et al., 2019; Retelletti Brogi et al., 2019; Layglon et al., 2020). Moreover, the application of chemical agents may hinder the inoculation of sterilized samples with model microorganisms (Langley et al., 2009a; Langley et al., 2009d; Langley et al., 2009e).

Although autoclaving tends to be more commonly used due to its lower cost and ease of accessibility, sterilization by gamma(γ)-irradiation has been determined to be the most appropriate method by several studies (McNamara et al., 2003; Herbert et al., 2005; Berns et al., 2008; Borisover et al., 2016; Lees et al., 2018; Buessecker et al., 2019). Such preference is attributed to its effectiveness as a biocide that precludes the use of toxic chemicals, and the harsh pressure and heat treatments through autoclaving especially where repeated treatments are required (Wolf et al., 1989; Lensi et al., 1991; McNamara et al., 2003; Zhao et al., 2017). Typically, elimination of microbial activity is dose-dependent where up to 70 kGy or higher may be necessary to inactivate certain radio-resistant bacteria (McNamara et al., 2003). The mechanism of sterilization by γ-radiation proceeds via direct and indirect pathways (McNamara et al., 2003). The latter leads to production of the radiolysis products (e.g., $^{\bullet}OH$, e^-_{aq}, H_2O_2) from water that are also associated with the alteration of the physicochemical properties of natural samples (Plötze et al., 2003; Bank et al., 2008; Berns et al., 2008). Although some studies found no discernible changes in the physicochemical properties of natural or synthetic samples at doses ranging from 10-60 kGy, or the observed changes were deemed minimal (McNamara et al., 2003; Herbert et al., 2005; Radloff et al., 2008; Langley et al., 2009a; Langley et al., 2009e; Borisover et al., 2016; Skulcova et al., 2018; Wehr and Kirchhof, 2021), others reported significant changes.

Irradiation induced changes associated with the organic matter fraction of soils/sediments were reported by a number of studies including a dose-dependent (1-500 kGy) increase of CO_2

production, and changes to the polycondensation, aromaticity, and molecular weight properties of humic and fulvic acids (Da Silva et al., 1997; Goraczko and Slawinski, 2008; Goraczko et al., 2008; Kelsey et al., 2010; Zhao et al., 2020; Zhao et al., 2021). Such changes also affected the complexation affinity of the organic compounds towards Ca^{2+}, Cs^{+}, Sr^{2+}, and Eu^{3+}, as well as the sorption and bioaccumulation behaviour of the organic contaminants p,p'-DDE and anthracene (Kelsey et al., 2010; Zhao et al., 2020; Zhao et al., 2021; Zhao et al., 2022a). Dose-dependent increase of dissolved organic matter (DOM) with lower polycondensation and aromaticity was also reported by a number of studies following irradiation of soils and sediments (McNamara et al., 2003; Zhang et al., 2016). Such changes were attributed to radical-induced cleavage of C-C bonds and depolymerization of carbohydrates (Salonius et al., 1967; Lensi et al., 1991; Tuominen et al., 1994; Berns et al., 2008; Schaller et al., 2011; Buchan et al., 2012; Zhang et al., 2016; Otte et al., 2018; Buessecker et al., 2019). Accompanying the release of DOM, Schaller et al. (2011) observed a concomitant increase of dissolved Fe and Mn, and the remobilization of As and U into solution following the irradiation of organic-rich sediments to a final dose of 60 kGy. At a lower dose (20 kGy), significant reduction of Fe(III)-bearing minerals (e.g. goethite) to Fe(II) within organic poor sediment was reported by Bank et al. (2008). Consequently, this significantly modified the cation exchange capacity thereby enhancing the adsorptive capacity of the sediment towards U(VI) (Bank et al., 2008). Other reported irradiation induced changes include: (1) a 16% decrease in soil surface area (10 kGy) (Lotrario et al., 1995), (2) changes in the aggregation state of soil, resulting in an increase in surface area (36 kGy) (Berns et al., 2008), (3) slight alterations in the surface area of specific minerals and a decrease in cation exchange capacity due to the radiation-induced reduction of Fe(III) to Fe(II) within clay minerals (1.1 MGy) (Plötze et al.,

2003), and (4) enhanced remobilization of uranium from sediments (30 kGy) (Seder-Colomina et al., 2022).

The contradictory findings or the extent of reported changes in the literature could be attributed to differences related to the dose applied, and the physicochemical properties of the natural sample, including mineralogy, moisture content, and organic matter content or type/stability, as well as the duration of the experiment (Salonius et al., 1967; Lotrario et al., 1995; Da Silva et al., 1997; McNamara et al., 2003; Radloff et al., 2008; Slizovskiy and Kelsey, 2010; Lees et al., 2018; Otte et al., 2018; Wehr and Kirchhof, 2021). Nonetheless, despite the fact that most studies reported an increase in DOM following γ-irradiation, few studies have examined the relationship between organic matter content and irradiation induced changes of the physicochemical properties of natural samples (Kelsey et al., 2010; Borisover et al., 2016; Skulcova et al., 2018; Buessecker et al., 2019). Moreover, given the apparent sensitivity of iron bearing minerals and organic matter to γ-irradiation, there is a significant gap in research concerning its impact on those constituents, particularly in cases where they coexist in close proximity.

Close association between organic matter and iron (oxyhydr)oxides in the environment occurs through a number of sequestration processes that remove organic matter from solution to the solid mineral particles (Kaiser et al., 1997; Kaiser, 2003; Fortin and Langley, 2005; Mikutta et al., 2008; Lalonde et al., 2012; Kleber et al., 2015; Bao et al., 2021; Curti et al., 2021; Possinger et al., 2021; Li et al., 2023). These processes include the adsorption of organic matter to the surface of preformed- and the coprecipitation of organic matter with neoformed- mineral phases where the latter comprises several interlinked complex processes (Kaiser et al., 1997; Kaiser, 2003; Schwertmann et al., 2005; Wagai and Mayer, 2007; Mikutta et al., 2008; Pedrot et al., 2011; Chen

et al., 2014; Kleber et al., 2015; Curti et al., 2021; Possinger et al., 2021; Li et al., 2023). Such processes are abundant in the environment and they occur within the porewaters of soils and sediments (Wagai and Mayer, 2007; Cismasu et al., 2011; Lalonde et al., 2012; Zhao et al., 2016), oxic-anoxic transition zones where Fe(II)-bearing anoxic solutions come into contact with O_2 (Riedel et al., 2013), and industrial coagulation water treatment landfills (Henneberry et al., 2012). In addition to plant-derived organic matter, microbes also contribute to this C pool by producing polysaccharides that serve as templates for the precipitating iron (oxyhydr)oxide minerals (Chan et al., 2004; Fortin and Langley, 2005; Chan et al., 2009; Kallenbach et al., 2016; ThomasArrigo et al., 2022). These organo-mineral coprecipitates possess distinct physicochemical and mineralogical properties than minerals formed in the absence of organic matter and mineral-organic associations that form by organic matter adsorption to pre-existing mineral surfaces (Schwertmann et al., 2005; Eusterhues et al., 2008; Mikutta et al., 2008; Cismasu et al., 2011; Kleber et al., 2015; ThomasArrigo et al., 2022). Organo-mineral coprecipitates are characterized by small crystal size, defective crystallographic structure, low specific surface area, distinct aggregation state, and distinct surface charge (Eusterhues et al., 2008; Mikutta et al., 2008; Toner et al., 2009; ThomasArrigo et al., 2022). Because of these properties, organo-mineral coprecipitates have been a subject of intense research to determine their role in the environment towards contaminant, nutrient, and trace metal mobility (Grybos et al., 2007; Mikutta et al., 2014; Fabisch et al., 2016; Hao et al., 2016; Sowers et al., 2017; Chen et al., 2018; Field et al., 2019; Xue et al., 2019; Dong et al., 2022), C storage (Lalonde et al., 2012; Han et al., 2019; Patzner et al., 2022; Martens et al., 2023), long term stability (Kaiser et al., 2007; Cismasu et al., 2016; Najem et al., 2016; Zhao et al., 2022c), and susceptibility/bioavailability to microbial degradation (Langley et al., 2009b; Pedrot et al., 2011; Amstaetter et al., 2012; Shimizu et al., 2013; Eusterhues

et al., 2014a; Adhikari et al., 2016; Poggenburg et al., 2016; Adhikari et al., 2017; Cooper et al., 2017; Zhao et al., 2017; Mejia et al., 2018; Poggenburg et al., 2018; Han et al., 2019; Zeng et al., 2020; Dong et al., 2023). Within this context, past and ongoing research have highlighted the importance of physicochemical and mineralogical properties as well as organic matter content/type in modulating the reactivity of organo-mineral coprecipitates. Therefore, given sensitivity in reactivity of iron (oxyhydr)oxides to changes in crystallinity and organic matter content, determining the extent of impact of γ-radiation on the reactivity of organo-mineral coprecipitates is important for future studies employing this technique to natural samples.

In this study, we examined the impact of γ-radiation on the physical and chemical properties, as well as bioavailability of various iron oxyhydroxides that were synthesized in the presence of organic matter (coprecipitation). Specifically, we synthesized 2-line ferrihydrite, lepidocrocite, and goethite - both in the presence and absence of Na-alginate. These minerals were selected for their representation of a range of thermodynamic stability, and their abundance in the environment including biogenic iron oxides (BIOS) (Cornell and Schwertmann, 2003; Fortin and Langley, 2005; Langley et al., 2009b; Gault et al., 2011; Fabisch et al., 2016; Najem et al., 2016; ThomasArrigo et al., 2022). Additionally, alginate was chosen as the organic compound due to its chemical resemblance to the twisted stalks and sheaths produced by the Fe(II)-oxidizing bacteria *Gallionella* spp. and *Leptothrix* spp., respectively, that contribute to the formation of BIOS (Chan et al., 2004; Chan et al., 2009). Polysaccharides are also important components of plant root exudates, contributing up to ~10% of the total organic matter pool in soils and sediments (Kleber et al., 2015). However, the reader should consider that alginate does not capture the response of other constituents from extracellular polymeric substances such as proteins, phosphate, and nucleic acids, as well as aromatic components from natural OM to irradiation (Tourney and Ngwenya,

2014; Kleber et al., 2015). Lastly, a total dose of 25 kGy was chosen for this study, because it represents the lower range of sterilization where most microbes in natural samples are reportedly eliminated (McNamara et al., 2003).

2. Materials and Methods

2.1. Synthesis of iron oxyhydroxides and coprecipitates

Prior to mineral syntheses, all necessary glassware and components were initially submerged in 10% HNO_3 bath for a minimum duration of 24 h then washed 3x with ultrapure water (UPW) (18 MΩ•cm). The glassware was then baked in a muffle-furnace at 450ºC for a duration of 8 h to remove any residual organic matter, and then sterilized by autoclaving. Prior to use, alginate was sterilized by spreading the dry powder on the base of a beaker or Pyrex bottle followed by irradiation with an ultraviolet light source for a period of 1 h. FTIR-ATR of the UV-irradiated alginate powder revealed no discernible structural changes (data not shown). To ensure sterility, all working solutions were prepared aseptically by using sterile UPW or by filtering (0.22 μm pore size filter).

2-line ferrihydrite (Fh), lepidocrocite (Lp), and goethite (Gt) were synthesized in the absence and presence of Na-alginate at C/Fe molar ratios of 0, 0.5, 1.0, and 1.5 according to published methodologies (Glasauer et al., 2003; Mikutta et al., 2008; Schwertmann and Cornell, 2008; Langley et al., 2009b). The selected C/Fe concentrations in the co-precipitates were representative of those found in BIOS, as well as commonly occurring concentrations in soils and sediments (Chen et al., 2014; Kleber et al., 2015; Zhao et al., 2016; Field et al., 2019). A detailed description of the mineral synthesis procedures is given in the Supplementary Material. Briefly, Fh was synthesized from the neutralization of a ferric chloride solution with a base (1 M NaOH) to pH ~7.00 (Glasauer et al., 2003; Langley et al., 2009b) consistent with studies researching

synthetic Fh-OM-coprecipitates (Shimizu et al., 2013; Adhikari et al., 2016; Adhikari et al., 2017). Lp was synthesized from the oxidation of a ferrous chloride solution while manually maintaining the pH at 6.7-6.9 with a base (1 M NaOH) (Schwertmann and Cornell, 2008). This chosen method precludes the addition of contaminating additives and high temperature (e.g. 50 °C or 70 °C) (Schwertmann and Cornell, 2008), which may damage the structure of alginate. High surface area Gts representative of those occurring in BIOS were synthesized at pH 7 from the oxidation of a ferrous chloride solution in the presence of bicarbonate (HCO_3^-:Fe ~2) (Schwertmann and Cornell, 2008; Gault et al., 2011). For each mineral, washing of the precipitates proceeded by centrifugation/vortexing and washing with sterile UPW until the conductivity of the supernatant decreased to <25 μS/cm. Subsequently, for each mineral, the precipitates were equally divided and aseptically combined into 2 separate straight sided glass jars (60 mL) with polypropylene screw caps, thoroughly homogenized in open atmosphere, and stored for a maximum period of 10 days at 4 °C until the radiation treatment. It should be noted that the wet precipitates occupied ~90% of the jar volume, and sterile UPW was added where deemed necessary to reduce the volume of the headspace. The final total Fe concentration for each mineral in the jars are given in Table S1.

2.2. Gamma (γ)-irradiation

For each mineral synthesized, one of the two jars was placed in a 2 L glass beaker and transported on ice to Nordion (Canada) Inc. where γ-irradiation proceeded using a ^{60}Co source at a rate of 12-15 kGy/hr to a total dose of ~25 kGy. Prior to irradiation, ice cubes were added to the beaker and distributed in between and on top of the jars to mitigate any temperature increase during the irradiation treatment. Ice was added again at the mid-point of the irradiation process at which point the ice was observed to have melted. Upon completion of the treatment, the samples were

transported back to the laboratory on ice and then quickly stored in the fridge at 4°C until use. Shipping, treatment, and handling of the samples were carried out within 3 h.

2.3. Characterization of the iron oxyhydroxides

For a particular mineral, both the non- and its γ-irradiated counterpart were subsampled in tandem to avoid any variability in reactivity due to ageing and/or handling. Initially, the jars were centrifuged at 4200 rpm for 10 min and, where possible, the supernatant was aseptically transferred in its entirety into a 40 mL VOA glass vial which was then immediately transferred into an anoxic chamber for subsequent analyses (*Section 2.4*). The separated iron oxyhydroxide precipitates were aseptically homogenised, and then characterized for their physicochemical properties (*Sections 2.3.1 – 2.3.5*) and bioavailability (*Section 2.5*) as described below.

2.3.1. ^{57}Fe Mössbauer spectroscopy

Given the sensitivity of ferrihydrite to structural alteration, only the native and post-irradiated 2-line ferrihydrite samples were analysed with ^{57}Fe Mössbauer spectroscopy. Samples for analyses were handled and dried under an anoxic atmosphere composed of a mixture of 95% N_2 and 5% H_2. The powdered samples were loaded into Plexiglas holders (area: 1 cm^2), forming a disc. These samples were kept in airtight jars at -20 °C until measurement. Holders were inserted into a closed-cycle exchange gas cryostat (Janis cryogenics, USA) under a backflow of He to minimize exposure to air. Spectra were collected at 77 K and 5 K using a constant acceleration drive system (WissEL, Germany) in transmission mode with a ^{57}Co/Rh source. All spectra were calibrated against a 7 μm thick α-^{57}Fe foil that was measured at room temperature. Analysis was carried out using Recoil (University of Ottawa) and the extended Voigt Based Fitting (VBF)

routine (Lagarec and Rancourt, 1997). The half width at half maximum (HWHM) was constrained to 0.123 mm/s during fitting.

2.3.2. Powder X-ray diffraction, specific surface area, and Fourier Transform Infrared Spectroscopy

The bulk mineralogy of the native and γ-irradiated iron oxyhydroxides was determined by X-ray diffraction (XRD). Air-dried samples were thoroughly ground to fine powders with an agate mortar and pestle and analysed with a Rigaku Ultima IV diffractometer using a Cu-Kα X-ray source, operating at 45 kV and 40 mA. Continuous scans were run from 10-80° 2Θ using a step size of 0.02° at a rate of 0.7°/min. Specific surface area (SSA) measurements on duplicate samples prepared in the same manner as XRD were carried out using a Quantachrome Autosorb-1. Approximately, 100-300 mg of a sample was initially degassed under vacuum at 50 °C for 24 h using a 9 mm cell. After the determination of degassing stability and final dry mass, 33 N_2 adsorption and 19 desorption points were recorded at 77 K in the partial pressure region $5x10^{-3}$-0.99 P/P_0. The SSA was determined by applying the BET equation on the standard partial pressure region (0.05-0.3 P/P_0) or by applying the criteria established by Rouquerol et al. (2007) where deemed necessary. The micropore volume was determined by applying the Dubinin-Radushkevich (DR) method to adsorption points below 0.01 P/P_0, whereas the mesopore volume (2-50 nm) was determined by applying the Barrett-Joyner-Halenda (BJH) method as determined by the accompanying Autosorb-1 software (Mikutta et al., 2008; Poggenburg et al., 2016). Total pore volume was determined from the last point of the N_2 adsorption isotherm (0.99 P/P_0). Lastly, the mineral SSA and pore volumes were corrected for the weight of retained alginate content as described in Mikutta et al. (2008).

Powdered samples were also analysed with Fourier Transform Infrared Spectroscopy (FTIR) using a *Nicolet 6700* spectrophotometer (ThermoFisher Scientific) equipped with a deuterated triglycine sulfate (*DTGS)* detector and a diamond crystal coated with ZnSe in attenuated total reflectance (ATR) mode. Prior to analyses, the powdered samples were dried under vacuum in an Oxoid^{TM} Anoxic jar (~27 inHg below atmosphere) at 50 °C for a period of 24 h to minimize the contribution of surface adsorbed H_2O to the spectra. While at 50 °C, the samples were flushed with pure nitrogen (GR 4.5) and allowed to cool in a desiccator until analyses. Four individual measurements were made on duplicated samples (2 measurements each) in order to determine the homogeneity of sample in terms of particle size and composition together with instrumental reproducibility. For each sample, spectra were acquired from 4000 to 500 cm^{-1} at 4 cm^{-1} resolution, with 128 scans averaged per spectrum. Subsequently, the spectra were processed using the OMNIC software package (Thermo Fisher Scientific, version 9) where the spectra were averaged, automatically baseline corrected, and normalized to the maximum absorbance value.

2.3.3. Iron and carbon content

The pseudo-total iron content of dry powdered or wet samples was determined by suspending a known amount into 6 mL of UPW, and fully digested by the addition of 4 mL trace metal grade 30% H_2O_2 and 2 mL trace metal grade HNO_3 followed by heating at 75 °C for 24 h. After dilution with 1% HNO_3 (v/v), the Fe content was determined via inductively coupled plasma ─ optical emission spectroscopy using a Varian Vista-PRO CCD Simultaneous ICP-OES, operating under standard conditions. All digestions were carried out in duplicates (powdered samples) or triplicates (wet samples). For carbon content determination, approximately 10 mg of a dry powdered sample was weighed into a tin capsule. The prepared samples were then analysed

for carbon content at the University of Ottawa at the Jan Veizer Stable Isotope Laboratory using the Elementar Vario Isotope Cube.

2.3.4. Chemical extractions

To determine the poorly-crystalline Fe fraction in the non- and γ-irradiated precipitates, chemical extractions were carried out in triplicates following a the methods outlined in Kostka and Luther (1994) with some modifications. Briefly, ~20 mg of wet sample was accurately weighed into 20 mL scintillation vials followed by the addition of either HCl (0.5 M) or ascorbate (pH 8.0). The HCl extraction proceeded under oxic conditions for a duration of 1 h, whereas the ascorbate extraction proceeded under anoxic conditions for a duration of 24 h in the dark. Following extraction with HCl (0.5 M), the digests were filtered (Cytiva polyethersulfone membrane, 0.22 μm) and an aliquot was analysed with the ferrozine assay to determine the Fe(II) content ($HCl_{Fe(II)}$), and another aliquot was reduced with 0.28 M ClH_4NO in 0.28M HCl for a duration of 30 min to determine total Fe ($HCl_{totalFe}$) concentration following determination with the ferrozine assay (Stookey, 1970; Kostka and Luther, 1994; Viollier et al., 2000). The 0.5M HCl extractable Fe(III) was calculated as $HCl_{Fe(III)} = HCl_{totalFe} - HCl_{Fe(II)}$. For the ascorbate extraction, the digests were filtered (Cytiva polyethersulfone membrane, 0.22 μm) under anoxic conditions and the filtrates were analysed using the ferrozine assay. To determine the fraction of amorphous Fe in the precipitates, the concentration of Fe extracted by ascorbate or HCl was normalized by the total Fe concentration (*Section 2.3.3.*).

2.3.5. Electrophoretic mobility and particle size

The electrophoretic mobility (EM) and particle size of the iron oxyhydroxides was measured in a filtered (Sartorius polyethersulfone membrane, 0.22 μm) 10 mM $NaNO_3$ solution

using a Zetasizer Nano-ZS (Malvern, Instruments) at 25°C. Initially, the iron oxyhydroxides were dispersed by adding a wet sample (equivalent to 25-30 mg of dry solid per litre) to 500 mL of background electrolyte and stirred for 1h. Subsequently, the pH of 50 mL aliquots was adjusted with filtered 10 mM NaOH or HNO_3 to a constant desired value between pH 3-9. The EM measurements were determined from the average of 5 runs comprising of 10 cycles each. Particle size of the suspensions was determined from the average of two individual measurements taken at pH ~6 in automatic mode.

2.4. Characterization of the supernatants

The liquid portions that remained after the separation of solids from the suspensions via centrifugation, i.e. supernatants, were vacuum filtered (Sartorius polyethersulfone membrane, 0.22 μm) into 40 mL glass VOA vials under anoxic conditions. Prior to filtering, the filter membrane was rinsed by passing 500 mL of anoxic deionized water through followed by a few mL of a sample which were discarded. Subsequently, a 0.5 mL aliquot of a filtrate was preserved in 4.5 mL of 0.5 M trace metal grade HCl in the dark until analysis for dissolved Fe(II) using the ferrozine assay. For the determination of total dissolved Fe, 0.5 mL of a filtrate was digested in duplicates and analysed as described above (*Section 2.3.3.*). For the determination of the dissolved carbon content, where possible, a known volume of a filtrate was diluted into UPW and analysed at the University of Ottawa using a modified OI Analytical model 1030 wet TOC analyser. No precipitation of separate iron oxyhydroxides phases was observed following dilution. Finally, where possible, aliquots of the filtrates were also dried at 40 °C for characterization with FTIR-ATR as described above (*Section 2.3.2.*).

2.5. Bioavailability

The sterility of the native and γ-irradiated precipitates was initially confirmed by aseptically suspending sub-samples of a precipitate into 5 mL of tryptic soy broth (TSB) and allowed to incubate for 1 week. Sterility of all precipitates was confirmed by the lack of development of turbidity.

2.5.1. Microbial Medium and Preparation of Cultures

Microbial Fe(III) reduction experiments were carried out with a well characterized, facultative, dissimilarity Fe(III)-reducing bacterium, *Shewanella putrefaciens* strain CN32 (*S. putrefaciens* CN32). Microcosm reduction experiments were carried out in a chemically defined medium (CDM) (pH ~6.7) composed of 20 mM sodium lactate as the electron donor, 4 mM 1,4-piperazinediethanesulfonic acid (PIPES) buffer, mineral salts solution, and trace metals solution (Glasauer et al., 2003; Langley et al., 2009a). For transfer into CDM, *S. putrefaciens* CN32 was initially revived from a glycerol stock solution by streaking onto tryptic soy agar (TSA) plates at room temperature (~22 °C). For inoculation, the bacteria were prepared according to the protocols of Glasauer et al. (2003) and Langley et al. (2009). Briefly, cells were prepared by aseptically inoculating 50 mL of TSB with a colony of *S. putrefaciens* CN32 from TSA plates, and kept on a stir plate (125 rpm) for 24 h at 22 °C. Subsequently, 0.5 mL of the culture was transferred into 50 mL of 50:50 CDM:TSB mixtures. After 24 h, the passaging procedure was repeated with 95:5 CDM:TSB containing 100 μM phosphate, and continued by transferring into 99:1 CDM:TSB containing 200 μM phosphate for a period of 30 h. The final step involved growing the bacteria in 100% CDM containing 400 μM phosphate for a period of 36 h. The concentration of phosphate was progressively increased to acclimate the bacteria to depleted nutrients and microcosm conditions (Glasauer et al., 2003; Langley et al., 2009b). Following the acclimation period, the bacteria were harvested by centrifugation at 4000 rpm and the cell pellet was re-suspended into 2

mL of fresh, sterile CDM. Finally, the BioRad Protein Assay II dye reagent was used to standardize the concentrated cell suspension in order for the microcosms to contain a cell density of ~10^7 CFU/mL (Glasauer et al., 2003; Langley et al., 2009b).

The experimental setup consisted of 500 mL acid-washed Pyrex bottles (microcosms) containing 450 mL of sterile CDM amended with 4 mM Fe in the form of iron oxyhydroxide, and 400 μM of sodium phosphate. The experiments were conducted in triplicates and controls to which no bacteria were added were included. Prior to inoculation with *S. putrefaciens* CN32, the microcosms were wrapped in aluminium foil in order to avoid potential photochemical reactions and then transferred into an anoxic chamber where inoculation proceeded. Throughout the paper, we refer to the microcosms to which cells were added as "biotic" microcosms, whereas controls to which no bacteria were added are referred to as "control" microcosms. It should be noted that for a mineral phase, the microcosms for the native precipitate and its γ-irradiated counterpart were set up and inoculated in tandem to minimize potential variations due to media preparation (pH, temperature) and culture preparation (inoculum size and the state of the cells) (Glasauer et al., 2003).

2.5.2. Sampling and analyses

Sampling of each system was performed immediately following the addition of the cells (time 0) and then periodically at selected time points. Sampling was carried out by vigorously shaking the microcosms to suspend the iron oxides into solution. Immediately, 20 mL of the suspension was poured into a sterile 20 mL scintillation vial from which all sub-sampling proceeded to minimize the potential contamination of the microcosms (Langley et al., 2009a). The sub-sampled suspensions were analysed for pH, cell viability (at the start and end of the experiment), total and dissolved Fe(II), and total Fe. pH was monitored utilizing standard

calibrated laboratory meters and probes, whereas cell viability was determined by colony counts on TSA plates (Glasauer et al., 2003; Langley et al., 2009a). Fe(II) associated with the solid phase (total Fe(II)) was determined by dispensing 1 mL of unfiltered iron oxyhydroxide suspension into 1 mL of trace metal grade 6 M HCl (final concentration of 3 M) and allowed to digest for at least 24 h under anoxic conditions prior to dilution and analysis via the ferrozine assay (Stookey, 1970; Viollier et al., 2000). Dissolved Fe(II) was determined by filtering (0.22 μm) 6 mL of the suspension into an acid-washed 20mL scintillation vial, and immediately dispensing 0.5 mL of the filtrate into 4.5 mL of trace metal grade 0.5 M HCl. Digestion proceeded for at least 24 h under anoxic conditions prior to analysis by the ferrozine assay. To determine total Fe, 2 mL of the unfiltered iron oxyhydroxide suspensions were digested with 2 mL of trace metal grade 12 M HCl for a period of 24 h. Following dilution, Fe determination proceeded by dispensing 100 μL aliquot of the digest into 900 μL of 0.28 M ClH_4NO in 0.28 M HCl for a duration of 30 min and then determining the concentration of Fe^{2+} using the ferrozine assay.

2.5.3. Biogenic solids

At the end of the experimental period, post-reduction minerals were collected by centrifugation (3000 rpm), washed 3x with anoxic UPW, and dried under anoxic conditions. The powdered precipitates were analysed by XRD as described above, using an air sensitive sample holder in order to prevent the oxidation of potential Fe(II)-bearing minerals.

3. Results

3.1. Chemistry of supernatants

Irradiation induced physical changes to the coprecipitates were visually apparent with changes being most obvious for the ferrihydrite (Fh) coprecipitates (C/Fe 0.5, 1.00, and 1.5)

(Figure S1). Prior to irradiation, the Fh coprecipitates exhibited a viscous gel-like texture which upon irradiation, 40-80% of their volume was converted into a brown liquid (Figure S1). The pH of the supernatants collected from the various iron oxyhydroxides remained more-or-less neutral and did not exhibit a substantial change following irradiation nor did it exhibit a specific trend (Figure S2). However, in some cases the pH of the supernatants slightly decreased following irradiation, which was attributed to the oxidation of ferrous iron and subsequent hydrolysis of ferric iron (Figure S2). Figure 1 shows the amount of dissolved Fe species (Fe(II) and total Fe (Fe(II) + Fe(III)) and organic carbon (DOC) in the filtered supernatants relative to the initial total concentration (Table S1). The amount of dissolved Fe species in the supernatants of the pure iron oxyhydroxides was low and did not change post-irradiation (Figure 1). For the native Fh coprecipitates, a liquid sample could only be collected from Fh coprecipitated with C/Fe of 0.5 and it did not contain a measurable amount of dissolved Fe species or DOC (Figure 1). However, following irradiation of the Fh coprecipitates, the amount of dissolved Fe species and DOC increased linearly with increasing initial C/Fe ratio (Figure 1). The relative amount of the dissolved Fe(II) and total Fe were within the range of 0.1-0.7%, and 3.5-9%, respectively (Figure 1). This increase was accompanied by an increase in DOC falling within the range of 2-35% (Figure 1).

Dissolved Fe species were also detected in the supernatants of the native lepidocrocite (Lp) and goethite (Gt) coprecipitates, a probable consequence of the incomplete oxidation of Fe(II) and complexation of Fe/stabilization of Fe-colloids by alginate which remained in suspension (Figure 1). Such notion is supported by the detection of DOC in the supernatants of these systems (Figure 1). As was observed for the Fh coprecipitates, irradiation led to significant difference in the amount of dissolved Fe(II), total Fe, and DOC in the supernatant of these systems when compared to their native controls ($P<0.05$) (Figure 1). Following irradiation of the Lp

coprecipitates, the amount of dissolved Fe(II), total Fe, and DOC increased by 9-15x, 16-23x, and 2.5-3x, respectively, relative to native controls (Figure 1). Similarly, for the irradiated Gt coprecipitates, the amount of dissolved Fe(II), total Fe, and DOC increased by 40-100x, 30-50x, and 1.1-2x, respectively, relative to the native controls (Figure 1). For the irradiated Lp and Gt coprecipitates, apart from Gt with C/Fe of 1.5, it was also observed the amount of the dissolved Fe species as well as DOC increased with increasing initial concentration of alginate (Figure 1). Across all the irradiated coprecipitates, dissolved Fe(II) made up a small proportion of the total dissolved Fe pool indicating that the majority of this pool was comprised of oxidized Fe(III) species (Figure 1).

3.2. Chemistry of solids

Figure 2 shows the total, ascorbate and 0.5 M HCl extractable Fe content of the native and irradiated iron oxyhydroxides normalized by their wet mass. Also shown is the proportion of 0.5 M HCl extractable Fe(II), as well as the C/Fe molar ratio measured in the dry native and post-irradiated iron oxyhydroxides (Figure 2). Post-irradiation, the total Fe content was found to increase especially for the coprecipitates (Figure 2). The amount of Fe extracted from the post-irradiated Fh precipitates by either extractant was either equivalent to the total Fe (100% extraction) or did not significantly differ ($P>0.05$, two tailed t-test) from that of the native controls (Figure 2). Also, as was observed with pure Fh, irradiation did not significantly affect the 0.5 M HCl nor the ascorbate extractable Fe fraction of the pure Lp and Gt ($P>0.05$, two tailed t-test, Figure 2). Conversely, post-irradiation, the 0.5 M HCl extractable Fe fraction from the Lp coprecipitates significantly decreased by 30-40%, but it did not exhibit a specific trend ($P<0.05$, two tailed t-test, Figure 2). However, ascorbate extractable Fe did not significantly differ between the corresponding native and irradiated Lp coprecipitates ($P>0.05$, two tailed t-test, Figure 2).

Interestingly, irradiation of Gt coprecipitated with C/Fe ratio of 0.5 significantly decreased the 0.5 M HCl and ascorbate extractable Fe by ~20% ($P<0.05$, two tailed t-test, Figure 2). In contrast, for Gt coprecipitates with C/Fe ratio of 1.0 or 1.5, both extractants recovered comparable amounts of Fe ($P>0.05$, two tailed t-test, Figure 2). The fraction of Fe(II) associated with the solid phase (adsorbed/structural) was expected to increase following irradiation, as was observed in the supernatants of the coprecipitates (Figure 2). However, among the iron oxyhydroxide studied, 0.5 M HCl extractable Fe(II) did not increase following irradiation nor did it show a specific trend, and this can be attributed to the possible oxidation of Fe(II) during mixing/weighing of the iron oxyhydroxides in open atmosphere (Figure 2).

Irradiation induced changes to the C/Fe content of the coprecipitates were also investigated (Figure 2). A minor amount of C was measured in the pure iron oxyhydroxides which likely originated from the adsorption of atmospheric carbonate (Fh and Lp) or from the addition of bicarbonate (Gt) during synthesis (Figure 2). Post-irradiation, no change was observed in the C/Fe ratio for the pure phases whereas the C/Fe ratio was observed to decrease for specific coprecipitates (Figure 2). For instance, the C/Fe remained the same for Fh with C/Fe ratio of 0.5, but significantly decreased by ~10 and 30% for Fh coprecipitated with C/Fe ratios of 1.0 and 1.5, respectively. Such changes appeared to increase with increasing initial alginate content ($P<0.05$, two tailed t-test, Figure 2). For the Lp coprecipitates with C/Fe ratios of 0.5 and 1.5, the C content significantly decreased by 12 and 9%, respectively, post-irradiation ($P<0.05$, two tailed t-test, Figure 2). Although the C content also decreased for the post-irradiated Lp coprecipitated with C/Fe 1.0 such decrease was not significant ($P>0.05$, two tailed t-test, Figure 2). Finally, irradiation did not significantly affect the C content of the Gt coprecipitates ($P>0.05$, two tailed t-test, Figure 2).

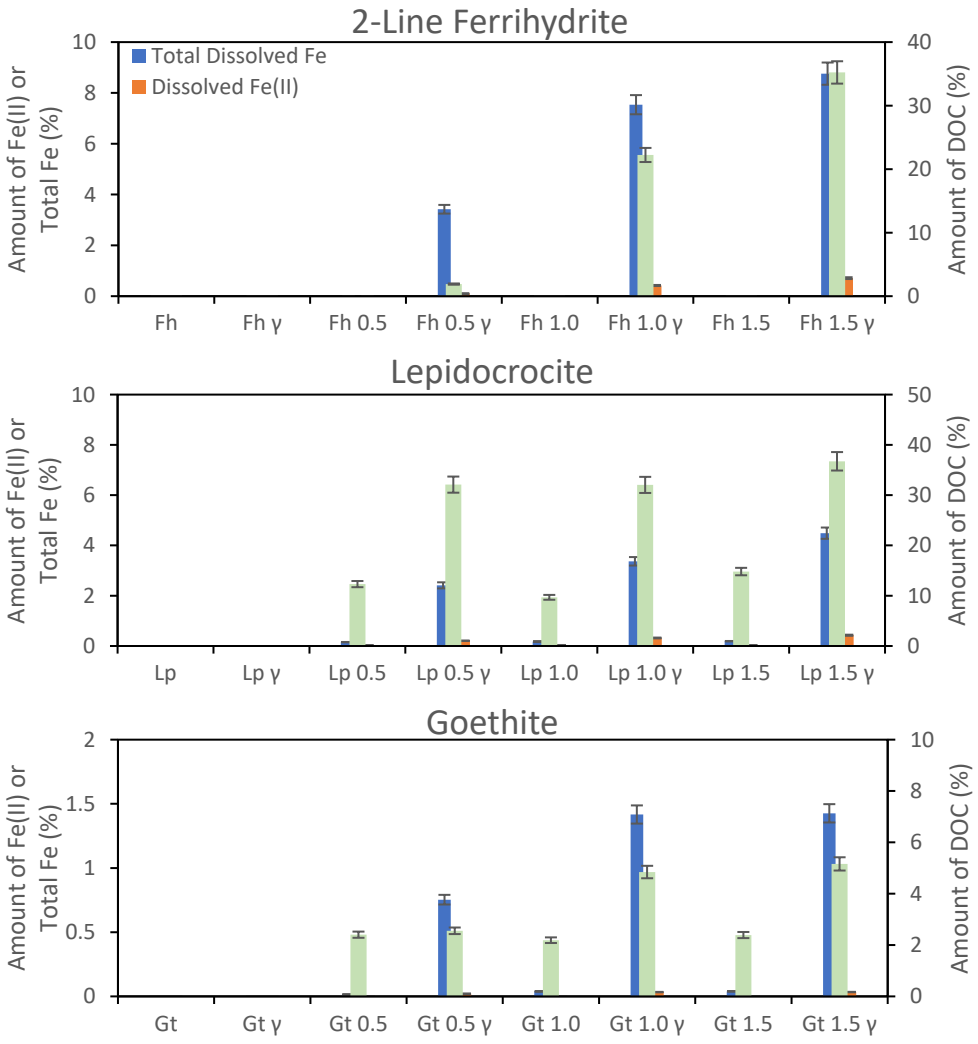

Figure 1: Amount of dissolved Fe(II), total Fe, and organic carbon (DOC) measured in the filtered (0.22 μm) aqueous supernatants collected following the centrifugation of the native iron oxyhydroxides and their corresponding γ-irradiated counterparts. The amounts are reported relative to the total initial amount in the jars. The data represents the mean ± standard deviation of two measurements from each supernatant collected. Note the scale for the goethite precipitates.

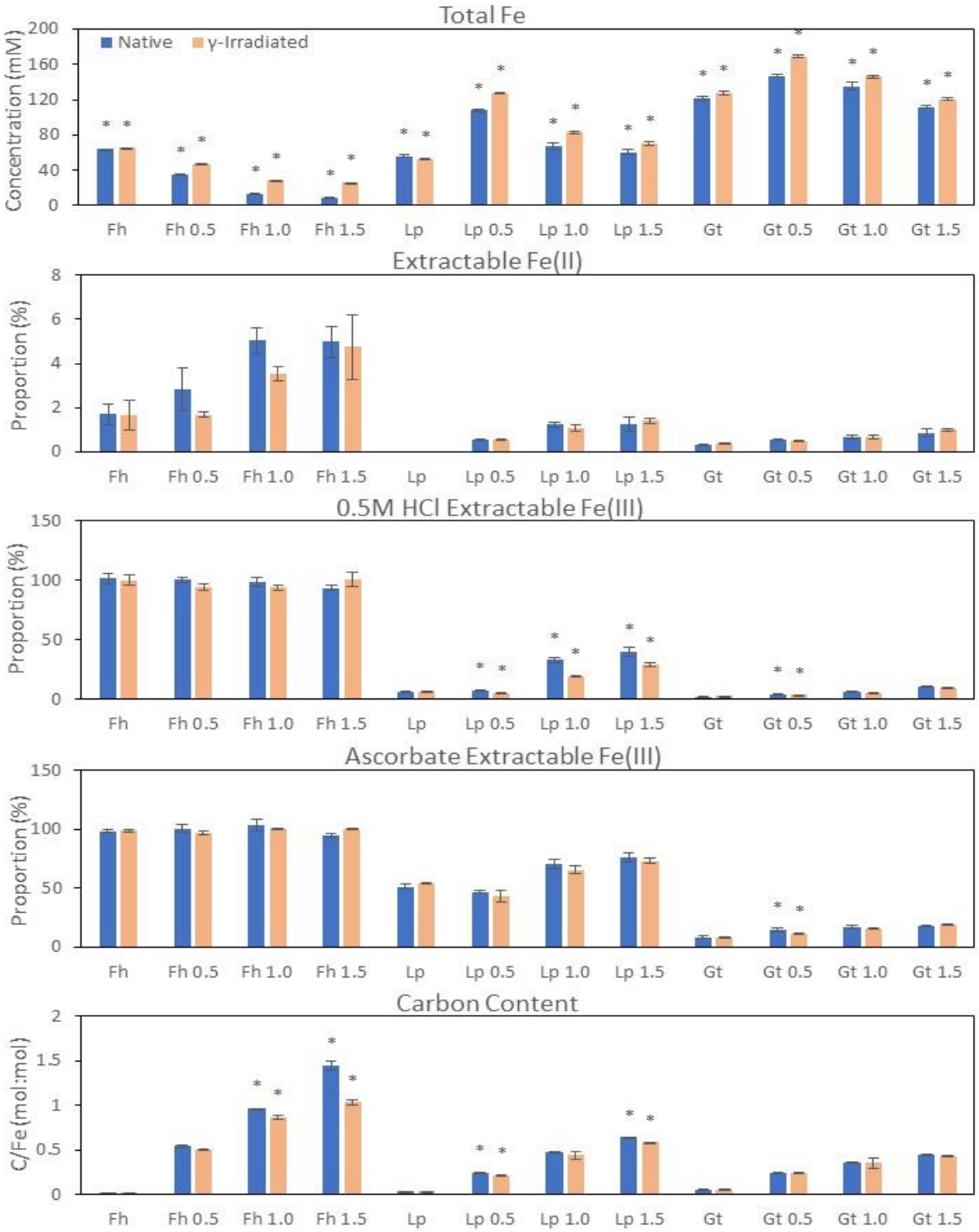

Figure 2: Chemical extractions of the solid iron phase of the native iron oxyhydroxides and their corresponding γ-irradiated counterparts. The fractions of poorly crystalline Fe containing phases as determined by 0.5 M HCl and ascorbate are presented relative to the total Fe. The figure includes the C/Fe molar ratios determined from the solid native and γ-irradiated precipitates. Values for the chemical extractions correspond to the mean ± standard deviation of three replicates, whereas values for the C/Fe molar ratios correspond to the mean ± standard deviation of two replicates. Fh, Lp, and Gt correspond to 2-line ferrihydrite, lepidocrocite, and goethite, respectively.

3.3. Specific surface area and porosity

The N_2 adsorption-desorption isotherms for the various studied iron oxyhydroxides are presented in Figures S3-S5, whereas Figure 3 summarizes the derived specific surface area (SSA) and pore volumes, including micropore (MIV), mesopore (MEV), and total pore (TPV) volumes. The N_2 adsorption-desorption isotherm shapes of the post-irradiated iron oxyhydroxides closely resembled their corresponding native controls (Figures S3-S5). However, a distinction was observed with the post-irradiated Fh coprecipitates, specifically those with C/Fe ratios of 0.5 and 1.0, which exhibited reduced N_2 adsorption compared to their native controls (Figures S3). It was found that irradiation had a significant impact on the porosity and SSA of Fh coprecipitates with C/Fe ratios of 0.5 or 1.0 ($P<0.05$, two tailed t-test. Figure 3). After irradiation, the MIV, TPV, and SSA of Fh coprecipitated with C/Fe of 0.5 decreased by approximately 15%, 20%, and 15%, respectively, while MEV remained unchanged (Figure 3). Similarly, the post-irradiated Fh coprecipitated with C/Fe of 1.0 exhibited a decrease of around 40% in MIV, 40% in MEV, 50% in TPV, and 45% in SSA (Figure 3). It was also found that despite having a similar C/Fe content, the SSA of irradiated Fh coprecipitated with C/Fe of 1.5 remained significantly lower than that of native Fh coprecipitated with C/Fe of 1.0 (Figures 2 and 3). Finally, for all other iron oxyhydroxides studied, there were no significant changes in MIV, MEV, TPV, or SSA post-irradiation in comparison to their native counterparts ($P>0.05$, two tailed t-test, Figure 3).

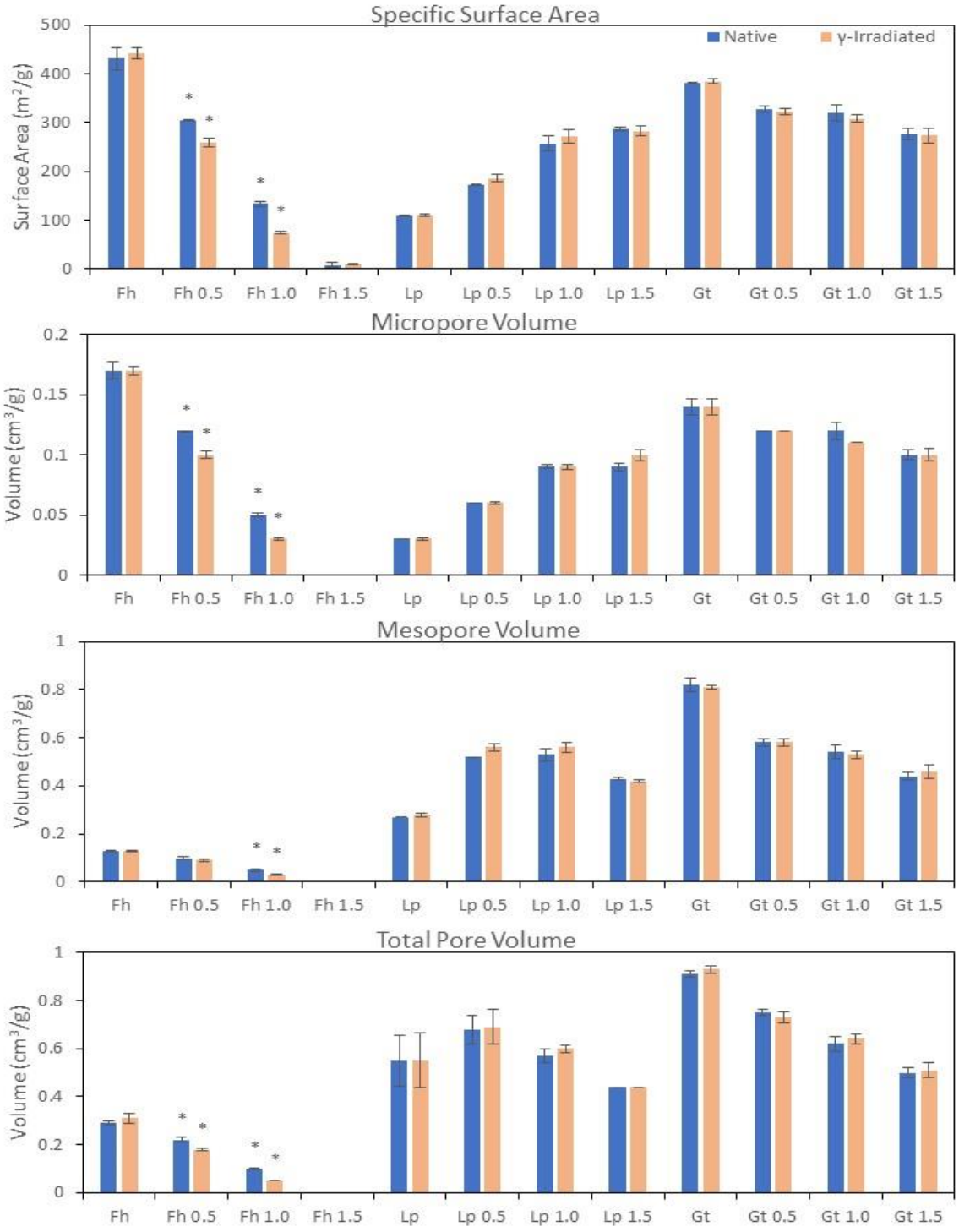

Figure 3: Specific surface area, micropore volume, mesopore volume, and total pore volume values of the native iron oxyhydroxides and their corresponding γ-irradiated counterparts. Data points represent the mean ± standard deviation of two replicates. Data extracted from the N_2 adsorption-desorption isotherms provided in Figure S3-S5. Fh, Lp, and Gt correspond to 2-line ferrihydrite, lepidocrocite, and goethite, respectively. Asterix indicates significance in difference between values at the 95% confidence interval ($P<0.05$, two tailed t-test).

3.4. Surface charge and particle size

Plots of the ζ-potential versus pH for the native and post-irradiated minerals are presented in Figures S6-S8. Native coprecipitates exhibited a reduced pH_{iep} when compared to that of their corresponding pure mineral phases, in agreement with past studies (Mikutta et al., 2008). The pH_{iep} of the native pure minerals Fh, Lp, and Gt were estimated to be 7.2, 7.4, and 7.6, respectively, which were comparable to those determined for their corresponding irradiated counterpart (Figures S6-S8). Irradiation of the Fh coprecipitates led to some changes in their surface charge when compared to that of their native corresponding counterparts. Namely, for the Fh coprecipitate with a C/Fe ratio of 0.5, the pH_{iep} decreased from ~6.6 to ~3.6 post-irradiation (Figure S6). The opposite was observed for the Fh coprecipitates with C/Fe ratio of 1.0 and 1.5, whereby their surface charge became more positive post-irradiation (Figure S6). In contrast, post-irradiation, the surface charge of the Lp and Gt coprecipitates remained comparable to that of their native counterparts (Figures S7 and S8).

Figure 4 shows the particle size measurements of the native and post-irradiated minerals. For the native Fh minerals, the particle size generally increased with increasing alginate content, although the particle size of the coprecipitates exhibited significant variability as seen from the large error bars indicative of variable particle size distribution (Figure 4). Following irradiation, the particle size of the pure Fh did not change, whereas for the Fh coprecipitates it substantially decreased suggesting changes in the particle size distribution (Figure 4). However, significant difference in the average particle size was only observed between native and post-irradiated Fh coprecipitated with C/Fe ratio of 1.0 ($P<0.05$, two tailed t-test, Figure 4).

For the native Lp minerals, the particle size decreased as the alginate content increased to C/Fe ratio of 0.5, which increased with increasing alginate content (Figure 4). Post-irradiation,

similar changes were observed for the Lp minerals as in Fh minerals; however, across all of the Lp coprecipitates analyzed, there was a significant decrease in particle size ($P<0.05$, two tailed t-test, Figure 4). The particle size of the native Gt minerals also decreased as the alginate content increased to C/Fe ratio of 0.5. This size remained constant as the initial C/Fe ratio increased to 1.0 but increased as the initial alginate content increased to C/Fe ratio of 1.5 (Figure 4). However, unlike Fh and Lp coprecipitates, the particle size of post-irradiated Gt coprecipitates did not show significant changes and remained relatively constant ($P>0.05$, two tailed t-test, Figure 4).

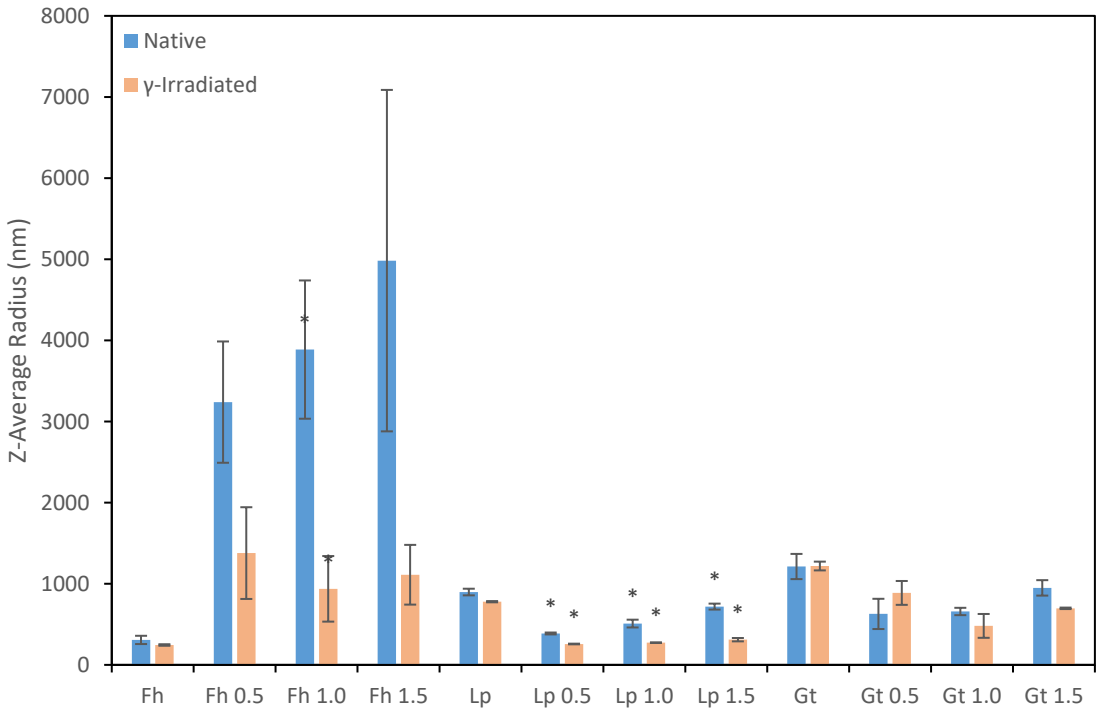

Figure 4: Size of particles (Z-average) measured native iron oxyhydroxides and their corresponding γ-irradiated counterparts. Data represents the mean ± standard deviation of 2 individual replicates. Asterix indicates significance in difference between values at the 95% confidence interval ($P<0.05$, two tailed t-test). Fh, Lp, and Gt correspond to 2-line ferrihydrite, lepidocrocite, and goethite, respectively.

3.5. Mineralogy

3.5.1. X-ray diffraction

Figure 5 shows the x-ray diffraction patterns of the different iron oxyhydroxide phases before and after γ-irradiation. Reflections indicative of 2-line ferrihydrite, lepidocrocite, and goethite were identified in the diffractograms, and they corresponded closely with those published in the literature (Schwertmann and Cornell, 2008). Substantial differences between the diffractograms of a native and its corresponding γ-irradiated counterpart were not evident, suggesting that, at the bulk level, γ-irradiation did not affect the mineralogy of the studied minerals (Figure 5). Additionally, a comparison of the full width at half maximum (FWHM) between native minerals and their γ-irradiated counterparts showed no substantial differences (data not shown).

3.5.2. Fourier Transform Infrared Spectroscopy

Additional information about the chemical composition, functional groups, and degree of crystallinity was obtained through FTIR spectroscopy. The IR spectrum for Na-alginate is presented in Figure S9, and the corresponding band assignments are given in Table S2. The IR spectra within the 1800 - 800 cm^{-1} region of the native and post-irradiated Fhs are presented in Figure 6. The complete IR spectra of the studied iron oxyhydroxides are presented in Figures S10-S12, and the assignments of the most characteristic vibrational modes are summarized in Tables S3-S5 as determined by theory and the literature (Sartori et al., 1997; Chandıa et al., 2001; Cornell and Schwertmann, 2003; Leal et al., 2008; Schwertmann and Cornell, 2008; Cardenas-Jiron et al., 2011).

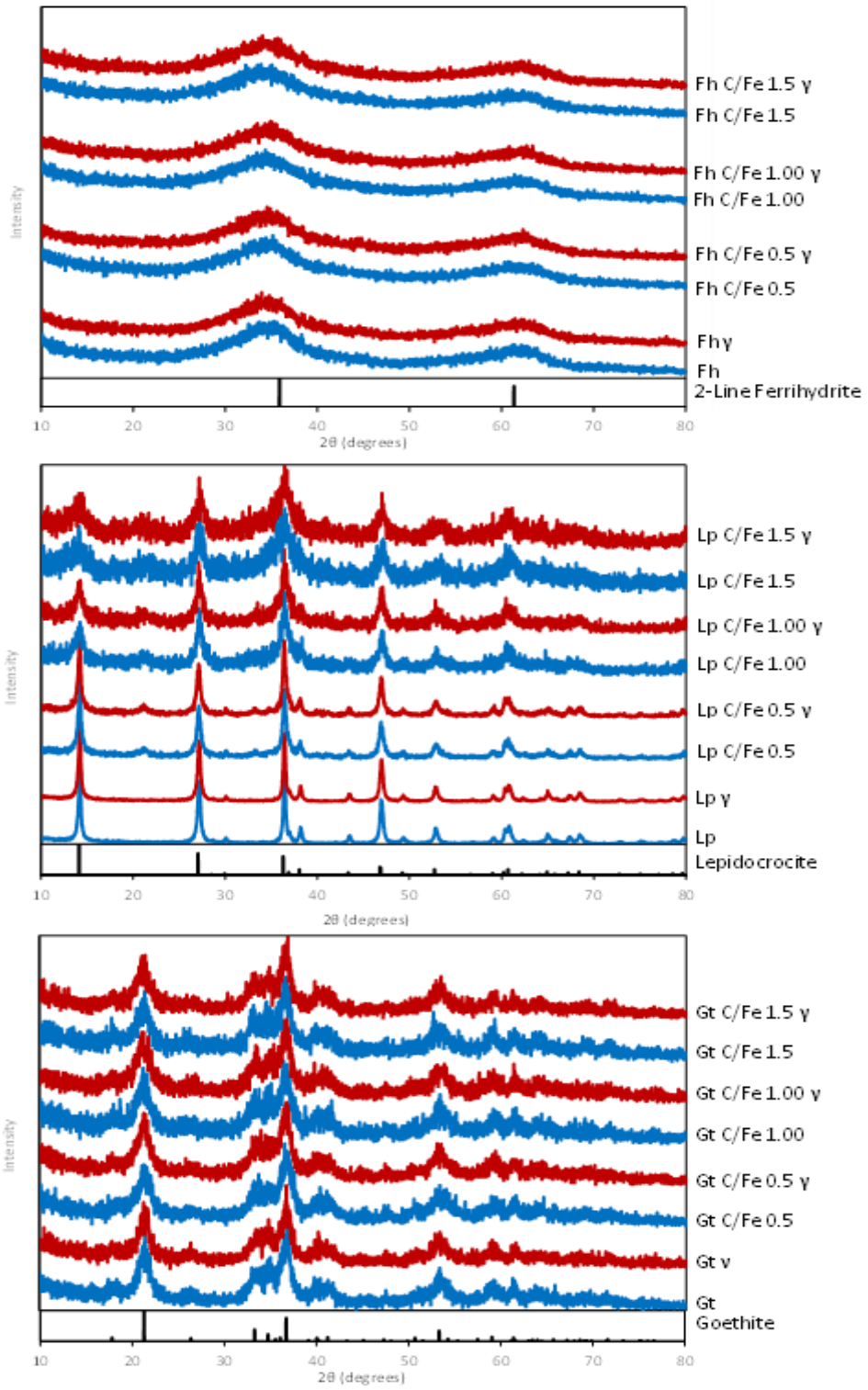

Figure 5: Powder x-ray diffractograms of the native iron oxyhydroxides and their corresponding γ-irradiated counterparts compared to the standard reference lines. For clarity, all patterns have been vertically separated on an arbitrary y-axis. Fh, Lp, and Gt correspond to 2-line ferrihydrite, lepidocrocite, and goethite, respectively.

The spectra of γ-irradiated Fh coprecipitates exhibited most of the characteristic absorption bands of their native counterparts with a slight shift in wavenumbers but displayed some notable differences (Figures 6 and S10). Among all of the post-irradiated Fh coprecipitates, the centre of the broad stretching O-H band ν(O-H) shifted to higher wavenumbers (Figure S10). Specifically, this band shifted from 3205 cm^{-1}, 3206 cm^{-1}, and 3177 cm^{-1} to 3215 cm^{-1}, 3216 cm^{-1}, and 3204 cm^{-1} post-irradiation for Fh coprecipitates with C/Fe ratios of 0.5, 1.0, and 1.5, respectively (Figure S10). Additionally, post-irradiation, the intensity of this band decreased for Fh coprecipitates with C/Fe of 0.5 and 1.0 but remained unchanged for Fh coprecipitated with C/Fe of 1.5 (Figure S10). The observed shifting and changes in intensity of this band suggests possible changes related to strength of the hydrogen bonds or water uptake. Changes to the intensity of the bands corresponding to alginate were also evident (as determined by measurement of peak heights), consistent with the decrease of C content, post-irradiation (Figures 3 and 6, and Figure S10). Specifically, for Fh with a C/Fe ratio of 0.5, the intensity of the carboxylate asymmetric stretching band (ν_{asym}(C-O-O), 1590-1592 cm^{-1}) increased by ~16%, the symmetric stretching band (ν_{sym}(C-O-O), 1406-1408 cm^{-1}) remained unchanged, while the asymmetric stretching of the glycosidic linkage band (ν_{asym}(C-O-C) ~1024-1030 cm^{-1}) decreased by ~20% post-irradiation (Figure 6). For Fh with a C/Fe ratio of 1.0, the intensity of the carboxylate asymmetric stretching band remained the same, the symmetric stretching band decreased by ~11%, and the asymmetric stretching of the glycosidic linkage band decreased by ~17% post-irradiation (Figure 6). For Fh with a C/Fe ratio of 1.5, the intensity of the carboxylate asymmetric stretching band remained the same, the symmetric stretching band decreased by ~16%, and the asymmetric stretching of the glycosidic linkage band decreased by ~21% post-irradiation (Figure 6). Across all post-irradiated Fh

coprecipitates, it was also observed that the band corresponding to the asymmetric stretching of the carboxylate groups broadened due to the possible appearance of a shoulder band (Figure 6).

Irradiation did not influence the mineralogy of pure Lp as the bands position and intensity were similar to those of the native Lp (Figure S11). Similarly, the IR spectra of the post-irradiated Lp coprecipitates also exhibited most of the characteristic absorption bands of their corresponding native counterparts, suggesting minimal irradiation induced changes in crystallinity and mineralogy (Figure S11). Across all post-irradiated coprecipitates, the intensity of the band centered at ~1022 cm^{-1} corresponding to the in-plane δ(O-H) vibration of the Lp mineral decreased (Figure S11). However, this band overlapped the band region corresponding to the vibrations due to mannuronic and guluronic acid residues within alginate (Figures S9 and S11, Table S4). This suggests that the decrease in intensity of this band region is likely related to the decrease in C content post-irradiation given that the other bands corresponding to alginate also decreased in intensity (Figure S11). For post-irradiated Lp coprecipitates, specifically those with C/Fe 0.5 or 1.0, the position of their ν_{asym}(C-O-O) band shifted towards higher wavenumbers by ~7 and 5 cm^{-1}, respectively (Figure S11). A slight decrease in intensity of the ν(O-H) band for the post-irradiated Lp coprecipitates with C/Fe ratio of 0.5 and 1.0 was also observed (Figure S11). However, for both coprecipitates, the position of this band did not substantially change. In contrast, for the post-irradiated Lp coprecipitate with C/Fe ratio of 1.5 the intensity of the ν(O-H) did not change, but slightly shifted by ~6 cm^{-1} towards lower wavenumbers (Figure S11). In addition to reduced intensity, the post-irradiated Lp coprecipitates exhibited broadening of the asymmetric band corresponding to the carboxylate functional group, also due to the appearance of a shoulder band as was observed with the post-irradiated Fh coprecipitates (Figure S11).

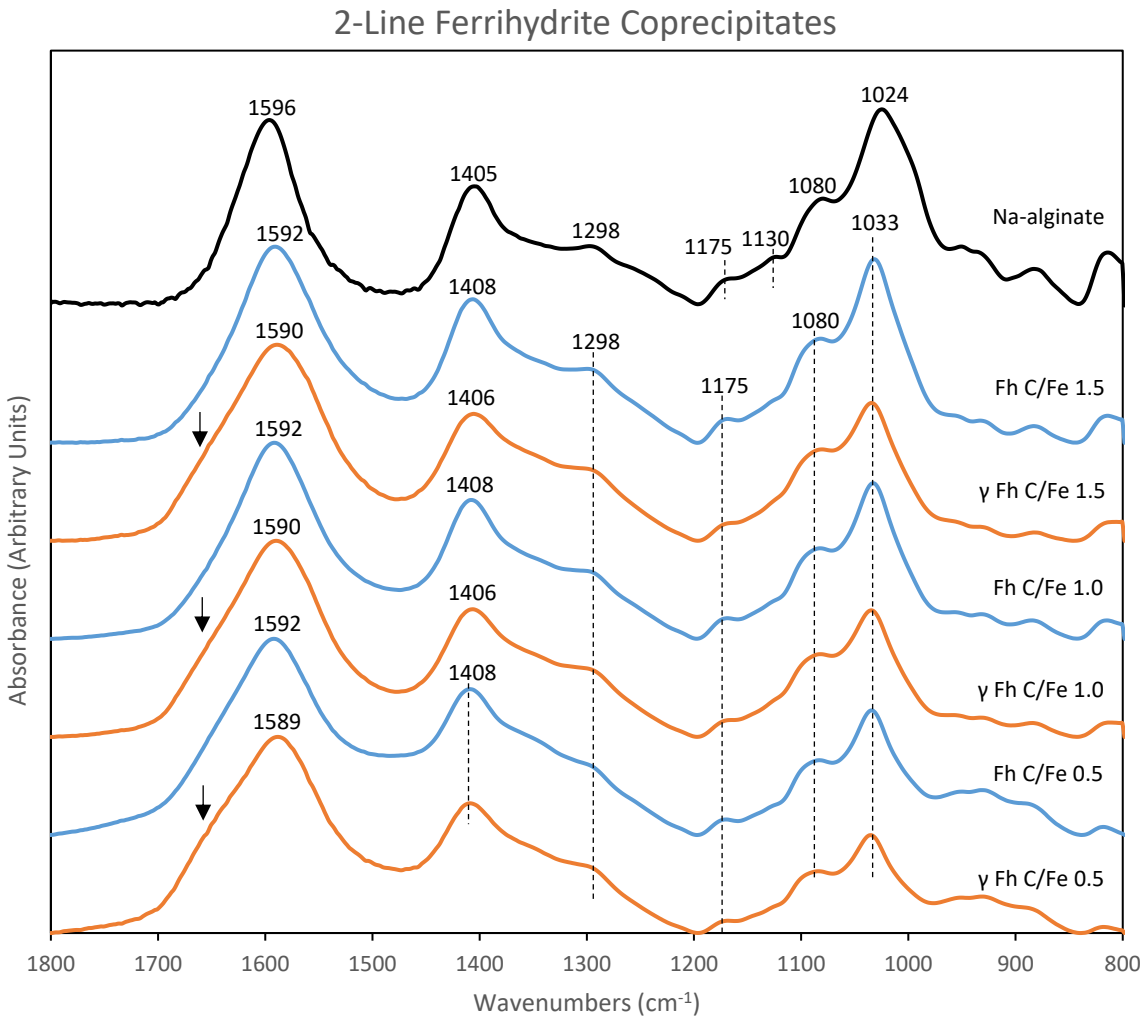

Figure 6: FTIR spectra in the 1800-800 cm^{-1} region of 2-line ferrihydrite coprecipitated with alginate (C/Fe ratio of 0.5, 1.0, and 1.5 mol:mol) before and after γ-irradiation. The spectrum of Na-alginate was added for comparison. Notice the changes in intensity of the bands centred at ~1400 and 1030 cm^{-1} and the broadening of the band centred at ~1590 cm^{-1} following the irradiation treatment. Arrows point to the possible appearance of a shoulder band.

Irradiation did not influence the mineralogy of pure Gt as the bands position and intensity were similar to those of the native Gt (Figure S12). Similarly, the intensity, peak positions, and peak separation distance of the in-plane (δ(O-H)) and out of plane (γ(O-H)) vibrational bands, which are indicators of crystallinity (Schwertmann et al., 1985; Cornell and Schwertmann, 2003; Villacís-García et al., 2015), were comparable to those determined for the corresponding native

controls. This suggests that irradiation did not affect the crystallinity of the Gt coprecipitates. In comparison to post-irradiated Fh and Lp coprecipitates, the IR spectra of the post-irradiated Gt coprecipitates did not exhibit substantial changes in the intensity or positions of the bands corresponding to ν(O-H) and alginate (Figure S12).

3.5.3. ^{57}Fe Mössbauer spectroscopy

Mössbauer spectra collected at 77 and 5 K were used to characterize changes in the crystallinity and redox state of the post-irradiated Fhs relative to the native controls. The Mössbauer spectra of the native and irradiated Fhs are shown in Figure 7, and the derived Mössbauer parameters are given in Table 1. In all spectra collected at 77 K, we observed a doublet with the parameter value of centre shift (CS): 0.35-0.5 mm/s and quadrupole split (QS): 0.7-0.85 mm/s, consistent with 2-line ferrihydrite. In spectra collected at 5 K, two sextets were observed: sextet A with parameters of CS = 0.48 mm/s, QS = 0 mm/s, hyperfine field (H) = 50 T, and sextet B with parameters of CS = 0.42 mm/s, QS = -0.03 mm/s, hyperfine field (H) = 45 T, consistent with ferrihydrite that is magnetically ordered at this temperature (Byrne and Kappler, 2022).

The post-irradiated Fhs show significant differences at both temperatures. All post-irradiation spectra collected at 77 K show a broadening of the Fe(III) doublet relative to the pre-irradiation spectra (Figure 7). This broadening may be fit by the addition of a collapsed sextet with a low hyperfine field (5.4-20.6 T) and may indicate ferric oxyhydroxides that are partially ordered (Murad and Cashion, 2004; Byrne and Kappler, 2022). As this ferric oxyhydroxide phase shows ordering at 77 K while 2-line ferrihydrite does not, this phase may be more crystalline than ferrihydrite (Table 1). The 77 K spectrum of post-irradiated Fh coprecipitated with C/Fe ratio of 1.5 also exhibited an Fe(II) doublet with the parameters CS = 1.3 mm/s and QS = 2.7 (4.5% of the total spectral area) (Table 1).

The results of the spectra collected at 5 K are consistent with those collected at 77 K (Figure 7). All spectra exhibit two sextets consistent with ferrihydrite. In the case of post-irradiated Fh coprecipitated with C/Fe ratio of 1.5, a small broadened Fe(II) doublet was added, consistent with the fits at 77 K (Figure 7). It should be noted that the proportion of relative area of the Fe(II) doublet differ slightly between the 77 and the 5 K spectra as the proportion approaches the lower limit of detection of the Mössbauer (~2%) and is consistent with past observations of broadening of the Fe(II) doublet upon Fe(II) sorption to iron oxyhydroxides (Table 1) (Notini et al., 2019).

Table 1: Mössbauer parameters for 2-line ferrihydrite and coprecipitates before and after γ-irradiation determined from spectra collected at liquid nitrogen (77 K) and liquid helium temperature (5 K).

Sample	T (K)	Site	CS (mm/s)	QS (mm/s)	H (T)	Relative area (%)	χ^2
Fh	77	Fe(III)	0.43	0.79		100	0.76
	5	Ferrihydrite A	0.46	-0.01	49.9	55.0	0.68
		Ferrihydrite B	0.44	-0.01	46.8	45.0	
γ Fh	77	Fe(III)	0.43	0.77		72.7	1.13
		Collapsed sextet	0.38	-0.05	10.6	27.3	
	5	Ferrihydrite A	0.46	0.0	50.1	48.7	0.79
		Ferrihydrite B	0.43	-0.02	46.9	51.3	
Fh C/Fe 0.5	77	Fe(III)	0.43	0.81		100	1.24
	5	Ferrihydrite A	0.48	0.0	50.2	30.0	0.70
		Ferrihydrite B	0.42	-0.01	47.1	70.0	
γ Fh C/Fe 0.5	77	Fe(III)	0.44	0.80		79.9	1.8
		Collapsed sextet	0.45	-0.05	20.7	20.1	
	5	Ferrihydrite A	0.46	0	50.0	39.9	0.71
		Ferrihydrite B	0.42	-0.02	46.6	60.1	
Fh C/Fe 1.0	77	Fe(III)	0.44	0.79		100	1.33
	5	Ferrihydrite A	0.48	-0.02	49.6	57.0	0.76
		Ferrihydrite B	0.42	-0.04	45.1	43.0	
γ Fh C/Fe 1.0	77	Fe(III)	0.45	0.78		86.4	0.84
		Collapsed sextet	0.45	0.00	10.8	13.6	
	5	Ferrihydrite A	0.47	0.00	49.8	54.0	0.76
		Ferrihydrite B	0.43	-0.04	45.7	46.0	
Fh C/Fe 1.5	77	Fe(III)	0.43	0.79		100	1.01
	5	Ferrihydrite A	0.45	0.00	49.1	54.0	0.68
		Ferrihydrite B	0.43	0.00	45.1	46.0	
γ Fh C/Fe 1.5	77	Fe(III)	0.46	0.80		63.4	
		Fe(II)	1.3	2.7		4.5	0.75
		Collapsed sextet	0.45	-0.05	5.4	32.1	
	5	Fe(II)	1.2	2.25		1.5	
		Ferrihydrite A	0.47	-0.02	49.3	61.5	1.73
		Ferrihydrite B	0.39	-0.05	44.6	37.0	

2-Line Ferrihydrite

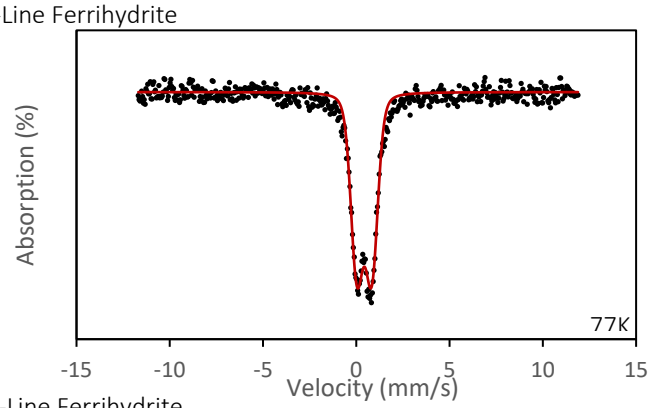

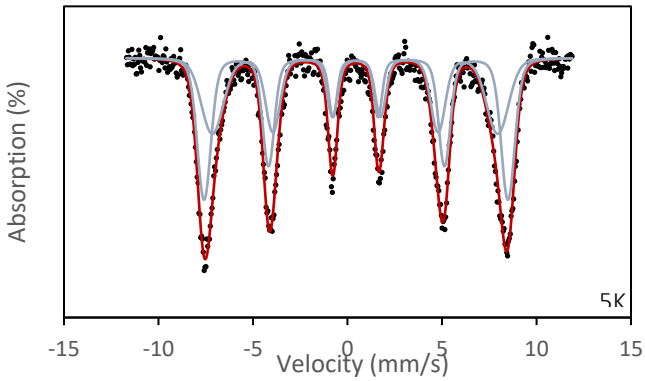

γ 2-Line Ferrihydrite

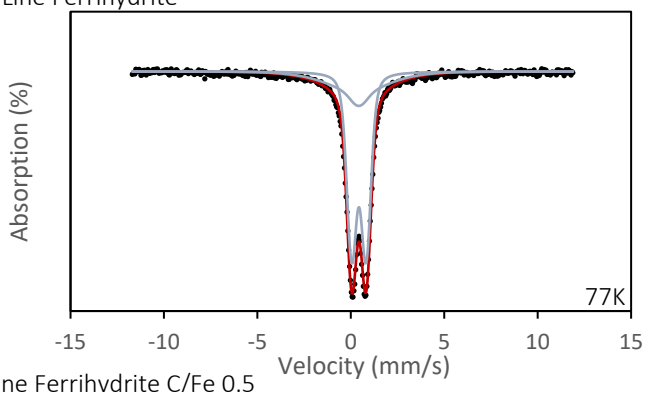

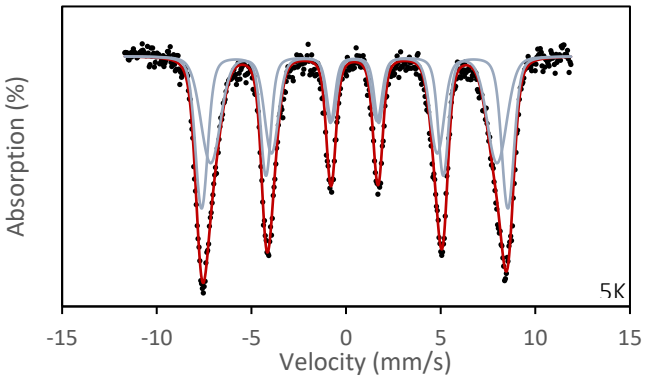

2-Line Ferrihydrite C/Fe 0.5

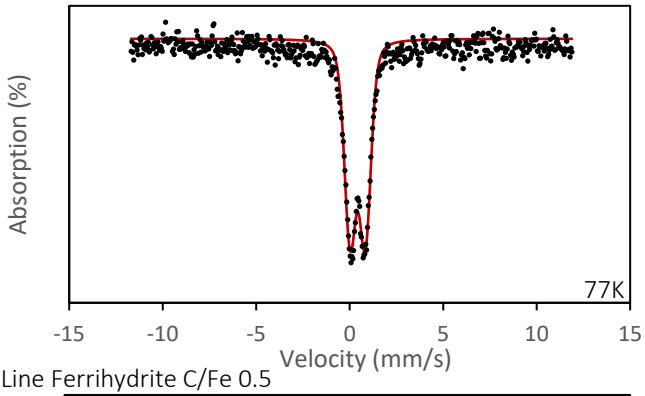

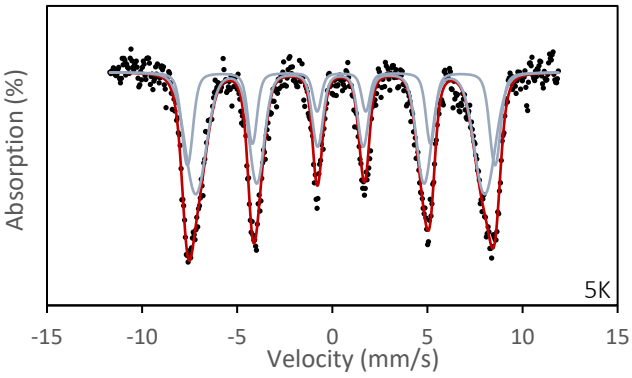

γ 2-Line Ferrihydrite C/Fe 0.5

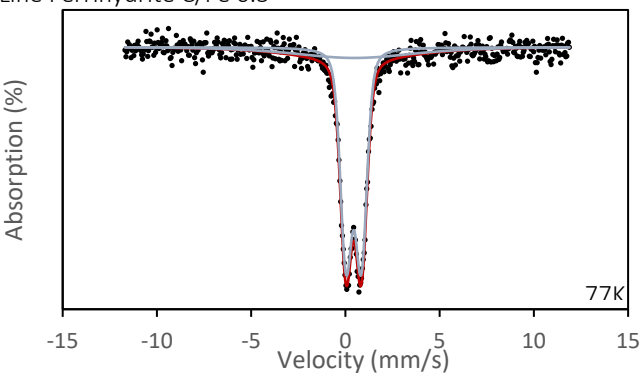

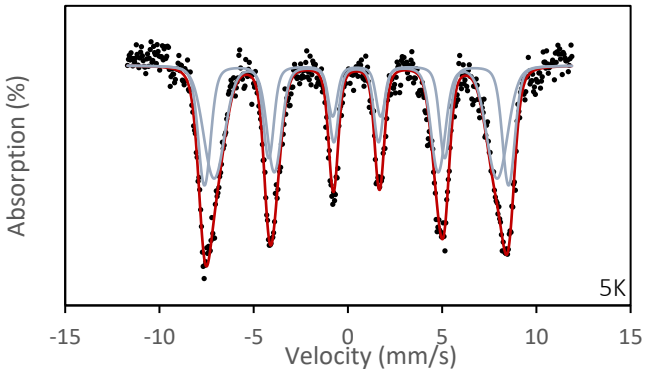

(Figure 7 continued)

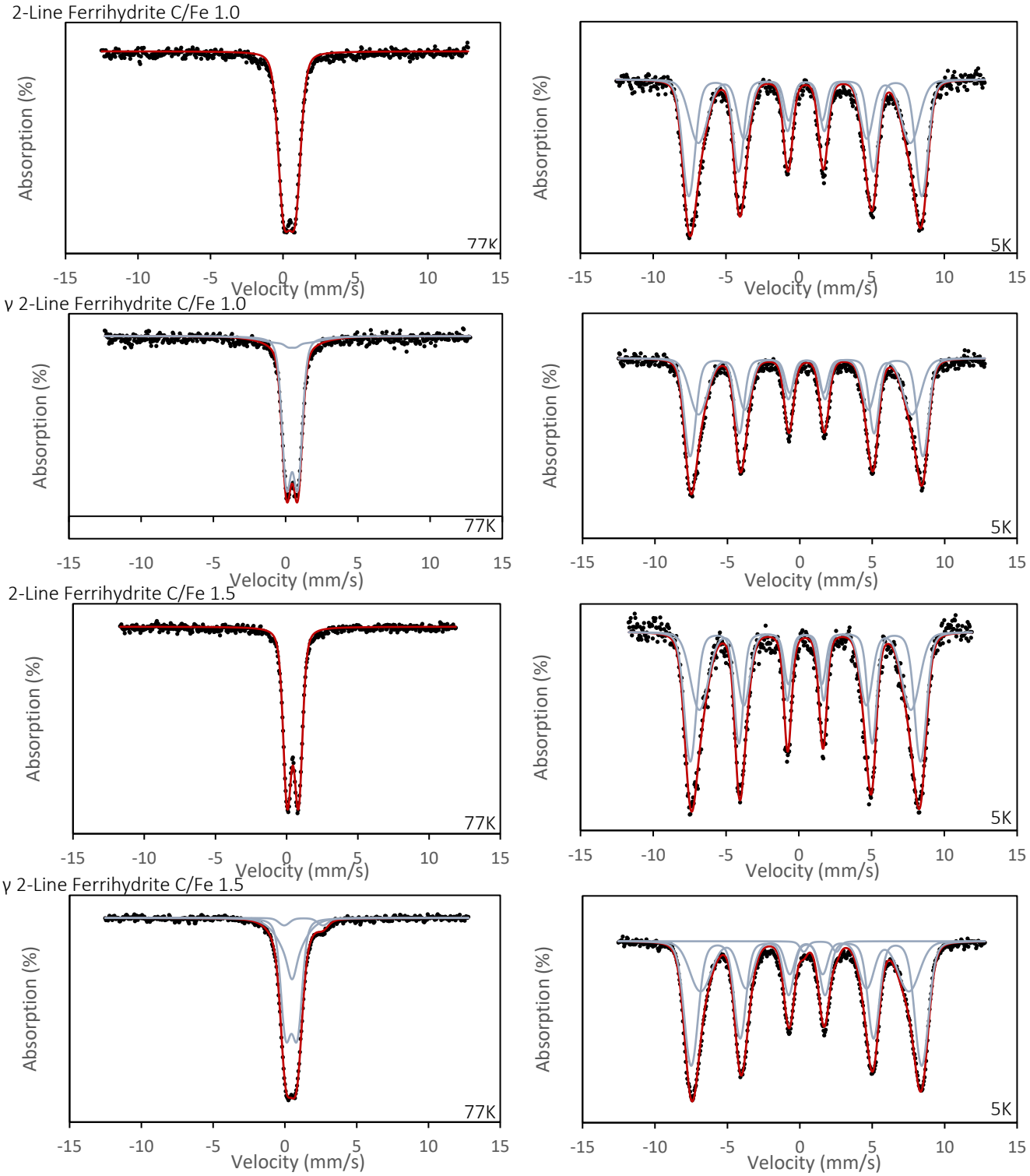

Figure 7: Mössbauer spectra of native and post γ-irradiated 2-line ferrihydrites coprecipitated with alginate (C/Fe ratios of 0, 0.5, 1.0, and 1.5 mol:mol), taken at liquid nitrogen (77 K) and liquid helium temperature (5 K). Symbols show experimental data and lines represent their fit.

3.6. Bioavailability

Microbial Fe(III) reduction curves of the native and irradiated iron oxyhydroxides are presented in Figure 8, which show the increase of total Fe(II) and dissolved Fe(II) relative to total Fe throughout the experimental period (up to 25 days). The rates of Fe(III) reduction by *S. putrefaciens* CN32 were calculated by linear regression of selected time points that corresponded to the period of maximum accumulation of total Fe(II) relative to total Fe (Figure 8). The extent of Fe(III) reduction was determined from the maximum amount of total Fe(II) relative to total Fe, which equated to the average of the last 3 measurement points of an experiment (n = 9). A summary of the regression data and the maximum amount of Fe reduced for the native and post-irradiated iron oxyhydroxides are presented in Figure 9 and Table S6. Control experiments showed no changes in the concentration of Fe(II) or pH throughout the experimental period, and their sterility was confirmed at the start and end of the experimental period (Figure S13).

The overall trends in the distribution of Fe(II) throughout the microbial reduction of the post-irradiated iron oxyhydroxides were similar to those observed for their corresponding native controls (Figure 8). However, a notable exception was found in the case of the post irradiated Fh coprecipitates, in which case a deviation in the extent of Fe reduction was observed at day 8 and gradually increased until termination of the experiment (Figure 8). The post-irradiated Fh coprecipitates exhibited a 23-28% increase in the amount of Fe reduced compared to the native Fh coprecipitates (Figure 9 and Table S6). Additionally, the extent of Fe(III) reduction among the irradiated Fh coprecipitates displayed significant variability based on C content ($P<0.05$, one-way ANOVA), peaking at a C/Fe ratio of 1.0 (Figure 9 and Table S6). However, relative to the irradiated Fh with C/Fe 0.5, the difference in the extent of Fe(III) reduction amounted to only ~5% (Figure 9 and Table S6). Concurrently, with the release of biogenic Fe(II), pH also increased over

the course of the experiment in the biotic systems (Figure S13). It was observed that the pH reached higher values by 0.2-0.3 pH units during the microbial reduction of the post-irradiated Fh coprecipitates when compared to their corresponding native counterparts (Figure S13). Despite these observations, however, the rate of Fe(III) reduction displayed no significant difference between the post-irradiated minerals and their corresponding native counterparts ($P>0.05$, two tailed t-test, Figure 9 and Table S6). Moreover, the concentrations of dissolved Fe(II) reached a similar proportion of the total Fe(II) as those measured for the corresponding native Fhs (Figure 9).

In contrast to the Fh coprecipitates, the impact of irradiation on the reduction extent of the more crystalline Lp and Gt coprecipitates exhibited variability (Figures 8 and 9). Significant deviations in the extent of Fe(III) reduction were only observed for the Lp and Gt coprecipitates, specifically in the cases of native Lp coprecipitated with a C/Fe ratio of 0.5 and native Gt coprecipitated with a C/Fe ratio of 1.5, when compared to their respective post-irradiated counterparts ($P<0.05$, two tailed t-test). These differences accounted for approximately 10% and 8% variation, respectively (Figure 9 and Table S6). The levels of pH also increased within the biotic systems, but in contrast to the Fh systems, the difference between the native and post-irradiated Lp and Gt coprecipitates was not as substantial (Figures S14 and S15). Similar to the observations made for the Fh systems, the rates of Fe(III) reduction for the native Lp and Gt precipitates paralleled those determined for their respective irradiated counterparts (Figure 9 and Table S6). Lastly, among all the post-irradiated Lps and Gts biotic microcosms, the concentrations of dissolved Fe(II) reached a comparable proportion of the total Fe(II) as measured for the corresponding native systems (Figure 8).

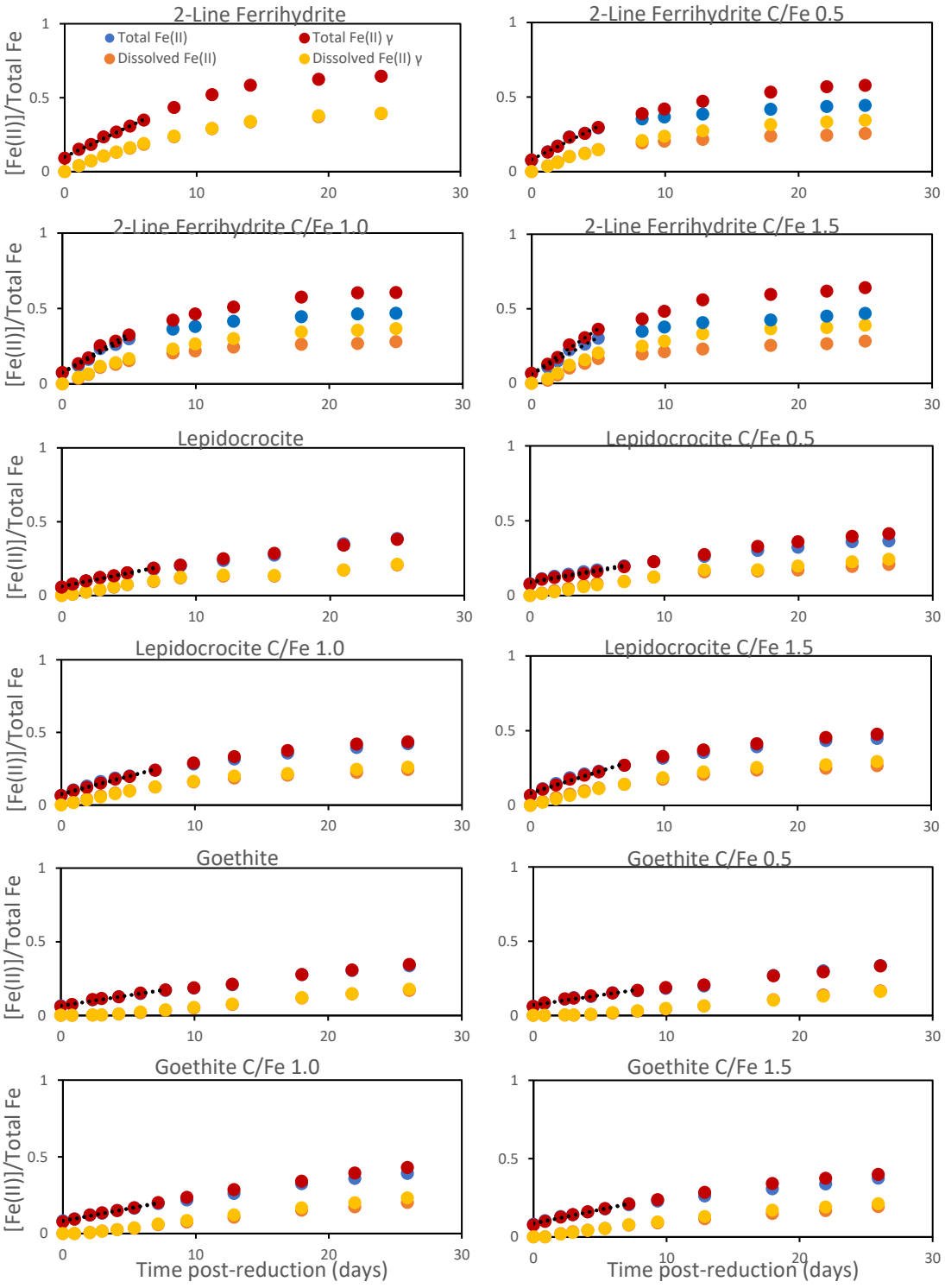

Figure 8: Changes in total and dissolved Fe(II) relative to total Fe for native iron oxyhydroxides and their corresponding γ-irradiated counterparts during anaerobic Fe reduction by *S. putrefaciens* CN32. Dashed lines represent the maximum production of total Fe(II) from which the rate of Fe reduction was calculated. Data markers represent means ± standard deviations derived from three experimental replicates of each system.

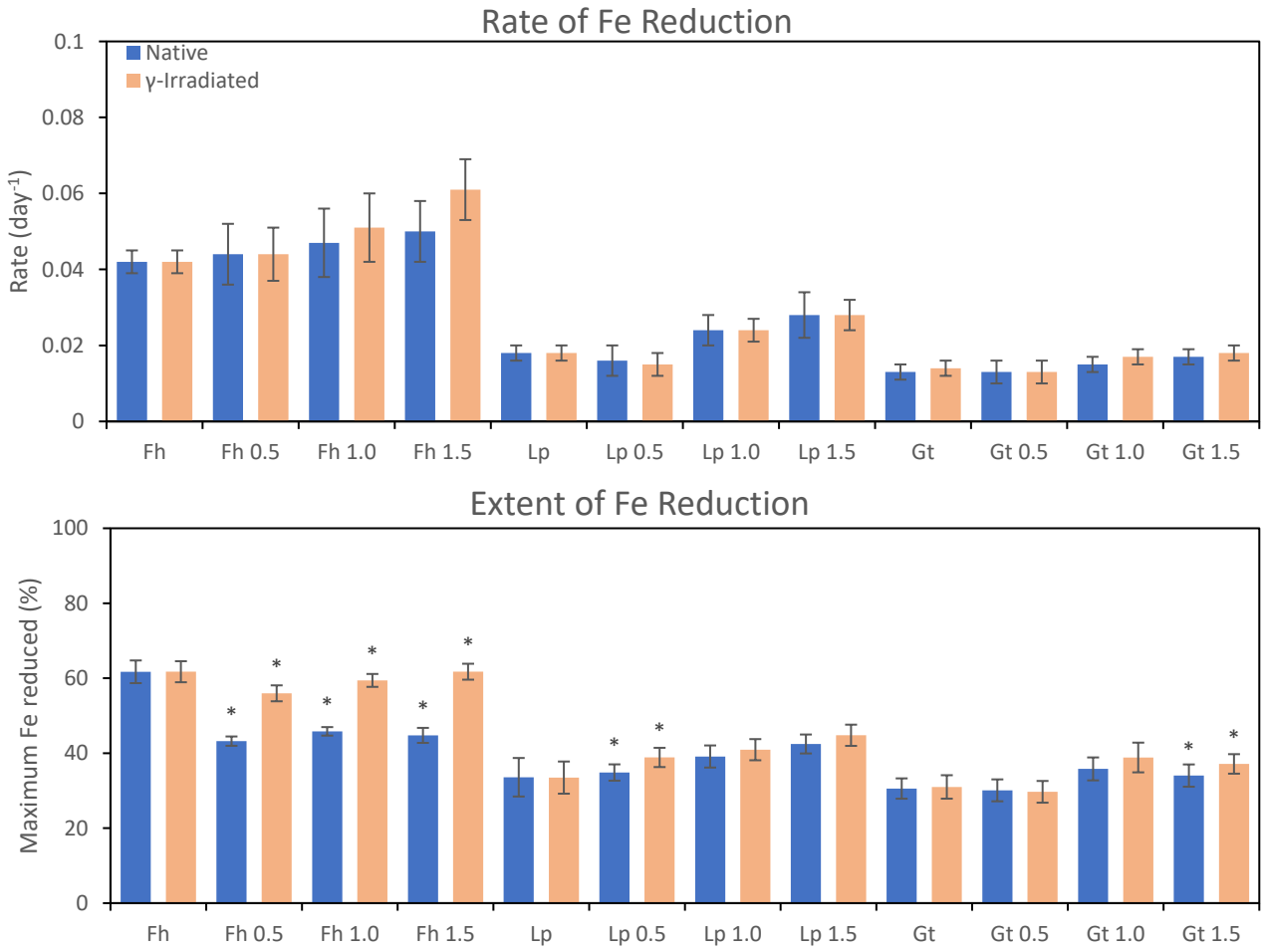

Figure 9: Derived rate and extent of Fe(III) reduction of the native iron oxyhydroxides and their corresponding γ-irradiated counterparts. Data was collected from three individual experimental replicates for each system. Asterix indicates significant difference between the values at the 95% confidence interval ($P<0.05$, two-tailed t-test). Fh, Lp, and Gt correspond to 2-line ferrihydrite, lepidocrocite, and goethite, respectively. Please see Table S6 for the numerical values.

3.6.1. Biogenic solids

X-ray diffractograms of the post-reduction minerals are shown in Figures S16-S18. Broad reflections of residual Fh were observed in the biogenic solids after microbial reduction of native and irradiated Fhs (Figure S16). Fe(III) reduction transformed pure native and post-irradiated Fh into Fh with slightly sharper reflections at 35 and 62 degrees, indicating higher crystallinity (Figure S16). However, no crystalline iron (oxyhydr)oxides such as goethite, lepidocrocite, or magnetite were detected in the biogenic solids following the microbial reduction of the native and post-

irradiated Fhs (Figure S16). The addition of 400 μM phosphate led to vivianite ($Fe_3(PO_4)_2 \bullet 8H_2O$) precipitation in the biogenic solids from the native and post-irradiated pure Fh as well as post-irradiated Fh coprecipitates, but not from the native Fh coprecipitates (Figure S16). Moreover, SEM and EDS analysis revealed plate-like morphologies rich in P and Fe, likely vivianite, where XRD confirmed its presence (Figures S19-S22).

Microbial reduction of the native and irradiated Lps or Gts led to biogenic solids consisting mainly of residual Lp or Gt, respectively, together with vivianite, with no other differences (Figures S17 and S18). SEM and EDS also confirmed the data observations made by XRD (Figures S23 and S24). Interestingly, vivianite was absent from the biogenic solids from the native and irradiated Gt coprecipitated with C/Fe of 0.5 (Figure S17).

4. Discussion

4.1. Effects of Na-alginate

The effects of γ-irradiation at a dose of 25 kGy on the physicochemical properties and bioavailability were tested on a range of synthetic iron oxyhydroxide minerals with variable thermodynamic stability and alginate content (C/Fe ratio of 0, 0.5, 1.0, and 1.5 mol:mol). Such effects were tested on minerals in the wet state since air-drying or freeze-drying significantly affects the aggregation state and reactivity of iron oxyhydroxides (Roden and Zachara, 1996; Raiswell et al., 2010). Coprecipitation of 2-line ferrihydrite (Fh), lepidocrocite (Lp), and goethite (Gt) with variable alginate content led to the precipitation of minerals with variable physicochemical properties, bioavailability, and therefore sensitivity. The effects of alginate content were evident through several analyses, including chemical extractions, measurements of porosity and SSA, XRD, FTIR spectroscopy, and the evaluation of bioavailability by *S. putrefaciens* CN32. Generally, coprecipitation with alginate led to the precipitation of minerals

with lower crystallinity and smaller particle size as a consequence of alginate-induced poisoning of crystal growth, but with variable effects on the porosity and in turn on the SSA as well as bioavailability. These observations agree with past studies that have investigated the impact of organic substances, encompassing polysaccharides, humic and fulvic acids, as well as simple organic compounds, on the physicochemical properties of various synthetic iron oxyhydroxides (Liu and Huang, 2003; Schwertmann et al., 2005; Eusterhues et al., 2008; Mikutta et al., 2008; Shimizu et al., 2013; Chen et al., 2014; Poggenburg et al., 2016; Liu et al., 2019b). Furthermore, the synthesized minerals exhibited similarities to the properties documented in literature for naturally occurring BIOS (Langley et al., 2009b; Toner et al., 2009; Gault et al., 2011; Najem et al., 2016; ThomasArrigo et al., 2022). Hence, the investigated iron oxyhydroxide minerals are of environmental relevance.

4.2. Impact of γ-irradiation: mineralogy

It is well established in the literature that the interaction of high energy γ-radiation with H_2O molecules leads to the production of a variety of primary and secondary radicals, and molecular products according to (Wren and Glowa, 2000; Joseph et al., 2008; Sutherland et al., 2017):

$$H_2O \xrightarrow{\gamma} e_{aq}^-,\ {}^{\bullet}H,\ {}^{\bullet}OH,\ H_2O_2,\ {}^{\bullet}HO_2,\ H_2,\ {}^{\bullet}O_2^-,\ \text{and}\ H_3O^+ \qquad (1)$$

Past and recent studies have exploited radiolysis products to investigate the formation of various iron oxyhydroxides using suspensions of dissolved ferrous iron, ferric iron, or ferric iron precipitates under various conditions (e.g. regarding pH and dissolved oxygen), and in the presence or absence of stabilizing agents (e.g. organic polymers) as well as ˙OH scavengers (e.g. alcohols)

under various doses of irradiation (Wang and Xin, 1999; Jurkin et al., 2011; Yakabuskie et al., 2011; Jurkin et al., 2016a; Jurkin et al., 2016b; Sutherland et al., 2017; Marić et al., 2019; Marić et al., 2020a; Marić et al., 2020b). Accordingly, the nature and concentration of the formed products depend on the dose rate, and conditions of the solution including temperature, pH, dissolved O_2 concentration, and solutes present in the system (Hochanadel and Ghormley, 1962; Joseph et al., 2008; Yakabuskie et al., 2011; Sutherland et al., 2017). Within neutral solutions with dissolved oxygen, initial reactions are likely driven by a range of oxidizing and reducing radicals including $^{\bullet}OH$, e_{aq}^-, and $^{\bullet}H$, and as the system rapidly reaches steady state, the contribution from H_2O_2 becomes more relevant as its concentration increases (Wren and Glowa, 2000; Joseph et al., 2008). Thus, in our systems, the radiolytic products react with each other, and available solutes leading to oxidation and reduction reactions as concurrent competitive processes. Upon irradiation of our systems, the reaction is initiated as rapid reduction of lattice ferric iron to ferrous iron according to:

$$Fe(III) + e_{aq}^- \rightarrow Fe^{2+}_{(aq)} \quad (2)$$

However, the mobility of Fe^{2+} is limited by rapid oxidation in solution and precipitation:

$$Fe^{2+}_{(aq)} + OH^{\bullet} \rightarrow Fe^{3+}_{(aq)} + OH^- \quad (3)$$

$$Fe^{3+} + 3OH^- \leftrightarrows Fe(OH)^{2+} + 2OH^- \leftrightarrows Fe(OH)_2^- + OH^- \leftrightarrows Fe(OH)_3 \quad (4)$$

The mobility of Fe^{2+} is also limited by adsorption and subsequent oxidation by H_2O_2, according to:

$$Fe^{2+}_{(aq)} \rightarrow Fe(II)_{ad} \quad (5)$$

$$Fe(II)_{ad} + H_2O_2 \rightarrow 2Fe(III)_{ad} + 2OH^- \quad (6)$$

Thus, in the absence of alginate, reactions 3-6 limit the release of Fe^{2+} into solution, explaining the lack of measurable concentrations of this species in the supernatants of the post-irradiated pure

minerals Fh, Lp, and Gt (Figure 1). Moreover, the lack of changes of pH may indicate an equal production of protons and hydroxide ions (Figure S2).

The cycle of concurrent radiolytically-induced reduction/oxidation reactions was also hypothesized to operate in a manner similar to Ostwald ripening, resulting in the coarsening of metal oxide nanoparticles through bridging and aggregation (Yakabuskie et al., 2011; Sutherland et al., 2017), which may eventually lead to transformation. This cycle may explain the observed increase in crystallinity of the Fhs in this study. Along the same lines, Brown et al. (2014) reported increased crystallite size and the partial transformation of 2-line ferrihydrite into a crystalline mineral phase resembling akageneite after irradiation to a total dose of 1 MGy. Their study suggested that the presence of trace amounts of Cl from the synthesis procedure, which involved neutralizing a $FeCl_3$ solution, could have facilitated the formation of akageneite. In a similar manner, the Fhs in our study were synthesized using a similar procedure. Hence, it is possible that the observed crystalline phase represents an intermediate state between akageneite and 2-line ferrihydrite, reflecting the findings of Brown et al. (2014). It is worth noting that the irradiated Fh coprecipitates exhibited similar changes in crystallinity compared to the irradiated pure Fh (Table 1). While no direct relationship was observed between the extent of the collapsed sextet at 77 K and alginate content, our results are intriguing, as the existing literature indicates that organic matter hinders the transformation of 2-line ferrihydrite into crystalline phases by binding particles and impeding dissolution-precipitation (goethite) and solid-state (hematite) conversion reactions (Cornell and Schwertmann, 2003; Chen et al., 2015; Najem et al., 2016). Nevertheless, despite the observed alterations in Fhs' crystallinity, they could not be distinguished through XRD, FTIR-ATR, chemical extractions, and, in the case of pure Fhs, their SSA and PV suggesting that at the

first glance the irradiated Fhs and their native counterparts exhibit similar reactivity (Figures 2 and 3).

In contrast to 2-line ferrihydrite, irradiation of a stable iron oxide phase such as hematite to a final dose of 1 MGy led to the partial formation of a poorly crystalline iron oxide phase (Brown et al., 2014). In our study, the fact that the extractable Fe fractions were comparable between the post-irradiated and native controls for pure Lp and Gt indicates that the possible formation of a poorly crystalline iron oxide phase is insignificant at the low dose (25 kGy) applied in this study (Figure 2). Conversely, 0.5 M HCl extracted a lower amount of Fe from the post-irradiated Lp coprecipitates when compared to their native controls (Figure 2). The reason for this is unknown, since we should expect the Gt coprecipitates to exhibit a similar trend (Figure 2). However, the comparability of PV, SSA, together with ascorbate extractable Fe measurements between the irradiated Lp and Gt coprecipitates and their native controls indicate minimal irradiation induced changes at their surface (Figures 2 and 3).

4.3. Impact of γ-irradiation: role of Na-alginate

The presence of alginate in our systems adds another level of complexity. When exposed to irradiation, alginate undergoes degradation (Al-Assaf et al., 2016). Several studies have proposed the mechanism behind this degradation, which, in dilute solutions, initiates with the abstraction of H from the alginate chain by the radicals $^{\bullet}H$ and $^{\bullet}OH$ generated during the radiolysis of water (1) (Nagasawa et al., 2000; Wasikiewicz et al., 2005; Le Quang and Vo Thi, 2009; Al-Assaf et al., 2016). The alginate derived radicals are inherently unstable, leading to the cleavage of the 1,4-glycosidic bonds thereby reducing the molecular weight of alginate to form oligosaccharides and additional organic radicals through multiple pathways (Nagasawa et al., 2000; Wasikiewicz et al., 2005; Le Quang and Vo Thi, 2009; Al-Assaf et al., 2016). Indeed,

irradiation of ≤1% alginate solutions, similar to the maximum alginate content in our jars, to a dose of 30 kGy led to a decrease in the molecular weight of alginate by ~96% (Nagasawa et al., 2000; Lee et al., 2003; Wasikiewicz et al., 2005). Degradation of alginate may also proceed by reaction with the radiolytically produced H_2O_2, however we expect this reaction to play a minor role given that the rate of this reaction increases with increasing temperature (Li et al., 2010). Accompanying the decrease in molecular weight, studies have also reported the concomitant reduction in the viscosity of the alginate solutions, mirroring our observations for the post-irradiated coprecipitates, particularly for the Fh coprecipitates (Figure S1) (Nagasawa et al., 2000; Lee et al., 2003; Wasikiewicz et al., 2005). This reduced viscosity likely explains the observed increased wet Fe content in the post-irradiated coprecipitates (Figure 2).

The irradiation of the coprecipitates resulted in elevated levels of DOC, total dissolved Fe, and Fe(II) in the supernatants (Figure 1). Notably, the absence of dissolved Fe species in the supernatants of post-irradiated pure iron oxyhydroxide phases, coupled with the apparent strong relationship between DOC and total dissolved Fe, provides compelling evidence for the role of alginate in promoting the dissolution of the coprecipitates during irradiation. FTIR-ATR analyses of the supernatants further confirmed the presence of alginate/alginate degradation products in solution (Figures S25-S27). The IR spectra of the products collected from the supernatants of the post-irradiated coprecipitates exhibited some differences when compared to the IR spectra of Na-alginate or, where possible, the products collected from the supernatants of the corresponding native coprecipitates (Figures S25-S27). Notably, the intensity of the band centered at ~1024-1030 cm^{-1}, presumed to correspond to the ν_{asym}(C-O-C) of the glycosidic linkage, was reduced relative to the intensity of the ν_{asym}(C-O-O) band centred at 1590-1592 cm^{-1}. Additionally, there was broadening and shifting of the ν_{asym}(C-O-O) band, centred at 1590-1592 cm^{-1}, by 4-6 cm^{-1} to lower

wavenumbers (Figures S25-S27). The former change could be attributed to the cleavage of the 1,4-glycosidic bonds in agreement with observations made by Le Quang and Vo Thi (2009), whereas the latter can be attributed to the complexation of the released Fe(III) by the carboxylate functional groups leading to changes in the local environment around these groups. The observed irradiation induced release of DOC into solution is in line with previous studies, which has been attributed to the breakdown of cellular biomass and carbohydrates by radicals, as described here for alginate (McNamara et al., 2003; Berns et al., 2008; Zhang et al., 2016; Otte et al., 2018). Moreover, the release of dissolved iron along with DOC corresponds to the findings of Schaller et al. (2011), who attributed this increase to the leaching of iron from microbial cells and/or organic/inorganic sediment particles.

The measurable amounts of Fe(II) detected in the supernatants of the post-irradiated coprecipitates indicate a reduction of lattice Fe that is likely mediated by the reducing radical, e_{aq}^-, as in reaction (2). However, it is apparent that alginate facilitated this reaction given that the concentration of dissolved Fe(II) increased with increasing initial concentration of alginate across all coprecipitates (Figure 1). Structural reduction of Fe(III) to Fe(II) by irradiation to a dose of ~84 kGy was also apparent by Mössbauer spectroscopy in clay powders intercalated with simple alcohols (ethylene glycol and tert-butanol) (Gournis et al., 2000). The reduction was attributed to the hydrogen generated from the homolysis of the irradiated alcohols, whereas the generated alcohol radicals either dimerize or react with each other to generate stable molecules (Gournis et al., 2000). Alcohols may also facilitate the reduction of Fe(III) by maintaining a reducing environment, to some extent, by scavenging the $^{\bullet}OH$ radical thereby hindering the oxidation of Fe(II) back to Fe(III) (Wang and Xin, 1999; Jurkin et al., 2016a; Jurkin et al., 2016b; Marić et al., 2020b). In our systems, alginate likely serves multiple roles. Firstly, alginate functions to stabilize

and disperse iron oxide particles in solution thereby enhancing the contact between solid and liquid phase upon irradiation and increasing the probability of contact with the irradiation generated reducing species (Wang and Xin, 1999; Gotić et al., 2009; Liu et al., 2009; Jurkin et al., 2011; Jurkin et al., 2016a; Marić et al., 2019; Marić et al., 2020b). Secondly, alginate and its degradation products function as scavengers for the oxidizing radical $^{\bullet}OH$ playing a role that is analogous to alcohols (Falkeborg et al., 2014). Thirdly, alginate and its degradation products bind Fe(II) and Fe(III) thereby providing further protection against oxidation and preventing the precipitation of new mixed Fe(II)/Fe(III) phases, respectively.

4.4. Impact of γ-irradiation: differences among the oxyhydroxides

The C content of the native coprecipitates increased with increasing initial alginate concentration, and at corresponding initial C/Fe ratio the final C content among the coprecipitates exhibited the following trend: Fh >> Lp ≥ Gt (Figure 2). Therefore, synthesis of Fh via neutralization of acidic Fe(III) solution led to a higher uptake of alginate as opposed to synthesis via Fe(II) oxidation and subsequent Fe(III) hydrolysis pathway for Lp and Gt (Figure 2). The C/Fe ratio for the Fh coprecipitates ranged from 0.5 to 1.5, whereas it varied from 0.24 to 0.64 for Lp coprecipitates and from 0.24 to 0.44 for Gt coprecipitates (Figure 2). Consequently, Lp and Gt that were coprecipitated with an initial C/Fe ratio of 1.0 or 1.5 retained a C/Fe ratio that is equivalent to- or close to- that of Fh coprecipitated with a C/Fe ratio of 0.5 (Figure 2). The former synthesis procedure also led to the formation of larger aggregates as determined by particle size analyses such that at corresponding initial C/Fe ratios, the native Fh coprecipitates exhibited the largest particle sizes among the studied coprecipitates (Figure 4). Moreover, for the native Fh with a C/Fe ratio of 0.5, the particles exhibited a pH_{iep} of ~6.6, which decreased to <4 as the C/Fe ratio increased to 1.0 and 1.5 (Figure S6). In contrast, all of the native Lp and Gt coprecipitates exhibited

a pH_{iep} of <4 (Figures S7 and S8). The different synthesis pathways of the studied minerals also led to different changes in PV and SSA (Figure 3). With increasing alginate content, the SSA of the Fh coprecipitates decreased, while the SSA of the Lp coprecipitates increased, whereas the SSA of the Gt coprecipitates decreased (Figure 3). Consequently, given the distinct mineralogy and physicochemical properties among the synthetic coprecipitates, it is not surprising that they would exhibit a varying response to the irradiation treatment.

For instance, changes in the PV and SSA were detected only in the post-irradiated Fh coprecipitates with a C/Fe ratio of 0.5 and 1.0 (Figure 3). The observed changes induced by irradiation could be attributed to the modification of the coprecipitates' surface that is likely associated with the release of DOC and Fe. These modifications are evidenced by the ζ-potential measurements for these minerals (Figure S6). For Fh with C/Fe ratio of 0.5, the C content did not change post-irradiation, and the amount of DOC in solution accounted for ~2% of the initial total C pool (Figures 1 and 2). This amount was considerably lower when compared to the amount of DOC measured following the irradiation of Fh coprecipitated with C/Fe ratios of 1.0 or 1.5 (Figure 1). This observation could be attributed to the re-adsorption of the negatively charged alginate products to the surface of the Fh particles as evidenced by the decrease of pH_{iep} for this mineral (Figure S6). Adsorption proceeds at the surface of Fh thereby blocking the pores and in turn reducing the SSA as was determined for this mineral (Figure 3). This reaction may also explain the observed decline in the PV and SSA for the post-irradiated Fh coprecipitated with a C/Fe ratio of 1.0, whereas the PV and SSA for post-irradiated Fh coprecipitated with a C/Fe ratio of 1.5 could not be assessed by N_2-adsorption as a consequence of the already blocked pores by alginate (Figure 3). For the latter coprecipitates, their surface charge became more positive relative to their corresponding native counterparts, which could be attributed to charge neutralization by the

adsorption of Fe(III) (Figure S6). Modifications to the surface of the post-irradiated Fh coprecipitates could be also reflected by the observed changes to the FTIR-ATR spectra (Figure 6). Notably, broadening of the bands corresponding to the carboxylate functional groups indicative of changes in the local environment around these groups as was observed for the supernatants post-irradiation (Figure S25).

In contrast to the Fh coprecipitates, the PV and SSA of the Lp and Gt coprecipitates did not change post-irradiation, even at equivalent or near equivalent C/Fe ratios to Fh coprecipitated with a C/Fe ratio of 0.5 (Figure 3). Moreover, their surface charge remained comparable to that of their native counterparts, whereas irradiation induced changes to the particle size were only evident among the Lp coprecipitates as opposed to the Gt coprecipitates (Figure 4). Likewise, irradiation induced surface modifications as highlighted by changes to the local environment around the carboxylate function groups were only evident among the Lp coprecipitates as opposed to the Gt coprecipitates (Figure S11). The apparent difference in the extent of irradiation induced changes between the Lp and Gt coprecipitates could be attributed to the higher poorly crystalline Fe fraction of the former as determined by the 0.5 M HCl and ascorbate chemical extractions (Figure 2). This poorly crystalline Fe fraction coprecipitated with alginate may be more susceptible to irradiation induced degradation than the crystalline phases such as Gt. However, despite the apparent similarity of changes in the discussed physicochemical properties of the Lp coprecipitates to those observed for the Fh coprecipitates, the lack of changes to PV and SSA of the former coprecipitates, especially at the highest C/Fe contents, is unknown and warrants further investigation. Likewise, the reason for the lack of irradiation induced changes to the physiochemical properties of the Gt coprecipitates in comparison to Lp and Fh coprecipitates is unknown. However, it remains possible that the difference in synthesis pathways may have resulted in variations in the distribution and

arrangement of alginate within the coprecipitates. Such notion may explain the different response of the coprecipitates to the irradiation treatment.

4.5. Impact of γ-irradiation: bioavailability

In addition to the analytical techniques employed in this study, microbial Fe(III) reduction experiments were carried out to further probe the impact of γ-irradiation on the bioavailability (rate and extent of Fe reduction) of the various iron oxyhydroxides studied (Figures 8 and 9, Table S6). It is very well established in the literature that the rate and extent of Fe(III) reduction by Fe(III) reducing bacteria (FeRB) is dictated by several factors, including: cell concentration (O'Loughlin et al., 2010), SSA (Roden and Zachara, 1996; Roden, 2003), particle aggregation (Roden and Zachara, 1996; Roden, 2003; Cutting et al., 2009), crystallinity and morphology (Cutting et al., 2009), solubility (Bonneville et al., 2004; Bonneville et al., 2009), Fe(II) concentration (Roden and Zachara, 1996; Fredrickson et al., 1998; Roden and Urrutia, 2002), the presence of simple organic ligands (Urrutia et al., 1999; O'Loughlin et al., 2010), and redox-active molecules (e.g. electron shuttles) (Jiang and Kappler, 2008). In the case of Fe-OM precipitates, additional factors control the bioavailability of Fe and these include: the mode of association between the mineral and OM (i.e. adsorption vs. coprecipitation) (Eusterhues et al., 2014a; Kleber et al., 2015), type of OM (Poggenburg et al., 2016), C/Fe molar ratio (Shimizu et al., 2013; Eusterhues et al., 2014a; Adhikari et al., 2017), surface charge (Amstaetter et al., 2012), extent of OM induced aggregation (Amstaetter et al., 2012; Adhikari et al., 2016; Poggenburg et al., 2016; Poggenburg et al., 2018), and the orientation of the experimental vessels (Dippon et al., 2015). In the current study, it was observed that the initial cell counts for a biotic system using both a native and a corresponding post-irradiated iron oxyhydroxide were comparable within the margin of error (Table S7). This observation indicates that any variations observed in the rate or extent of Fe(III) reduction can be

confidently attributed to differences associated with the physicochemical properties of the mineral phases.

SSA is commonly employed as a quantitative measure to assess the availability of reactive sites for FeRB (Roden and Zachara, 1996; Roden, 2003). Therefore, this parameter can serve as an indicator of the potential bioavailability of iron oxyhydroxides, with an increase in SSA generally favouring microbial Fe(III) reduction, and conversely, a decrease impeding it (Roden and Zachara, 1996; Roden, 2003). In the case of the Fh coprecipitates with a C/Fe ratio of 0.5 or 1.0, we observed a reduction in SSA following the irradiation treatment (Figure 3). As a result, one might expect that the bioavailability of those minerals would be lower than that of their corresponding native controls. However, the rates of Fe(III) reduction for those minerals were comparable, while the extent of Fe(III) reduction was noticeably higher for the irradiated Fh coprecipitates compared to their native controls (Figures 8 and 9, Table S6). This suggests that SSA alone is an unreliable predictor of mineral bioavailability, especially in the context of Fe-OM-coprecipitates (Mikutta and Kretzschmar, 2008; Mikutta et al., 2008; Chen et al., 2014; Poggenburg et al., 2016; Poggenburg et al., 2018). Our findings align with those of several other studies (Mikutta and Kretzschmar, 2008; Langley et al., 2009d; Langley et al., 2009e; Poggenburg et al., 2016), and suggest that other factors control the bioavailability of the studied minerals.

An increased rate of Fe(III) reduction by *Shewanella oneidensis* MR-1 was reported for 2-line ferrihydrite post-irradiation to a dose of 1 MGy (Brown et al., 2014). Furthermore, the rate and extent of Fe(III) reduction were doubled in the presence of an electron shuttle (riboflavin) (Brown et al., 2014). This enhancement was attributed to the partial transformation of ferrihydrite into an akageneite-like phase, and reduced aggregation of ferrihydrite particles (Brown et al., 2014). While we observed a similar partial conversion of Fh into a phase with higher crystallinity

following irradiation, the rate and extent of reduction for the irradiated Fh were found to be comparable to that of the native control (Figures 8 and 9, Table S6). Additionally, we found that the particle size of the irradiated Fh aggregates in suspension was similar to that of the native control (Figure 4). Consequently, the lower dosage used in this study (25 kGy) did not appear to significantly affect the aggregation state of Fh particles, as opposed to the high dosage applied by Brown et al. (2014). Similarly, the bioavailability of pure Lp and Gt did not change post-irradiation (Figures 8 and 9, Table S6), consistent with the lack of alterations in their bulk mineralogy, PV, SSA, particle size, and poorly crystalline Fe fraction as determined by chemical extractions compared to their native controls. Brown et al. (2014) observed that in the absence of an electron shuttle, there was no difference in the bioavailability between irradiated (1 MGy) and native hematite, despite the irradiation induced partial transformation of the mineral into a poorly crystalline Fe(III) phase. However, a difference was observed only when an electron shuttle (riboflavin) was present. Therefore, the addition of an electron shuttle, combined with spectroscopic analyses, might reveal a different outcome for these minerals (Lp and Gt).

In contrast to pure ferrihydrite, the aggregation state of the post-irradiated coprecipitates differed from that of the native controls (Figure 4). When the coprecipitates were suspended in the chemically defined medium, we observed variations in the stability of the aggregates (Figure S28). Specifically, the native Fh coprecipitates appeared to form large aggregates that settled quickly at the bottom of the microcosm bottles. In contrast, the irradiated Fh coprecipitates appeared to form both stable suspensions and larger aggregates, probably due to irradiation-induced degradation of alginate. This observation became more apparent throughout the experimentation period (Figure S28), and measurements of particle size further corroborated our findings (Figure 4). This observation might elucidate the difference in the extent of reduction for the post-irradiated

ferrihydrite coprecipitates compared to their native controls (Figures 8 and 9, Table S6). Larger aggregates would impede the accessibility for the bacteria to available sites, whereas the smaller aggregates would increase site accessibility (Amstaetter et al., 2012; Adhikari et al., 2017). Furthermore, the similarity of the particle size among the post-irradiated Fh coprecipitates likely explains their comparability of the extent of Fe(III) reduction (Figures 4 and 9). It is also possible that as Fe reduction progresses, the aggregation state of the coprecipitates undergoes changes due to the release and re-adsorption of alginate, a process that may differ between alginate and alginate oligosaccharides.

The particle size of the Lp coprecipitates similarly decreased after irradiation, and yet the degree of microbial Fe reduction in comparison to their native counterparts was not as substantial as seen for the Fh coprecipitates (Figure 4). However, it is also possible that distinctions may become more apparent over a longer time period, exceeding 25 days, due to the slower rates of Fe(III) reduction of the Lp coprecipitates (Figure 8). The difference in the extent of Fe(III) reduction between the native and post-irradiated Gt coprecipitates was also not as substantial as seen for the Fh coprecipitates (Figure 8). The lack of changes in the particle size for the Gt coprecipitates might account for the similarity of bioavailability between the irradiated and native coprecipitates for Gt coprecipitates.

In addition to OM controlling the aggregation state and thus the bioavailability of iron oxyhydroxide coprecipitates, OM, depending on the C/Fe ratio and type, may also enhance the bioavailability of iron oxyhydroxides through multiple pathways. Enhancement may proceed through (1) the alleviation of the thermodynamic constraint from the buildup of enzymatically generated Fe(II) on the oxyhydroxide surface (Fredrickson et al., 1998; Urrutia et al., 1999; Roden, 2003; Hyacinthe et al., 2006), and (2) the stabilization of thermodynamically unstable minerals,

particularly Fh and Lp, against Fe(II)-catalyzed transformation into minerals that are less susceptible to microbial Fe(III) reduction, such as magnetite or goethite (Fredrickson et al., 1998; Zachara et al., 2002; Kleber et al., 2015). However, alginate and alginate oligosaccharides exhibit a limited capacity to chelate Fe(II) (Falkeborg et al., 2014). Among the minerals studied, this is further emphasized by the similar proportion of dissolved Fe(II) in relation to total Fe(II) between a native and its corresponding post-irradiated coprecipitate, which also matches that of a corresponding pure phase (Figure 8).

4.6. Characterization of bioreduced solids

The specific identity of biogenic minerals formed during Fe(III) reduction depends on various factors including: the stability of the iron oxide phase (Fredrickson et al., 1998; Cutting et al., 2009), Fe(II) concentration and rate of release (Fredrickson et al., 1998; Hansel et al., 2003; Amstaetter et al., 2012), solution's chemistry (e.g. buffer type and PO_4 concentration) (Fredrickson et al., 1998; Zachara et al., 2002; Borch et al., 2007), OM content (Shimizu et al., 2013; Chen et al., 2015; Poggenburg et al., 2016; Adhikari et al., 2017), and the orientation of the microcosm vessel (Dippon et al., 2015). The absence of crystalline phases in our Fh experiments is partly due to phosphate, which inhibits goethite and magnetite formation by binding to Fh surfaces and forming vivianite and Fe(II) complexes (Hansel et al., 2003; Borch et al., 2007; Amstaetter et al., 2012). Experimental work at our laboratory indicated that at a concentration of 400 μM, phosphate is fully adsorbed by the native Fhs studied (data not shown). Thus, vivianite precipitation occurs as Fe(III) reduction exceeds the adsorption capacity of a mineral phase towards phosphate (Figure 8). However, irradiation induced changes to the surface area of Fh coprecipitates (C/Fe 0.5 and C/Fe 1.0) may have reduced their capacity to adsorb phosphate, thereby allowing for vivianite to reach saturation and precipitate.

In addition to phosphate, OM also contributes to stabilizing Fh against transformation (Cornell and Schwertmann, 2003; Kleber et al., 2015). OM has been shown to hinder surface interactions with Fe(II), thereby reducing the rate of electron transfer between Fe(II) and Fe(III) necessary for the formation of goethite and magnetite (Amstaetter et al., 2012; Shimizu et al., 2013; Chen et al., 2015). Furthermore, OM can alter the pathway of mineral transformation, a property that is dependent on the C/Fe ratio (Shimizu et al., 2013; Chen et al., 2015; Adhikari et al., 2017). At a high C/Fe ratio of 4.3, Shimizu et al. (2013) postulated that the aggregation of Fh-OM-coprecipitates created microenvironments that limited the diffusion of Fe(II) and HCO_3^- into the solution, effectively trapping these species and creating favourable conditions for the precipitation of green rust. However, considering the influence of irradiation on aggregate stability and the reduction of the C content in the Fh coprecipitates, it leads us to hypothesize that irradiation might lead to erroneous conclusions regarding the pathways of mineral transformation and the specific minerals that may form in natural samples.

5. Conclusions

In this study, we found that γ-irradiation to a total dose of 25 kGy led to significant reduction and dissolution of synthetic iron oxyhydroxides coprecipitated with varying concentrations of Na-alginate. The extent of such reactions was found to increase with increasing alginate content. Our results may explain the observations made by Schaller et al. (2011) who reported a significant release of DOC and a concomitant release of Fe and Mn as well as U and As following irradiation of organic rich sediments. Irradiation was also found to have a significant impact on the physicochemical and mineralogical properties of Fh coprecipitates (C/Fe 0.5, 1.0, and 1.5). The observed irradiation induced decrease in SSA and aggregation of these coprecipitates may lead to over-or-underestimation of the adsorption capacity of a natural sample towards

contaminants and nutrients (e.g. As, P, Cu). Likewise, enhanced bioavailability may lead to erroneous conclusions regarding the extent of Fe reduction and organic matter release, which has important implications for research relevant to C cycling that is associated with the iron oxyhydroxide mineral fractions.

We attempted to investigate the impact of irradiation on the physicochemical properties of iron oxyhydroxides with variable thermodynamic stability to reflect those occurring in natural samples, including BIOS (Gault et al., 2011; ThomasArrigo et al., 2022). Synthesis of such minerals required the use of variable synthesis procedures that led to the formation of minerals with distinct physicochemical properties as a consequence of the variations in the distribution and arrangement of alginate within the coprecipitates. Consequently, whether the observed irradiation-induced changes, particularly in Fh coprecipitates, accurately reflect those found in natural samples or are solely attributable to the chosen synthesis pathway, remains uncertain. For example, whether or not Fh that is synthesized in the absence of Cl (e.g. $Fe(NO_3)_3$) will undergo similar changes in crystallinity remains to be determined in future studies.

For this research, we opted for Na-alginate as the representative organic compound, because the impact of irradiation on this polysaccharide is well characterized in the literature (Le Quang and Vo Thi, 2009). However, it is important to note that the impact of irradiation varies with OM type and stability, which may lead to soil/sediment specific effects (Da Silva et al., 1997; Zhao et al., 2020; Zhao et al., 2021). Moreover, the chemistry of the natural sample plays an important role in modulating the impact of irradiation due to the presence of redox sensitive compounds capable of scavenging the reducing and oxidizing radicals (Cataldo and Angelini, 2012; Brown et al., 2015). In addition to this consideration, it is important to note that the response

of OM to irradiation is dose-dependent (Da Silva et al., 1997; Zhao et al., 2020). Consequently, irradiation induced changes to Fe-coprecipitates may become more apparent at higher doses.

Finally, the results from this study could be also relevant to deep geological repository (DGR) environments where spent fuel is intended to be stored (Brown et al., 2015; Zhao et al., 2021; Zhao et al., 2022a), and deep subsurface environments (Blair et al., 2007). Within such conditions where radioactive decay fuels the flux of γ-radiation may enhance the dissolution of Fe-OM-coprecipitates and the microbial reduction of Fe(III). Nonetheless, from a sterilization point of view, our results indicate that γ-irradiation induced physicochemical changes to the minerals tested which is contrary to numerous other studies identifying γ-sterilization as a minimally invasive technique. Therefore, future researchers must be cognizant of the potential effects of sterilization through γ-irradiation on Fe-OM-coprecipitates.

Supplementary Materials

Supplementary materials to this article can be found online at:

Data Availability

Raw data for data from this manuscript and supplementary materials are available through Mendeley Data: https://data.mendeley.com/datasets/ycw92c3ywy/1

Acknowledgements

The present research was entirely funded by a NSERC Discovery grant to D. Fortin. The authors are very thankful to Nordion (Canada) Inc. for sterilizing our samples. We are grateful to 2 anonymous reviewers and the editor for their very constructive comments. We would like to thank Nimal DeSilva and *Smita* Mohanty (University of Ottawa) for their expertise and analyzing our samples with the ICP-OES, the Ján Veizer Stable Isotope Lab (University of Ottawa) for their expertise and analysis of DOC and carbon content, and Dr. Javier Giorgi (University of Ottawa) for providing the access and training to use the Autosorb-1 for sample analysis. We would also like to thank Glenn Poirier (University of Ottawa) for his guidance and expertise in using the SEM.

Declaration of Competing Interest

The authors declare that they have no known competing financial interests or personal relationships that could have appeared to influence the work reported in this paper.

References

Adhikari, D., Poulson, S.R., Sumaila, S., Dynes, J.J., McBeth, J.M., Yang, Y., 2016. Asynchronous reductive release of iron and organic carbon from hematite–humic acid complexes. Chem. Geol., 430: 13-20.

Adhikari, D., Zhao, Q., Das, K., Mejia, J., Huang, R., Wang, X., Poulson, S.R., Tang, Y., Roden, E.E., Yang, Y., 2017. Dynamics of ferrihydrite-bound organic carbon during microbial Fe reduction. Geochim. Cosmochim. Acta, 212: 221-233.

Al-Assaf, S., Coqueret, X., Zaman, H.M.D.K., Sen, M., Ulański, P., 2016. The Radiation Chemistry of Polysaccharides. International Atomic Energy Agency Vienna, Austria.

Amstaetter, K., Borch, T., Kappler, A., 2012. Influence of humic acid imposed changes of ferrihydrite aggregation on microbial Fe (III) reduction. Geochim. Cosmochim. Acta, 85: 326-341.

Bank, T.L., Kukkadapu, R.K., Madden, A.S., Ginder-Vogel, M.A., Baldwin, M.E., Jardine, P.M., 2008. Effects of gamma-sterilization on the physico-chemical properties of natural sediments. Chem. Geol., 251(1-4): 1-7.

Bao, Y., Bolan, N.S., Lai, J., Wang, Y., Jin, X., Kirkham, M.B., Wu, X., Fang, Z., Zhang, Y., Wang, H., 2021. Interactions between organic matter and Fe (hydr)oxides and their influences on immobilization and remobilization of metal(loid)s: A review. Crit. Rev. Environ. Sci. Technol., 52(22): 4016-4037.

Berns, A.E., Philipp, H., Narres, H.D., Burauel, P., Vereecken, H., Tappe, W., 2008. Effect of gamma-sterilization and autoclaving on soil organic matter structure as studied by solid state NMR, UV and fluorescence spectroscopy. Eur. J. Soil Sci., 59(3): 540-550.

Blair, C.C., D'Hondt, S., Spivack, A.J., Kingsley, R.H., 2007. Radiolytic hydrogen and microbial respiration in subsurface sediments. Astrobiology, 7(6): 951-970.

Bonneville, S., Behrends, T., Van Cappellen, P., 2009. Solubility and dissimilatory reduction kinetics of iron (III) oxyhydroxides: A linear free energy relationship. Geochim. Cosmochim. Acta, 73(18): 5273-5282.

Bonneville, S., Van Cappellen, P., Behrends, T., 2004. Microbial reduction of iron (III) oxyhydroxides: effects of mineral solubility and availability. Chem. Geol., 212(3-4): 255-268.

Borch, T., Masue, Y., Kukkadapu, R.K., Fendorf, S., 2007. Phosphate imposed limitations on biological reduction and alteration of ferrihydrite. Environ. Sci. Technol., 41(1): 166-172.

Borisover, M., Keren, Y., Usyskin, A., Bukhanovsky, N., 2016. Effects of gamma-irradiation of original and organic matter-amended soils on the sorption of triclosan and diuron from aqueous solutions. Chemosphere, 152: 62-70.

Brown, A.R., Boothman, C., Pimblott, S.M., Lloyd, J.R., 2015. The impact of gamma radiation on sediment microbial processes. Appl. Environ. Microbiol., 81(12): 4014-25.

Brown, A.R., Wincott, P.L., LaVerne, J.A., Small, J.S., Vaughan, D.J., Pimblott, S.M., Lloyd, J.R., 2014. The impact of gamma radiation on the bioavailability of Fe(III) minerals for microbial respiration. Environ. Sci. Technol., 48(18): 10672-80.

Buchan, D., Moeskops, B., Ameloot, N., De Neve, S., Sleutel, S., 2012. Selective sterilisation of undisturbed soil cores by gamma irradiation: Effects on free-living nematodes, microbial community and nitrogen dynamics. Soil Biol. Biochem., 47: 10-13.

Buessecker, S., Tylor, K., Nye, J., Holbert, K.E., Urquiza Muñoz, J.D., Glass, J.B., Hartnett, H.E., Cadillo-Quiroz, H., 2019. Effects of sterilization techniques on

chemodenitrification and N_2O production in tropical peat soil microcosms. Biogeosciences, 16(23): 4601-4612.
Byrne, J.M., Kappler, A., 2022. A revised analysis of ferrihydrite at liquid helium temperature using Mössbauer spectroscopy. Am. Min., 107(8): 1643-1651.
Cardenas-Jiron, G., Leal, D., Matsuhiro, B., Osorio-Roman, I.O., 2011. Vibrational spectroscopy and density functional theory calculations of poly-D-mannuronate and heteropolymeric fractions from sodium alginate. J. Raman Spectrosc., 42(4): 870-878.
Cataldo, F., Angelini, G., 2012. Radiolysis and ozonolysis of a landfill leachate. Radioanal. Nucl. Chem., 293(1): 141-148.
Chan, C.S., De Stasio, G., Welch, S.A., Girasole, M., Frazer, B.H., Nesterova, M.V., Fakra, S., Banfield, J.F., 2004. Microbial polysaccharides template assembly of nanocrystal fibers. Science, 303(5664): 1656-8.
Chan, C.S., Fakra, S.C., Edwards, D.C., Emerson, D., Banfield, J.F., 2009. Iron oxyhydroxide mineralization on microbial extracellular polysaccharides. Geochim. Cosmochim. Acta, 73(13): 3807-3818.
Chandıa, N., Matsuhiro, B., Vásquez, A., 2001. Alginic acids in Lessonia trabeculata: characterization by formic acid hydrolysis and FT-IR spectroscopy. Carbohydr. Polym., 46(1): 81-87.
Chen, C., Dynes, J.J., Wang, J., Sparks, D.L., 2014. Properties of Fe-organic matter associations via coprecipitation versus adsorption. Environ. Sci. Technol., 48(23): 13751-9.
Chen, C., Kukkadapu, R., Sparks, D.L., 2015. Influence of Coprecipitated Organic Matter on Fe^{2+}(aq)-Catalyzed Transformation of Ferrihydrite: Implications for Carbon Dynamics. Environ. Sci. Technol., 49(18): 10927-36.
Chen, K.-Y., Hsu, L.-C., Chan, Y.-T., Cho, Y.-L., Tsao, F.-Y., Tzou, Y.-M., Hsieh, Y.-C., Liu, Y.-T., 2018. Phosphate removal in relation to structural development of humic acid-iron coprecipitates. Sci. Rep., 8(1): 10363.
Cismasu, A.C., Michel, F.M., Tcaciuc, A.P., Tyliszczak, T., Brown, J.G.E., 2011. Composition and structural aspects of naturally occurring ferrihydrite. Comptes Rendus Geoscience, 343(2-3): 210-218.
Cismasu, A.C., Williams, K.H., Nico, P.S., 2016. Iron and Carbon Dynamics during Aging and Reductive Transformation of Biogenic Ferrihydrite. Environ. Sci. Technol., 50(1): 25-35.
Cooper, R.E., Eusterhues, K., Wegner, C.-E., Totsche, K.U., Küsel, K., 2017. Ferrihydrite-associated organic matter (OM) stimulates reduction by Shewanella oneidensis MR-1 and a complex microbial consortia. Biogeosciences, 14(22): 5171-5188.
Cornell, R.M., Schwertmann, U., 2003. The iron oxides: structure, properties, reactions, occurrences, and uses, 664. Wiley-vch Weinheim.
Curti, L., Moore, O.W., Babakhani, P., Xiao, K.-Q., Woulds, C., Bray, A.W., Fisher, B.J., Kazemian, M., Kaulich, B., Peacock, C.L., 2021. Carboxyl-richness controls organic carbon preservation during coprecipitation with iron (oxyhydr)oxides in the natural environment. Commun. Earth Environ., 2(1).
Cutting, R., Coker, V., Fellowes, J., Lloyd, J., Vaughan, D., 2009. Mineralogical and morphological constraints on the reduction of Fe (III) minerals by Geobacter sulfurreducens. Geochim. Cosmochim. Acta, 73(14): 4004-4022.
Da Silva, W., Da Silva, S., de Oliveira Rezende, M., 1997. Influence of gamma-radiation on the behavior of humic acids from peat and tropical soil. Radioanal. Nucl. Chem., 222: 29-34.

Dippon, U., Schmidt, C., Behrens, S., Kappler, A., 2015. Secondary mineral formation during ferrihydrite reduction by Shewanella oneidensis MR-1 depends on incubation vessel orientation and resulting gradients of cells, Fe^{2+} and Fe minerals. Geomicrobiol. J., 32(10): 878-889.

Dong, H., Huang, L., Zhao, L., Zeng, Q., Liu, X., Sheng, Y., Shi, L., Wu, G., Jiang, H., Li, F., Zhang, L., Guo, D., Li, G., Hou, W., Chen, H., 2022. A critical review of mineral–microbe interaction and co-evolution: mechanisms and applications. National Science Review, 9(10).

Dong, H., Zeng, Q., Sheng, Y., Chen, C., Yu, G., Kappler, A., 2023. Coupled iron cycling and organic matter transformation across redox interfaces. Nature Reviews Earth & Environment, 4(9): 659-673.

Eusterhues, K., Hädrich, A., Neidhardt, J., Küsel, K., Keller, T., Jandt, K., Totsche, K., 2014. Reduction of ferrihydrite with adsorbed and coprecipitated organic matter: microbial reduction by Geobacter bremensis vs. abiotic reduction by Na-dithionite. Biogeosciences, 11(18): 4953-4966.

Eusterhues, K., Wagner, F.E., Häusler, W., Hanzlik, M., Knicker, H., Totsche, K.U., Kögel-Knabner, I., Schwertmann, U., 2008. Characterization of ferrihydrite-soil organic matter coprecipitates by X-ray diffraction and Mossbauer spectroscopy. Environ. Sci. Technol., 42(21): 7891-7897.

Fabisch, M., Freyer, G., Johnson, C.A., Buchel, G., Akob, D.M., Neu, T.R., Kusel, K., 2016. Dominance of 'Gallionella capsiferriformans' and heavy metal association with Gallionella-like stalks in metal-rich pH 6 mine water discharge. Geobiology, 14(1): 68-90.

Falkeborg, M., Cheong, L.-Z., Gianfico, C., Sztukiel, K.M., Kristensen, K., Glasius, M., Xu, X., Guo, Z., 2014. Alginate oligosaccharides: Enzymatic preparation and antioxidant property evaluation. Food Chem., 164: 185-194.

Field, H.R., Whitaker, A.H., Henson, J.A., Duckworth, O.W., 2019. Sorption of copper and phosphate to diverse biogenic iron (oxyhydr) oxide deposits. Sci. Total Environ., 697: 134111.

Fortin, D., Langley, S., 2005. Formation and occurrence of biogenic iron-rich minerals. Earth-Sci. Rev., 72(1-2): 1-19.

Fredrickson, J.K., Zachara, J.M., Kennedy, D.W., Dong, H., Onstott, T.C., Hinman, N.W., Li, S.-m., 1998. Biogenic iron mineralization accompanying the dissimilatory reduction of hydrous ferric oxide by a groundwater bacterium. Geochim. Cosmochim. Acta, 62(19-20): 3239-3257.

Gault, A.G., Ibrahim, A., Langley, S., Renaud, R., Takahashi, Y., Boothman, C., Lloyd, J.R., Clark, I.D., Ferris, F.G., Fortin, D., 2011. Microbial and geochemical features suggest iron redox cycling within bacteriogenic iron oxide-rich sediments. Chem. Geol., 281(1-2): 41-51.

Glasauer, S., Weidler, P.G., Langley, S., Beveridge, T.J., 2003. Controls on Fe reduction and mineral formation by a subsurface bacterium. Geochimica et Cosmochimica Acta, 67(7): 1277-1288.

Goraczko, W., Slawinski, J., 2008. Luminescence from γ-irradiated humic acid. Journal of Luminescence, 128(7): 1155-1161.

Goraczko, W., Slawiński, J., Staninski, K., 2008. Spectral distribution of the radiochemiluminescence from gamma-irradiated humic acid. Radioanal. Nucl. Chem., 277(3): 613-618.
Gotić, M., Jurkin, T., Musić, S., 2009. From iron(III) precursor to magnetite and vice versa. Mater. Res. Bull., 44(10): 2014-2021.
Gournis, D., Mantaka-Marketou, A., Karakassides, M., Petridis, D., 2000. Effect of γ-irradiation on clays and organoclays: a Mössbauer and XRD study. Phys. Chem. Miner., 27: 514-521.
Grybos, M., Davranche, M., Gruau, G., Petitjean, P., 2007. Is trace metal release in wetland soils controlled by organic matter mobility or Fe-oxyhydroxides reduction? J. Colloid Interface Sci., 314(2): 490-501.
Han, L., Sun, K., Keiluweit, M., Yang, Y., Yang, Y., Jin, J., Sun, H., Wu, F., Xing, B., 2019. Mobilization of ferrihydrite-associated organic carbon during Fe reduction: Adsorption versus coprecipitation. Chem. Geol., 503: 61-68.
Hansel, C.M., Benner, S.G., Neiss, J., Dohnalkova, A., Kukkadapu, R.K., Fendorf, S., 2003. Secondary mineralization pathways induced by dissimilatory iron reduction of ferrihydrite under advective flow. Geochim. Cosmochim. Acta, 67(16): 2977-2992.
Hao, L., Guo, Y., Byrne, J.M., Zeitvogel, F., Schmid, G., Ingino, P., Li, J., Neu, T.R., Swanner, E.D., Kappler, A., Obst, M., 2016. Binding of heavy metal ions in aggregates of microbial cells, EPS and biogenic iron minerals measured in-situ using metal- and glycoconjugates-specific fluorophores. Geochim. Cosmochim. Acta, 180: 66-96.
Henneberry, Y.K., Kraus, T.E.C., Nico, P.S., Horwath, W.R., 2012. Structural stability of coprecipitated natural organic matter and ferric iron under reducing conditions. Org. Geochem., 48: 81-89.
Herbert, R.B., Malmström, M., Ebenå, G., Salmon, U., Ferrow, E., Fuchs, M., 2005. Quantification of abiotic reaction rates in mine tailings: evaluation of treatment methods for eliminating iron-and sulfur-oxidizing bacteria. Environ. Sci. Technol., 39(3): 770-777.
Hochanadel, C., Ghormley, J., 1962. Effect of temperature on the decomposition of water by gamma rays. Radiat. Res., 16(5): 653-660.
Hyacinthe, C., Bonneville, S., Van Cappellen, P., 2006. Reactive iron(III) in sediments: Chemical versus microbial extractions. Geochim. Cosmochim. Acta, 70(16): 4166-4180.
Jiang, J., Kappler, A., 2008. Kinetics of microbial and chemical reduction of humic substances: implications for electron shuttling. Environ. Sci. Technol., 42(10): 3563-3569.
Joseph, J.M., Seon Choi, B., Yakabuskie, P., Clara Wren, J., 2008. A combined experimental and model analysis on the effect of pH and O_2(aq) on γ-radiolytically produced H_2 and H_2O_2. Radiat. Phys. Chem., 77(9): 1009-1020.
Jurkin, T., Gotić, M., Štefanić, G., Pucić, I., 2016a. Gamma-irradiation synthesis of iron oxide nanoparticles in the presence of PEO, PVP or CTAB. Radiat. Phys. Chem., 124: 75-83.
Jurkin, T., Štefanić, G., Dražić, G., Gotić, M., 2016b. Synthesis route to δ-FeOOH nanodiscs. Mater. Lett., 173: 55-59.
Jurkin, T., Zadro, K., Gotić, M., Musić, S., 2011. Investigation of solid phase upon γ-irradiation of ferrihydrite-ethanol suspension. Radiat. Phys. Chem., 80(7): 792-798.
Kaiser, K., 2003. Sorption of natural organic matter fractions to goethite (α-FeOOH): effect of chemical composition as revealed by liquid-state ^{13}C NMR and wet-chemical analysis. Org. Geochem., 34(11): 1569-1579.

Kaiser, K., Guggenberger, G., Haumaier, L., Zech, W., 1997. Dissolved organic matter sorption on sub soils and minerals studied by ^{13}C-NMR and DRIFT spectroscopy. Eur. J. Soil Sci., 48(2): 301-310.
Kaiser, K., Mikutta, R., Guggenberger, G., 2007. Increased stability of organic matter sorbed to ferrihydrite and goethite on aging. Soil Sci. Soc. Am. J., 71(3): 711-719.
Kallenbach, C.M., Frey, S.D., Grandy, A.S., 2016. Direct evidence for microbial-derived soil organic matter formation and its ecophysiological controls. Nat. Commun., 7(1): 13630.
Kelsey, J.W., Slizovskiy, I.B., Peters, R.D., Melnick, A.M., 2010. Sterilization affects soil organic matter chemistry and bioaccumulation of spiked p,p'-DDE and anthracene by earthworms. Environ. Pollut., 158(6): 2251-7.
Kleber, M., Eusterhues, K., Keiluweit, M., Mikutta, C., Mikutta, R., Nico, P.S., 2015. Mineral–Organic Associations: Formation, Properties, and Relevance in Soil Environments. 130: 1-140.
Kostka, J.E., Luther, G.W., 1994. Partitioning and speciation of solid phase iron in saltmarsh sediments. Geochim. Cosmochim. Acta, 58(7): 1701-1710.
Lagarec, K., Rancourt, D.G., 1997. Extended Voigt-based analytic lineshape method for determining N-dimensional correlated hyperfine parameter distributions in Mössbauer spectroscopy. Nuclear Instruments and Methods in Physics Research Section B: Beam Interactions with Materials and Atoms, 129(2): 266-280.
Lalonde, K., Mucci, A., Ouellet, A., Gélinas, Y., 2012. Preservation of organic matter in sediments promoted by iron. Nature, 483(7388): 198-200.
Langley, S., Gault, A., Ibrahim, A., Renaud, R., Fortin, D., Clark, I.D., Ferris, F.G., 2009a. A Comparison of the Rates of Fe(III) Reduction in Synthetic and Bacteriogenic Iron Oxides by Shewanella putrefaciens CN32. Geomicrobiology Journal, 26(2): 57-70.
Langley, S., Gault, A., Ibrahim, A., Renaud, R., Fortin, D., Clark, I.D., Ferris, F.G., 2009b. A Comparison of the Rates of Fe(III) Reduction in Synthetic and Bacteriogenic Iron Oxides byShewanella putrefaciensCN32. Geomicrobiol. J., 26(2): 57-70.
Langley, S., Gault, A.G., Ibrahim, A., Takahashi, Y., Renaud, R., Fortin, D., Clark, I.D., Ferris, F.G., 2009c. Strontium desorption from bacteriogenic iron oxides (BIOS) subjected to microbial Fe(III) reduction. Chem. Geol., 262(3-4): 217-228.
Langley, S., Igric, P., Takahashi, Y., Sakai, Y., Fortin, D., Hannington, M.D., Schwarz-Schampera, U., 2009d. Preliminary characterization and biological reduction of putative biogenic iron oxides (BIOS) from the Tonga-Kermadec Arc, southwest Pacific Ocean. Geobiology, 7(1): 35-49.
Layglon, N., Misson, B., Mounier, S., Lenoble, V., Omanovic, D., Garnier, C., 2020. Have decades of abiotic studies in sediments been misinterpreted? Sci. Total Environ., 707: 135949.
Le Quang, L., Vo Thi, T.H., 2009. A study of degradation mechanism of alginate by gamma-irradiation. Radioisotopes, 58(1): 1-11.
Leal, D., Matsuhiro, B., Rossi, M., Caruso, F., 2008. FT-IR spectra of alginic acid block fractions in three species of brown seaweeds. Carbohydr Res, 343(2): 308-16.
Lee, D.W., Choi, W.S., Byun, M.W., Park, H.J., Yu, Y.-M., Lee, C.M., 2003. Effect of γ-irradiation on degradation of alginate. J. Agric. Food Chem., 51(16): 4819-4823.
Lees, K., Fitzsimons, M., Snape, J., Tappin, A., Comber, S., 2018. Soil sterilisation methods for use in OECD 106: How effective are they? Chemosphere, 209: 61-67.

Lensi, R., Lescure, C., Steinberg, C., Savoie, J.-M., Faurie, G., 1991. Dynamics of residual enzyme activities, denitrification potential, and physico-chemical properties in a γ-sterilized soil. Soil Biol. Biochem., 23(4): 367-373.
Li, Q., Hu, W., Li, L., Li, Y., 2023. Interactions between organic matter and Fe oxides at soil micro-interfaces: Quantification, associations, and influencing factors. Sci. Total Environ., 855: 158710.
Li, X., Xu, A., Xie, H., Yu, W., Xie, W., Ma, X., 2010. Preparation of low molecular weight alginate by hydrogen peroxide depolymerization for tissue engineering. Carbohydr. Polym., 79(3): 660-664.
Liu, C., Huang, P., 2003. Kinetics of lead adsorption by iron oxides formed under the influence of citrate. Geochim. Cosmochim. Acta, 67(5): 1045-1054.
Liu, Q., Li, X., Tang, J., Zhou, Y., Lin, Q., Xiao, R., Zhang, M., 2019. Characterization of goethite-fulvic acid composites and their impact on the immobility of Pb/Cd in soil. Chemosphere, 222: 556-563.
Liu, Y., Chen, S., Zhong, L., Wu, G., 2009. Preparation of high-stable silver nanoparticle dispersion by using sodium alginate as a stabilizer under gamma radiation. Radiat. Phys. Chem., 78(4): 251-255.
Lotrario, J., Stuart, B., Lam, T., Arands, R., O'Connor, O., Kosson, D., 1995. Effects of sterilization methods on the physical characteristics of soil: implications for sorption isotherm analyses. Bull. Environ. Contam. Toxicol., 54: 668-675.
Marić, I., Dražić, G., Štefanić, G., Zadro, K., Gotić, M., Jurkin, T., 2020a. Characterization of radiolytically synthesized feroxyhyte and oxidized magnetite nanoparticles. Mater. Charact., 159: 110038.
Marić, I., Gotić, M., Štefanić, G., Pustak, A., Jurkin, T., 2020b. γ-irradiation generated ferrous ions affect the formation of magnetite and feroxyhyte. Radiat. Phys. Chem., 170: 108648.
Marić, I., Štefanić, G., Gotić, M., Jurkin, T., 2019. The impact of dextran sulfate on the radiolytic synthesis of magnetic iron oxide nanoparticles. J. Mol. Struct., 1183: 126-136.
Martens, J., Mueller, C.W., Joshi, P., Rosinger, C., Maisch, M., Kappler, A., Bonkowski, M., Schwamborn, G., Schirrmeister, L., Rethemeyer, J., 2023. Stabilization of mineral-associated organic carbon in Pleistocene permafrost. Nat Commun, 14(1): 2120.
McNamara, N.P., Black, H.I.J., Beresford, N.A., Parekh, N.R., 2003. Effects of acute gamma irradiation on chemical, physical and biological properties of soils. Appl. Soil Ecol., 24(2): 117-132.
Mejia, J., He, S., Yang, Y., Ginder-Vogel, M., Roden, E.E., 2018. Stability of Ferrihydrite-Humic Acid Coprecipitates under Iron-Reducing Conditions. Environ. Sci. Technol., 52(22): 13174-13183.
Mikutta, C., Kretzschmar, R., 2008. Synthetic coprecipitates of exopolysaccharides and ferrihydrite. Part II: Siderophore-promoted dissolution. Geochim. Cosmochim. Acta, 72(4): 1128-1142.
Mikutta, C., Mikutta, R., Bonneville, S., Wagner, F., Voegelin, A., Christl, I., Kretzschmar, R., 2008. Synthetic coprecipitates of exopolysaccharides and ferrihydrite. Part I: Characterization. Geochim. Cosmochim. Acta, 72(4): 1111-1127.
Mikutta, R., Lorenz, D., Guggenberger, G., Haumaier, L., Freund, A., 2014. Properties and reactivity of Fe-organic matter associations formed by coprecipitation versus adsorption: Clues from arsenate batch adsorption. Geochim. Cosmochim. Acta, 144: 258-276.

Murad, E., Cashion, J., 2004. Mössbauer spectroscopy of environmental materials and their industrial utilization. Springer Science & Business Media.
Nagasawa, N., Mitomo, H., Yoshii, F., Kume, T., 2000. Radiation-induced degradation of sodium alginate. Polym. Degradation Stab., 69(3): 279-285.
Najem, T., Langley, S., Fortin, D., 2016. A comparison of Fe(III) reduction rates between fresh and aged biogenic iron oxides (BIOS) by Shewanella putrefaciens CN32. Chem. Geol., 439: 1-12.
Notini, L., Latta, D.E., Neumann, A., Pearce, C.I., Sassi, M., N'Diaye, A.T., Rosso, K.M., Scherer, M.M., 2019. A closer look at Fe (II) passivation of goethite. ACS Earth Space Chem., 3(12): 2717-2725.
O'Loughlin, E.J., Gorski, C.A., Scherer, M.M., Boyanov, M.I., Kemner, K.M., 2010. Effects of oxyanions, natural organic matter, and bacterial cell numbers on the bioreduction of lepidocrocite (γ-FeOOH) and the formation of secondary mineralization products. Environ. Sci. Technol., 44(12): 4570-4576.
Otte, J.M., Blackwell, N., Soos, V., Rughoft, S., Maisch, M., Kappler, A., Kleindienst, S., Schmidt, C., 2018. Sterilization impacts on marine sediment---Are we able to inactivate microorganisms in environmental samples? FEMS Microbiol. Ecol., 94(12).
Patzner, M.S., Logan, M., McKenna, A.M., Young, R.B., Zhou, Z., Joss, H., Mueller, C.W., Hoeschen, C., Scholten, T., Straub, D., Kleindienst, S., Borch, T., Kappler, A., Bryce, C., 2022. Microbial iron cycling during palsa hillslope collapse promotes greenhouse gas emissions before complete permafrost thaw. Commun. Earth Environ., 3(1).
Pedrot, M., Le Boudec, A., Davranche, M., Dia, A., Henin, O., 2011. How does organic matter constrain the nature, size and availability of Fe nanoparticles for biological reduction? J. Colloid Interface Sci., 359(1): 75-85.
Plötze, M., Kahr, G., Hermanns Stengele, R., 2003. Alteration of clay minerals—gamma-irradiation effects on physicochemical properties. Applied Clay Science, 23(1-4): 195-202.
Poggenburg, C., Mikutta, R., Sander, M., Schippers, A., Marchanka, A., Dohrmann, R., Guggenberger, G., 2016. Microbial reduction of ferrihydrite-organic matter coprecipitates by Shewanella putrefaciens and Geobacter metallireducens in comparison to mediated electrochemical reduction. Chem. Geol., 447: 133-147.
Poggenburg, C., Mikutta, R., Schippers, A., Dohrmann, R., Guggenberger, G., 2018. Impact of natural organic matter coatings on the microbial reduction of iron oxides. Geochim. Cosmochim. Acta, 224: 223-248.
Possinger, A.R., Zachman, M.J., Dynes, J.J., Regier, T.Z., Kourkoutis, L.F., Lehmann, J., 2021. Co-precipitation induces changes to iron and carbon chemistry and spatial distribution at the nanometer scale. Geochim. Cosmochim. Acta, 314: 1-15.
Radloff, K.A., Manning, A.R., Mailloux, B., Zheng, Y., Rahman, M.M., Huq, M.R., Ahmed, K.M., van Geen, A., 2008. Considerations for conducting incubations to study the mechanisms of As release in reducing groundwater aquifers. Appl. Geochem., 23(11): 3224-3235.
Raiswell, R., Vu, H.P., Brinza, L., Benning, L.G., 2010. The determination of labile Fe in ferrihydrite by ascorbic acid extraction: Methodology, dissolution kinetics and loss of solubility with age and de-watering. Chem. Geol., 278(1-2): 70-79.
Retelletti Brogi, S., Derrien, M., Hur, J., 2019. In-Depth Assessment of the Effect of Sodium Azide on the Optical Properties of Dissolved Organic Matter. J Fluoresc, 29(4): 877-885.

Riedel, T., Zak, D., Biester, H., Dittmar, T., 2013. Iron traps terrestrially derived dissolved organic matter at redox interfaces. Proc. Natl. Acad. Sci., 110(25): 10101-10105.
Roden, E.E., 2003. Fe (III) oxide reactivity toward biological versus chemical reduction. Environ. Sci. Technol., 37(7): 1319-1324.
Roden, E.E., Urrutia, M.M., 2002. Influence of biogenic Fe (II) on bacterial crystalline Fe (III) oxide reduction. Geomicrobiol. J., 19(2): 209-251.
Roden, E.E., Zachara, J.M., 1996. Microbial reduction of crystalline iron (III) oxides: influence of oxide surface area and potential for cell growth. Environ. Sci. Technol., 30(5): 1618-1628.
Rouquerol, J., Llewellyn, P., Rouquerol, F., 2007. Is the BET equation applicable to microporous adsorbents. Stud. Surf. Sci. Catal, 160(07): 49-56.
Salonius, P., Robinson, J., Chase, F., 1967. A comparison of autoclaved and gamma-irradiated soils as media for microbial colonization experiments. Plant Soil, 27(2): 239-248.
Sartori, C., Finch, D.S., Ralph, B., Gilding, K., 1997. Determination of the cation content of alginate thin films by FTIR spectroscopy. Polymer, 38(1): 43-51.
Schaller, J., Weiske, A., Dudel, E.G., 2011. Effects of gamma-sterilization on DOC, uranium and arsenic remobilization from organic and microbial rich stream sediments. Sci. Total Environ., 409(17): 3211-4.
Schwertmann, U., Cambier, P., Murad, E., 1985. Properties of goethites of varying crystallinity. Clays Clay Miner., 33: 369-378.
Schwertmann, U., Cornell, R.M., 2008. Iron oxides in the laboratory: preparation and characterization. John Wiley & Sons.
Schwertmann, U., Wagner, F., Knicker, H., 2005. Ferrihydrite–Humic Associations. Soil Sci. Soc. Am. J., 69(4): 1009-1015.
Seder-Colomina, M., Mangeret, A., Bauda, P., Brest, J., Stetten, L., Merrot, P., Julien, A., Diez, O., Barker, E., Billoir, E., Poupin, P., Thouvenot, A., Cazala, C., Morin, G., 2022. Influence of microorganisms on uranium release from mining-impacted lake sediments under various oxygenation conditions. Environ Sci Process Impacts, 24(10): 1830-1843.
Shimizu, M., Zhou, J., Schroder, C., Obst, M., Kappler, A., Borch, T., 2013. Dissimilatory reduction and transformation of ferrihydrite-humic acid coprecipitates. Environ. Sci. Technol., 47(23): 13375-84.
Skulcova, L., Scherr, K.E., Chrast, L., Hofman, J., Bielska, L., 2018. Influence of soil gamma-irradiation and spiking on sorption of p,p'-DDE and soil organic matter chemistry. Ecotoxicol. Environ. Saf., 155: 125-132.
Slizovskiy, I.B., Kelsey, J.W., 2010. Soil sterilization affects aging-related sequestration and bioavailability of p,p'-DDE and anthracene to earthworms. Environ. Pollut., 158(10): 3285-9.
Sowers, T.D., Harrington, J.M., Polizzotto, M.L., Duckworth, O.W., 2017. Sorption of arsenic to biogenic iron (oxyhydr) oxides produced in circumneutral environments. Geochim. Cosmochim. Acta, 198: 194-207.
Stookey, L.L., 1970. Ferrozine---a new spectrophotometric reagent for iron. Anal. Chem., 42(7): 779-781.
Sutherland, T., Sparks, C., Joseph, J., Wang, Z., Whitaker, G., Sham, T., Wren, J., 2017. Effect of ferrous ion concentration on the kinetics of radiation-induced iron-oxide nanoparticle formation and growth. Phys. Chem. Chem. Phys., 19(1): 695-708.

ThomasArrigo, L.K., Notini, L., Shuster, J., Nydegger, T., Vontobel, S., Fischer, S., Kappler, A., Kretzschmar, R., 2022. Mineral characterization and composition of Fe-rich flocs from wetlands of Iceland: Implications for Fe, C and trace element export. Sci. Total Environ., 816: 151567.
Toner, B.M., Santelli, C.M., Marcus, M.A., Wirth, R., Chan, C.S., McCollom, T., Bach, W., Edwards, K.J., 2009. Biogenic iron oxyhydroxide formation at mid-ocean ridge hydrothermal vents: Juan de Fuca Ridge. Geochim. Cosmochim. Acta, 73(2): 388-403.
Tourney, J., Ngwenya, B.T., 2014. The role of bacterial extracellular polymeric substances in geomicrobiology. Chem. Geol., 386: 115-132.
Tuominen, L., Kairesalo, T., Hartikainen, H., 1994. Comparison of methods for inhibiting bacterial activity in sediment. Appl. Environ. Microbiol., 60(9): 3454-3457.
Urrutia, M.M., Roden, E.E., Zachara, J.M., 1999. Influence of aqueous and solid-phase Fe (II) complexants on microbial reduction of crystalline iron (III) oxides. Environ. Sci. Technol., 33(22): 4022-4028.
Villacís-García, M., Ugalde-Arzate, M., Vaca-Escobar, K., Villalobos, M., Zanella, R., Martínez-Villegas, N., 2015. Laboratory synthesis of goethite and ferrihydrite of controlled particle sizes. Boletín de la Sociedad Geológica Mexicana, 67(3): 433-446.
Viollier, E., Inglett, P.W., Hunter, K., Roychoudhury, A.N., Van Cappellen, P., 2000. The ferrozine method revisited: Fe(II)/Fe(III) determination in natural waters. Applied Geochemistry, 15(6): 785-790.
Wagai, R., Mayer, L.M., 2007. Sorptive stabilization of organic matter in soils by hydrous iron oxides. Geochim. Cosmochim. Acta, 71(1): 25-35.
Wang, S., Xin, H., 1999. The γ-irradiation-induced chemical change from β-FeOOH to Fe_3O_4. Radiat. Phys. Chem., 56(5-6): 567-572.
Wasikiewicz, J.M., Yoshii, F., Nagasawa, N., Wach, R.A., Mitomo, H., 2005. Degradation of chitosan and sodium alginate by gamma radiation, sonochemical and ultraviolet methods. Radiat. Phys. Chem., 73(5): 287-295.
Wehr, J.B., Kirchhof, G., 2021. Gamma irradiation with 50 kGy has a limited effect on agronomic properties of air-dry soil. Soil syst., 5(2): 28.
Wolf, D., Dao, T., Scott, H., Lavy, T., 1989. Influence of sterilization methods on selected soil microbiological, physical, and chemical properties. 0047-2425, Wiley Online Library.
Wren, J.C., Glowa, G.A., 2000. A simplified kinetic model for the degradation of 2-butanone in aerated aqueous solutions under steady-state gamma-radiolysis. Radiat. Phys. Chem., 58(4): 341-356.
Xue, Q., Ran, Y., Tan, Y., Peacock, C.L., Du, H., 2019. Arsenite and arsenate binding to ferrihydrite organo-mineral coprecipitate: Implications for arsenic mobility and fate in natural environments. Chemosphere, 224: 103-110.
Yakabuskie, P.A., Joseph, J.M., Keech, P., Botton, G.A., Guzonas, D., Wren, J.C., 2011. Iron oxyhydroxide colloid formation by gamma-radiolysis. Phys Chem Chem Phys, 13(15): 7198-206.
Zachara, J.M., Kukkadapu, R.K., Fredrickson, J.K., Gorby, Y.A., Smith, S.C., 2002. Biomineralization of poorly crystalline Fe (III) oxides by dissimilatory metal reducing bacteria (DMRB). Geomicrobiol. J., 19(2): 179-207.
Zeng, Q., Huang, L., Ma, J., Zhu, Z., He, C., Shi, Q., Liu, W., Wang, X., Xia, Q., Dong, H., 2020. Bio-reduction of ferrihydrite-montmorillonite-organic matter complexes: Effect of montmorillonite and fate of organic matter. Geochim. Cosmochim. Acta, 276: 327-344.

Zhang, S., Cui, S., Gong, X., Chang, L., Jia, S., Yang, X., Wu, D., Zhang, X., 2016. Effects of gamma irradiation on soil biological communities and C and N pools in a clay loam soil. Appl. Soil Ecol., 108: 352-360.

Zhao, Q., Adhikari, D., Huang, R., Patel, A., Wang, X., Tang, Y., Obrist, D., Roden, E.E., Yang, Y., 2017. Coupled dynamics of iron and iron-bound organic carbon in forest soils during anaerobic reduction. Chem. Geol., 464: 118-126.

Zhao, Q., Goto, R., Saito, T., Kobayashi, T., Sasaki, T., 2020. Effect of gamma-irradiation on complexation of humic substances with divalent calcium ion. Chemosphere, 256: 127021.

Zhao, Q., Kobayashi, T., Saito, T., Sasaki, T., 2021. Gamma-irradiation-induced molecular-weight distribution and complexation affinity of humic acid with Cs(+), Sr(2+), and Eu(3). J. Hazard. Mater., 411: 125071.

Zhao, Q., Poulson, S.R., Obrist, D., Sumaila, S., Dynes, J.J., McBeth, J.M., Yang, Y., 2016. Iron-bound organic carbon in forest soils: quantification and characterization. Biogeosciences, 13(16): 4777-4788.

Zhao, Q., Saito, T., Miyakawa, K., Sasamoto, H., Kobayashi, T., Sasaki, T., 2022a. Sorption of Cs(+) and Eu(3+) ions onto sedimentary rock in the presence of gamma-irradiated humic acid. J. Hazard. Mater., 428: 128211.

Zhao, Y., Moore, O.W., Xiao, K.-Q., Curti, L., Fariña, A.O., Banwart, S.A., Peacock, C.L., 2022b. The role and fate of organic carbon during aging of ferrihydrite. Geochim. Cosmochim. Acta, 335: 339-355.

Supplementary Material for

Effects of Gamma(γ)-Irradiation on the Physicochemical Properties and Bioavailability of Iron Oxyhydroxides Coprecipitated with Varying Concentrations of Na-Alginate

Tarek Najem[a], Prachi Joshi[b], Andreas Kappler[b], and Danielle Fortin[a]*

[a] Department of Earth and Environmental Sciences, University of Ottawa, 75 Laurier Ave. East, K1N5N6, Ottawa, Ontario, Canada

[b] Geomicrobiology, Department of Geoscience, University of Tuebingen, Geschwister-Scholl-Platz, 72074 Tübingen, Germany

*Corresponding Author:
Email address: dfortin@uottawa.ca

This supplementary material document includes 44 pages, 7 tables, and 33 figures.

Mineral syntheses

Pure 2-line ferrihydrite (Fh) was synthesized by the rapid addition of 1M NaOH to a solution of 80mmol $FeCl_3$•$6H_2O$ under vigorous stirring to a final pH of 7.0 (Langley et al., 2009b). The ferrihydrite-alginate coprecipitates were synthesized in a similar fashion to pure Fh from the point of NaOH addition to the Fe(III) solution (Mikutta et al., 2008). For the synthesis, an appropriate amount of Na-alginate powder was initially dissolved in 450 mL of sterile UPW for a period of 24 h in the dark. Subsequently, the pH of the alginate-solution was adjusted to ~2.5 with 6M trace metal grade HCl using a sterile pH probe while vigorously mixing. Following pH adjustment, the alginate solution obtained a homogenous milky appearance at which point 200 mL of $FeCl_3$•$6H_2O$ solution of appropriate concentration was added to the alginate solution while vigorously mixing. At this point the pH of the mixture dropped to 1.4-1.8 and had an orange-milky appearance. 1 M NaOH was then added rapidly as described with Fh until a red-brown precipitate had formed. The pH of the final solution was ~7.00, which was monitored and adjusted for at least 20 min until pH fluctuation had ceased. While in suspension, the final mixture was aseptically and equally divided into sterile 50 mL flacon tubes. Washing of the precipitate proceeded by centrifugation/vertexing and washing with sterile UPW until the conductivity of the supernatant decreased to <25 µS/cm.

Pure lepidocrocite (Lp) was synthesized following the method outlined in Schwertmann and Cornell (2008). Briefly, 11.93 g of $FeCl_2$•$4H_2O$ (60 mmol) was dissolved in 100 mL UPW and filtered (Cytiva polyethersulfone membrane, 0.22 µm) to sterilize and to remove any oxidized products directly into sterile 200 mL UPW while stirring. Subsequently, the pH of the acidic solution was adjusted to 6.7 with 1 M NaOH, at which point filtered compressed air was introduced at a rate of 100-115 mL/min. During the oxidation process, the pH of the solution was manually adjusted (6.7 – 6.9) by the addition of base until fluctuation had stabilised for at least 30 min. Synthesis of lepidocrocite-alginate coprecipitates proceeded in the same manner described for Lp with some modifications. Initially, an appropriate amount of Na-alginate was dissolved in 300 mL of sterile UPW in the dark for a duration of 24 h. After the pH adjustment of the alginate solution to 2.5, synthesis and pH adjustment proceeded as described with Lp. However, it was noted that the synthesis time of Lp increased with increasing organic matter content, in which case the time increased from 3 h (pure Lp) to 6-8 h (C/Fe 1.0 and 1.5). Consequently, minor amounts of goethite had formed likely as a result of the long exposure time of the solution to CO_2 (HCO_3^-) from the compressed air. Therefore, to eliminate/minimize such contamination, lepidocrocite-alginate coprecipitates (C/Fe of 1.0 and 1.5) were synthesized by bubbling with pure O_2 at a rate of ~25 mL/min. Division and washing of the Lp precipitates proceeded as described for Fh.

Pure goethite (Gt) was synthesized via the oxidation of a Fe(II) solution following the method outlined in Schwertmann and Cornell (2008). Prior to synthesis, deoxygenated sterile UPW was prepared by sparging with filtered N_2 for 1 h to remove oxygen, and then transferred into a Coy Labs anaerobic chamber operating with an atmosphere of 95:5 N_2:H_2. Subsequently, inside the anaerobic chamber, 15 g of $FeCl_2$•$4H_2O$ (75.45 mmol) was dissolved into 150 mL of the anaerobic UPW and then filtered (Cytiva polyethersulfone membrane, 0.22 µm) directly into 850 mL of DI water in a 2 L Pyrex glass bottle and stirred. Outside the anaerobic chamber, 170 mL of a freshly prepared and filter sterilized solution of 1 M $NaHCO_3$ was aseptically added to the Fe(II) solution while stirring at 800-900 rpm. This final mixture was then sparged with compressed air at a rate of 30-40 mL/min for a duration of 48 h. Goethite-alginate coprecipitates were prepared by

dissolving an appropriate amount of alginate into 500 mL of deoxygenated UPW for 24 h inside the anaerobic chamber and covered with aluminium foil. Under anaerobic conditions, 150 mL of 75.45 mmol of Fe(II) solution was then filtered directly into the alginate solution while vigorously stirring, and then topped off with anaerobic UPW to a final volume of 1 L. Subsequent synthesis proceeded as described for pure Gt. The final Gt precipitates were allowed to settle for up to 1 week prior to division and washing as described for Fh.

Table S1: Total Fe concentration in the experimental jars. Both native and irradiated jars had comparable concentrations. Fh, Lp, and Gt, correspond to 2-line ferrihydrite, lepidocrocite, and goethite, respectively.

C/Fe (mol:mol)	Fh (mM)	Lp (mM)	Gt (mM)
0	573.62±10.8	419.01±10.9	545.22±2.8
0.5	572.98±11.8	482.58±10.1	658.10±8.8
1	236.81±9.6	442.73±5.5	604.75±6.8
1.5	166.81±8.5	452.07±12.9	600.87±3.4

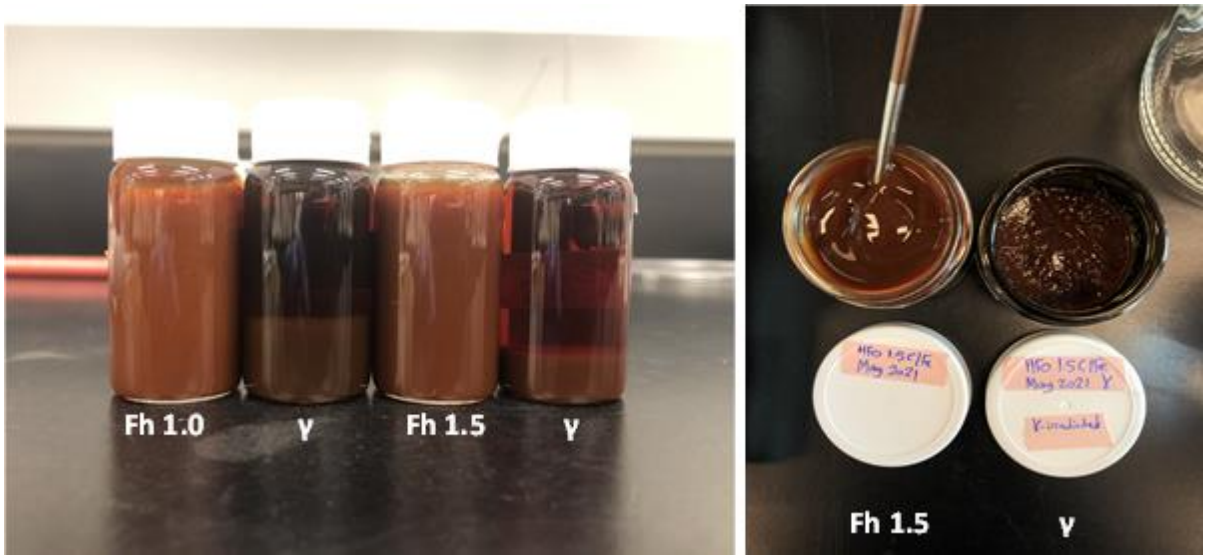

Fig. S1: 2-line ferrihydrite coprecipitated with alginate (C/Fe 1.0 and 1.5) before and after γ-irradiation (25 kGy). The pictures show loss of viscosity following the irradiation treatment and a clear separation of phases (liquid and solid).

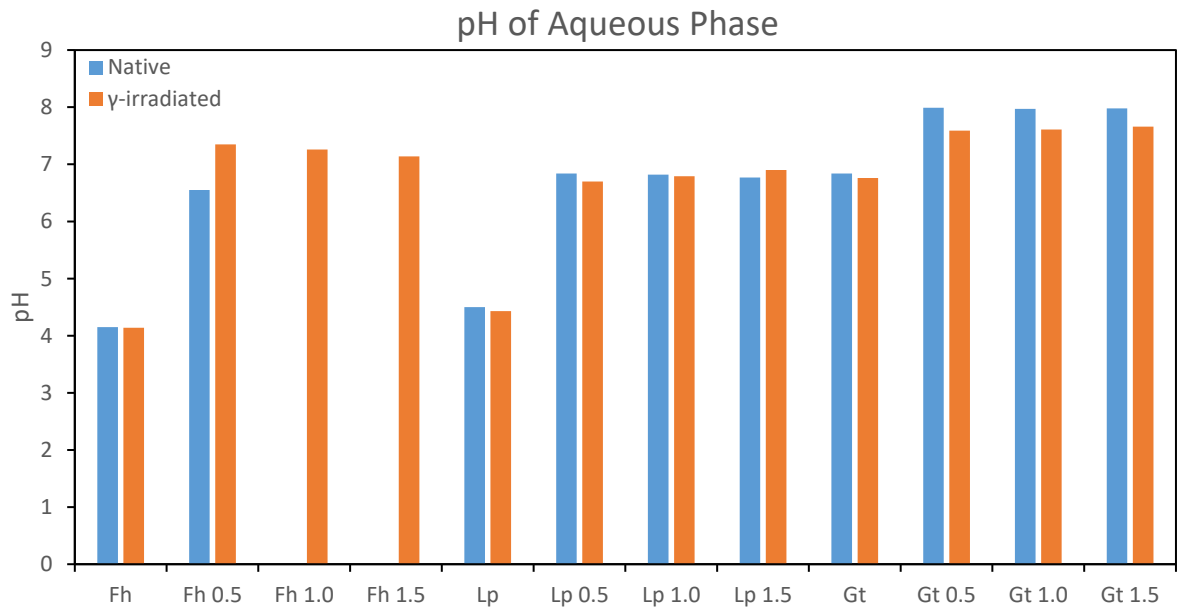

Fig. S2: pH of the aqueous supernatants collected following the centrifugation of the native iron oxyhydroxides and their corresponding γ-irradiated counterparts. pH was measured under anaerobic conditions to prevent changes due to the oxidation of ferrous iron. Fh, Lp, and Gt correspond to 2-line ferrihydrite, lepidocrocite, and goethite, respectively.

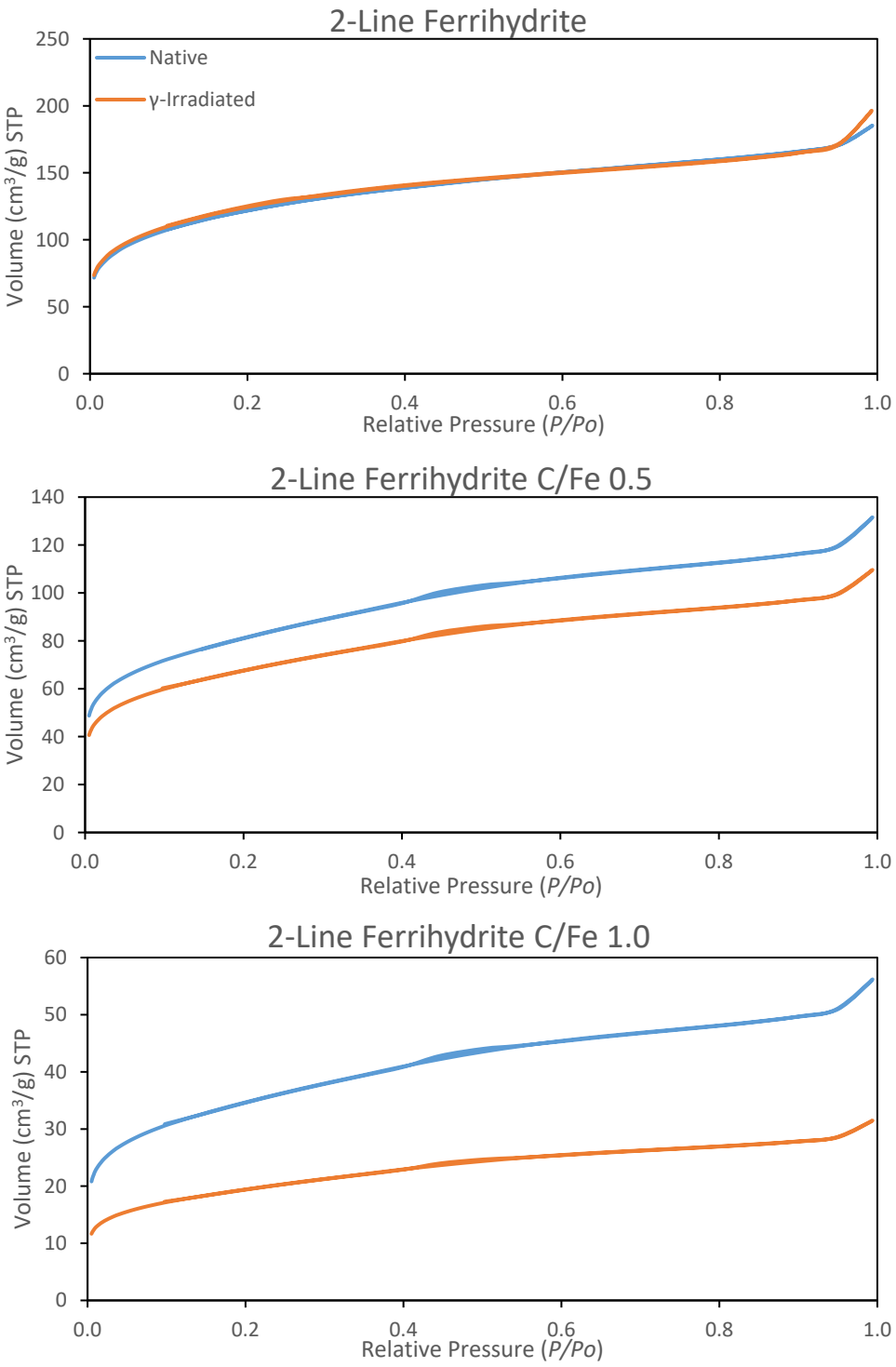

Fig. S3: N_2-adsorption-desorption isotherms of the various 2-line ferrihydrite-alginate coprecipitates (C/Fe 0, 0.5, and 1.0 mol:mol) before and after γ-irradiation (25 kGy). Data points represent the average of two measurements. Note the difference in the Y-axes scales.

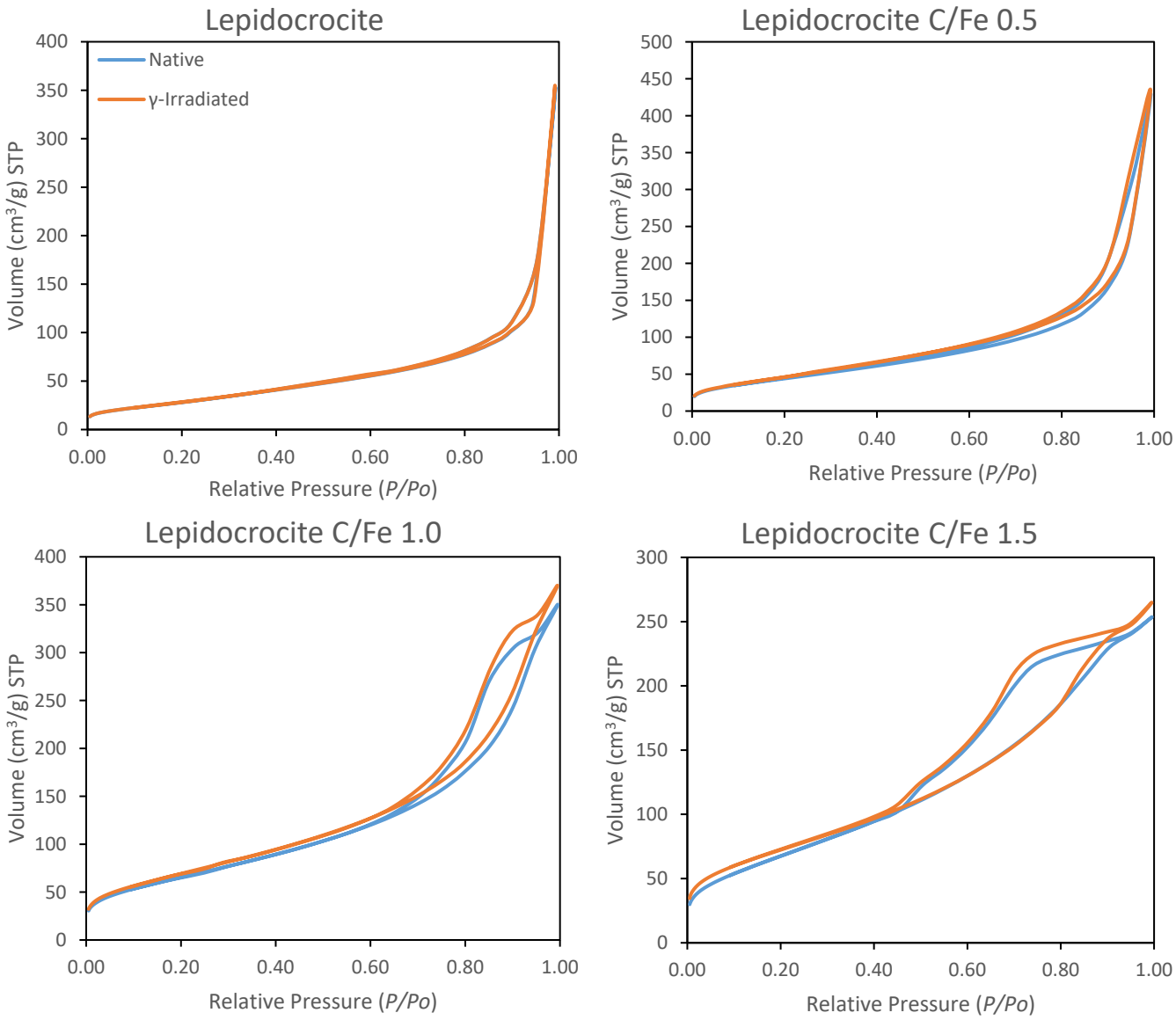

Fig. S4: N_2-adsorption-desorption isotherms of the various lepidocrocite-alginate coprecipitates (C/Fe 0, 0.5, 1.0, and 1.5 mol:mol) before and after γ-irradiation (25 kGy). Data points represent the average of two measurements. Note the difference in the Y-axes scales.

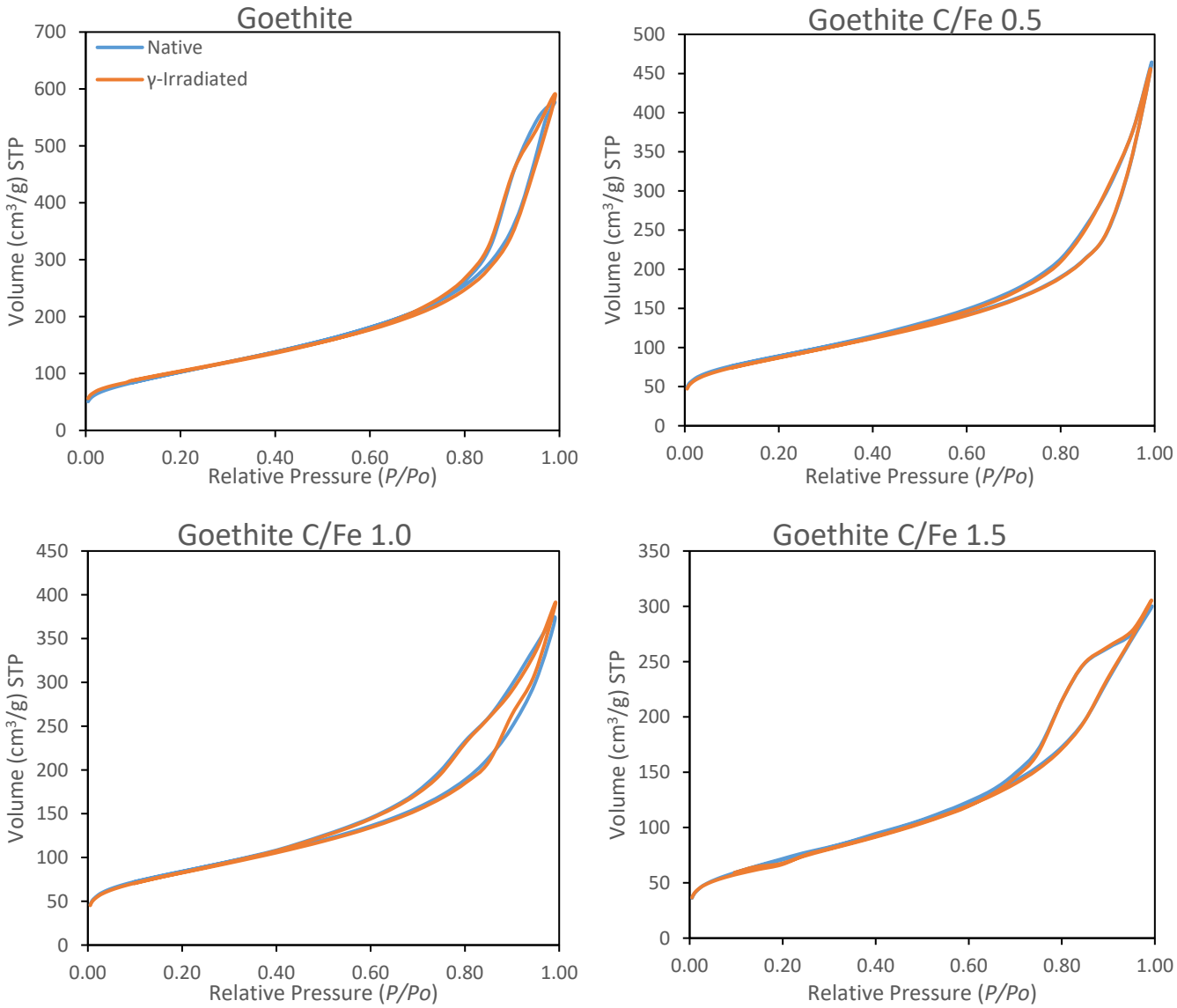

Fig. S5: N_2-adsorption-desorption isotherms of the various goethite-alginate coprecipitates (C/Fe 0, 0.5, 1.0, and 1.5 mol:mol) before and after γ-irradiation (25 kGy). Data points represent the average of two measurements. Note the difference in the Y-axes scales.

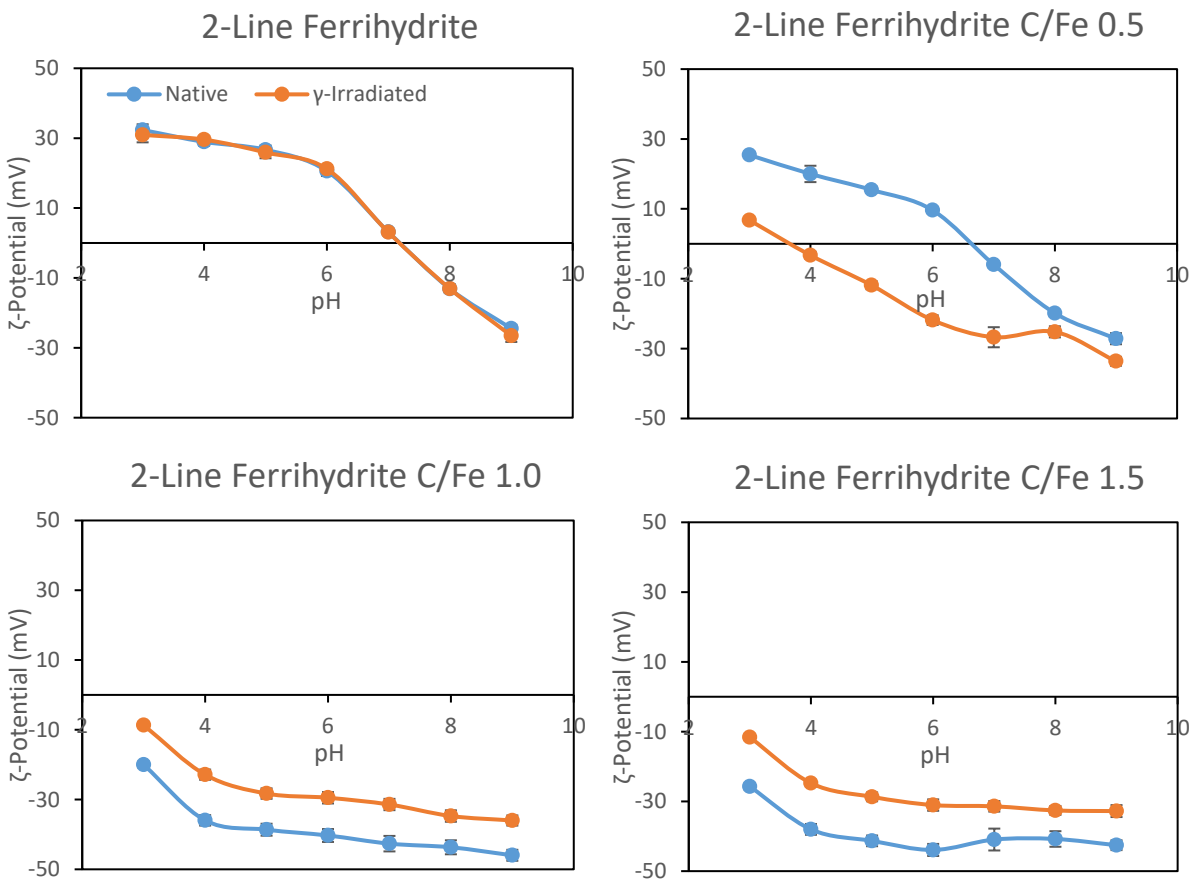

Fig. S6: Plot of the zeta potential versus pH for native and γ-irradiated 2-line ferrihydrite coprecipitated with alginate (C/Fe 0, 0.5, 1.0, and 1.5 mol:mol). Data markers represent means ± standard deviations derived from 5 electrophoretic mobility measurements.

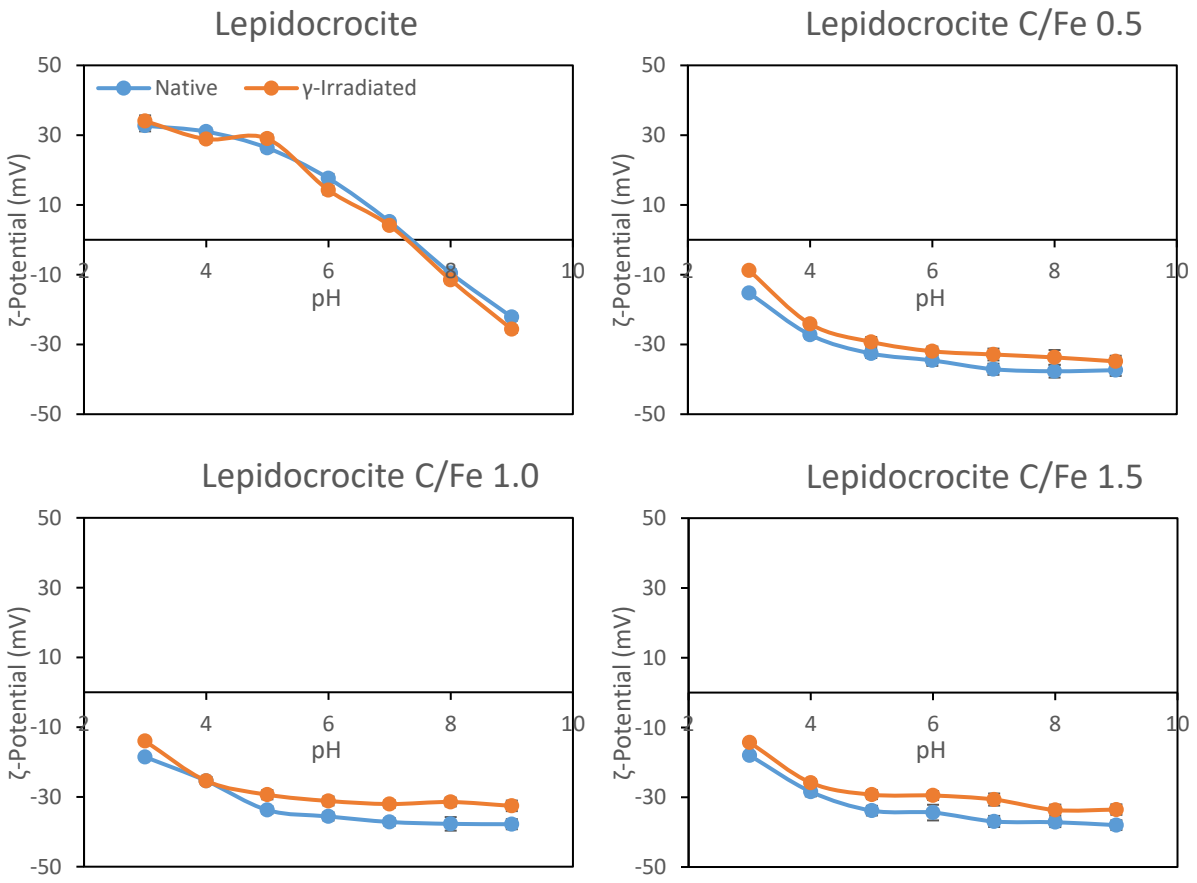

Fig. S7: Plot of the zeta potential versus pH for native and γ-irradiated lepidocrocite coprecipitated with alginate (C/Fe 0, 0.5, 1.0, and 1.5 mol:mol). Data markers represent means ± standard deviations derived from 5 electrophoretic mobility measurements.

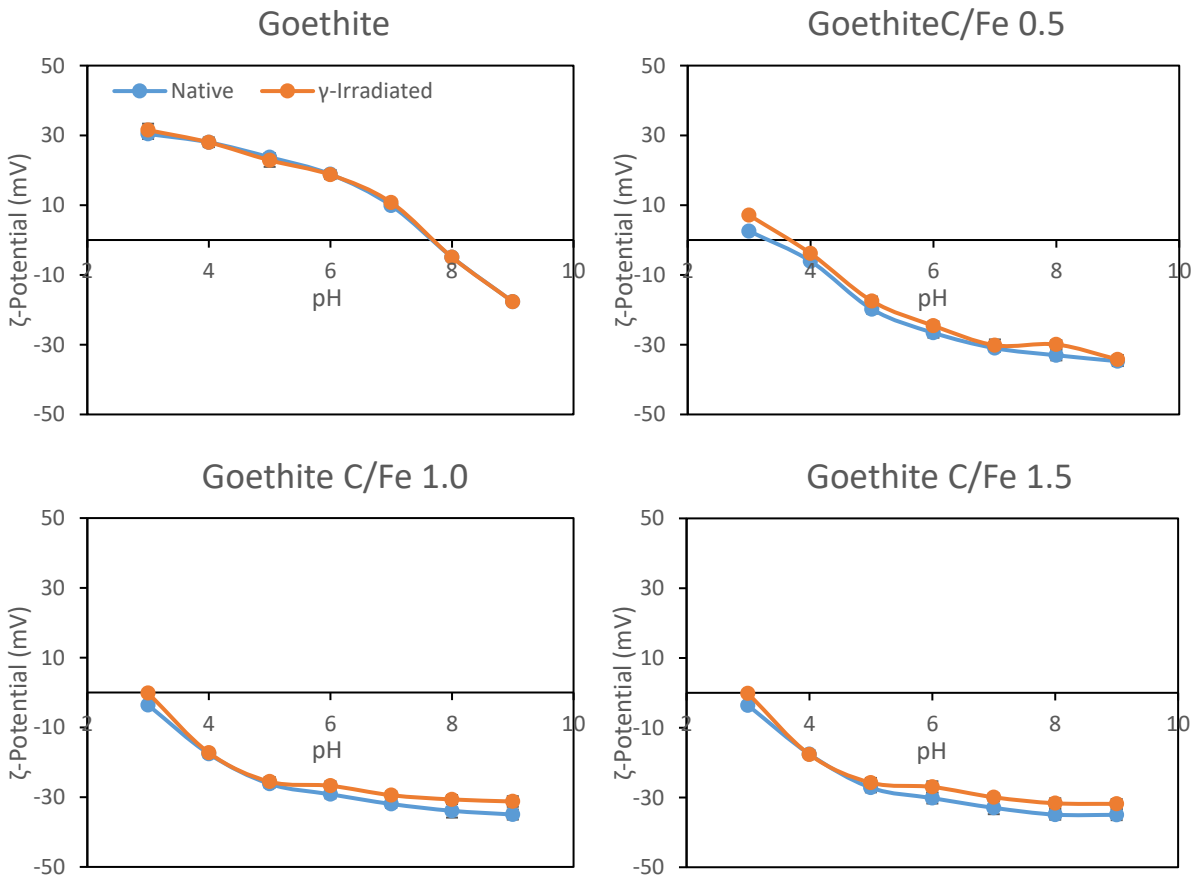

Fig. S8: Plot of the zeta potential versus pH for native and γ-irradiated goethite coprecipitated with alginate (C/Fe 0, 0.5, 1.0, and 1.5 mol:mol). Data markers represent means ± standard deviations derived from 5 electrophoretic mobility measurements.

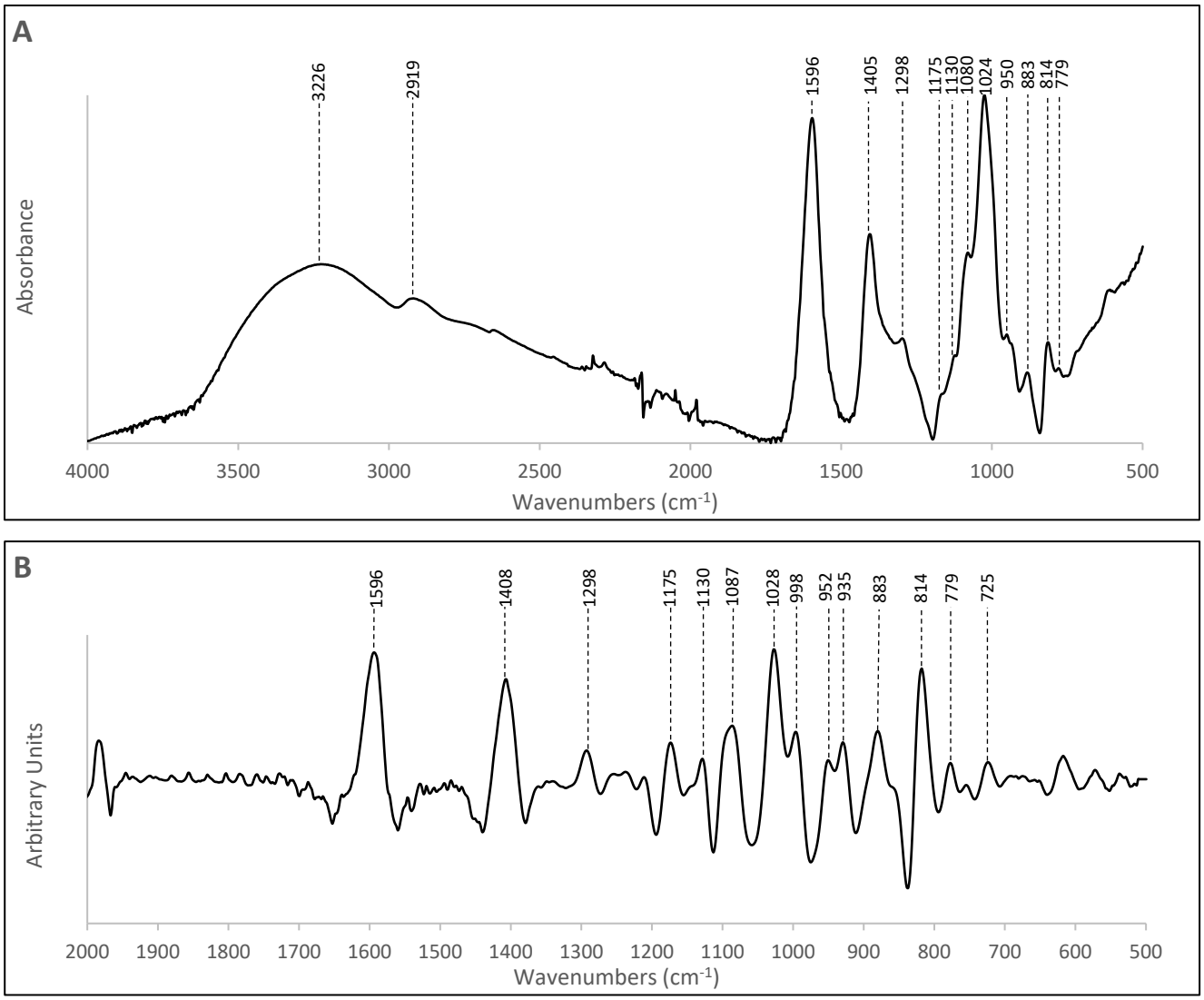

Fig. S9: FTIR spectra of dried Na-alginate (A) normal spectrum and (B) Savitsky-Golay secondary derivative spectrum with 19 points of smoothing. The latter spectrum was multiplied by -1. Refer to Table S2 for the band assignments.

Table S2: IR band assignments for pure Na-alginate. Italicized wavenumber values correspond to bands obtained from the Savitsky-Golay secondary derivative with 19 points of smoothing.

Wavenumbers (cm^{-1})	**Assignment**
3226	ν(O-H)
2919	ν(C-H)
1596	ν_{asym}(C-O-O) carboxylate
1408, 1405	ν_{sym}(C-O-O) carboxylate
1298	δ(C-H)
1175	ν_{sym}(C-O) of glycosidic linkage
1130	ν(C-O) of pyranose ring
	ν(C-C) of pyranose ring
	δ(C-C-C) of pyranose ring
1087, 1080	ν(C-O-C) of pyranose ring
	ν(C-C) of pyranose ring
	ν_{asym}(C-O-C) of glycosidic linkage
1028, 1025	Vibrations due to mannuronic and guluronic acid residues:
	ν_{asym}(C-O-C) of glycosidic linkage
	ν(C-O) of pyranose ring
	ν(C-C)
	ν(C-O) of secondary alcohols
998	ν(C-O) of pyranose ring
	ν(C-C) of pyranose ring
	δ(C-C-C) of pyranose ring
952, 950	Vibrations due to mannuronic acid residues:
	ν(C-C)
	δ(C-C-H)
935	ν(C-C) of mannuronic acid residues
883	δ(C1-H) β-mannuronic acid residues
814	Vibrations due to mannuronic acid residues:
	δ(C-O-C) of glycosidic linkage
	δ(C-C-C) of pyranose ring
	δ(O-C-C) of pyranose ring
	δ(C-C-H)
779	α-L-guluronic acid residues
725	Ring breathing

Band identification acquired from: Sartori et al. (1997); Chandıa et al. (2001); Leal et al. (2008); Cardenas-Jiron et al. (2011).

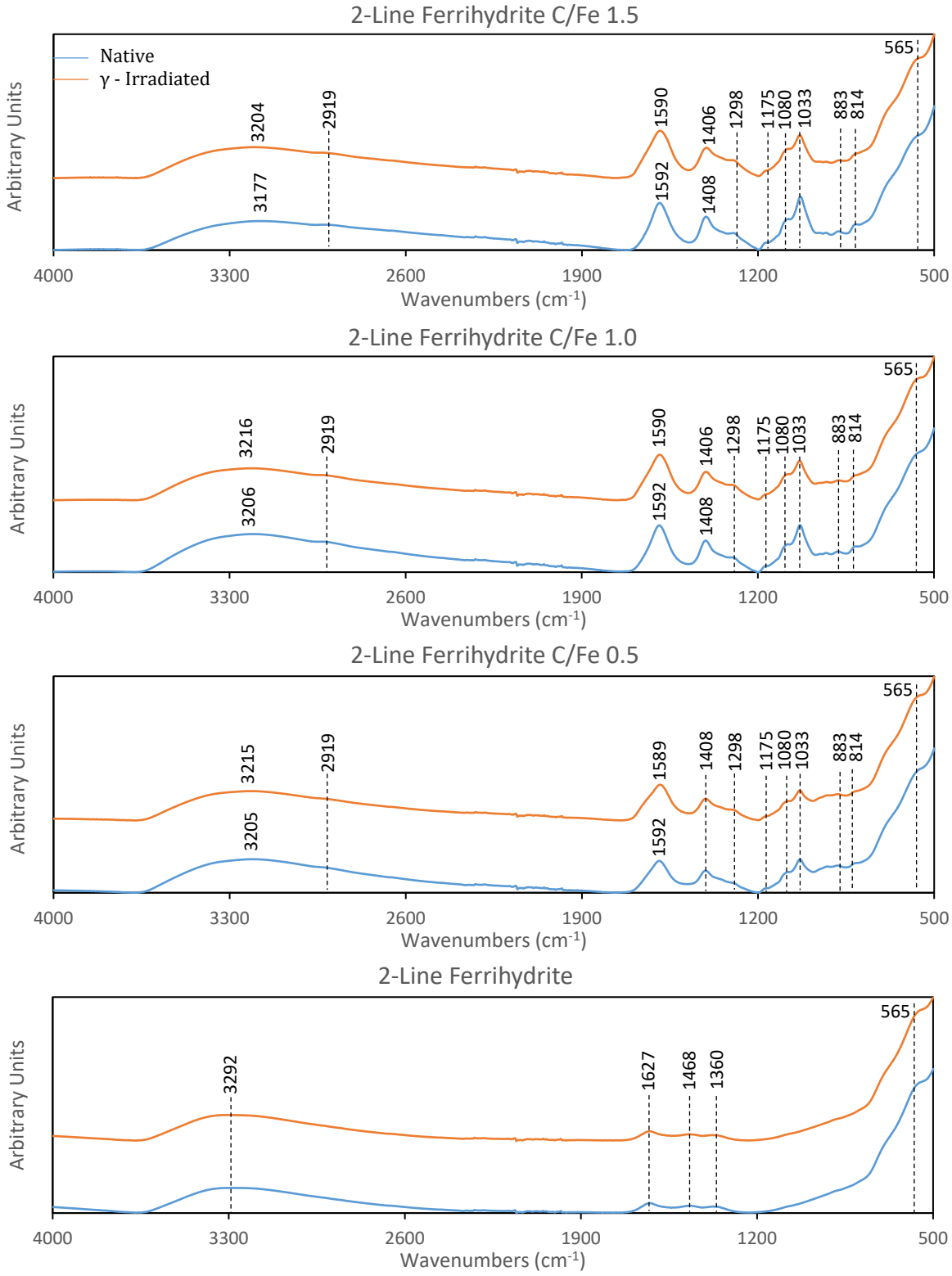

Fig. S10: FTIR spectra of 2-line ferrihydrite coprecipitated with alginate (C/Fe of 0, 0.5, 1.0, and 1.5 mol:mol) before and after γ-irradiation to a total dose of 25 kGy. Refer to Table S3 for the band assignments.

Table S3: IR band assignments for native and post-irradiated ferrihydrites coprecipitated with and without Na-alginate (C/Fe 0, 0.5, 1.0, and 1.5 mol:mol).

Wavenumbers (cm^{-1})	**Assignment**
3292-3177	ν(O-H)
2919	ν(C-H)
1627	δ(O-H)
1468, 1360	2-line ferrihydrite: ν_{asym}(C-O), ν_{sym}(C-O) adsorbed carbonate
1592-1589	ν_{asym}(C-O-O) carboxylate
1408-1406	ν_{sym}(C-O-O) carboxylate
1298	δ(C-H)
1175	ν_{sym}(C-O) of glycosidic linkage
1080	ν(C-O-C) of pyranose ring
	ν(C-C) of pyranose ring
1033	Vibrations due to mannuronic and guluronic acid residues:
	ν_{asym}(C-O-C) of glycosidic linkage
	ν(C-O) of pyranose ring
	ν(C-C)
	ν(C-O) of secondary alcohols
883	δ(C1-H) β-mannuronic acid residues
814	Vibrations due to mannuronic acid residues:
	δ(C-O-C) of glycosidic linkage
	δ(C-C-C) of pyranose ring
	δ(O-C-C) of pyranose ring
	δ(C-C-H)
565	2-line ferrihydrite: ν(Fe-O)

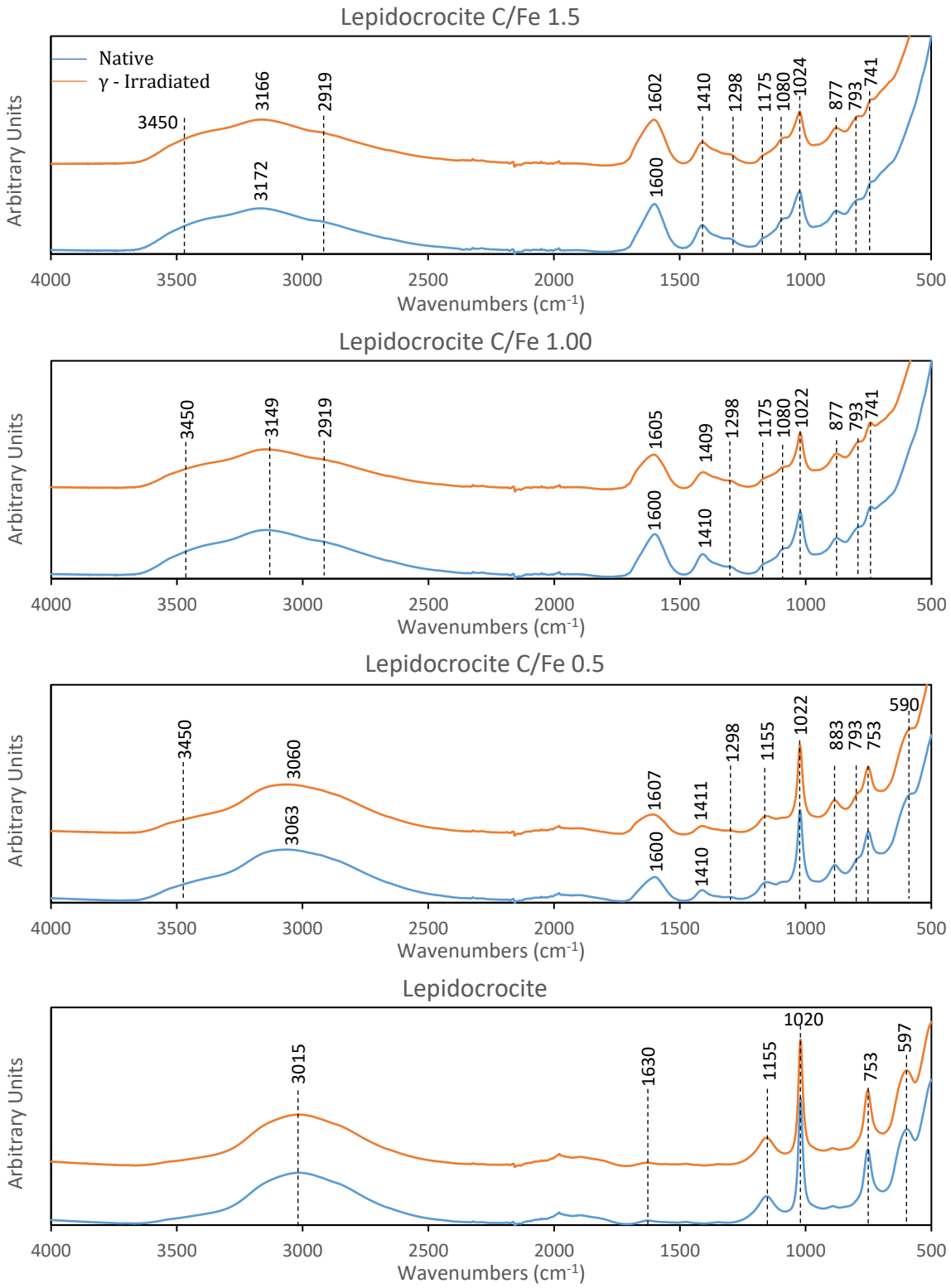

Fig. S11: FTIR spectra of lepidocrocite coprecipitated with alginate (C/Fe of 0, 0.5, 1.0, and 1.5 mol:mol) before and after γ-irradiation to a total dose of 25 kGy. Refer to Table S4 for the band assignments.

Table S4: IR band assignments for native and post-irradiated lepidocrocite coprecipitated with and without Na-alginate (C/Fe 0, 0.5, 1.0, and 1.5 mol:mol).

Wavenumbers (cm^{-1})	**Assignment**
3450	ν(O-H) of adsorbed H_2O
3172-3015	ν(O-H) structural
2919	ν(C-H)
1630	δ(O-H) of adsorbed H_2O
1607-1600	ν_{asym}(C-O-O) carboxylate
1411-1409	ν_{sym}(C-O-O) carboxylate
1298	δ(C-H)
1175	ν_{sym}(C-O) of glycosidic linkage
1080	ν(C-O-C) of pyranose ring
	ν(C-C) of pyranose ring
1155	Lepidocrocite: In-plane δ(O-H)
1020-1024	Lepidocrocite: In-plane δ(O-H)
	Vibrations due to mannuronic and guluronic acid residues:
	ν_{asym}(C-O-C) of glycosidic linkage
	ν(C-O) of pyranose ring
	ν(C-C)
883-877	δ(C1-H) β-mannuronic acid residues
	Goethite (possible): δ(O-H) in plane
793	Goethite (possible): γ(O-H) out of plane
753-741	Lepidocrocite: γ(O-H) out of plane
597-590	Lepidocrocite: τ(O) out of plane (twisting)

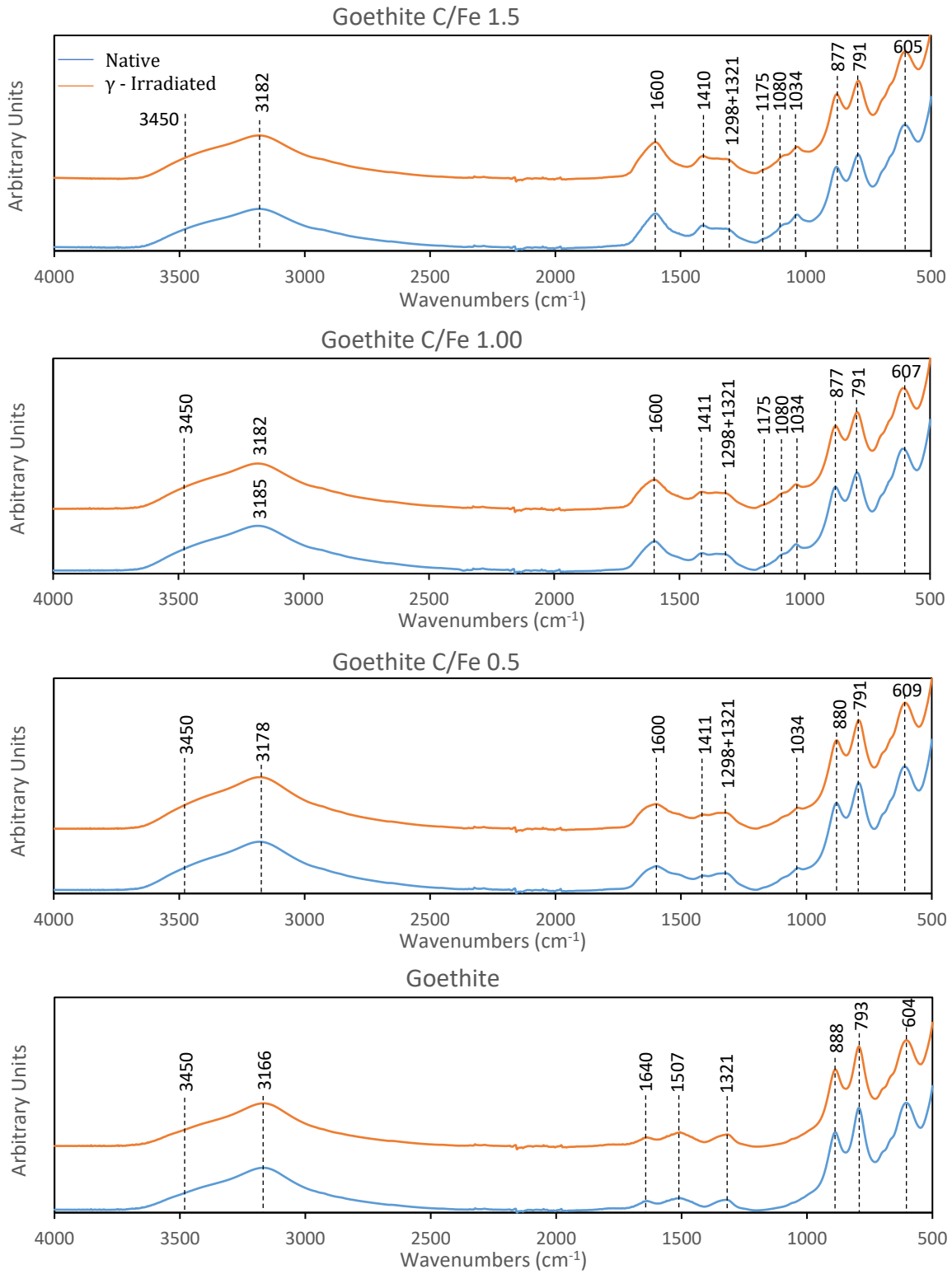

Fig. S12: FTIR spectra of goethite coprecipitated with alginate (C/Fe of 0, 0.5, 1.0, and 1.5 mol:mol) before and after γ-irradiation to a total dose of 25 kGy. Refer to Table S5 for the band assignments.

Table S5: IR band assignments for native and post-irradiated lepidocrocite coprecipitated with and without Na-alginate (C/Fe 0, 0.5, 1.0, and 1.5 mol:mol).

Wavenumbers (cm^{-1})	**Assignment**
3450	ν(O-H) of adsorbed H_2O
3185-3166	ν(O-H) structural
1640	δ(O-H) of adsorbed H_2O
1507, 1321	ν_{asym}(C-O), ν_{sym}(C-O) bound carbonate
1600	ν_{asym}(C-O-O) carboxylate
1411-1410	ν_{sym}(C-O-O) carboxylate
1298	δ(C-H)
1175	ν_{sym}(C-O) of glycosidic linkage
1080	ν(C-O-C) of pyranose ring
	ν(C-C) of pyranose ring
1033	Vibrations due to mannuronic and guluronic acid residues:
	ν_{asym}(C-O-C) of glycosidic linkage
	ν(C-O) of pyranose ring
	ν(C-C)
	ν(C-O) of secondary alcohols
888-877	Goethite: In-plane δ(O-H)
793-791	Goethite: Out-of-plane γ (O-H)
609-604	Goethite: ν_{sym}(Fe-O)

Table S6: Linear Fe(III) reduction rates and maximum percentage of total Fe reduced for the non-irradiated and γ-irradiated precipitates. The values represent the mean ± standard deviation of 3 replicate experiments for each precipitate.

Sample	Rate (day^{-1})		Maximum Fe reduced (%)	
	Native	γ	Native	γ
Fh	0.042±0.003 (R^2 = 0.995)	0.042±0.003 (R^2 = 0.995)	61.72±3.03	61.73±2.80
Fh 0.5	0.044±0.008 (R^2 = 0.976)	0.044±0.007 (R^2 = 0.982)	43.22±1.24*	55.97±2.13*
Fh 1.0	0.047±0.009 (R^2 = 0.976)	0.051±0.009 (R^2 = 0.976)	45.83±1.13*	59.41±1.72*
Fh 1.5	0.050±0.008 (R^2 = 0.981)	0.061±0.008 (R^2 = 0.989)	44.75±2.00*	61.74±2.13*
Lp	0.018±0.002 (R^2 = 0.987)	0.018±0.002 (R^2 = 0.990)	33.58±5.14	33.49±4.29
Lp 0.5	0.016±0.004 (R^2 = 0.962)	0.015±0.003 (R^2 = 0.973)	34.85±2.18*	38.87±2.57*
Lp 1.0	0.024±0.004 (R^2 = 0.975)	0.024±0.003 (R^2 = 0.991)	39.12±2.95	40.94±2.82
Lp 1.5	0.028±0.007 (R^2 = 0.963)	0.028±0.004 (R^2 = 0.984)	42.46±2.53	44.78±2.83
Gt	0.013±0.002 (R^2 = 0.985)	0.014±0.002 (R^2 = 0.984)	30.57±2.71	31.00±3.13
Gt 0.5	0.013±0.003 (R^2 = 0.960)	0.013±0.003 (R^2 = 0.967)	30.09±2.92	29.70±2.90
Gt 1.0	0.015±0.002 (R^2 = 0.993)	0.017±0.002 (R^2 = 0.993)	35.81±3.06	38.85±3.96
Gt 1.5	0.017±0.002 (R^2 = 0.986)	0.018±0.002 (R^2 = 0.987)	34.03±2.97*	37.14±2.60*

* Significant difference between treatments at the 95% confidence interval ($P<0.05$, two-tailed t-test)

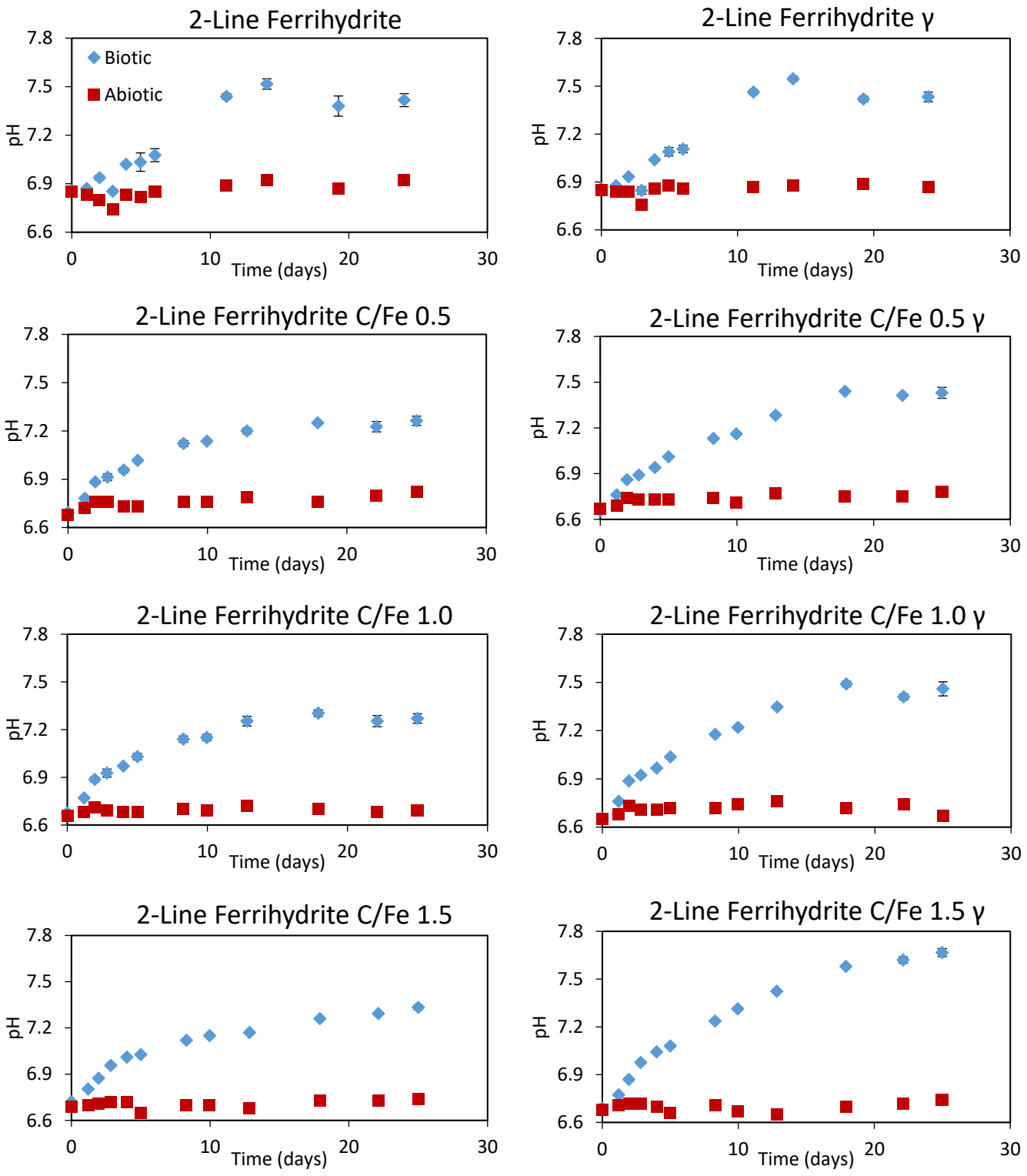

Fig. S13: Changes in pH during the anaerobic reduction of the native ferrihydrite-alginate coprecipitates (C/Fe 0, 0.5, 1.0, and 1.5 mol:mol) and their corresponding γ-irradiated counterparts by *S. putrefaciens* CN32. Data markers represent means ± standard deviations derived from three experimental replicates of each system.

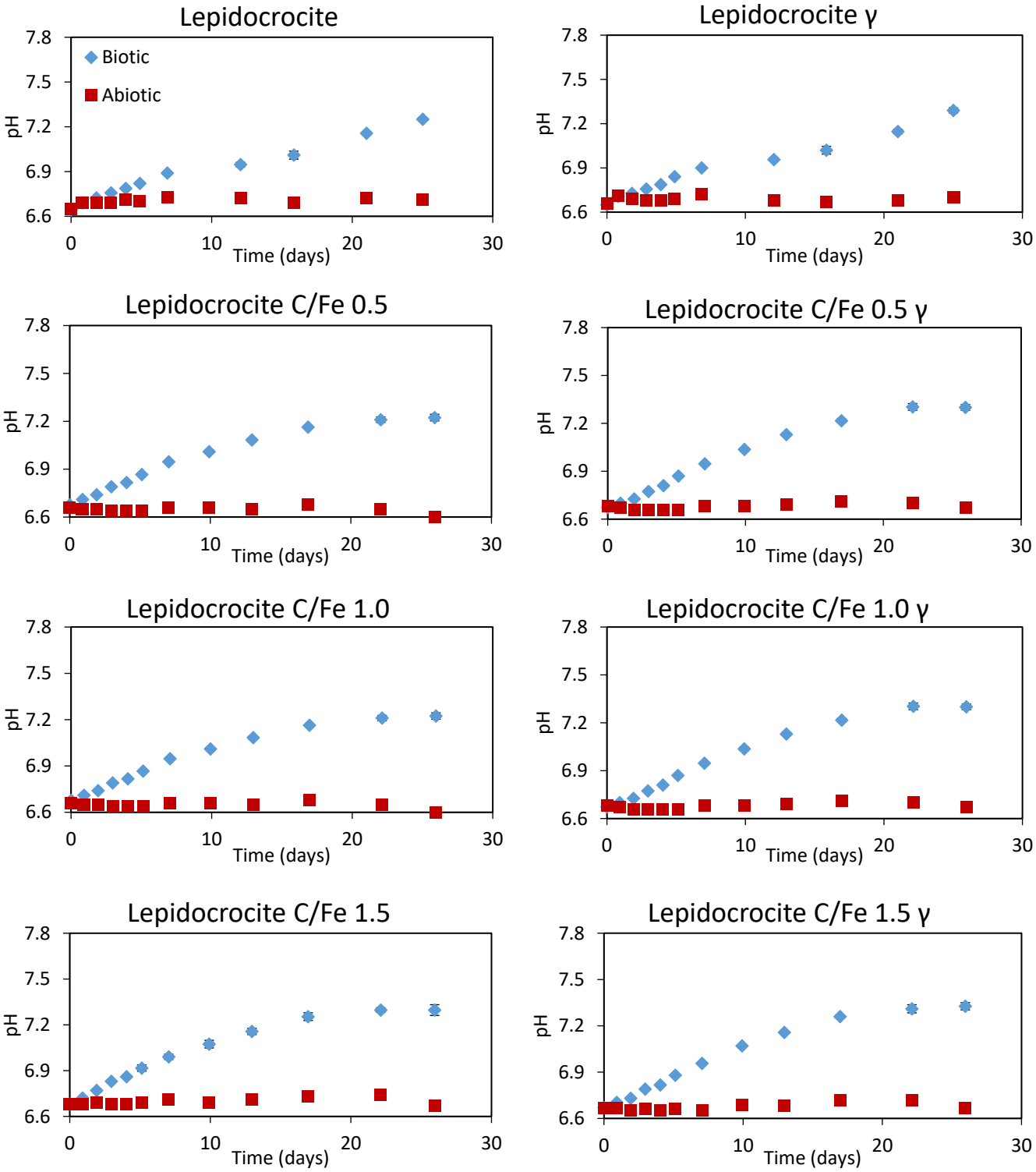

Fig. S14: Changes in pH during the anaerobic reduction of the native lepidocrocite-alginate coprecipitates (C/Fe 0, 0.5, 1.0, and 1.5 mol:mol) and their corresponding γ-irradiated counterparts by *S. putrefaciens* CN32. Data markers represent means ± standard deviations derived from three experimental replicates of each system.

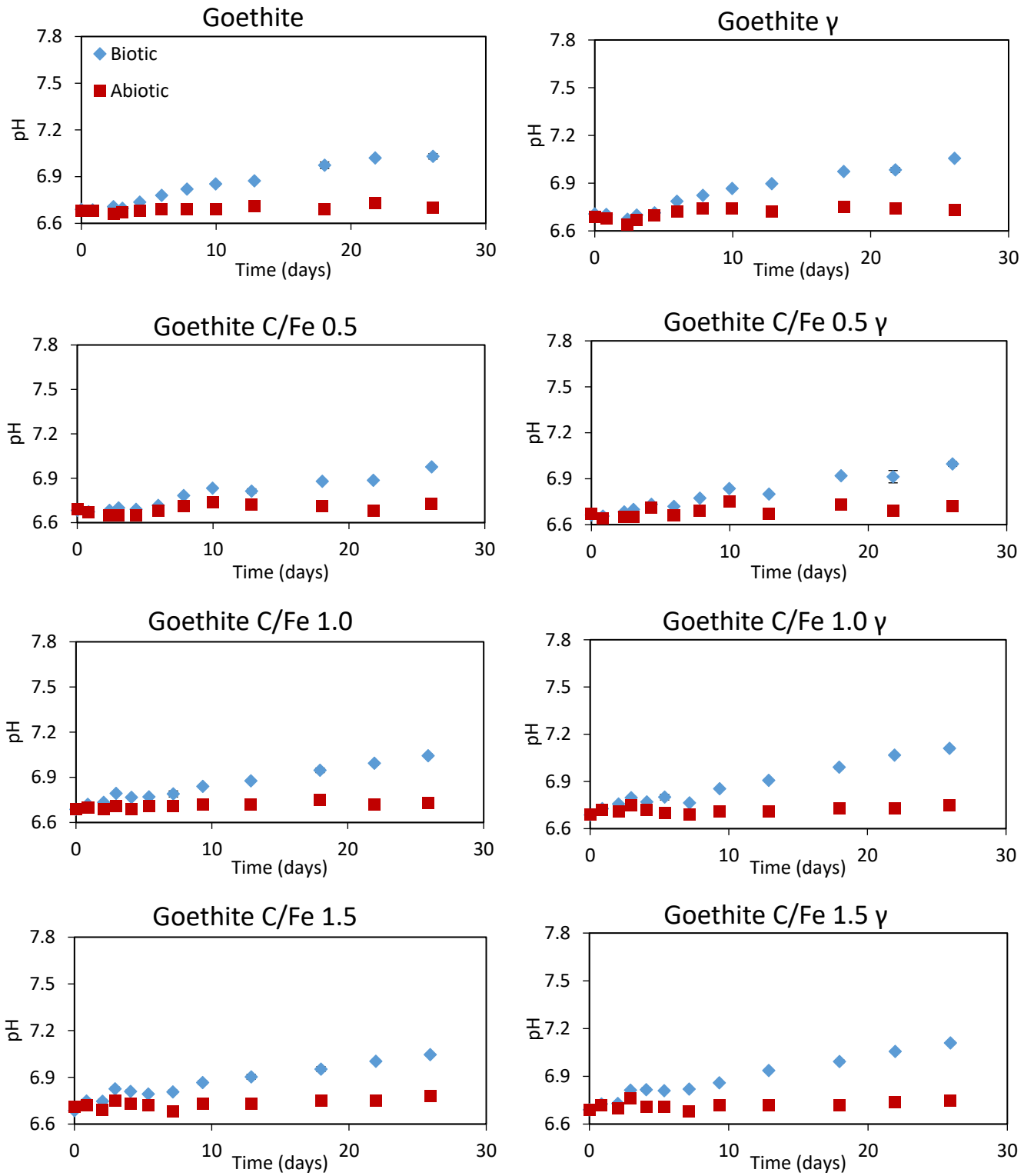

Fig. S15: Changes in pH during the anaerobic reduction of the native goethite-alginate coprecipitates (C/Fe 0, 0.5, 1.0, and 1.5 mol:mol) and their corresponding γ-irradiated counterparts by *S. putrefaciens* CN32. Data markers represent means ± standard deviations derived from three experimental replicates of each system.

Table S7: Cell concentration (log colony forming unit CFU/mL) of *S. putrefaciens* CN32 measured at the start and end of the reduction experiments for the various native and irradiated iron oxyhydroxide coprecipitates. Data represents the mean ± standard deviation of 3 replicates for each experiment. Across all experiments, no growth of any bacteria was observed in the control microcosms.

Sample		Average Log_{10} Colony Forming Unit	
		Initial	Final
Fh*	Native	7.84±0.12	6.49±0.04
	γ	7.72±0.03	6.53±0.09
Fh C/Fe 0.5	Native	7.84±0.18	6.44±0.11
	γ	7.93±0.12	6.86±0.04
Fh C/Fe 1.0	Native	7.70±0.10	6.37±0.06
	γ	7.85±0.11	6.67±0.14
Fh C/Fe 1.5	Native	7.67±0.04	6.18±0.23
	γ	7.67±0.10	6.46±0.10
Lp*	Native	7.87±0.11	6.49±0.04
	γ	7.80±0.25	6.53±0.09
Lp C/Fe 0.5	Native	7.62±0.15	7.11±0.03
	γ	7.67±0.14	7.25±0.03
Lp C/Fe 1.0	Native	7.93±0.11	7.00±0.04
	γ	7.92±0.10	6.99±0.06
Lp C/Fe 1.5	Native	7.76±0.10	6.83±0.05
	γ	7.91±0.17	6.77±0.03
Gt*	Native	7.93±0.10	7.34±0.02
	γ	7.76±0.09	7.33±0.02
Gt C/Fe 0.5	Native	7.53±0.36	7.09±0.09
	γ	7.86±0.19	7.02±0.07
Gt C/Fe 1.0	Native	7.92±0.12	6.94±0.05
	γ	7.75±0.16	7.10±0.01
Gt C/Fe 1.5	Native	7.87±0.02	6.80±0.14
	γ	7.88±0.09	6.92±0.08

*Fh: 2-line ferrihydrite
Lp: lepidocrocite
Gt: goethite

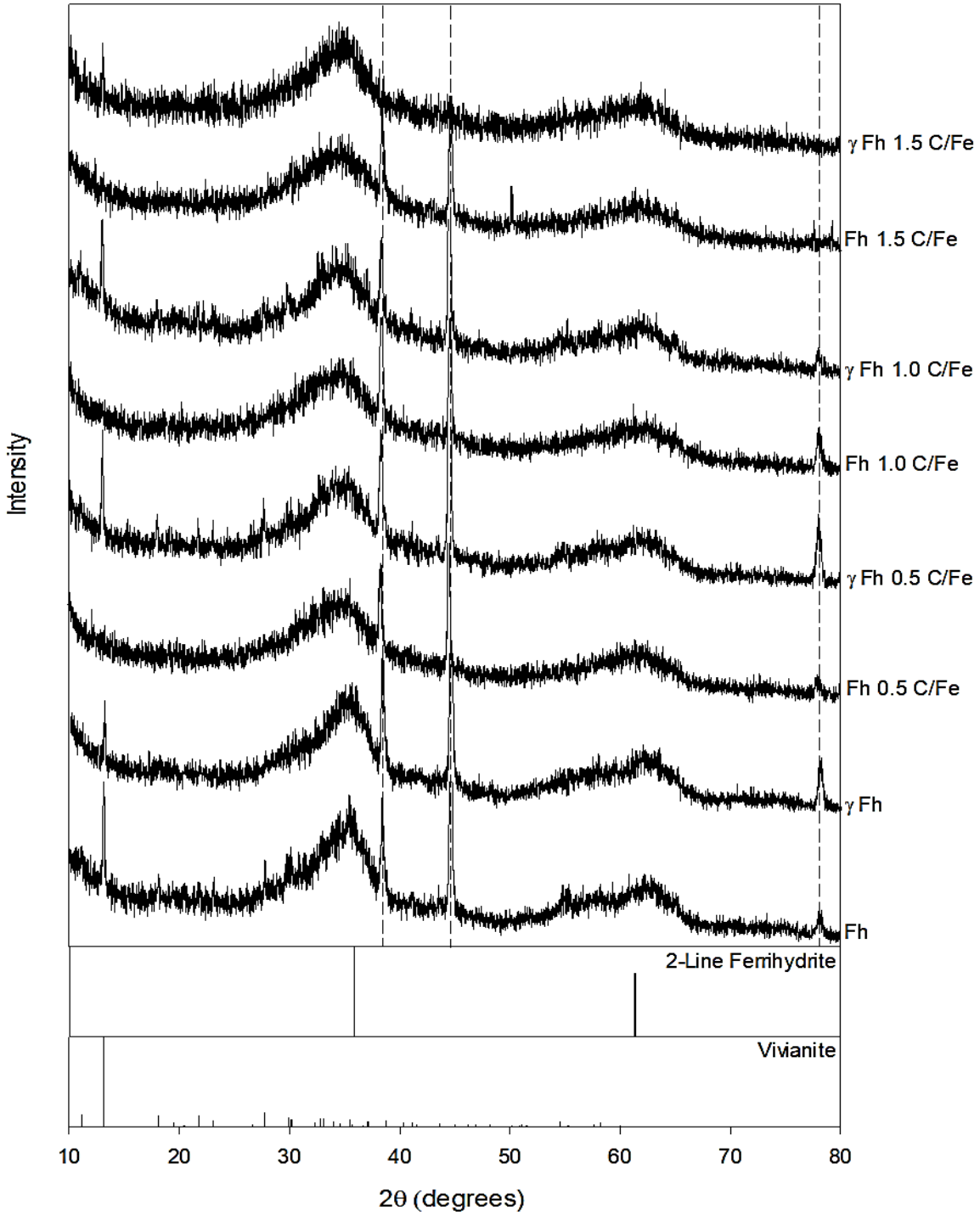

Fig. S16: X-ray diffraction patterns of post-reduction precipitates formed during the microbial reduction of the native ferrihydrite-alginate coprecipitates (C/Fe 0, 0.5, 1.0, and 1.5 mol:mol) and their corresponding γ-irradiated counterparts. Dashed lines highlight the peaks from the sample holder. For clarity, all patterns have been vertically separated on an arbitrary y-axis.

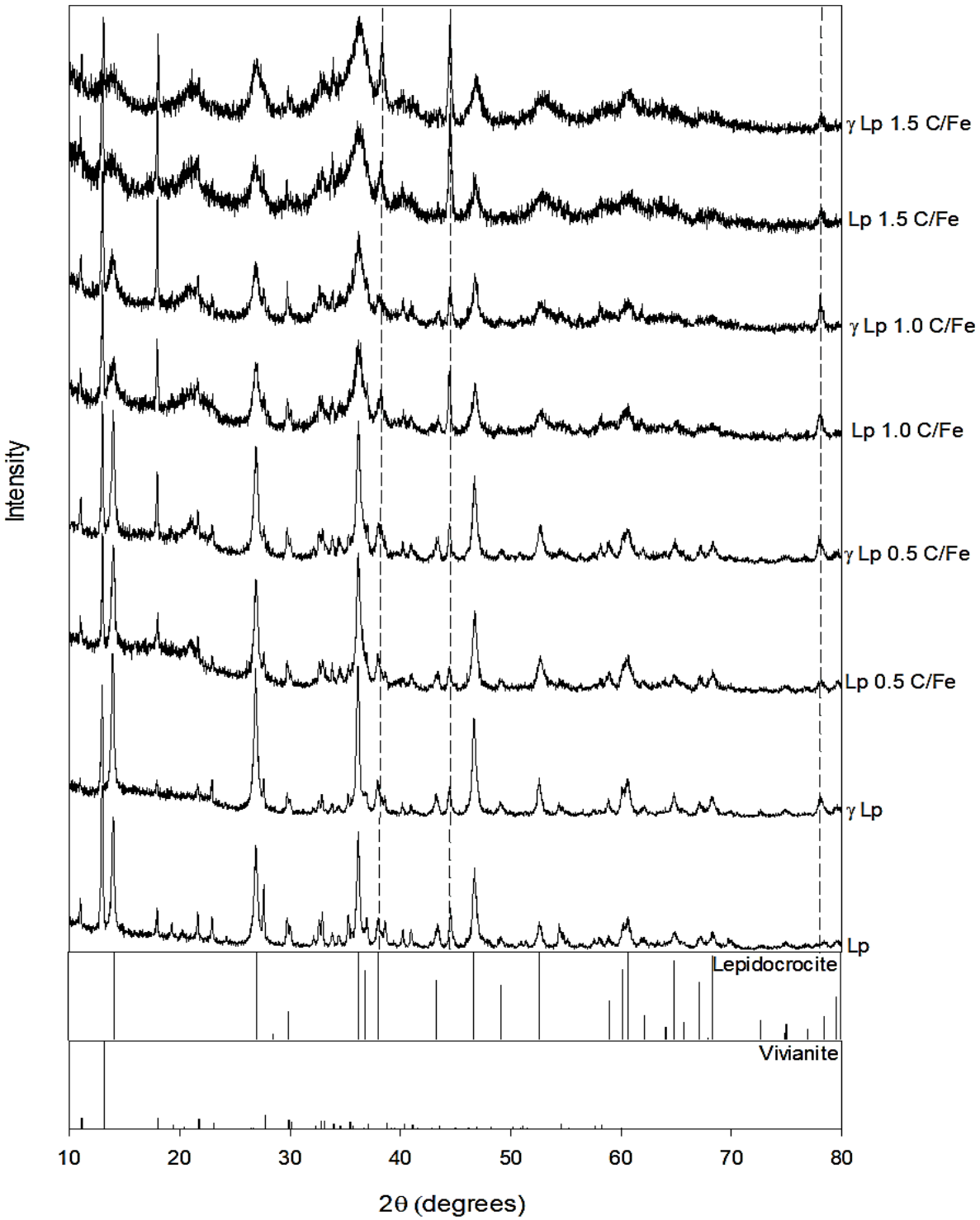

Fig. S17: X-ray diffraction patterns of post-reduction precipitates formed during the microbial reduction of the native lepidocrocite-alginate coprecipitates (C/Fe 0, 0.5, 1.0, and 1.5 mol:mol) and their corresponding γ-irradiated counterparts. Dashed lines highlight the peaks from the sample holder. For clarity, all patterns have been vertically separated on an arbitrary y-axis.

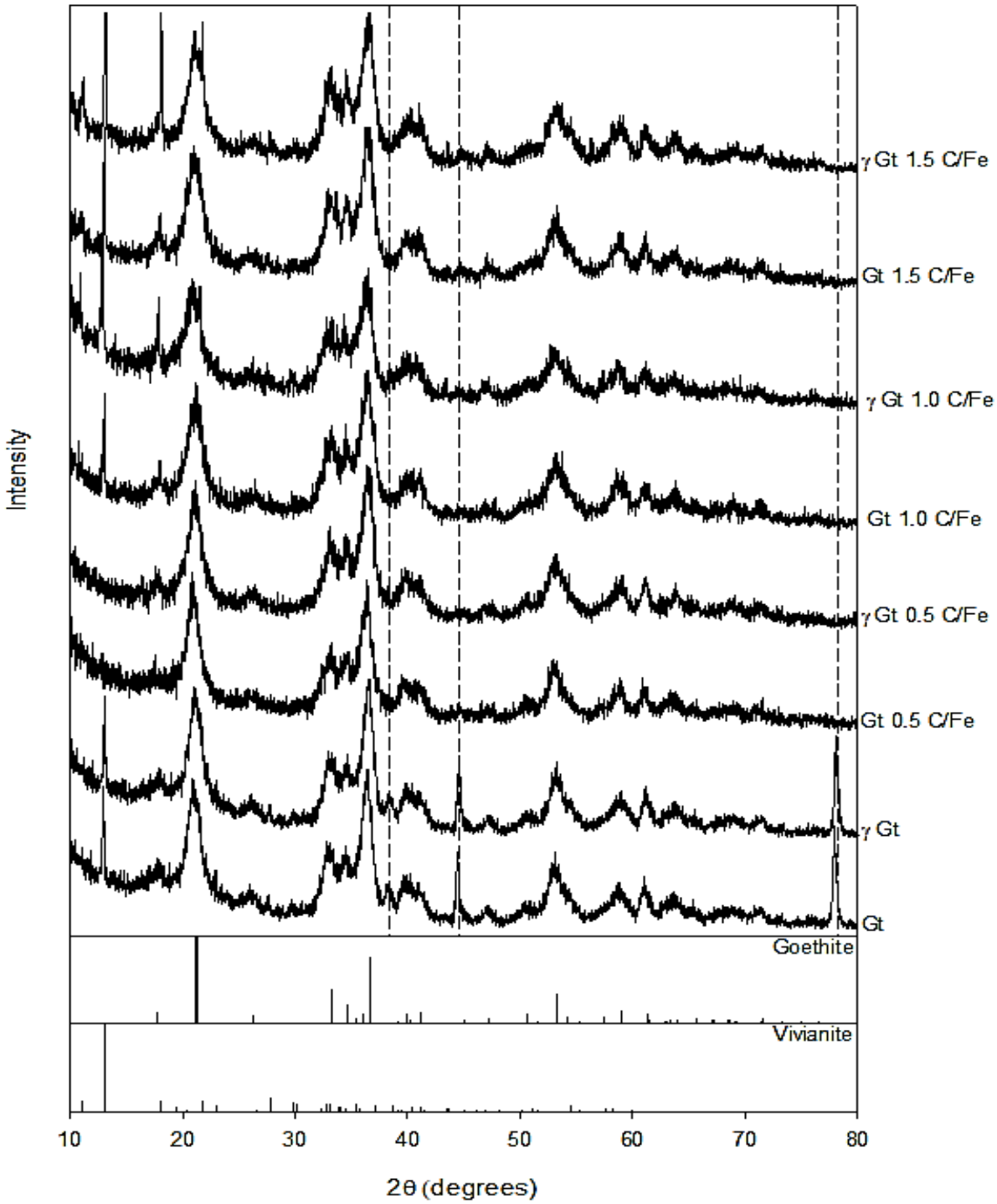

Fig. S18: X-ray diffraction patterns of post-reduction precipitates formed during the microbial reduction of the native goethite-alginate coprecipitates (C/Fe 0, 0.5, 1.0, and 1.5 mol:mol) and their corresponding γ-irradiated counterparts. Dashed lines highlight the peaks from the sample holder. For clarity, all patterns have been vertically separated on an arbitrary y-axis.

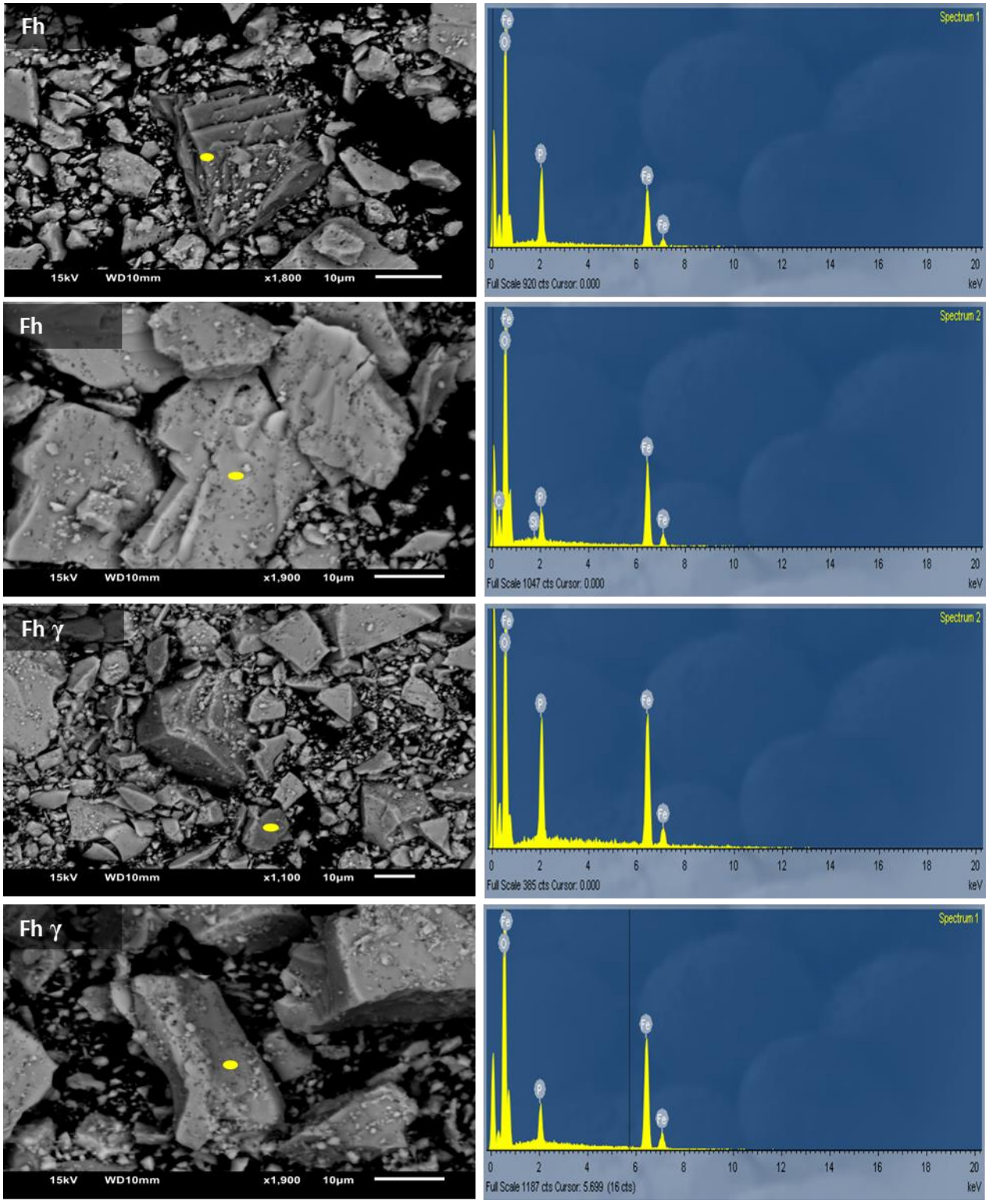

Fig. S19: SEM micrographs and EDX spectra of post-reduction precipitates formed during the microbial reduction of pure native and γ-irradiated 2-line ferrihydrite by *S. putrefaciens* CN32. The yellow circle corresponds to the area scanned to produce the EDX spectra.

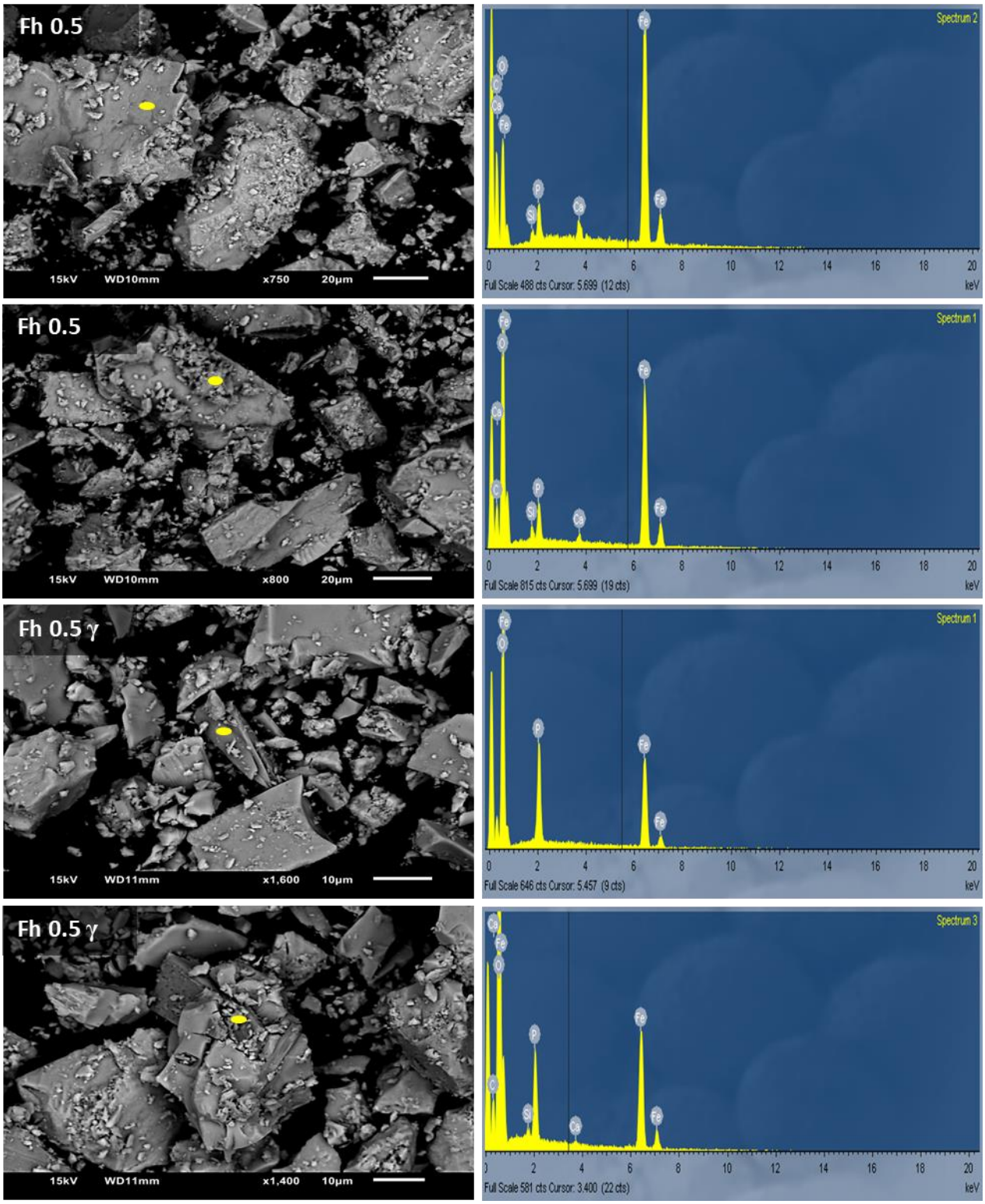

Fig. S20: SEM micrographs and EDX spectra of post-reduction precipitates formed during the microbial reduction of native and γ-irradiated 2-line ferrihydrite coprecipitated with alginate (C/Fe 0.5 mol:mol) by *S. putrefaciens* CN32. The yellow circle corresponds to the area scanned to produce the EDX spectra.

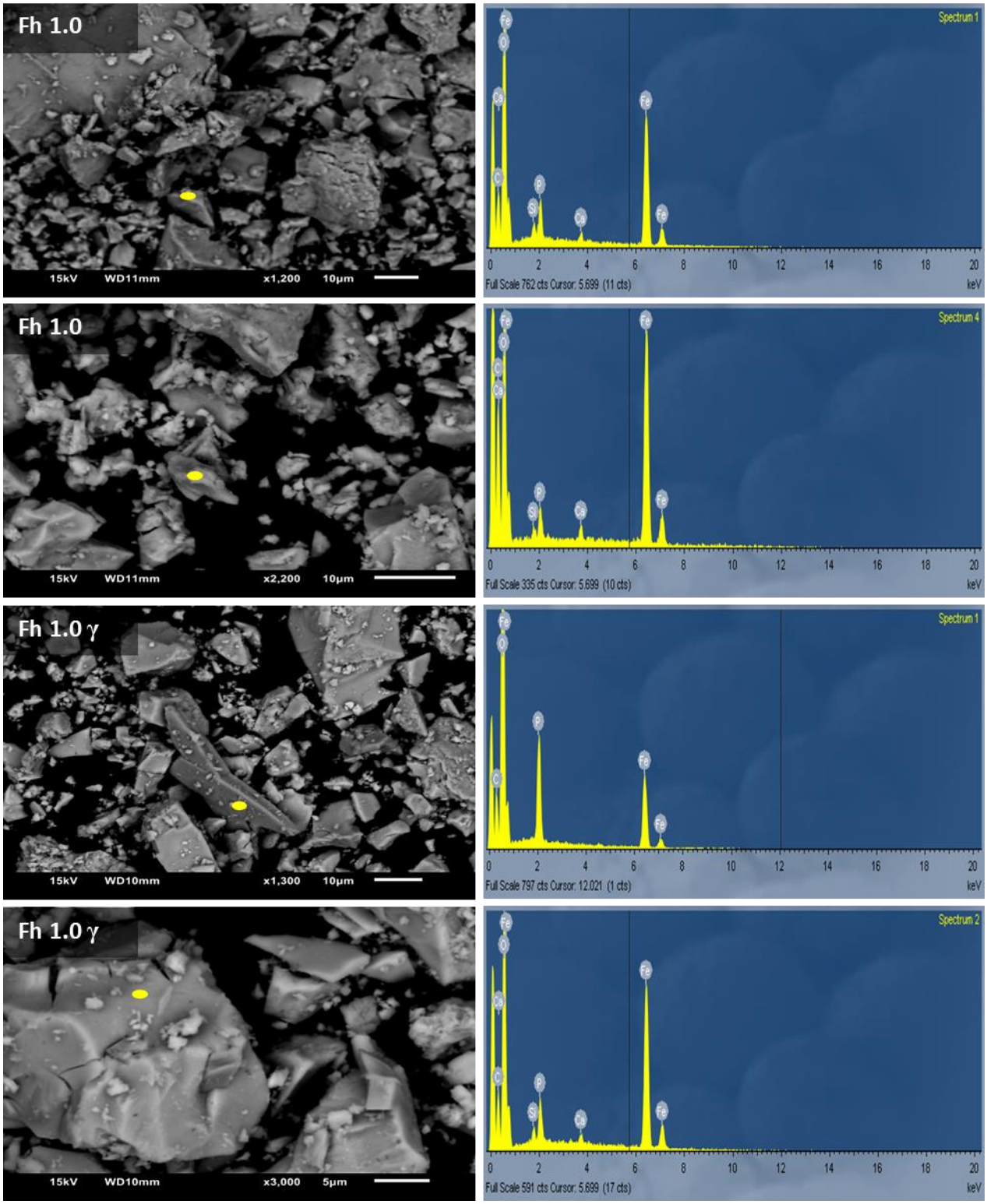

Fig. S21: SEM micrographs and EDX spectra of post-reduction precipitates formed during the microbial reduction of native and γ-irradiated 2-line ferrihydrite coprecipitated with alginate (C/Fe 1.0 mol:mol) by *S. putrefaciens* CN32. The yellow circle corresponds to the area scanned to produce the EDX spectra.

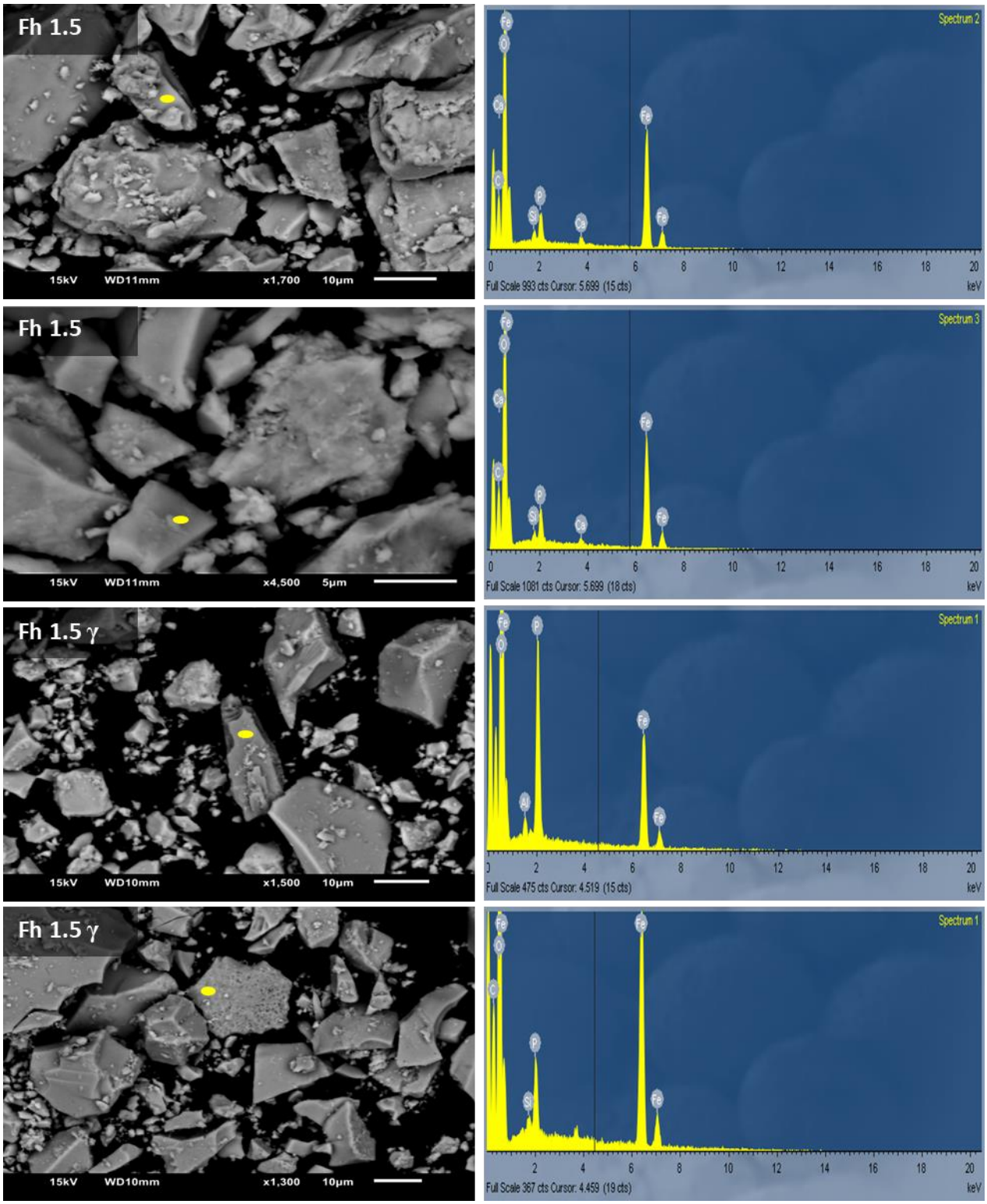

Fig. S22: SEM micrographs and EDX spectra of post-reduction precipitates formed during the microbial reduction of native and γ-irradiated 2-line ferrihydrite coprecipitated with alginate (C/Fe 1.5 mol:mol) by *S. putrefaciens* CN32. The yellow circle corresponds to the area scanned to produce the EDX spectra.

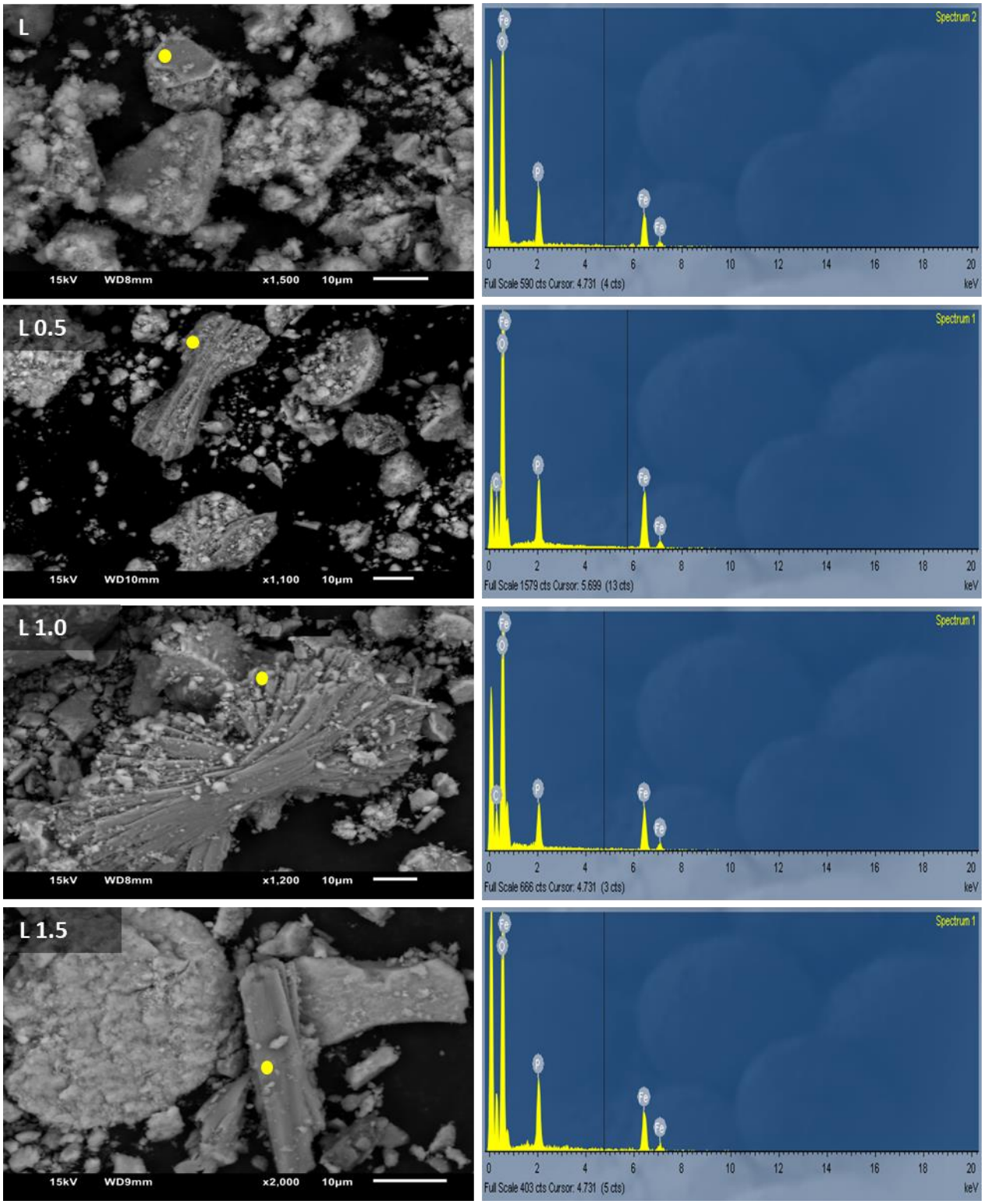

Fig. S23: SEM micrographs and EDX spectra of post-reduction precipitates formed during the microbial reduction of native lepidocrocite coprecipitated with alginate (C/Fe of 0, 0.5, 1.0 and 1.5 mol:mol) by *S. putrefaciens* CN32. The yellow circle corresponds to the area scanned to produce the EDX spectra.

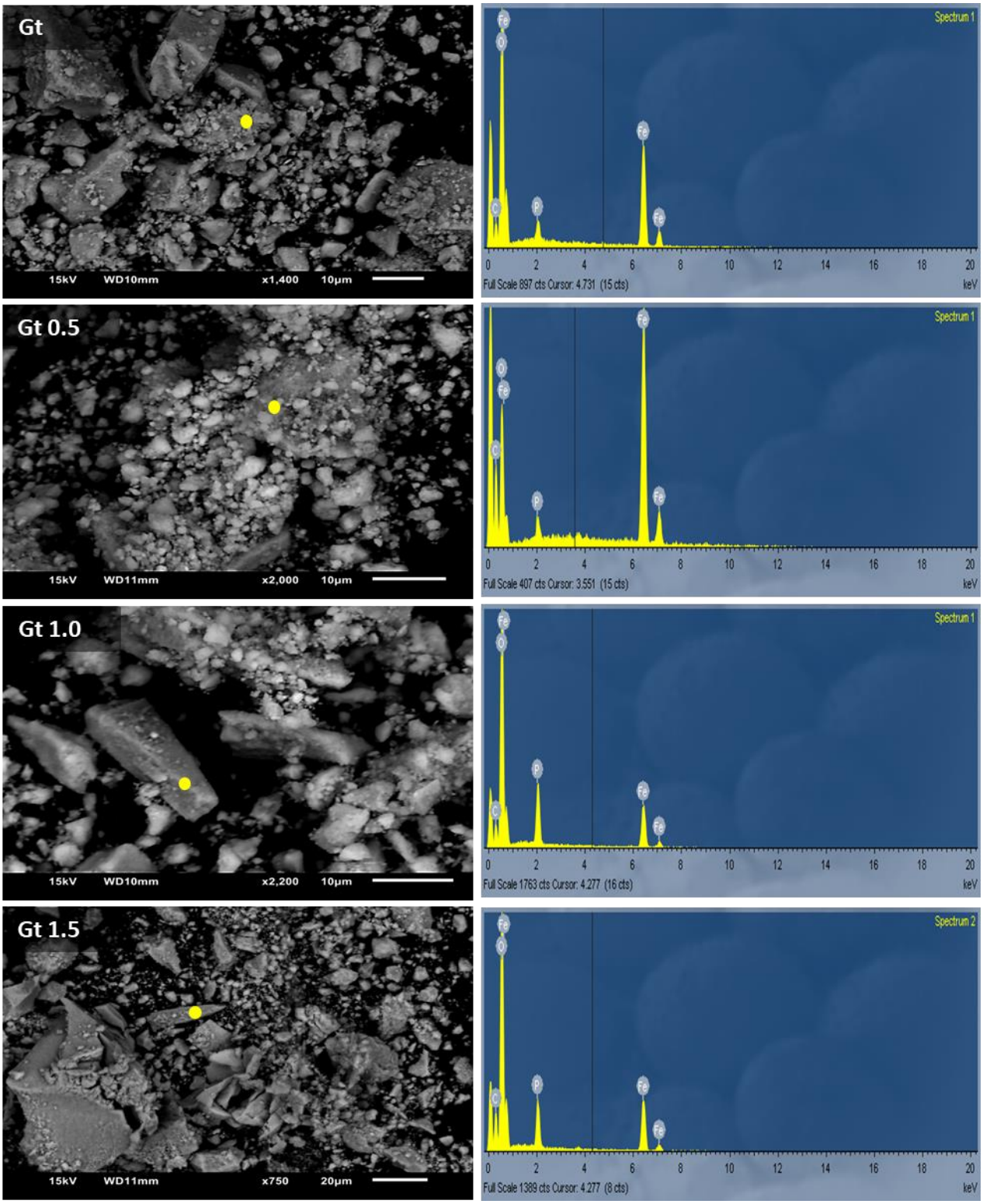

Fig. S24: SEM micrographs and EDX spectra of post-reduction precipitates formed during the microbial reduction of native goethite coprecipitated with alginate (C/Fe of 0, 0.5, 1.0 and 1.5 mol:mol) by *S. putrefaciens* CN32. The yellow circle corresponds to the area scanned to produce the EDX spectra.

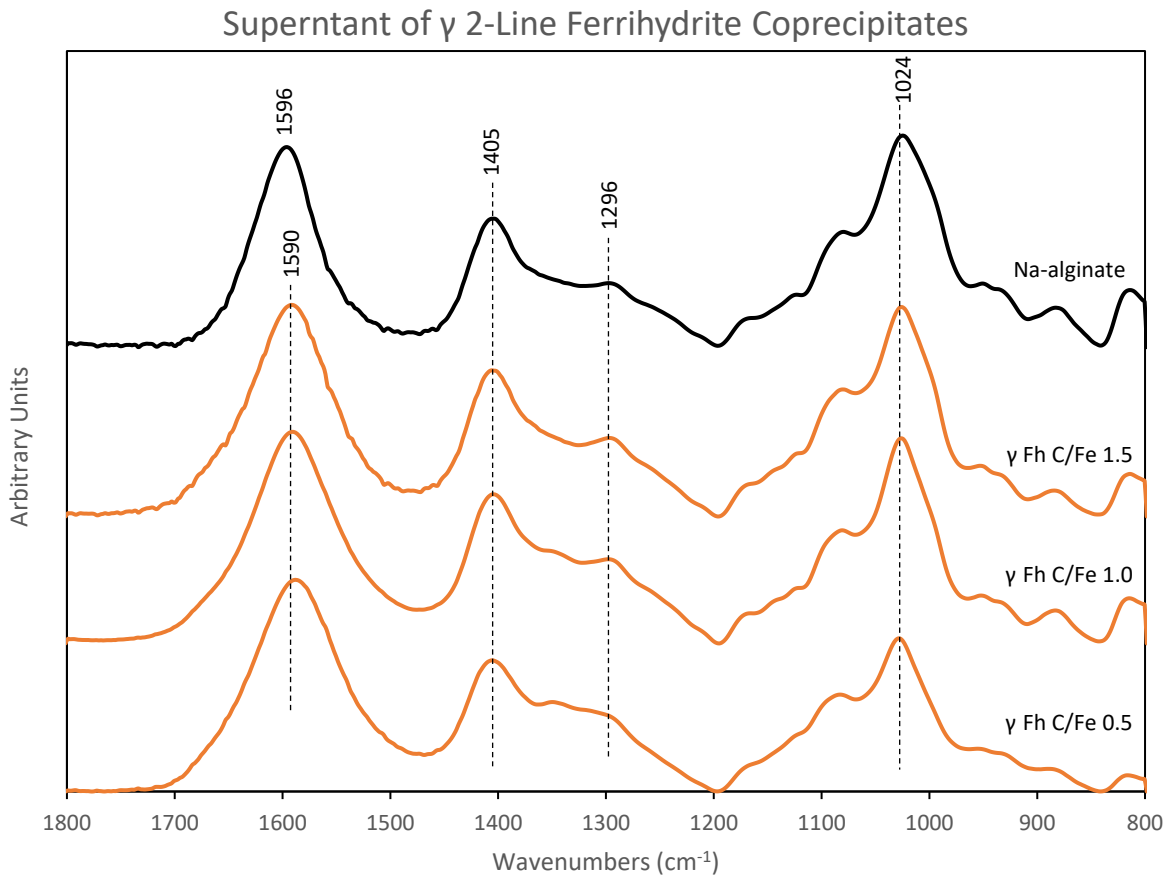

Fig. S25: FTIR spectra in the 1800 – 800 cm^{-1} region of the dried supernatant collected from 2-line ferrihydrite-alginate coprecipitates (C/Fe 0.5, 1.0, and 1.5 mol:mol) following γ-irradiation, centrifugation, and filtration (0.22 μm). The spectra indicate irradiation induced dissolution and release of dissolved alginate into solution. The spectrum of dried Na-alginate was included for comparison.

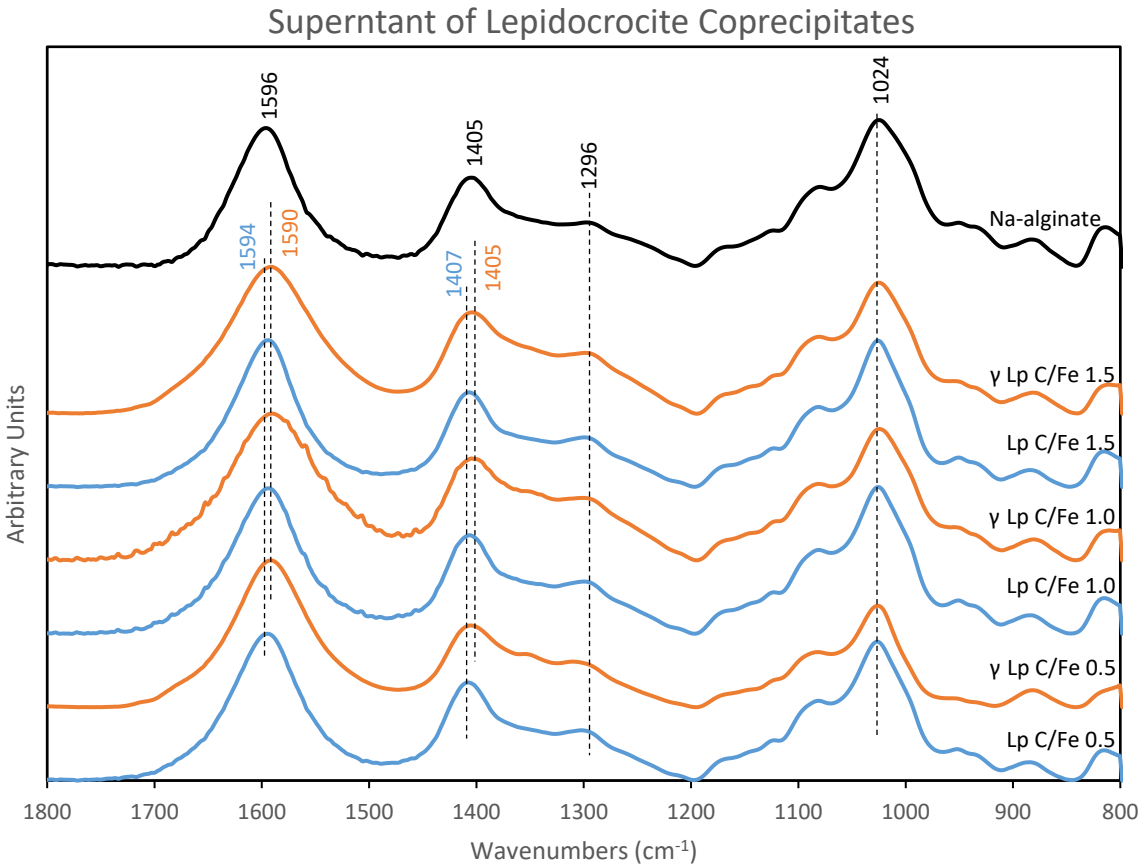

Fig. S26: FTIR spectra in the 1800 – 800 cm^{-1} region of the dried supernatant collected from the native and γ-irradiated lepidocrocite-alginate coprecipitates (C/Fe 0.5, 1.0, and 1.5 mol:mol) following centrifugation, and filtration (0.22 μm). The spectra indicate irradiation induced dissolution and release of dissolved alginate into solution. The spectrum of dried Na-alginate was included for comparison.

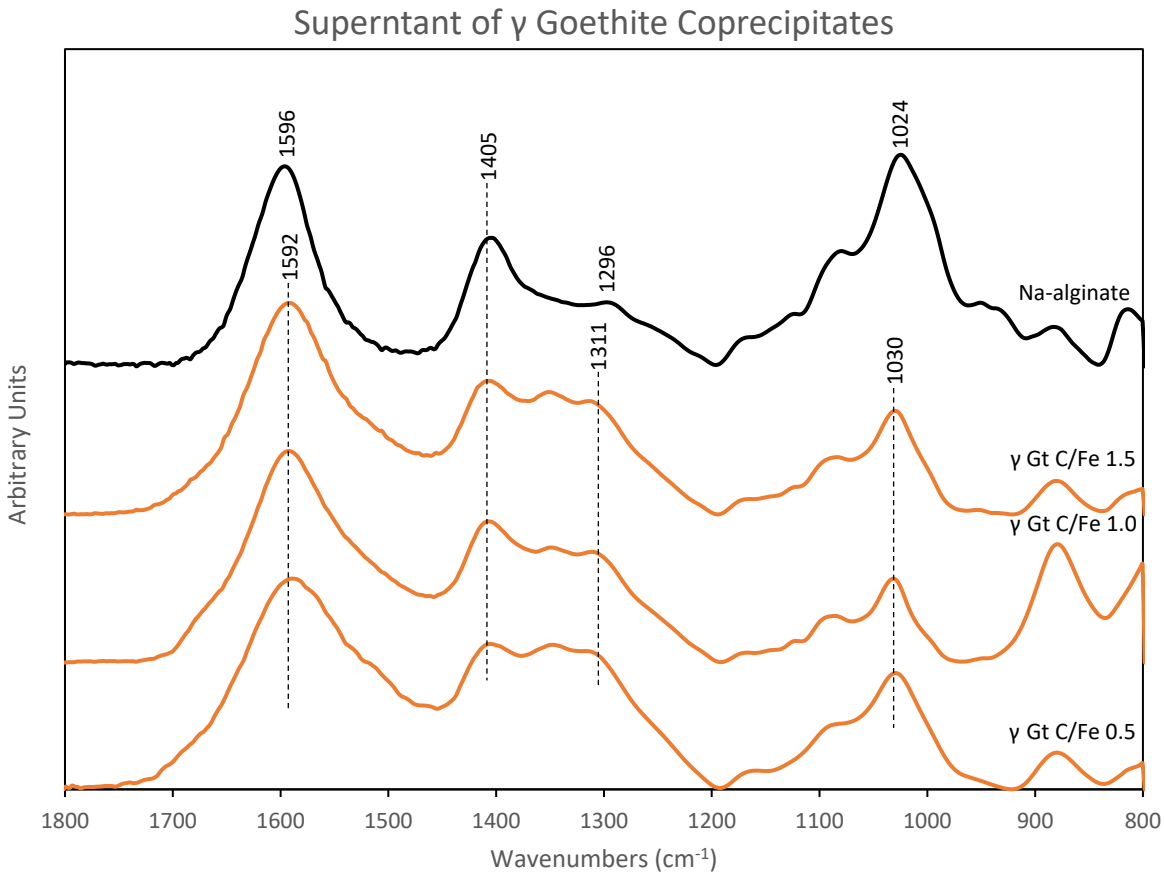

Fig. S27: FTIR spectra in the 1800 – 800 cm^{-1} region of the dried supernatant collected from goethite-alginate coprecipitates (C/Fe 0.5, 1.0, and 1.5 mol:mol) following γ-irradiation, centrifugation, and filtration (0.22 μm). The spectra indicate irradiation induced dissolution and release of dissolved alginate into solution. The spectrum of dried Na-alginate was included for comparison.

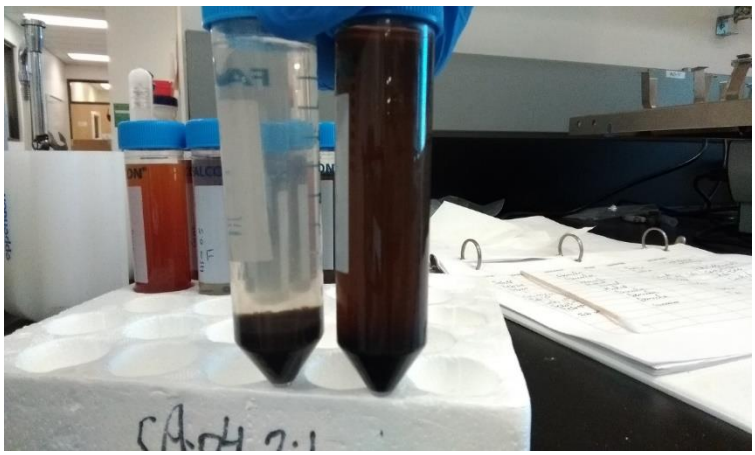

Fig. S28: Difference in the aggregation and coagulation of the native (left) and post-irradiated (right) ferrihydrite coprecipitated with C/Fe ratio of 0.5. The picture was taken at the end of the experimental period (25 days) of exposure to *Shewanella putrefaciens* CN32.

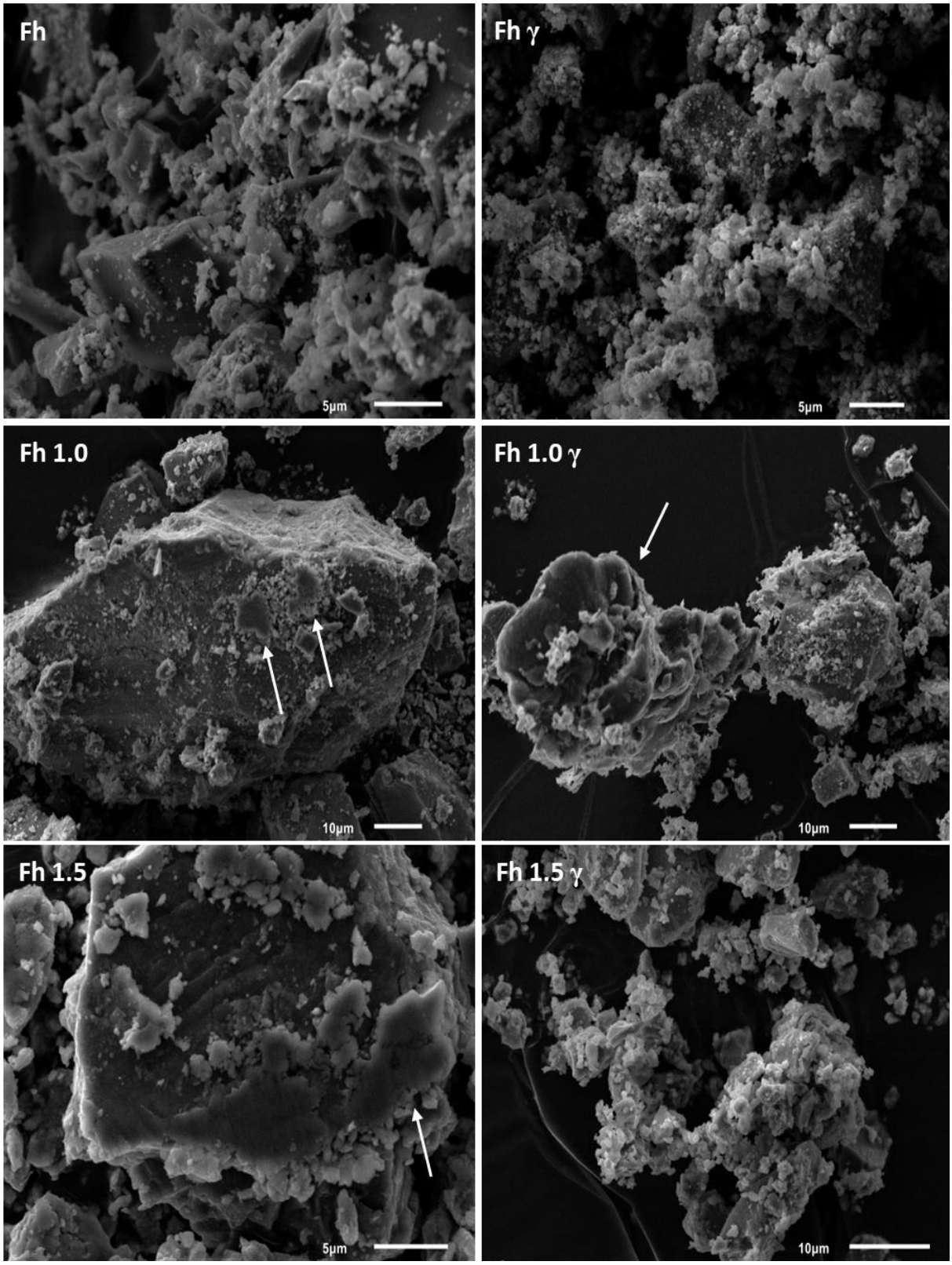

Fig. S29: Electron micrographs of carbon coated native 2-line ferrihydrite-alginate coprecipitates (C/Fe 0, 1.0, and 1.5 mol:mol) and their corresponding γ-irradiated counterparts. The micrographs show alginate induced aggregation. Arrows point to the possible presence of alginate.

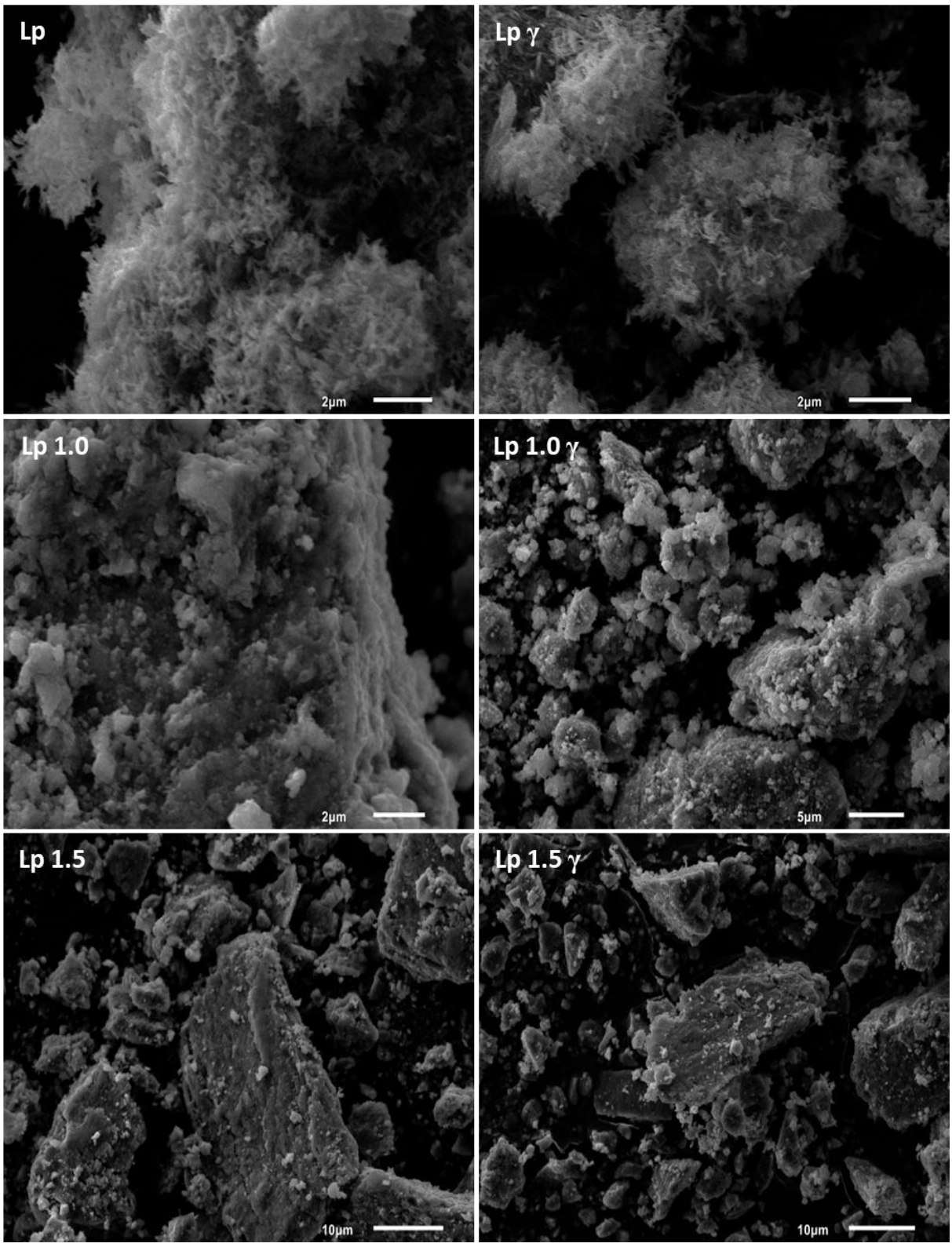

Fig. S30: Electron micrographs of carbon coated native lepidocrocite-alginate coprecipitates (C/Fe 0, 1.0, and 1.5 mol:mol) and their corresponding γ-irradiated counterparts. The micrographs show alginate induced aggregation and alginate induced transition from the typical needle shape for lepidocrocite crystals to nano-sized crystals.

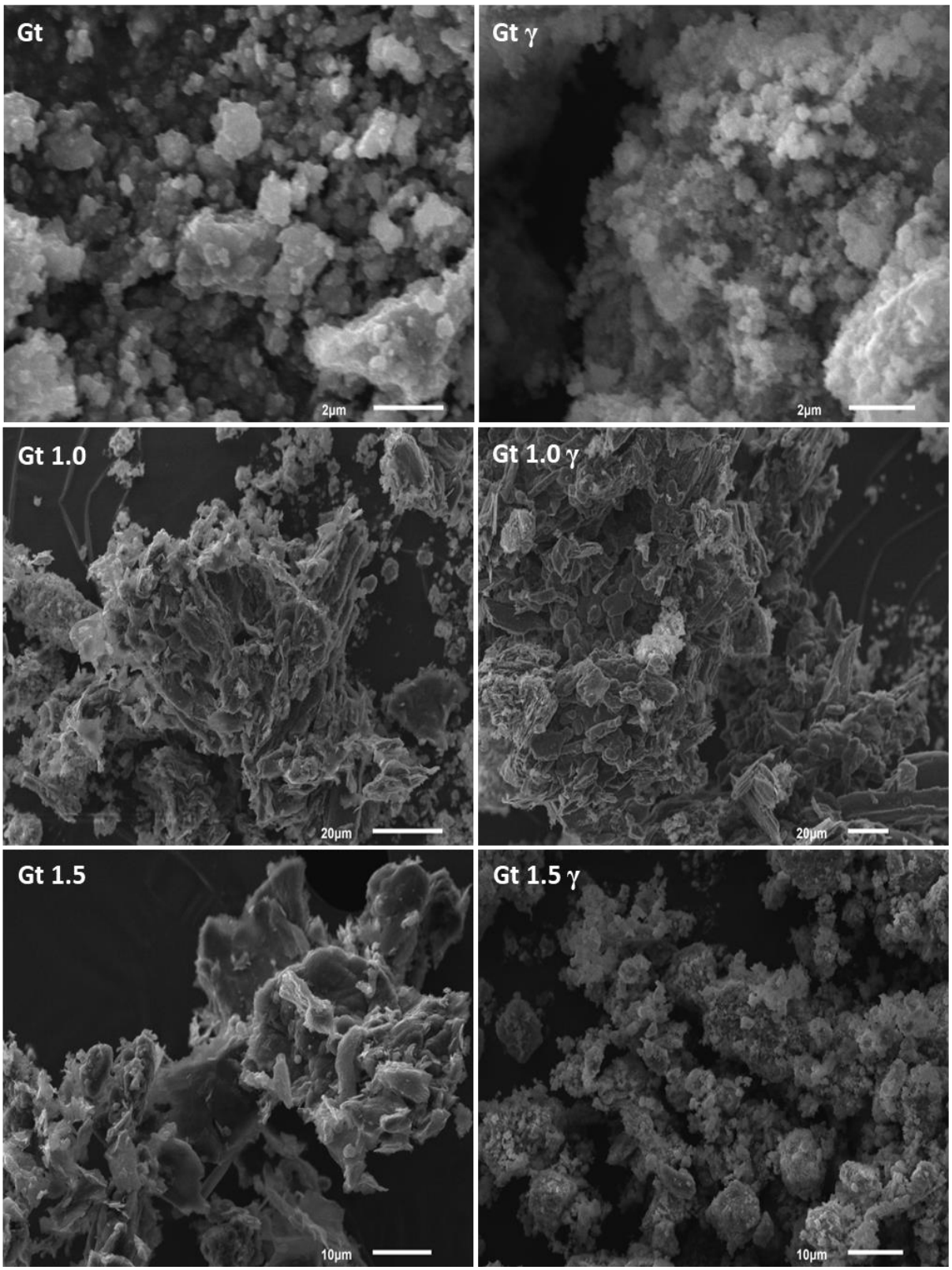

Fig. S31: Electron micrographs of carbon coated native goethite-alginate coprecipitates (C/Fe 0, 1.0, and 1.5 mol:mol) and their corresponding γ-irradiated counterparts. The electron micrographs show the alginate induced aggregation of goethite particles.

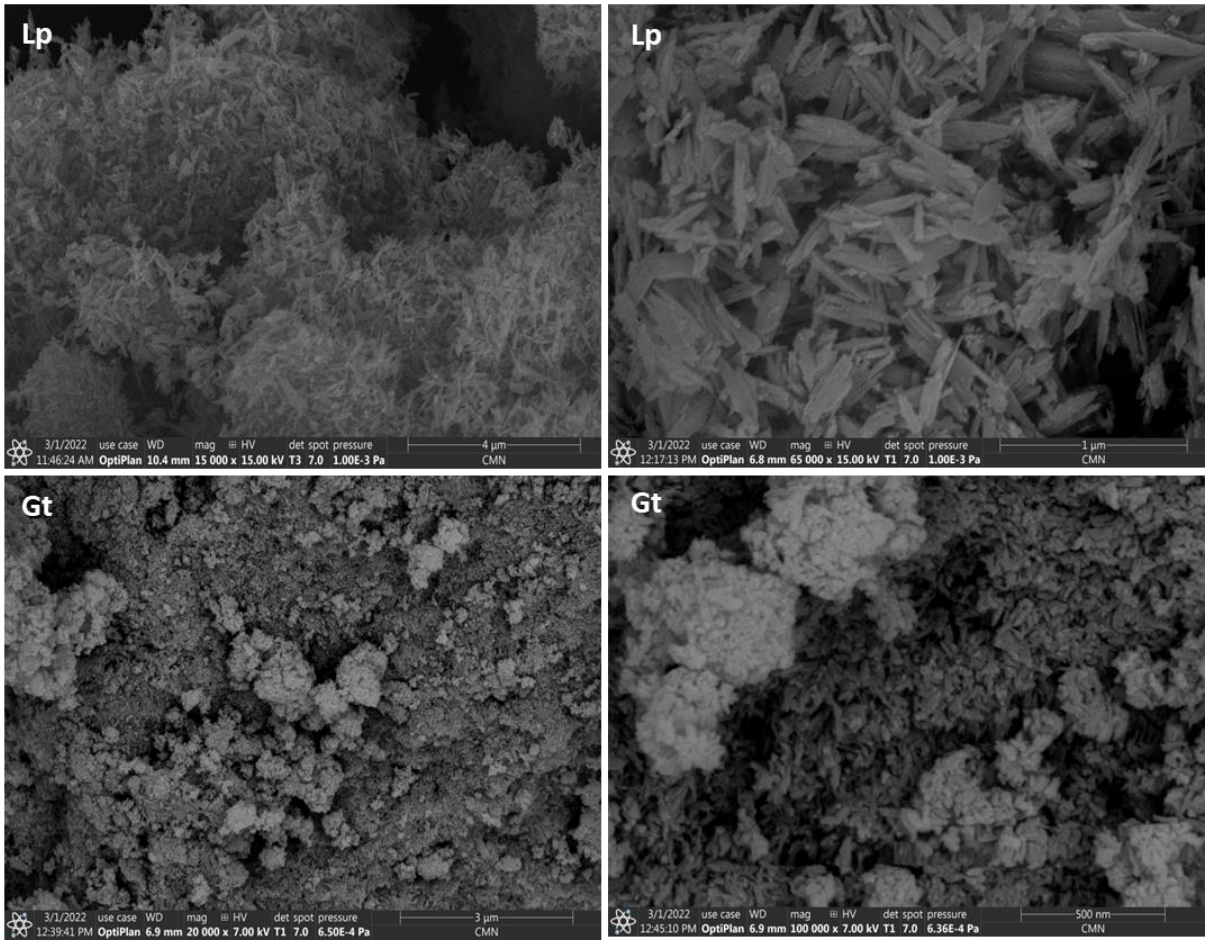

Fig. S32: Field-emission SEM micrographs of gold coated native pure lepidocrocite (Lp) and goethite (Gt). The micrographs show the typical needle-like shape crystals for lepidocrocite and nano-sized rod-like shape crystals for goethite.

References:

Cardenas-Jiron, G., Leal, D., Matsuhiro, B. and Osorio-Roman, I. O., 2011. Vibrational spectroscopy and density functional theory calculations of poly-D-mannuronate and heteropolymeric fractions from sodium alginate. J. Raman Spectrosc. 42(4): 870-878.

Chandıa, N., Matsuhiro, B. and Vásquez, A., 2001. Alginic acids in Lessonia trabeculata: characterization by formic acid hydrolysis and FT-IR spectroscopy. Carbohydr. Polym. 46(1): 81-87.

Langley, S., Gault, A., Ibrahim, A., Renaud, R., Fortin, D., Clark, I. D. and Ferris, F. G., 2009. A Comparison of the Rates of Fe(III) Reduction in Synthetic and Bacteriogenic Iron Oxides byShewanella putrefaciensCN32. Geomicrobiol. J. 26(2): 57-70.

Leal, D., Matsuhiro, B., Rossi, M. and Caruso, F., 2008. FT-IR spectra of alginic acid block fractions in three species of brown seaweeds. Carbohydr Res 343(2): 308-316.

Mikutta, C., Mikutta, R., Bonneville, S., Wagner, F., Voegelin, A., Christl, I. and Kretzschmar, R., 2008. Synthetic coprecipitates of exopolysaccharides and ferrihydrite. Part I: Characterization. Geochim. Cosmochim. Acta 72(4): 1111-1127.

Sartori, C., Finch, D. S., Ralph, B. and Gilding, K., 1997. Determination of the cation content of alginate thin films by FTIR spectroscopy. Polymer 38(1): 43-51.

Schwertmann, U. and Cornell, R. M., 2008. Iron oxides in the laboratory: preparation and characterization, John Wiley & Sons.

Chapter 5: General Conclusions and Future Work

The general conclusions of this thesis are as follows:

Chapter 2: The study demonstrates that the coprecipitation of OM with iron oxides significantly alters their structural and surface properties, leading to increased Fe extractability and decreased crystallinity with rising OM content, especially for lepidocrocite and goethite. These changes are consistent with OM-induced inhibition of crystal growth and reflect characteristics observed in naturally occurring BIOS. Chemical extractants such as 0.5 M HCl and ascorbate, commonly used as proxies for Fe bioavailability, showed a clear increase in extractable Fe with increasing OM content, suggesting a higher proportion of poorly crystalline, and presumably more labile, Fe phases. However, microbial Fe(III) reduction did not increase proportionally; for lepidocrocite and goethite-OM coprecipitates, reduction rates were equivalent to- and reduction extent only slightly higher than-those of their pure mineral counterparts. This disconnect highlights that chemical extractability does not necessarily equate to microbial bioavailability. Overall, the findings emphasize that OM-driven changes in mineral properties can influence chemical reactivity, but not always in ways that predict microbial behavior. Biogeochemical models must therefore distinguish between chemical and biological indicators of Fe availability to accurately assess the role of dissimilatory iron reduction in Fe and C cycling in natural environments.

Chapter 3: The study indicates that varying P loading, the sorption mechanism, and coprecipitation with OM play an important role in determining the reactivity of a commonly occurring iron oxide, 2-line ferrihydrite. Collectively, our findings show that coprecipitation is a less effective mechanism for stabilizing and sequestering P compared to adsorption. Moreover, the cooperative role of OM and P renders the P-OM-Fe coprecipitates less stable and more labile towards microbial and chemical reduction than OM-Fe coprecipitates with pre-adsorbed P or OM-Fe coprecipitates.

Interestingly, this same interaction appears to inhibit the transformation of ferrihydrite into more crystalline iron phases at high P loadings, suggesting a dual role where P and OM jointly increase solubility while suppressing crystallization sustaining further reduction and potential release of constituents. This suggests a fast turnover of P-OM-Fe within aquatic reducing environments, particularly eutrophic lakes. These findings highlight the complex interplay between P, OM, and Fe mineral phases and have important implications for nutrient cycling, contaminant mobility, and iron oxide stability in redox-dynamic environments.

Chapter 4: The study indicates that γ-irradiation at a relatively low dose (25 kGy) can significantly impact the physicochemical and mineralogical properties of OM-iron oxide coprecipitates. Even the mineralogically sensitive iron oxide, 2-line ferrihydrite, exhibited an increase in crystallinity following irradiation. These findings highlight a critical consideration for researchers employing γ-irradiation as a sterilization method: such treatment can modify the physicochemical properties of OM–Fe associations, potentially influencing their adsorptive behavior and bioavailability. Therefore, caution is warranted when interpreting results from irradiated samples, especially in studies aiming to assess natural geochemical reactivity or microbially mediated processes.

Future work:

OM is a heterogeneous mixture of molecular compounds formed by the decay of terrestrial organic material or produced in aquatic systems by microbiota, and it is ubiquitous in natural waters (Kleber et al., 2015). Thus, different types of OM possess different functional groups with variable reactivity towards iron oxides. Although we chose Na-alginate as the representative OM for this research future studies should further investigate the impact of different types of OM on the reactivity of lepidocrocite-OM and goethite-OM coprecipitates towards abiotic and biotic

reducing agents. Additionally, future studies should investigate how different types of OM influences the reactivity of P-OM-Fe coprecipitates. In our study, we did not investigate the release of OM following the reduction of P-OM-Fe coprecipitates and OM-Fe with pre-adsorbed P. Further, we only investigated the impact of the sorption mode of P on OM-Fe coprecipitates with a C/Fe ratio of 1.0 (mol:mol), although naturally occurring OM-Fe coprecipitates can have variable C/Fe ratio that is less or above a ratio of 1. Thus, future investigations should determine the impact of varying OM content on the reactivity of P-OM-Fe coprecipitates. Overall, these investigations would enhance our understanding of the complex role of OM in regulating C, P and Fe cycling in terrestrial and aquatic environments.

The past decade has seen a spike in research pertaining to understanding OM-Fe associations under oxic and anoxic conditions. Given how important it is to determine the fate of OM in relation to the rise of CO_2 and global warming, this type of research will likely continue to expand. Therefore, researchers may seek sterilization methods to study naturally occurring samples. Although we investigated the impact of γ-irradiation on alginate-iron oxide coprecipitates, different types of OM will likely yield varying results. Given the complexity of OM, naturally occurring OM may respond differently to γ-irradiation (e.g. mechanism of degradation) as a consequence of varying functional groups and complex molecular structure. Therefore, future studies should investigate the impact of γ-irradiation on the physicochemical and mineralogical properties, and bioavailability of OM-Fe adsorbates/coprecipitates of varying OM type and content. Furthermore, we only considered the impact of γ-irradiation at a relatively low dose, however microbes exhibit varying tolerance to radiation and may require a higher dose (up to 75 kGy). A higher dose may lead to higher changes.

The γ-irradiation of alginate and the production of alginate oligosaccharides has found several applications as a plant growth promoter in agricultural industries (Liu et al., 2019a; Wang et al., 2019; Vasudevan et al., 2021; Baig et al., 2024; Li et al., 2024). We also observed the production of Fe(III)-oligosaccharides complexes following the irradiation of the alginate-iron oxide coprecipitates (Figure 1-5). The complexes were stable and remained in solution for ~4 years at 4°C or 22°C at pH ~7. These complexes could be used to address Fe deficiency in plants, whilst promoting growth.

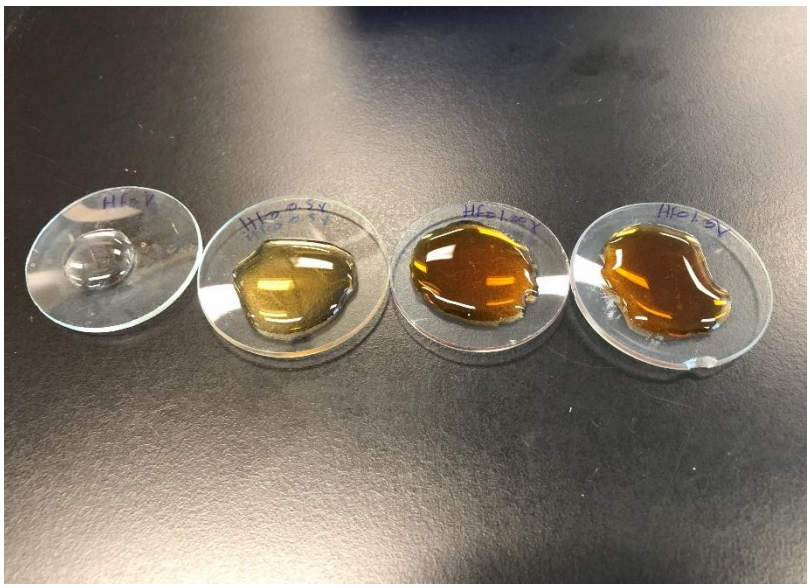

Figure 1: Filtered (0.22 μm) supernatant following the γ-irradiation of ferrihydrite-alginate coprecipitates with varying C content (C/Fe 0, 0.5, 1.0, and 1.5 mol:mol). The picture shows dissolved Fe(III)-alginate oligosaccharides that formed following γ-irradiation at 25 kGy.

References

Baig, J. A., Akhtar, K. and Talpur, F. N., 2024. Production of alginate oligosaccharides and their plant growth-promoting activity: Effect of ionizing radiation processing. Handbook of Natural Polymers, Volume 2, Elsevier**:** 377-399.

Kleber, M., Eusterhues, K., Keiluweit, M., Mikutta, C., Mikutta, R. and Nico, P. S., 2015. Mineral–Organic Associations: Formation, Properties, and Relevance in Soil Environments. 130: 1-140.

Li, Z., Duan, S., Ouyang, X., Song, S., Chen, D., Fan, X., Ding, H. and Shen, H., 2024. Coupled soil moisture management and alginate oligosaccharide strategies enhance citrus orchard production, water and potassium use efficiency by improving the rhizosphere soil environment. Agric. Water Manage. 297: 108828.

Liu, J., Yang, S., Li, X., Yan, Q., Reaney, M. J. and Jiang, Z., 2019. Alginate oligosaccharides: Production, biological activities, and potential applications. Comprehensive Reviews in Food Science and Food Safety 18(6): 1859-1881.

Vasudevan, U. M., Lee, O. K. and Lee, E. Y., 2021. Alginate derived functional oligosaccharides: Recent developments, barriers, and future outlooks. Carbohydr. Polym. 267: 118158.

Wang, B., Wan, Y., Zheng, Y., Lee, X., Liu, T., Yu, Z., Huang, J., Ok, Y. S., Chen, J. and Gao, B., 2019. Alginate-based composites for environmental applications: a critical review. Crit. Rev. Environ. Sci. Technol. 49(4): 318-356.